SANDIA REPORT

SAND2005-2743
Unlimited Release
Printed April 26, 2005

Multi-model Simulation for Optimal Control of Aeroacoustics

Guoquan Chen (Rice University)

S. Scott Collis (Sandia National Laboratories)

Prepared by
Sandia National Laboratories
Albuquerque, New Mexico 87185 and Livermore, California 94550

Sandia is a multiprogram laboratory operated by Sandia Corporation,
a Lockheed Martin Company, for the United States Department of Energy's
National Nuclear Security Administration under Contract DE-AC04-94-AL85000.

Issued by Sandia National Laboratories, operated for the United States Department of Energy by Sandia Corporation.

Available to DOE and DOE contractors from
U.S. Department of Energy
Office of Scientific and Technical Information
P.O. Box 62
Oak Ridge, TN 37831

Telephone: (865) 576-8401
Facsimile: (865) 576-5728
E-Mail: reports@adonis.osti.gov
Online ordering: http://www.doe.gov/bridge

Available to the public from
U.S. Department of Commerce
National Technical Information Service
5285 Port Royal Rd
Springfield, VA 22161

Telephone: (800) 553-6847
Facsimile: (703) 605-6900
E-Mail: orders@ntis.fedworld.gov
Online ordering: http://www.ntis.gov/ordering.htm

SAND2005-2743XX
Unlimited Release
Printed on April 26, 2005

Multi-model Simulation for Optimal Control of Aeroacoustics

by

Guoquan Chen
Mechanical Engineering & Materials Science
Rice University

S. Scott Collis
Computational Mathematics & Algorithms
Sandia National Laboratories [1]

[1]Sandia is a multiprogram laboratory operated by Sandia Corporation, a Lockheed-Martin Company, for the United States Department of Energy under Contract DE-AC04-94AL85000.

Abstract

Flow-generated noise, especially rotorcraft noise has been a serious concern for both commercial and military applications. A particular important noise source for rotorcraft is Blade-Vortex-Interaction (BVI) noise, a high amplitude, impulsive sound that often dominates other rotorcraft noise sources. Usually BVI noise is caused by the unsteady flow changes around various rotor blades due to interactions with vortices previously shed by the blades. A promising approach for reducing the BVI noise is to use on-blade controls, such as suction/blowing, micro-flaps/jets, and smart structures. Because the design and implementation of such experiments to evaluate such systems are very expensive, efficient computational tools coupled with optimal control systems are required to explore the relevant physics and evaluate the feasibility of using various micro-fluidic devices before committing to hardware.

In this thesis the research is to formulate and implement efficient computational tools for the development and study of optimal control and design strategies for complex flow and acoustic systems with emphasis on rotorcraft applications, especially BVI noise control problem. The main purpose of aeroacoustic computations is to determine the sound intensity and directivity far away from the noise source. However, the computational cost of using a high-fidelity flow-physics model across the full domain is usually prohibitive and it might also be less accurate because of the numerical diffusion and other problems. Taking advantage of the multi-physics and multi-scale structure of this aeroacoustic problem, we develop a multi-model, multi-domain (near-field/far-field) method based on a discontinuous Galerkin discretization. In this approach the coupling of multi-domains and multi-models is achieved by weakly enforcing continuity of normal fluxes across a coupling surface. For our interested aeroacoustics control problem, the adjoint equations that determine the sensitivity of the cost functional to changes in control are also solved with same approach by weakly enforcing continuity of normal fluxes across a coupling surface. Such formulations have been validated extensively for several aeroacoustics state and control problems.

A multi-model based optimal control framework has been constructed and applied to our interested BVI noise control problem. This model problem consists of the interaction of a compressible vortex with Bell AH-1 rotor blade with wall-normal

velocity used as control on the rotor blade surface. The computational domain is decomposed into the near-field and far-field. The near-field is obtained by numerical solution of the Navier–Stokes equations while far away from the noise source, where the effect of nonlinearities is negligible, the linearized Euler equations are used to model the acoustic wave propagation. The BVI wave packet is targeted by defining an objective function that measures the square amplitude of pressure fluctuations in an observation region, at a time interval encompassing the dominant leading edge compressibility waves. Our control results show that a 12dB reduction in the observation region is obtained. Interestingly, the control mechanism focuses on the observation region and only minimize the sound level in that region at the expense of other regions. The vortex strength and trajectory get barely changed. However, the optimal control does alter the interaction of the vortical and potential fields, which is the source of BVI noise. While this results in a slight increase in drag, there is a significant reduction in the temporal gradient of lift leading to a reduction in BVI sound levels.

Acknowledgments

The first author would like to thank my advisor, Dr. Scott Collis, for his guidance and support in my research over the past four years. He has always been ready with much appreciated encouragement and advice. His sharp mind and hands-on help have helped me not to get lost along the curvy road, whether through inspiring my idea, or simply helping to track down coding problems from time to time. My gratitude to him is beyond description and I look forward to further collaborations in the future.

I would like to thank Dr. Pol D. Spanos, Dr. Michael M. Carroll and Dr. Matthias Heinkenschloss for serving on my dissertation committee. My thanks goes to the members of our research team: Dr. Kaveh Ghayour, Dr. Alexander Dobrinsky, and Srinivas Ramakrishnan. The team is excellent and we learned a lot from each other. And special thanks to Dr. Matthias Heinkenschloss and Dr. Kaveh Ghayour in Rice Aeroacoustic Control group, I learned a lot from the broad and beneficial discussions with them. My thanks also goes to all my friends, especially Fuchun Gao, Zhongping Jian, Hongli Zhan for their enthusiastic help and encouragement. For her generous assistance during the thesis revision, I would like to acknowledge Ms. Janie Hammons of Rice CAIN project.

My special thanks are for my wife, my parents and parents-in-law, for sharing my ups and downs during those tough days, and for their full support and encouragement in my endeavor. This thesis is dedicated to my son, Daniel.

This research has been supported in part by the Texas Advanced Technology Program under Grant numbers 003604-017-1997 and 003604-0011-2001. Computations were performed on an 82 processor Pentium IV Beowulf cluster that was purchased with the aid of NSF MRI grant 0116289-2001. Some computations were performed on the Rice Terascale Cluster funded by NSF under Grant EIA-0216467, Intel, and HP. The second author's work on this project has been partially supported by the ASC Algorithms Program as funded by the United States Department of Energy under Contract DE-AC04-94AL85000.

Nomenclature

Accents, Superscripts, and Subscripts

$()_{max}$	Maximum value
$()_{rms}$	Root-mean-square value
$\overline{()}$	Mean flow variables
$()'$	Disturbance quantity
(x, y, z)	Cartesian coordinates
x_i	Cartesian coordinates
(u, v, w)	Velocity components in the Cartesian coordinates
u_i	Velocity components in the Cartesian coordinates
$\mathbf{U}$	Vector of conservative variables
$\boldsymbol{u}$	Vector of primitive variables
$\boldsymbol{u}'$	Vector of primitive fluctuation variables
$\bar{\boldsymbol{u}}$	Vector of primitive mean flow variables
$\boldsymbol{Q}$	Vector of quasi-conservative variables
$\mathbf{Y}$	Vector of primitive variables
$\overline{\mathbf{Y}}$	Vector of primitive mean flow variables
$\mathbf{y}$	Vector of primitive fluctuation variables
U_∞	The magnitude of the freestream velocity
t	Time

Re	Reynolds number
ρ	Fluid density
p	Pressure
T	Fluid temperature
e	Internal energy
E	Total energy
c	Sound speed
k	Wavenumber magnitude
c_p	Specific heat at constant pressure
c_v	Specific heat at constant volume
τ_{ij}	Stress tensor
Ω	Total computational domain
Γ	The boundary of the computational domain
Γ_c	The control boundary
Γ_s	The solid wall
Γ_∞	The far filed boundary
μ	Dynamic viscosity coefficient
R	Surface curvature
L	Reference length scale

Abbreviations

CG	Conjugate Gradient method
ANS	Adjoint Navier-Stokes
DNS	Direct Numerical Simulation
LES	Large Eddy Simulation
RANS	Reynolds Averaged Navier Stokes
LHS	Left-Hand-Side
LNS	Linearized Navier-Stokes
LEE	Linearized Euler equation
NS	Navier–Stokes
RHS	Right-Hand-Side
TKE	Terminal Kinetic Energy
FD	Finite Difference
DG	Discontinuous Galerkin
DGM	Discontinuous Galerkin method
CAA	Computational Aeroacoustics
CFL	Courant–Friedrichs–Lewy number

Table of Contents

Abstract 3

Acknowledgments 5

Nomenclature 7

1 Introduction 1

1.1 Flow Control 1

1.2 Aeroacoustics 1

1.3 Motivation and Objectives 8

1.4 Accomplishments and Overview 10

2 Governing Equations 15

2.1 Nondimensionalization 15

2.2 Euler 16

2.3 Navier-Stokes 18

2.4 Linearized Euler 18

2.4.1 Formulation of the Conservative Variable 19

2.4.2 Formulation of the Primitive Variable 20

2.5 Wave Equation 21

3 Numerical Discretization 23

3.1 Discontinuous Galerkin Method 24

3.2 Weak Formulation 24

3.2.1 Navier–Stokes 24

3.2.2 Euler 28

3.2.3 Linearized Euler Equation (LEE) 29

3.2.4 Wave 31

3.2.5 Remarks . . . 32
3.3 Multi-domain/Multi-model simulations . . . 32
3.3.1 Motivation . . . 33
3.3.2 Formulation . . . 36
3.3.3 Implementation . . . 38

4 Optimal Control Formulations . . . 43
4.1 The Objective Functional . . . 43
4.1.1 Cost Functional . . . 44
4.1.2 Regularization . . . 44
4.2 Adjoint equations . . . 45
4.2.1 Adjoint Euler . . . 45
4.2.2 Adjoint Navier–Stokes . . . 45
4.2.3 Adjoint Linearized Euler . . . 46
4.2.4 Adjoint Wave . . . 46
4.3 Adjoint Formulations for Multi-Model System . . . 46
4.3.1 State Coupling . . . 47
4.3.2 Adjoint Coupling . . . 49
4.3.3 Optimal Control of Multi-model System . . . 55
4.4 Optimization Algorithm . . . 55
4.4.1 Conjugate Gradient . . . 55

5 State Validation . . . 59
5.1 Planar Acoustic Waves . . . 59
5.1.1 1D Gaussian Acoustics . . . 60
5.2 Acoustic Scattering from Cylinder . . . 62
5.2.1 Euler/Wave . . . 65
5.3 Vortex-Cylinder Interaction . . . 65
5.4 Vortex-Rotor Interaction . . . 68

6 Optimal Control of Fluids Problem . . . 99
6.1 Acoustic Pulse Reflection . . . 99
6.1.1 Boundary Implementation . . . 100
6.1.2 Results Analysis . . . 101
6.2 TKE control of Vortex Rebound . . . 102
6.3 Cylinder Wake Control . . . 105
6.3.1 Steady Control . . . 105
6.3.2 Unsteady Control . . . 109

7 Optimal Control for the Coupling Systems . . . 133
7.1 Problem Setup . . . 133
7.2 Result and Analysis . . . 135
7.2.1 Noise Reduction . . . 135
7.2.2 Adjoint Analysis . . . 136
7.2.3 Discussion . . . 136
7.3 Summary . . . 138

8 Conclusions and Future Work . . . 147
8.1 Conclusions . . . 147
8.2 Future Work . . . 148

A Derivation of Adjoint Equations . . . 151
A.1 Adjoint Euler and Navier–Stokes Equations and Gradient Equations . 151
A.1.1 Adjoint Equation and Boundary Condition for Euler . . . 160
A.1.2 Adjoint Equation and Boundary Condition for Navier–Stokes . 162
A.1.3 Adjoint Far Field Boundary . . . 175

B Spatial Discretization of Adjoint Navier-Stokes Equations . . . 177
B.1 Transformation of the Adjoint Equations . . . 177
B.1.1 Spatial Discretization in DG . . . 179

C Optimal Control of Burgers Equation 183
C.1 Problem Formulation 184
C.1.1 Governing Equations 184
C.1.2 Objective Functional 185
C.1.3 Optimality Equations 185
C.2 Numerical Method 187
C.2.1 Spatial Discretization 187
C.2.2 Temporal Discretization 189
C.3 Results 189
C.3.1 Distributed Control 190
C.3.2 Boundary Control 192
C.3.3 Summary of Burgers Control 200

Bibliography 203

List of Tables

6.1 Comparison of acoustics reflection $J_{obs} = \frac{1}{2}\int_{t_0}^{t_f}\int_{\Omega_{\text{obs}}}\alpha_0(p-p_a)^2 d\mathbf{x}dt$ using optimal control, Riemann boundary and sponge. Data for FD is from [35] 111

6.2 Comparison of objective function values for boundary control of terminal kinetic energy with [36, 38] 111

List of Figures

1.1 BVI blade surface pressure from the review [125] 13
1.2 Aerodynamics of blade-vortex interactions from [125] 13
1.3 Schematic of parallel BVI on a helicopter from [84] 14

3.1 Schematic of DGM discretization [31], the solution and weighting functions discontinuous across element interfaces 41
3.2 Coupling of different fidelity models in the multi-domain, near-field and far-field 42
3.3 Coupling NS and LEE at two element edges 42

4.1 Schematic of optimal control problem for coupled system 57
4.2 Optimization strategy for the multi-model system using the adjoint approach 57
4.3 Schematic of multi-domain/model for blade-vortex interaction 58
4.4 Schematic of adjoint coupling for the NS/LEE coupling 58

5.1 Inviscid vortex cylinder interaction 66
5.2 Schematic of Bell AH1 rotorblade vortex interaction 69
5.3 One-dimensional Gaussian pulse propagation using 25 elements with polynomial order $p = 5$, quadrilateral mesh 71
5.4 LEE: density fluctuation ρ' with polynomial order $p = 3$: —— initial profile; ---- the profile at $t = 12$; 71
5.5 LEE: density fluctuation ρ' with polynomial order $p = 5$: —— initial profile; ---- the profile at $t = 12$; 72
5.6 LEE: density fluctuation ρ' with polynomial order $p = 8$: —— initial profile; ---- the profile at $t = 12$; 72
5.7 Wave: density fluctuation ρ' with polynomial order $p = 5$: —— initial profile; ---- the profile at $t = 12$; 73

5.8 Euler: density fluctuation ρ' with polynomial order $p = 5$: —— initial profile; ---- the profile at $t = 12$; 73
5.9 Relative error Vs. Polynomial order p 74
5.10 Mesh for the planar acoustics scattering with the circular cylinder 75
5.11 Scattered pressure from Euler solver 75
5.12 (a) Comparison of RMS pressure along the ray $\theta = \pi$, (b) Comparison of RMS pressure along radius $r = 10$ 76
5.13 Full domain for wave/Euler coupling 77
5.14 Total pressure (incident and scattered pressure) near the cylinder 78
5.15 Scattered pressure 78
5.16 (a) Comparison of RMS pressure along the ray $\theta = \pi$, (b) Comparison of RMS pressure along radius $r = 10$ (that is outside the coupling interface). 79
5.17 Domain/model decomposition for inviscid vortex cylinder interaction . . 80
5.18 Mesh (grid+vorticity) for inviscid vortex cylinder interaction 80
5.19 Pressure contours from direct Euler and Euler/Wave coupled solver, both are in the same contour levels: (a) Pressure contour from direct Euler solver at $t = 15.0$, (b) Pressure contour from coupled Euler/Wave solver at $t = 15.0$. 81
5.20 Pressure closeup around the coupling interface 82
5.21 Time history at P_0 using the smaller coupling interface: (a) Density ρ, (b) Pressure p, (c) Velocity u (d) Velocity v. —— Euler/Wave; ---- Euler/LEE; ····· Euler; 83
5.22 Time history at P_1 using the smaller coupling interface: (a) Density ρ, (b) Pressure p, (c) Velocity u (d) Velocity v. —— Euler/Wave; ---- Euler/LEE; ····· Euler. 84
5.23 Time history at P_2 using the smaller coupling interface: (a) Density ρ, (b) Pressure p, (c) Velocity u (d) Velocity v. —— Euler/Wave; ---- Euler/LEE; ····· Euler. 85

5.24 Time history at P_0 using the larger coupling interface: (a) Density ρ, (b) Pressure p, (c) Velocity u (d) Velocity v. —— Euler/Wave; ---- Euler/LEE; ····· Euler. 86
5.25 Time history at P_1 using the larger coupling interface: (a) Density ρ, (b) Pressure p, (c) Velocity u (d) Velocity v. —— Euler/Wave; ---- Euler/LEE; ····· Euler. 87
5.26 Time history at P_2 using the larger coupling interface: (a) Density ρ, (b) Pressure p, (c) Velocity u (d) Velocity v. —— Euler/Wave; ---- Euler/LEE; ····· Euler. 88
5.27 Pressure error history $|p-p_{\text{Euler}}|$ at P_0: —— Euler/LEE with large surface; ---- Euler/LEE with small surface; ····· Euler/Wave with large surface; —·— Euler/Wave with small surface. 89
5.28 Pressure error history $|p-p_{\text{Euler}}|$ at P_1: —— Euler/LEE with large surface; ---- Euler/LEE with small surface; ····· Euler/Wave with large surface; —·— Euler/Wave with small surface. 89
5.29 Pressure error history $|p-p_{\text{Euler}}|$ at P_2: —— Euler/LEE with large surface; ---- Euler/LEE with small surface; ····· Euler/Wave with large surface; —·— Euler/Wave with small surface. 90
5.30 Bell AH1 rotorblade vortex interaction: Motivation 91
5.31 Bell AH1 rotorblade vortex interaction: scattered pressure evolution . . . 91
5.32 Scattered pressure contours from direct NS and NS/Wave coupled solver, both are in the same contour levels: (a)Scattered pressure contour from direct NS solver at $t = 68.4$, (b)Scattered pressure contour from coupled NS/Wave solver at $t = 68.4$. 92
5.33 Time history at P_0: (a) Density ρ, (b) Pressure p, (c) Velocity u (d) Velocity v. —— NS/Wave; ---- NS/LEE; ····· NS. 93
5.34 Time history at P_1: (a) Density ρ, (b) Pressure p, (c) Velocity u (d) Velocity v. —— NS/Wave; ---- NS/LEE; ····· NS. 94

5.35 Time history at P_2: (a) Density ρ, (b) Pressure p, (c) Velocity u (d) Velocity v. —— NS/Wave; ---- NS/LEE; ····· NS. 95
5.36 Time history at P_3: (a) Density ρ, (b) Pressure p, (c) Velocity u (d) Velocity v. —— NS/Wave; ---- NS/LEE; ····· NS. 96
5.37 Pressure error history $|p - p_{NS}|$ at P_0: —— NS/LEE; ---- NS/Wave. . 97
5.38 Pressure error history $|p - p_{NS}|$ at P_1: —— NS/LEE; ---- NS/Wave. . 97
5.39 Pressure error history $|p - p_{NS}|$ at P_2: —— NS/LEE; ---- NS/Wave. . 98
5.40 Pressure error history $|p - p_{NS}|$ at P_3: —— NS/LEE; ---- NS/Wave. . 98

6.1 Contours of $p - p_a$ at instants $t = 2, 4, 8, 9$ without control, FD (left) and DG (right). Data of FD is from [35] 112
6.2 Contours of $p - p_a$ at instants $t = 2, 4, 8, 9$ with optimal control, FD(left) and DG (right). Data for FD is from [35] 113
6.3 Evolution of the Objective functional from FD and DG: • result from FD; ▲ result from DG. 114
6.4 Time history of pressure reflection: —— reflection from optimal control; ---- reflection using the Riemann boundary treatment; ····· reflection using the sponge. 114
6.5 Contours of KE at instants $t = 0, 10, 20, 30, 40$ without and with control, No control (left) and Optimal control(right). 115
6.6 Contours of vorticity at instants $t = 0, 10, 20, 30, 40$ without and with control, No control (left) and Optimal control(right). 116
6.7 Optimal wall-normal velocity distributions for TKE control. 117
6.8 Evolution of the objective functional J: —— J at $p = 5$, $\alpha_1 = 0.005$ and $\alpha_2 = 0$, ---- J at $p = 5$, $\alpha_1 = 0.005$ and $\alpha_2 = 0.002$, ····· J at $p = 7$, $\alpha_1 = 0.005$ and $\alpha_2 = 0.002$. 118
6.9 Evolution of the objective functional J_{obs}: —— J_{obs} at $p = 5$, $\alpha_1 = 0.005$ and $\alpha_2 = 0$, ---- J_{obs} at $p = 5$, $\alpha_1 = 0.005$ and $\alpha_2 = 0.002$, ····· J_{obs} at $p = 7$, $\alpha_1 = 0.005$ and $\alpha_2 = 0.002$. 118

6.10 Element mesh for cylinder wake control. 119
6.11 Contours of streamwise momentum, ρu, for the uncontrolled steady-state solution at $Re = 20$. 119
6.12 Contours of streamwise momentum, ρu, for one vortex shedding period for the uncontrolled flow at $Re = 100$: (a) $t = 0.2$, (b) $t = 0.8$, (c) $t = 1.4$, and (d) $t = 2$. 120
6.13 Optimization history for the objective functional and the norm of the gradient of the objective functional squared. The optimization time window is one shedding period which corresponds to 2 time units: • gradient norm squared; ▲ objective functional. 121
6.14 Contours of streamwise momentum, ρu, for the controlled flow at $Re = 100$: (a) $t = 2$, (b) $t = 14$, (c) $t = 26$, (d) $t = 30$, (e) $t = 40$. Note that the steady optimal control is obtained over the first two time units, but is then used throughout the remainder of the computation. 122
6.15 Time history of drag coefficients for $Re = 20$ and $Re = 100$ with/ without steady control: —— $Re = 20$ without control; ---- $Re = 100$ without control; ····· $Re = 100$ with control. 123
6.16 Time history of drag coefficients with the flow advancing using the optimal control. 123
6.17 Time history of lift coefficients for $Re = 20$ and $Re = 100$ with/ without steady control: —— $Re = 20$ without control; ---- $Re = 100$ without control; ····· $Re = 100$ with control. 124
6.18 Time history of lift coefficients with the flow advancing using the optimal boundary 124
6.19 Optimal boundary control profile after 16 control iterations 125
6.20 Contours of streamwise momentum, ρu, for the uncontrolled flow at $Re = 100$: (a) $t = 1.2$, (b) $t = 2.4$, (c) $t = 3.6$, (d) $t = 4.8$, (e) $t = 6.0$. 126

6.21 Contours of streamwise momentum, ρu, for the controlled flow with temporal regularization at $Re = 100$: (a) $t = 1.2$, (b) $t = 2.4$, (c) $t = 3.6$, (d) $t = 4.8$, (e) $t = 6.0$. 127

6.22 Optimization history for the objective functional J and the pure objective J_{obs}, the optimization time window is two shedding period which corresponds to 6 time units: —— J_{obs} without g_t, ····· J_{obs} with g_t, ---- J without g_t, —-— J with g_t 128

6.23 Time history of drag coefficients for $Re = 100$ with/without control: —— $Re = 100$ without control; ---- $Re = 100$ with control, $\omega_1 = 360$, $\omega_2 = 0$; ····· $Re = 100$ with control, $\omega_1 = 30$, $\omega_2 = 60$. 129

6.24 Time history of lift coefficients for $Re = 100$ with/without control: —— $Re = 100$ without control; ---- $Re = 100$ with control, $\omega_1 = 360$, $\omega_2 = 0$; ····· $Re = 100$ with control, $\omega_1 = 30$, $\omega_2 = 60$. 129

6.25 Optimal boundary control profile after 13 control iterations without $g_{,t}$. 130

6.26 Optimal boundary control profile after 20 control iterations with $g_{,t}$ . . . 130

6.27 Optimal boundary control profile after 20 control iterations with $g_{,t}$ at $t = 6.0$ 131

7.1 Optimal control of BVI noise: problem setup 139

7.2 Contours of scattered pressure $p - p_{\mathrm{a}}$ at instants $t = 1.36$, 1.76, 2.16, 2.56, 2.96 for no control (left) and optimal control (right). 141

7.3 Time history of pressure at observations (a) station 1, (b) station 2, (c) station 3, (d) station 4: —— no control; ---- optimal control. 142

7.4 Adjoint variable λ_4, the time goes backward in the adjoint solution (a) t=2.56, (b) t=2.16, (c) t=1.76, (d) t=1.40 143

7.5 Vortex trajectories with/without control during the interaction 144

7.6 Vorticity field $w - w_0$(a) t=1.76, (b) t=2.16, (c) t=2.56, (d) t=2.96 . . . 145

7.7 Time history of drag coefficients C_d for BVI noise control with/ without control: —— no control; ---- optimal control. 146

7.8 Time history of lift coefficients C_l for BVI noise control with/ without control: —— no control; ---- optimal control. 146

C.1 Distributed control of Burgers equation for $p = 4$: —— initial profile; ---- the profile without control at $t = 1$; —-— profile with control at $t = 1$ after first iteration; —·— profile with control at $t = 1$ after second iteration; ····· profile with control $t = 1$ after third iteration. 191

C.2 Distributed control profile after fourth iteration at $t = 0.2$, 0.4, 0.6, and 0.8.191

C.3 Objective functional, J, at different iterations for distributed control: ▪ $p = 2$; △ $p = 4$; ◇ $p = 6$. 192

C.4 State solution with prescribed Dirichlet boundary condition $\phi_L^* = 2t^2$ for $p = 4$: —··— initial profile; —— the profile at $t = 0.2$; ---- profile at $t = 0.4$; —·— profile at $t = 0.6$; ····· profile at $t = 0.8$; ––– profile at $t = 1$. 194

C.5 Final optimal state solution using Dirichlet boundary control for $p = 4$: —··— initial profile; —— the profile at $t = 0.2$; ---- profile at $t = 0.4$; —·— profile at $t = 0.6$; ····· profile at $t = 0.8$; ––– profile at $t = 1$. . . 194

C.6 Iteration history for Dirichlet optimal control with $p = 4$. The arrow shows the direction of increasing optimization iterations. 195

C.7 Iteration history for the error in the Dirichlet optimal control with $p = 4$. The arrow shows the direction of increasing optimization iterations. . . . 195

C.8 Evolution of the objective functional, J, for Dirichlet control, ▪ $p = 2$; • $p = 4$; △ $p = 6$; ▽ $p = 7$. 196

C.9 State solution with prescribed Neumann boundary condition $\phi_R^* = -31.52(1-2\sqrt{t})$ using $p = 4$: —— initial profile; ---- the profile at $t = 0.25$; —·— profile at $t = 0.5$; ····· profile at $t = 0.75$; ––– profile at $t = 1$. . . 197

C.10 Final optimal state solution for Neumann boundary control using $p = 4$: —— initial profile; ---- the profile at $t = 0.25$; —·— profile at $t = 0.5$; ····· profile at $t = 0.75$; ––– profile at $t = 1$. 197

C.11 Iteration history for Neumann optimal control using $p = 4$. The arrow shows the direction of increasing optimization iterations. 198

C.12 Iteration history for the error in the Neumann optimal control for $p = 4$. The arrow shows the direction of increasing optimization iterations. . . . 198

C.13 Evolution of the objective functional, J, for optimal Neumann boundary control: ▪ $p = 2$; • $p = 4$; △ $p = 6$; ▽ $p = 7$. 199

C.14 Iteration history for Neumann boundary control starting from initial control $\phi_R = -31.52(1 - 2\sqrt{t}) + 30t(1 - t)$ and using $p = 6$. The arrow shows the direction of increasing optimization iterations. 200

C.15 Iteration history for the error in the Neumann boundary control starting from initial control $\phi_R = -31.52(1 - 2\sqrt{t}) + 30t(t_f - t)$ and using $p = 6$. The arrow shows the direction of increasing optimization iterations. . . . 201

C.16 Comparison of objective functionals J for Neumann control with different initial control profiles using $p = 6$: ▴ initial control profile $\phi_R = -31.52(1 - 2\sqrt{t_f}t/t_f)$; • initial control profile $\phi_R = -31.52(1 - 2\sqrt{t}) + 30t(t_f - t)$. . 201

Chapter 1

Introduction

1.1 Flow Control

Flow control is a science at the intersection of several disciplines: fluid dynamics, control theory, and numerical methods. It aims to achieve a desired objective by altering the flow characteristics passively or actively. Such ability to actively or passively manipulate the flow field to effect a desired change is very important; it offers the great potential to modify the complex flows, which may lead to drag reduction, lift enhancement and flow induced noise suppression, *etc.*

Because of our special interest in the noise suppression and control, both passive and active control strategies can be employed to suppress flow-induced noise. In the next session, we will review the background and current progress of the aeroacoustics research and the noise control techniques.

1.2 Aeroacoustics

Generally, noise is undesired sound. It usually denotes audible pressure fluctuations in the ambient air, but it can also propagate, reflect, refract, scatter and dissipate as well in liquids and solids. Particularly flow-induced noise (*i.e.,* acoustics generated by a fluid flow) is our primary concern.

Flow-induced noise hasn't drawn enough attention until the environment protection and the several noise regulations from Federal Aviation Agency (FAA) due to the increasing use of airplanes and helicopters. Since then, much research work has been carried on to study the mechanisms of the aerodynamic sound and find ways

for the reduction of the noise. Both theoretical and experimental studies using the flight-test and wind-tunnel test are being conducted to investigate the basic noise mechanisms. Among many types of noise, aerodynamic noise generated from fluids is especially important, which includes turbine jet noise, impulsive noise due to unsteady flow around wings and rotors, and broadband noise due to inflow turbulence and boundary layer separated flow, *etc.* In [41], the field of aerodynamic sound (sometimes called aeroacoustics) is thought to have evolved around two fundamental problems, the first is to derive a physically accurate and mathematically rigorous definition of sound, the second is to predict the aeroacoustics and uncover the physical mechanisms of sound, which is also essential to control or modify them to achieve noise reduction and comply with noise regulations. Although for the first problem, the complete acoustics model has not been constructed, numerical simulation with a proper model has been employed for the acoustics source simulation and modeling, resulted from the development of the computational power. Once the sound source has been identified, the further concern is the acoustic propagation. Both two define a relatively new field: Computational Aeroacoustics (CAA). [55, 78–80] give very detailed review and current progress of CAA. Basically, CAA is concerned with the prediction of the aerodynamic sound source and the propagation of generated acoustics. In the sound source categories, there are several kinds of problem, one is related with the turbulence flow (*i.e.,* the turbulence generated noise), such as jet noise, boundary layer noise and shock/turbulence interaction noise. An accurate turbulence model is usually required for this case as done in many works of Reynolds Averaged Navier Stokes (RANS) [60], Large Eddy Simulation (LES) [118] or Direct Numerical Simulation (DNS) [49, 50]. The other general category of source noise is the impulsive noise generated by the rotating machinery, such as the helicopter rotor noise, propeller noise, fan noise, *etc.* For those problems, an Euler/Navier–Stokes or

even a full potential model [63] is adequate because the turbulence is not so important. Once the noise source is predicted, several approaches can be used to describe acoustics propagation. There are basically four approaches as reviewed in [79–81].

The first, also the obvious strategy, is to extend the computational domain for the full nonlinear Navier–Stokes equations far enough to encompass the location where the sound is calculated as done in [41]. It is also called full flow-field Computational Fluid Dynamics (CFD) in [79]. Such approach is too expensive and has many drawbacks. It requires tremendous computer storage and time because of the mesh refinement to resolve the far field acoustics. Furthermore, the dissipation and dispersion properties of traditional CFD numerical schemes tend to generate the artificial disturbance and damp the acoustic fluctuations. Both make it impractical to solve the full field Navier–Stokes equation for the large scale acoustics computation. It is a great challenge to solve the full field acoustics that requires a delicate numerical operator to avoid the numerical dissipation and dispersion. For this kind of full field acoustics solver, there are several specified numerical operators for the acoustics computation. One is the Dispersion Relation Preserving (DRP) scheme pioneered by Tam and Webb [114], another is the spectral like high order finite difference scheme by Lele [72]. Because of its high accuracy, low dispersion, and diffusion property [59], the discontinuous Galerkin (DG) method has been applied to the aeroacoustics computation. In [45] the full Euler equations are solved with DG method for the sound radiation from aircraft engine sources to the far field.

For the aeroacoustics problems, most CAA techniques are based on the domain split approach, separating the whole domain into two domains, *near field* with the nonlinear acoustic effects, and *far field* with the linear acoustics for the sound propagation. Among those techniques used to describe the sound propagation in the far field, one is the acoustic analogy, the nonlinear near-field CFD calculation plus

the application of an integral equation, the breakthrough work by Lighthill [75]. In the acoustic analogy, the Navier–Stokes equations are rearranged to be in wave-type form with some terms identified as part of the sound source in the right-hand of the equation. The far field sound pressure is then obtained by the volume integral of the domain containing the sound source. Based on the original Lighthill formula, several kinds of formulation [42, 48, 76, 95, 122] have been proposed and developed, considering the different sound-flow interactions and other effects. Among those formulas, the most general form is the Ffowcs-Williams Hawkings equation (*i.e.,* FW-H equation) [122] extended in the case of solid surfaces, which is an exact rearrangement of continuity and momentum equations into the form of an inhomogeneous wave equation with two surface source terms (monopoles and dipoles) and a volume source term (quadrupole). All the integrals are evaluated in the retarded time, so a long record of the time-history of the sound source solution must be kept for the integral. The challenge is from the volume integral for the quadrupole term, which is ignored in most of work. [15] gives more details. Instead of evaluating the near-field sound source numerically, the experimental data can also be used when available.

Besides the traditional acoustic analogy, the other surface-integral based method for the far field acoustics is the Kirchhoff method, which is thoroughly reviewed in [79] by Lyrintzis. Kirchhoff method consists of the numerical simulation of the nonlinear near or middle field sound source with far field sound propagation evaluated with surface integral around the domain containing all the nonlinear flow effects and the noise source, where it is assumed that the sound transmission is governed by the simple wave equation. It has quite a long history with the original idea from Kirchhoff for the electromagnetic wave as the classical formulation [66]. Morgans [86] derived a Kirchhoff formula for a moving surface, followed by some extended work by Farassat and Myers [47] by using the generalized function theory [46]. The biggest advantage

from Kirchhoff method compared with the FW-H equation, is avoiding the volume integral of quadrupole, but the tricky part is the location of the Kirchhoff surface, which can give misleading results and make the far field solution unreliable [16, 17]. For the detailed comparison between those Kirchhoff method and FW-H equations, [17] gives more details.

Similar to the first approach, but based on the domain and scale decomposition approach, the much simpler equations, which are often the Linearized Euler Equations (LEE), are used in the far field instead of solving the full field Navier–Stokes equations. Such approach is based on the domain (near field/far field) and variable decomposition (mean and fluctuation) with the very sound physical approximation that the acoustics propagation is hardly affected by the viscosity and the time-dependent acoustic perturbation is so small that it can be ignored compared with the convection velocity of the flow. For the near field, it is solved with a nonlinear solver, which may require the turbulence modeling depending on the specific physics problem. In the far field a less expensive linearized Euler is applied which makes the computation very efficient. The focus becomes how to couple the near field flow simulation and far field acoustics propagation. One approach is to define proper boundary conditions between the near field and far field as in the work done by Freund *et al.* [52], propeller noise prediction by Lim [77] and for the supersonic jet noise by Viswanathan *et al.* [120]. Another alternative is to rearrange the terms from the nonlinear field to the right hand of the acoustic equation as the source. Application of such techniques is given by Viswanathan *et al.* [119]. A slight modification of such approach is done by Djambazov *et al.* [43, 44], where they only consider the source term from the nonlinear sound source in the continuum equation. In 1997, Freund [51] further simplified the far field linearized Euler equations with a field of wave equations with the acoustics source from the temporal derivative of the density from the nonlinear

sound source, which can be transformed into the traditional acoustic analogy form. Such an approach has been applied in his work for the jet noise prediction [49].

When the aeroacoustics research is applied to the rotorcraft aeroacoustics from the helicopters, it becomes extremely complicated due to the combination of the rotation of the blades and the translation of the helicopter. It may be further complicated by other conditions as discussed in [84]. The rotorcraft noise generated by the aerodynamic interactions includes several kinds of noise source, broadband noise by the random fluctuations of the forces on the blades, the rotational noise by the rotor blades exerting a force on the air, the noise from thickness effects created when a rotor blade passes through and displaces the air, the high speed impulsive noise due to the shock wave occurring on the blade tips when a rotor blade travels fast enough and the Blade-Vortex Interaction (BVI) noise. BVI noise is one of the most important among the several types of helicopter noise. It is from the unsteady pressure fluctuations on a rotor blade due to interactions with vortices generated by previous blades. Figure 1.1 shows the contours of blade surface pressure. It usually happens when the trailing vortices pass close to the rotor blades and interacts with it in certain low speed, decent flight paths as in Figure 1.2. When the trailing vortex is nearly parallel to the blade, which is called parallel BVI, as in Figure 1.3, the BVI noise is the strongest because the whole blades along its entire span interacts with the vortex. Such phenomenon also provides a very good physics basis to simplify it as a two dimensional problem. BVI noise is loud, impulsive, tends to dominate other sources and propagates out-of-plane, usually forward and down at about 30 to 40 degree angle, which makes it more audible to the observer on the grounds and causes significant effects on both military detection and community annoyance when it occurs.

Extensive research, both experimental [14, 73, 83, 104] and computational [2, 18, 53, 68, 82, 112, 121, 123, 124] has been performed to investigate the aerodynamics and

the aeroacoustics mechanisms of the BVI noise. These studies have improved the basic physical understanding of the mechanisms generating rotor-blade interaction noise and also of controlling techniques. In particular, the experimental studies have shown that the intensity of BVI noise depends on many factors: the rotor blade tip shape and velocity, vortex strength and structure, the distance between the vortex and the subsequent rotor and the rotor wakes. Based on these research and studies, many methods have been proposed to control the noise, including flight path control, passive leading-edge suction, passive blade design and active rotor control. [125, 126] gives excellent review for the active control of rotorcraft noise. Active rotor control can take several forms including Higher-harmonic pitch control (HHC), individual blade control (IBC) and on-blade control technologies using smart structure/materials.

In general, the control of a complex physical process like BVI requires a thorough understanding of the underlying physics and mechanisms. Besides the extensive experimental work, a lot of numerical study using the computational aeroacoustics have been focused on predicting BVI noise with great success. However, very little work has been conducted for the control of BVI noise except some experiment work using the passive and active control design [7, 71, 103, 125, 126]. Due to the complexity of the BVI acoustics, prior research on the noise control has largely been through trial and error applications of various control strategies based on physical intuition. Such an approach is relatively useful to devise the control strategies. Considering the importance of the impact of BVI noise from the helicopter and other rotorcraft on the environment and military application and the complexity of BVI noise physics, it is very important to combine the efficient numerical method for the aeroacoustics simulation with the optimal control theory to devise the controls that are aware of the full physics of the BVI generation process. Given that, it will enhance our understanding of the fundamental aeroacoustic noise generation while enabling us to

evaluate the relevant physics about the rotorcraft noise. Such approach relies on the fidelity of the mathematical model of the flow physics, the efficiency and accuracy of the numerical method and the optimal control algorithm. With this approach we will be able to develop and evaluate different control strategies for noise reduction and guide the design of control strategies for this complex problem. It was first applied by Collis *et al.* [33] for a model BVI problem with some prior work for optimal control of flows governed by the unsteady compressible Navier–Stokes equations [36–38]. However, considering the complexity of the coupled physics inherent in BVI noise, the model vortex cylinder interaction problem in [33] can not represent the realistic problem with the complex rotor geometries and multi-structure physics. An efficient and high accuracy numerical method definitely needs to be developed to investigate the feasibility of using the wall-normal suction/blowing actuation for controlling the BVI noise, which should be able to deal with the complex geometries and take into account the flow physics of near-field and far-field.

1.3 Motivation and Objectives

The coupling of efficient and accurate computational fluid dynamics analysis with optimal control theory has the potential to advance active flow-control for complex flows including flows involving aeroacoustic noise generation, especially a particularly important noise source for rotorcraft–BVI noise. Recent advances in numerical algorithms and computer performance have enabled the computational simulation of flow induced noise. However, to better understand the relevant physics and devise control necessary to minimize the noise, coupling the optimal control theory with the high-fidelity computational fluid dynamics simulation to devise the control is very necessary.

The overall objective of the present research is two fold. The first is to develop

efficient physical model and numerical methods which can be used to efficiently and accurately compute the near field hydrodynamics (*i.e.,* sound source) and the far field acoustics. It will be very useful to study the relevant flow physics of the rotorcraft acoustics and to exploit the multi-physics and multi-scale structure of this problem. The second objective is to couple the optimal control theory with this efficient numerical method to investigate the feasibility of using wall–normal suction/blowing actuation for controlling this Blade-Vortex Interaction (BVI) phenomenon.

The main purpose of aeroacoustic computations is to determine the sound intensity and directivity far away from the noise source. The computational cost of using a high-fidelity model of flow physics across such large domains is usually prohibitive and most researchers resort to multi–physics domain decomposition methods. The near field is presented by a numerical solution of the Navier–Stokes equations, while far away from the noise source the effect of nonlinearities is negligible and the linearized Euler equation or isentropic wave equation can be used to propagate acoustic waves. In this thesis, we construct and implement a multi-model (linearized Euler/Navier-Stokes), multi-domain(near field/far field) method for optimal control of aeroacoustics, based on a discontinuous Galerkin discretization. With such methods, we are interested in developing an optimal control framework for aeroacoustic applications that may help to identify novel strategies for controlling BVI noise in a systematic manner. Derivation of the optimality conditions for multi–domain systems obviously requires an in–depth knowledge of the optimal control formulations of each subsystem. In short, our research focus is the formulation and implementation of multi-model simulation for optimal control of aeroacoustics with application to BVI noise control.

1.4 Accomplishments and Overview

In this section we review the progress we have made in accordance with the objectives set out in the last section. The accomplishments of this research include:

1. A numerical scheme for the two dimensional linearized Euler and isentropic Wave equations based on the discontinuous Galerkin formulation (DG) has been developed. It has very low numerical dissipation and dispersion which is critical for the aeroacoustics simulation. To make the computation efficient, it has been reformulated into the quasi-conservative flux form for the discontinuous Galerkin discretizations, which avoids the source term from the mean flow most linearized solver has. It has been validated in several classical acoustics benchmark problems.

2. A general multi-domain/model solver has been developed and implemented based on the discontinuous Galerkin discretizations. In this approach, the coupling of multi-domains (near-field and far-field) and multi-models is achieved by weakly enforcing continuity of normal fluxes across a coupling surface. It has been built for Navier–Stokes (NS)/linearized Euler (LEE), Navier–Stokes/Wave, Euler/linearized Euler (LEE) and Euler/Wave coupling inside a single-grid framework, which is very efficient for the aeroacoustics computation.

3. A suite of model acoustics problems have been presented for the demonstration for our multi-model solver. These problems include: planar acoustics propagation, acoustics scattering from a circular cylinder, an inviscid vortex interacting with a circular cylinder, and viscous Bell AH-1 rotor blade vortex interaction. Results from each of these problems are in excellent agreement with the exact solutions or those from the direct solvers.

4. A general continuous adjoint gradient based flow control framework has been developed using discontinuous Galerkin discretizations. It can apply to distributed/boundary (Dirichlet/Neumann/Robin) control for linear Advection–Diffusion equations and nonlinear Burger equations, inviscid boundary control for Euler equations based on the linear characteristic relation, and viscous boundary control for Navier–Stokes equations. Several model control problems have been solved for the validation purpose. The first problem is optimal control of the acoustic pulse reflecting, which is to validate the non-reflecting behavior of the optimal transpiration control. The second is a vortex rebound model problem with wall normal suction and blowing used to minimize the kinetic energy at the final time. The third is the suppression of vortex shedding in the wake of a circular cylinder with boundary blowing/suction around the cylinder. All those results give excellent optimization results and have very good agreement with the work in the relevant literatures.

5. A multi-model solver for optimal control has been developed based on a non-overlapping decomposition of the spatial domain and model and the introduction of the transmission conditions between the subdomains and submodels which couple the state and adjoint solutions in the optimality system. Both the state and adjoint coupling of the multi-models are achieved by weakly enforcing continuity of normal fluxes across a coupling surface. This novel multi-model optimization solver has been successfully applied to noise control of realistic Blade-Vortex-Interaction (BVI) problem, where a vortex interacted with a Bell AH1 rotor blade in a freestream. Through optimization, the sound level in the observation region is reduced about 12dB. To our best knowledge, it is the first time to study the optimal control of realistic BVI problem numerically and with multi-domain/model approach.

We begin in Chapter 2 with a summary of the governing equations, including formulation of Navier–Stokes and Euler equations, the derivation of linearized Euler and isentropic wave equations. In Chapter 3, details are given for the numerical discretizations for all the governing equations based on the discontinuous Galerkin method. In this chapter, the multi-domain/model formulation has also been constructed for the general model coupling, including the inviscid and viscous flux coupling. The gradient-based control equations system using continuous adjoint derivation are given in Chapter 4. Optimal control formulations for the multi-model system are also shown in Chapter 4. Extensive validation of our numerical discretizations is performed in Chapter 5 for some classical acoustics problems and several multi-model test problems are also presented in this chapter. In Chapter 6, three boundary control problems are presented for the validation of our control solver, several issues are investigated. The main focus of our research is presented in Chapter 7 where an extensive study for the BVI noise control with on-blade blowing/suction using our multi-model formulation is given. Finally, the results of this thesis are summarized in Chapter 8 with conclusions and directions for future work.

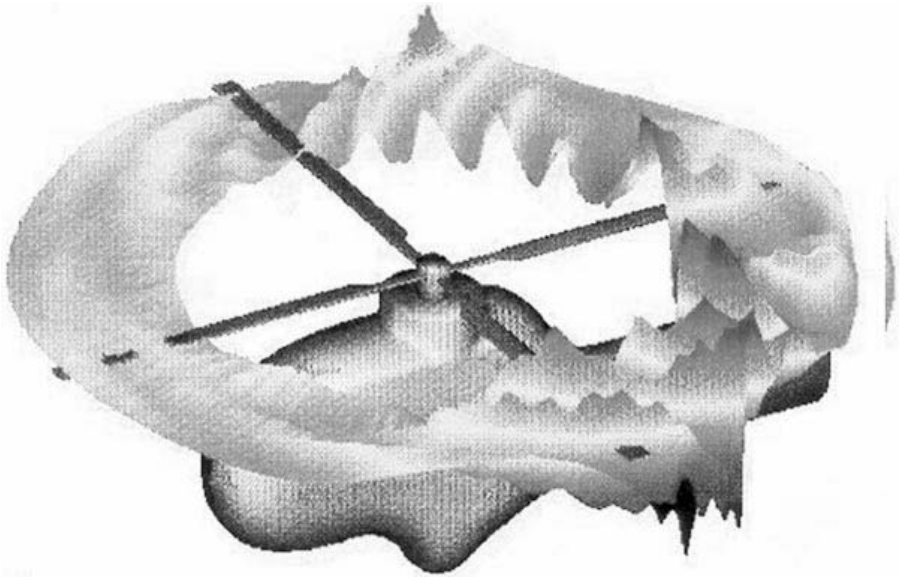

Figure 1.1: Blade surface pressure from the review [125]).

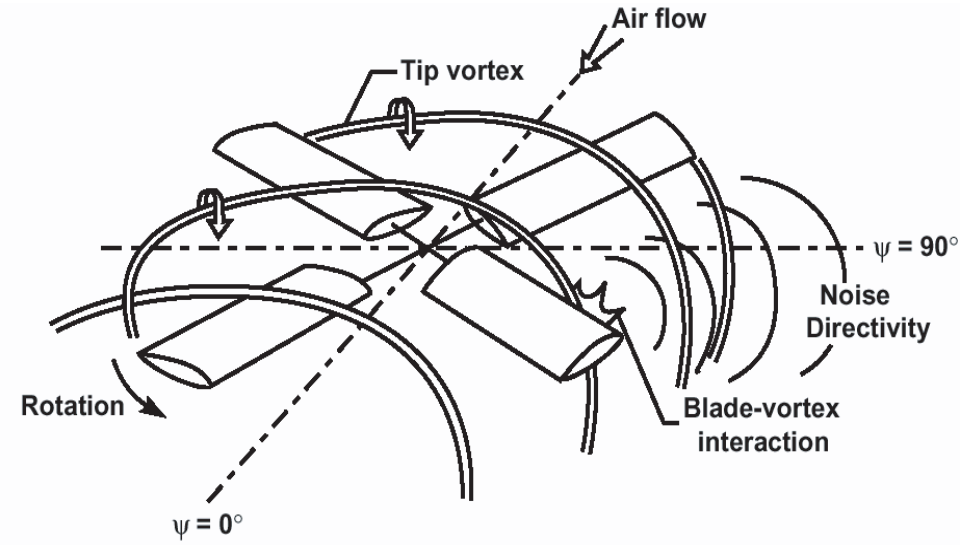

Figure 1.2: Aerodynamics of blade-vortex interactions from the review [125]

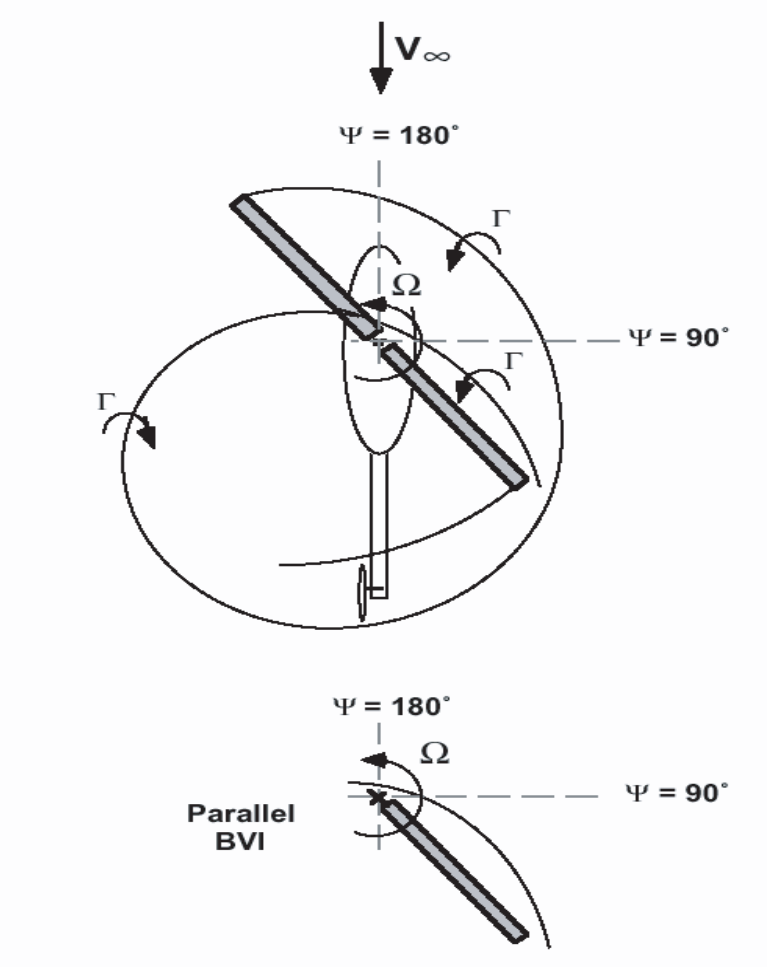

Figure 1.3: Schematic of parallel BVI on a helicopter from [84]

Chapter 2

Governing Equations

2.1 Nondimensionalization

Denote the reference length, velocity, density, temperature, sound speed, the coefficients of thermal diffusivity and viscosity by L_r, U_r, ρ_r, T_r, c_r, κ_r and μ_r respectively. Here the reference state is usually the state of freestream flow.

$$\mathbf{v}_i = \frac{{\mathbf{v}_i}^*}{U_r} \quad \rho = \frac{\rho^*}{\rho_r} \quad M_r = \frac{U_r}{c_r} \quad T = \frac{T^* M_r^2}{T_r}$$
$$p = \frac{p^*}{\rho_r {U_r}^2} \quad \tau = \frac{\tau^* L_r}{\mu_r U_r} \quad \lambda = \frac{\lambda_r}{\mu_r} \quad \kappa = \frac{\kappa^*}{\kappa_r}$$

where the variables with the asterisk sign are dimensional quantities. With this choice of the reference variables, the equation of state becomes

$$p = \frac{\rho T}{\gamma}$$

and the total energy per unit mass E is

$$E = \frac{T}{\gamma(\gamma - 1)} + \frac{1}{2}\mathbf{v}^T\mathbf{v}$$

The constitutive equation becomes

$$\tau = (\frac{L_r}{\mu_r U_r})\tau^* = \mu(\nabla\mathbf{v} + \nabla\mathbf{v}^T) + \lambda(\nabla \cdot \mathbf{v})I$$

For the nondimensionalization for the heat diffusion term,

$$\begin{aligned}
&(\frac{L_r}{\rho_r {U_r}^3})(\kappa^* {T^*}_{,x^*})_{,x^*} \\
&= (\frac{\mu_r}{\rho_r U_r L_r})\frac{\kappa}{Pr(\gamma-1)}T_{,xx} \\
&= \frac{1}{Re}\frac{\kappa}{Pr(\gamma-1)}T_{,xx}
\end{aligned}$$

where $Pr = \frac{\mu^* {C_p}^*}{\kappa^*}$ and $Re = \frac{\rho_r U_r L_r}{\mu_r}$. For the state discretizations, actually the following form is used, considering internal energy per unit $e^* = {C_v}^* T^*$ or $e^* = \frac{{C_p}^*}{\gamma} T^*$

$$\begin{aligned}
&(\frac{L_r}{\rho_r {U_r}^3})(\kappa^* {T^*}_{,x^*})_{,x^*} \\
&= (\frac{L_r}{\rho_r {U_r}^3})(\kappa^* {e^*}_{,x^*})_{,x^*} \\
&= (\frac{L_r}{\rho_r {U_r}^3})\frac{{U_r}^2}{{L_r}^2}\frac{\gamma\kappa^*}{{C_p}^*}e_{,xx} \\
&= (\frac{\mu_r}{\rho_r U_r L_r})\frac{\mu}{Pr}e_{,xx} \\
&= \frac{1}{Re}\frac{\mu}{Pr}e_{,xx}
\end{aligned}$$

Define $\mu = \frac{1}{Re}\mu$, we get

$$(\frac{L_r}{\rho_r {U_r}^3})(\kappa^* {T^*}_{x^*})_{x^*} = \frac{\mu}{Pr}e_{,xx}$$

In the final form for the heat diffusion term and the viscous stress term, the Re is integrated into μ implicitly.

2.2 Euler

The spatial domain occupied by the fluid is $\Omega = \{\mathbf{x} \in I\!R^2 : \}$ and Γ denotes its spatial boundary.

Let

$$\boldsymbol{u} = (\rho, u_1, u_2, T)^T$$

denote the primitive flow variables, where $\rho(t, \mathbf{x})$ is the density; $u_i(t, \mathbf{x})$ denotes the velocity in the x_i-direction, $i = 1, 2$; $\mathbf{v} = (u_1, u_2)^T$; and $T(t, \mathbf{x})$ denotes the temperature. The pressure p and the total energy per unit mass E are given by

$$p = \frac{\rho T}{\gamma}, \quad E = \frac{T}{\gamma(\gamma - 1)} + \frac{1}{2}\mathbf{v}^T\mathbf{v},$$

respectively, where γ is the ratio of specific heats. We write the conserved variables $\rho, \rho u_1, \rho u_2, \rho E$ as functions of the primitive variables,

$$\mathbf{U}(\boldsymbol{u}) = (\rho, \rho u_1, \rho u_2, \rho E)^T,$$

and we define the inviscid flux vectors as

$$\mathbf{F}_1(\boldsymbol{u}) = \begin{pmatrix} \rho u_1 \\ \rho u_1^2 + p \\ \rho u_2 u_1 \\ (\rho E + p) u_1 \end{pmatrix}, \quad \mathbf{F}_2(\boldsymbol{u}) = \begin{pmatrix} \rho u_2 \\ \rho u_1 u_2 \\ \rho u_2^2 + p \\ (\rho E + p) u_2 \end{pmatrix},$$

The two-dimensional compressible Euler equations for the time interval $[t_0, t_f]$ can now be written as

$$\mathbf{U}(\boldsymbol{u})_{,t} + \sum_{i=1}^{2} (\mathbf{F}_i(\boldsymbol{u})_{,x_i}) = \mathbf{0} \quad \text{in } (t_0, t_f) \times \Omega \tag{2.1}$$

with boundary conditions

$$\mathbf{B}(\boldsymbol{u}) = \mathbf{0} \quad \text{on } (t_0, t_f) \times \Gamma \tag{2.2}$$

and initial conditions

$$\boldsymbol{u}(t_0, \mathbf{x}) = \boldsymbol{u}_0(\mathbf{x}) \quad \text{in } \Omega. \tag{2.3}$$

Here, $\mathbf{n}$ is the unit outward normal.

2.3 Navier-Stokes

Considering the additional viscous flux term $\mathbf{F}^v$, we get the compressible Navier–Stokes equations in strong form

$$\mathbf{U}(\boldsymbol{u})_{,t} + \sum_{i=1}^{2} \left(\mathbf{F}_i(\boldsymbol{u})_{,x_i} - \mathbf{F}_i^v(\boldsymbol{u}, \nabla \boldsymbol{u})_{,x_i}\right) = \mathbf{0} \quad \text{in } (t_0, t_f) \times \Omega \tag{2.4}$$

with boundary condition (2.2) and initial condition (2.3).

We define the viscous flux $\mathbf{F}_i^v$

$$\mathbf{F}_i^v(\boldsymbol{u}, \nabla \boldsymbol{u}) = \begin{pmatrix} 0 \\ \tau_{1i} \\ \tau_{2i} \\ \tau_{1i} u_1 + \tau_{2i} u_2 + \frac{\mu}{Pr} e_{,x_i} \end{pmatrix},$$

$i = 1, 2$, where τ_{ij} are the elements of the stress tensor $\tau = \mu(\nabla \mathbf{v} + \nabla \mathbf{v}^T) + \lambda(\nabla \cdot \mathbf{v})I$. Here μ, λ are first and second coefficients of viscosity, κ is the thermal conductivity, Pr is the reference Prandtl number. For the problems presented in this thesis, constant Prandtl number and fluid properties (viscosities and thermal conductivity) are assumed along with Stokes hypothesis for the second coefficient of viscosity, $\lambda = -2\mu/3$.

2.4 Linearized Euler

For the linearized Euler, based on the linear perturbation theory we assume that $\boldsymbol{u} = \bar{\boldsymbol{u}} + \boldsymbol{u}'$ where $\bar{\boldsymbol{u}}$ is mean flow variables and $\boldsymbol{u}'$ is flow fluctuation variables, so

$$\mathbf{U}(\bar{\boldsymbol{u}} + \boldsymbol{u}')_{,t} + \sum_i \left(\mathbf{F}_i(\bar{\boldsymbol{u}} + \boldsymbol{u}')_{,x_i}\right) = \mathbf{0} \quad \text{in } (t_0, t_f) \times \Omega \tag{2.5}$$

Expand the terms in (2.5),

$$\mathbf{U}(\bar{\boldsymbol{u}}+\boldsymbol{u}^{'})_{,t}=\mathbf{U}(\bar{\boldsymbol{u}})_{,t}+(\mathbf{U}(\bar{\boldsymbol{u}})_{,\bar{\boldsymbol{u}}}\boldsymbol{u}^{'})_{,t}+...$$
$$\mathbf{F}_i(\bar{\boldsymbol{u}}+\boldsymbol{u}^{'})_{,x_i}=\mathbf{F}_i(\bar{\boldsymbol{u}})_{,x_i}+(\mathbf{F}_i(\bar{\boldsymbol{u}})_{,\bar{\boldsymbol{u}}}\boldsymbol{u}^{'})_{,x_i}+...$$

Assume the steady mean flow $\bar{\boldsymbol{u}}$, so

$$(\mathbf{U}(\bar{\boldsymbol{u}})_{,\bar{\boldsymbol{u}}})_t=0 \qquad (\mathbf{U}(\bar{\boldsymbol{u}})_{,\bar{\boldsymbol{u}}}\boldsymbol{u}^{'})_{,t}=\mathbf{U}_{,\bar{\boldsymbol{u}}}\boldsymbol{u}^{'}{}_{,t}$$

If ignoring the high order terms in (2.5), we get

$$\mathbf{U}(\bar{\boldsymbol{u}})_{,t}+\sum_i\mathbf{F}_i(\bar{\boldsymbol{u}})_{,x_i}+\mathbf{U}_{,\bar{\boldsymbol{u}}}\boldsymbol{u}^{'}{}_{,t}+\sum_i(\mathbf{F}_i(\bar{\boldsymbol{u}})_{,\bar{\boldsymbol{u}}}\boldsymbol{u}^{'})_{,x_i}=\mathbf{0} \quad \text{in } (t_0,t_f)\times\Omega \tag{2.6}$$

Considering the mean flow,

$$\mathbf{U}(\bar{\boldsymbol{u}})_{,t}+\sum_i\mathbf{F}_i(\bar{\boldsymbol{u}})_{,x_i}=\mathbf{0} \quad \text{in } (t_0,t_f)\times\Omega \tag{2.7}$$

Deducting (2.7) from (2.6), we get

$$\mathbf{U}_{,\bar{\boldsymbol{u}}}\boldsymbol{u}^{'}{}_{,t}+\sum_i(\mathbf{F}_i(\bar{\boldsymbol{u}})_{,\bar{\boldsymbol{u}}}\boldsymbol{u}^{'})_{,x_i}=\mathbf{0} \quad \text{in } (t_0,t_f)\times\Omega \tag{2.8}$$

To transform (2.8) in the conservative form, we have the following two formulations based on the conservative and primitive variable, respectively.

2.4.1 Formulation of the Conservative Variable

Define

$$\bar{\mathbf{M}}=\frac{\partial\mathbf{U}}{\partial\boldsymbol{u}}\,|_{\bar{\boldsymbol{u}}} \tag{2.9}$$

, the equation (2.8) becomes

$$(\bar{\mathbf{M}}\boldsymbol{u}')_{,t} + \sum_i \left(\frac{\partial \mathbf{F}_i}{\partial \boldsymbol{u}} |_{\bar{\boldsymbol{u}}} \, \boldsymbol{u}' \right)_{,x_i} = 0 \tag{2.10}$$

Let

$$\boldsymbol{Q} = \bar{\mathbf{M}}\boldsymbol{u}'$$

$$\frac{\partial \mathbf{F}_i}{\partial \boldsymbol{u}} |_{\bar{\boldsymbol{u}}} \, \boldsymbol{u}' = \frac{\partial \mathbf{F}_i}{\partial \boldsymbol{u}} |_{\bar{\boldsymbol{u}}} \, \bar{\mathbf{M}}^{-1}\bar{\mathbf{M}}\boldsymbol{u}' = \frac{\partial \mathbf{F}_i}{\partial \boldsymbol{u}} |_{\bar{\boldsymbol{u}}} \, \frac{\partial \boldsymbol{u}}{\partial \mathbf{U}} \big|_{\mathbf{U}(\bar{\boldsymbol{u}})} \, \bar{\mathbf{M}}\boldsymbol{u}' = \frac{\partial \mathbf{F}_i}{\partial \mathbf{U}} \big|_{\mathbf{U}(\bar{\boldsymbol{u}})} \, \bar{\mathbf{M}}\boldsymbol{u}'$$

we get

$$\boldsymbol{Q}_{,t} + \sum_i \left(\frac{\partial \mathbf{F}_i}{\partial \mathbf{U}} \big|_{\mathbf{U}(\bar{\boldsymbol{u}})} \, \boldsymbol{Q} \right)_{,x_i} = 0 \tag{2.11}$$

Define

$$\bar{\mathbf{A}}_i = \frac{\partial \mathbf{F}_i}{\partial \mathbf{U}} \big|_{\mathbf{U}(\bar{\boldsymbol{u}})}$$

we obtain

$$\boldsymbol{Q}_{,t} + \sum_i \left(\bar{\mathbf{A}}_i \boldsymbol{Q} \right)_{,x_i} = 0 \tag{2.12}$$

where our quasi-conservative variable

$$\boldsymbol{Q} = \bar{\mathbf{M}}\boldsymbol{u}'$$

and $\boldsymbol{u}'$ is got from

$$\boldsymbol{u}' = \bar{\mathbf{M}}^{-1}\boldsymbol{Q}$$

For two dimensional problem, the $\bar{\mathbf{A}}_i$ is shown in the following appendix.

2.4.2 Formulation of the Primitive Variable

Considering the steady mean flow for (2.9)

$$\bar{\mathbf{M}}_{,t} = 0$$

The equation (2.10) becomes

$$\boldsymbol{u}^{'}{}_{,t} + \sum_i \bar{\mathbf{M}}^{-1} \left(\frac{\partial \mathbf{F}_i}{\partial \mathbf{U}} \Big|_{\mathbf{U}(\bar{\boldsymbol{u}})} \boldsymbol{u}^{'} \right)_{,x_i} = 0$$

$$\boldsymbol{u}^{'}{}_{,t} + \sum_i \left(\bar{\mathbf{M}}^{-1} \frac{\partial \mathbf{F}_i}{\partial \mathbf{U}} \Big|_{\mathbf{U}(\bar{\boldsymbol{u}})} \boldsymbol{u}^{'} \right)_{,x_i} = \sum_i \left(\bar{\mathbf{M}}^{-1} \right)_{,x_i} \frac{\partial \mathbf{F}_i}{\partial \mathbf{U}} \Big|_{\mathbf{U}(\bar{\boldsymbol{u}})} \boldsymbol{u}^{'}$$

Introducing

$$\mathbf{G}_i = \bar{\mathbf{M}}^{-1} \frac{\partial \mathbf{F}_i}{\partial \mathbf{U}} \Big|_{\mathbf{U}(\bar{\boldsymbol{u}})}$$
$$\mathbf{S} = \sum_i (\bar{\mathbf{M}}^{-1})_{,x_i} \frac{\partial \mathbf{F}_i}{\partial \mathbf{U}} \Big|_{\mathbf{U}(\bar{\boldsymbol{u}})} \boldsymbol{u}^{'}$$

we get the primitive-variable based formulation

$$\boldsymbol{u}^{'}{}_{,t} + \sum_i (\mathbf{G}_i \boldsymbol{u}^{'})_{,x_i} = \mathbf{S} \tag{2.13}$$

where $\mathbf{G}$ and $\mathbf{S}$ are defined in the appendix.

2.5 Wave Equation

For a simplified model under isentropic condition, the energy equation is replaced by the isentropic relation

$$\frac{p}{\rho^\gamma} = \frac{p_0}{\rho_0^\gamma} = \text{constant} \tag{2.14}$$

Considering the definition of sound speed

$$c^2 = \frac{\partial p}{\partial \rho} \Big|_s$$

and the Taylor expansion based on the mean flow $\bar{\boldsymbol{u}}$

$$dp \approx p' \; d\rho \approx \rho' \;\text{ and } c^2 = c_0^2 + O(\varepsilon)$$

We obtain

$$p' = c_0^2 \rho' \tag{2.15}$$

where c_0 is the local sound speed from mean flow $\bar{\boldsymbol{u}}$.

Define

$$\boldsymbol{u}' = (\rho', {u_1}', {u_2}')^T$$

We get formulations of quasi-conservative $\boldsymbol{Q}$ and primitive variable $\boldsymbol{u}'$ under the isentropic condition, which are very similar to (2.12) and (2.13) as

$$\boldsymbol{Q}_{,t} + \sum_i \left(\bar{\mathbf{A}}_i \boldsymbol{Q}\right)_{,x_i} = 0 \tag{2.16}$$

and

$$\boldsymbol{u}'_{,t} + \sum_i \left(\mathbf{G}_i \boldsymbol{u}'\right)_{,x_i} = \mathbf{S} \tag{2.17}$$

where $\boldsymbol{Q}$, $\bar{\mathbf{A}}$ and $\mathbf{G}$ are defined in the appendix.

Chapter 3

Numerical Discretization

Accurate and efficient prediction of flow fluctuations representing sound is the goal of computational aeroacoustics, which is only based on the fundamental physical principles. Besides traditional acoustics analogy, Kirchhoff method, to name a few, quite a lot of work has focused on the improvements to traditional finite difference methods [72, 113, 114] to increase the accuracy and to implement the specialized boundary conditions. However, these methods have difficulty with the application to highly complex geometries and the spatial operators are not applicable for some critical flow phenomenon(*i.e.,* shocks). Because of our special interest in the application to optimal control of the aeroacoustics problem, it requires the computational solver with high accuracy, low dissipation and dispersion for the aeroacoustics simulation and its optimal control. From those studies [5, 6, 59, 99], it indicates that, compared with other numerical methods, discontinuous Galerkin method offers clear advantages in terms of high accuracy, spectrally small phase and dissipation errors when applied to acoustics problems as shown in [13, 45, 67, 100, 111]. Kopriva *et al.* [13, 67] also shows that discontinuous Galerkin method is very efficient for the aeroacoustics simulation, waves propagates over a large number of wavelengths with a minimal number of points per wavelength. Considering the efficiency and accuracy, a discontinuous Galerkin method is chosen to be applied for our state simulation and its optimal control.

3.1 Discontinuous Galerkin Method

Discontinuous Galerkin method can be thought of as a hybrid of finite-volume and finite-element methods that has a number of potential advantages including: high-order accuracy on unstructured meshes, local *hp*-refinement, weak imposition of boundary conditions, local conservation, and orthogonal hierarchical bases that support multiscale and multiphysics modeling. For a recent update on the status of discontinuous Galerkin, the interested reader can refer to [25].

3.2 Weak Formulation

As our typical case, we begin with a presentation of the DG method applied to the compressible Navier–Stokes equations that follows a similar discussion in Ref. [30, 31, 38]. For the mathematic details, they can be referred to Refs. [3, 24]. For the inviscid Euler equations, which is only subset of Navier–Stokes equations, the whole formulation is almost same except without viscous flux and difference in the boundary conditions. The same is for other linear equations. Most of the following formulation and implementation of DG discretizations for compressible Navier–Stokes equations basically follows Collis [31, 38].

3.2.1 Navier–Stokes

Consider the compressible Navier–Stokes equations in strong form

$$\mathbf{U}_{,t} + \mathbf{F}_{i,i} - \mathbf{F}^v_{i,i} = \mathbf{S} \quad \text{in } \Omega, \tag{3.1a}$$

$$\mathbf{U}(\mathbf{x}, 0) = \mathbf{U}_0(\mathbf{x}) \quad \text{at} \quad t = 0, \tag{3.1b}$$

where $\mathbf{U} = \{\rho, \rho u_1, \rho u_2, \rho E\}^T$ is the vector of conserved variables for our interested two dimensional problem. Regarding other parameters, more details are given in §2.3.

The fixed spatial domain for the problem is denoted by Ω, which is divided into a collection of elements in finite element formulations, with boundary $\partial\Omega$.

$$\bar{\Omega} = \bigcup_{e=1}^{N} \bar{\Omega}_e \quad \text{and} \quad \Omega_e \cap \Omega_f = \emptyset \quad \text{for} \quad e \neq f\,. \tag{3.2}$$

Consider a single subdomain Ω_e, we introduce the weighting function $\boldsymbol{W}$, which is continuous in Ω_e, for the strong form of the compressible Navier–Stokes equations (3.1a), and integrate the flux terms by parts

$$\begin{aligned} \int_{\Omega_e} \left(\boldsymbol{W}^T \mathbf{U}_{,t} + \boldsymbol{W}_{,i}^T (\mathbf{F}_i^v - \mathbf{F}_i) \right) d\mathbf{x} \;\; + \;\; & \int_{\partial\Omega_e} \boldsymbol{W}^T \left(\mathbf{F}_n - \mathbf{F}_n^v \right) d\mathbf{s} \\ = \;\; & \int_{\Omega_e} \boldsymbol{W}^T \mathbf{S}\, d\mathbf{s} \end{aligned} \tag{3.3}$$

where $\mathbf{F}_n = \mathbf{F}_i n_i$ and $\mathbf{F}_n^v = \mathbf{F}_i^v n_i$. If the solution was assumed to be continuous and this equation was summed over all the elements, then all the flux terms would telescope to the boundary $\partial\Omega$ and we would obtain the standard continuous Galerkin form of the compressible Navier–Stokes equations. However, in discontinuous Galerkin, one instead allows the solution and weighting functions to be discontinuous across element interfaces (see Figure 3.1) and the solutions on each element are coupled using appropriate numerical fluxes for both the inviscid flux $\mathbf{F}_n(\mathbf{U}) \rightarrow \widehat{\mathbf{F}}_n(\mathbf{U}^-, \mathbf{U}^+)$ and the viscous flux, $\mathbf{F}_i^v(\mathbf{U}, \nabla\mathbf{U}) \rightarrow \widehat{\mathbf{F}}_i^v(\mathbf{U}^-, \nabla\mathbf{U}^-, \mathbf{U}^+, \nabla\mathbf{U}^+)$.

We discretize the problem based on the single subdomain Ω_e in the element level and assume each subdomain Ω_e as an element with a Lipschitz boundary $\partial\Omega$. Considering the locality of discontinuous Galerkin method, we rewrite the above form based on the element level Ω_e. We denote the boundary of the domain Ω as $\partial\Omega = \Gamma_D \cup \Gamma_N$ where Γ_D is the portion of the boundary where Dirichlet conditions are specified and Γ_N is the portion of the boundary where Neumann conditions are set. The element

boundary is denoted as $\Gamma = \{\Gamma_D, \Gamma_N, \Gamma_0\}$ where Γ_0 are the inter-element boundaries. Let Ω_1 and Ω_2 be two adjacent elements; let $\Gamma_{12} = \partial\Omega_1 \cap \partial\Omega_2$; let $\mathbf{n}^{(1)}$ and $\mathbf{n}^{(2)}$ be the corresponding outward unit normal vectors at that point, and let $\mathbf{U}^{(e)}$ and $\mathbf{F}_i^{(e)}$ be the trace of a state vector $\mathbf{U}$ and flux vectors $\mathbf{F}_i$, respectively, on Γ_{12} from the interior of sub-domain Ω_e. Then, we define the average $\langle \cdot \rangle$ and jump $[\cdot]$ operators on Γ_{12} as

$$[\mathbf{U}n_i] = \mathbf{U}^{(1)}n_i^{(1)} + \mathbf{U}^{(2)}n_i^{(2)}, \quad [\mathbf{F}_n] = \mathbf{F}_i^{(1)}n_i^{(1)} + \mathbf{F}_i^{(2)}n_i^{(2)},$$
$$\langle \mathbf{U} \rangle = \frac{1}{2}\left(\mathbf{U}^{(1)} + \mathbf{U}^{(2)}\right), \quad \langle \mathbf{F}_i \rangle = \frac{1}{2}\left(\mathbf{F}_i^{(1)} + \mathbf{F}_i^{(2)}\right),$$

where $\mathbf{F}_n = \mathbf{F}_i n_i$.

With this notation, summing over all elements for (3.3), the primal formulation $B(\boldsymbol{W}, \mathbf{U})$ for discontinuous Galerkin applied to the Navier–Stokes equations (3.1a) is

$$\begin{aligned} B_{DG}(\boldsymbol{W}, \mathbf{U}) &= \sum_{\Omega_e} \int_{\Omega_e} \left(\boldsymbol{W}^T \mathbf{U}_{,t} + \boldsymbol{W}_{,i}^T (\mathbf{F}_i^v - \mathbf{F}_i)\right) d\mathbf{x} \\ &- \int_{\Gamma} \Big(\left[\boldsymbol{W}^T n_i\right] \langle \widehat{\mathbf{F}}_i^v - \widehat{\mathbf{F}}_i \rangle - \langle (\boldsymbol{D}_i \boldsymbol{W})^T \rangle \left[(\widehat{\mathbf{U}} - \mathbf{U}) n_i\right] \Big) d\mathbf{s} \\ &- \int_{\Gamma_0} \Big(\langle \boldsymbol{W}^T \rangle \left[\widehat{\mathbf{F}}_n^v - \widehat{\mathbf{F}}_n\right] - \left[(\boldsymbol{D}_n \boldsymbol{W})^T\right] \langle (\widehat{\mathbf{U}} - \mathbf{U}) n_i \rangle \Big) d\mathbf{s}, \end{aligned} \tag{3.4}$$

where

$$\mathbf{F}_n(\mathbf{U}) = \mathbf{F}_i(\mathbf{U}) n_i,$$
$$\mathbf{F}_n^v(\mathbf{U}) = \mathbf{F}_i^v(\mathbf{U}) n_i = \boldsymbol{D}_n \mathbf{U}.$$

Quantities with a hat $\widehat{\cdot}$ in (3.4) are numerical fluxes that must be appropriately defined. More details can be seen in [3, 24]

Similar to the primary form (3.4), we can also get the following by introducing

numerical fluxes and summing over all elements yields

$$\sum_{e=1}^{N} \int_{\partial\Omega_e} \boldsymbol{W}^T \left(\widehat{\mathbf{F}}_n(\mathbf{U}^-, \mathbf{U}^+) - \widehat{\mathbf{F}}_n^v(\mathbf{U}^-, \nabla\mathbf{U}^-, \mathbf{U}^+, \nabla\mathbf{U}^+) \right) d\mathbf{s} +$$
$$\sum_{e=1}^{N} \int_{\Omega_e} \left(\boldsymbol{W}^T \mathbf{U}_{,t} + \boldsymbol{W}_{,i}^T (\mathbf{F}_i^v - \mathbf{F}_i) \right) d\mathbf{x} = \sum_{e=1}^{N} \int_{\Omega_e} \boldsymbol{W}^T \mathbf{S}\, d\mathbf{s} \tag{3.5}$$

where the $\mathbf{U}^+$ and $\mathbf{U}^-$ states are defined in Figure 3.1. For an element edge on the physical boundary $\partial\Omega$, $\mathbf{U}^+ = \mathbf{U}_{bc}$. Likewise, for inter-element boundaries, $\mathbf{U}^+$ comes from the neighboring element. Thus, all interface and boundary conditions are set through the numerical fluxes.

A simple Lax–Friedrichs flux is chosen for the inviscid flux

$$\widehat{\mathbf{F}}_n(\mathbf{U}^-, \mathbf{U}^+) = \frac{1}{2} \left(\mathbf{F}_n(\mathbf{U}^-) + \mathbf{F}_n(\mathbf{U}^+) + \lambda_m \left(\mathbf{U}^- - \mathbf{U}^+ \right) \right) \tag{3.6}$$

where λ_m is the maximum, in absolute value, of the eigenvalues of the Euler Jacobian $\mathbf{A}_n = \partial\mathbf{F}_n/\partial\mathbf{U}$.

For the numerical viscous flux, we use the method of [8]. First, a "jump savvy" gradient of the state, $\boldsymbol{\sigma} \sim \nabla\mathbf{U}$ is computed by solving

$$\sum_{e=1}^{N} \int_{\Omega_e} \boldsymbol{V}^T \boldsymbol{\sigma}_j\, d\mathbf{x} = -\sum_{e=1}^{N} \int_{\Omega_e} \boldsymbol{V}_{,j}^T \mathbf{U}\, d\mathbf{x} + \sum_{e=1}^{N} \int_{\partial\Omega_e} \boldsymbol{V}^T \widehat{\mathbf{U}} n_j\, d\mathbf{s} \tag{3.7}$$

$\forall \boldsymbol{V} \in \mathcal{V}(\mathcal{P}_h)$ and for j from 1 to d, where

$$\widehat{\mathbf{U}} = \frac{1}{2} \left(\mathbf{U}^- + \mathbf{U}^+ \right) . \tag{3.8}$$

The Bassi–Rebay viscous flux is then computed using

$$\widehat{\mathbf{F}}_n^v(\mathbf{U}^-, \boldsymbol{\sigma}^-, \mathbf{U}^+, \boldsymbol{\sigma}^+) = \frac{1}{2} \left(\mathbf{F}_n^v(\mathbf{U}^-, \boldsymbol{\sigma}^-) + \mathbf{F}_n^v(\mathbf{U}^+, \boldsymbol{\sigma}^+) \right) . \tag{3.9}$$

For other numerical flux formulations, [4, 24] gives more details and extensive discussion.

Boundary Conditions

In setting boundary conditions weakly through the numerical fluxes, one must construct a state, $\mathbf{U}_{bc}$, that enforces the appropriate boundary conditions, and [5] provides a discussion of the important issues involved in selected $\mathbf{U}_{bc}$. For the Navier–Stokes calculations reported here, we use the following approach. At far-field boundaries $\mathbf{U}_{bc}$ is set to freestream values. At isothermal wall boundaries, we evaluate $\mathbf{U}_{bc}$ separately for the convective and viscous fluxes. Let $q_1 = (u^- n_y - v^- n_x)n_y$ and $q_2 = (v^- n_x - u^- n_y)n_x$ then the reconstructed state at a wall for the convective flux is

$$\mathbf{U}_{bc} = \left\{ \begin{array}{c} \rho^- \\ \rho^- q_1 \\ \rho^- q_2 \\ \rho^- e^- + 0.5\rho^-(q_1^2 + q_2^2) \end{array} \right\} . \tag{3.10}$$

This state enforces the no-penetration condition which is appropriate for both inviscid and viscous calculations. For the viscous flux, the no-slip condition is enforced using

$$\mathbf{U}_{bc} = \left\{ \begin{array}{c} \rho^- \\ 0 \\ 0 \\ \rho^- T_w/(\gamma(\gamma-1)) \end{array} \right\} \tag{3.11}$$

where T_w is the prescribed wall temperature, γ is the ratio of specific heats.

3.2.2 Euler

As the subset of viscous Navier–Stokes equations, the discretizations of Euler equations are very similar to (3.3) as

$$\int_{\Omega_e} \left(\boldsymbol{W}^T \mathbf{U}_{,t} + \boldsymbol{W}_{,i}^T \mathbf{F}_i \right) \, d\mathbf{x} + \int_{\partial\Omega_e} \boldsymbol{W}^T \mathbf{F}_n \, d\mathbf{s} = \int_{\Omega_e} \boldsymbol{W}^T \mathbf{S} \, d\mathbf{s} \tag{3.12}$$

Introducing numerical fluxes and summing over all elements yields the similar formulation for Euler equations (3.12)

$$\sum_{e=1}^{N} \int_{\partial\Omega_e} \boldsymbol{W}^T \widehat{\mathbf{F}}_n(\mathbf{U}^-, \mathbf{U}^+) \, d\mathbf{s} + \sum_{e=1}^{N} \int_{\Omega_e} \left(\boldsymbol{W}^T \mathbf{U}_{,t} - \boldsymbol{W}_{,i}^T \mathbf{F}_i \right) \, d\mathbf{x} = \sum_{e=1}^{N} \int_{\Omega_e} \boldsymbol{W}^T \mathbf{S} \, d\mathbf{s} \tag{3.13}$$

All interface and boundary conditions are set through the numerical fluxes. We also use a Lax–Friedrichs flux (3.6) for the numerical inviscid flux.

Boundary Implementation

Atkins [5] gives very good discussion for the boundary condition implementation for the inviscid calculation in DG, inflow/outflow and wall boundary. At far-field boundaries $\mathbf{U}_{bc}$ is set to freestream values. At wall boundaries, we evaluate $\mathbf{U}_{bc}$ for the convective fluxes. Let $q_1 = (u^- n_y - v^- n_x) n_y$ and $q_2 = (v^- n_x - u^- n_y) n_x$ then the reconstructed state at a wall for the convective flux is

$$\mathbf{U}_{bc} = \left\{ \begin{array}{c} \rho^- \\ \rho^- \, q_1 \\ \rho^- \, q_2 \\ \rho^- E^- - 0.5\rho^-(u^{-2} + v^{-2}) + 0.5\rho^-(q_1^2 + q_2^2) \end{array} \right\} . \tag{3.14}$$

3.2.3 Linearized Euler Equation (LEE)

Consider the general form of linearized Euler equations, it can be expressed by

$$\boldsymbol{Q}(\boldsymbol{u}')_{,t} + \sum_{i=1}^{2} \left(\mathbf{F}^i(\boldsymbol{u}')_{,x_i} \right) = \mathbf{S} \quad \text{in } (t_0, t_f) \times \Omega \tag{3.15}$$

where $\mathbf{S}$ is the source term, zero for the conservative form (2.12), nonzero for

the primitive form (2.13) which is from the mean flow and defined in the appendix. Because of the similar formulation as (2.1), their formulations can be easily obtained. The major difference is the definition of the fluxes $\mathbf{F}$ and the source $\mathbf{S}$.

Conservative Form

For the conservative formulation (2.12), its weak formulation is

$$\int_{\Omega_e} \left(\boldsymbol{W}^T \boldsymbol{Q}_{,t} - \boldsymbol{W}_{,i}^T \bar{\mathbf{A}}_i \boldsymbol{Q} \right) \, d\mathbf{x} + \int_{\partial\Omega_e} \boldsymbol{W}^T \bar{\mathbf{A}}_i n_i \boldsymbol{Q} \, d\mathbf{s} = 0 \tag{3.16}$$

Introducing numerical fluxes and summing over all elements yields the similar formulation for (3.16)

$$\sum_{e=1}^{N} \int_{\partial\Omega_e} \boldsymbol{W}^T \widehat{\bar{\mathbf{A}}_n \boldsymbol{Q}}(\boldsymbol{u}'^-, \boldsymbol{u}'^+) \, d\mathbf{s} + \sum_{e=1}^{N} \int_{\Omega_e} \left(\boldsymbol{W}^T \boldsymbol{Q}_{,t} - \boldsymbol{W}_{,i}^T \bar{\boldsymbol{A}}_i \boldsymbol{Q} \right) \, d\mathbf{x} = \sum_{e=1}^{N} \int_{\Omega_e} \boldsymbol{W}^T \mathbf{S} \, d\mathbf{s} \tag{3.17}$$

All interface and boundary conditions are set through the numerical fluxes. We also use a Lax–Friedrichs flux (3.6) for the numerical inviscid flux, where it is defined as

$$\widehat{\bar{\mathbf{A}}_n \boldsymbol{Q}}(\boldsymbol{u}'^-, \boldsymbol{u}'^+) = \frac{1}{2} \left(\bar{\mathbf{A}}_n \boldsymbol{Q}(\boldsymbol{u}'^-) + \bar{\mathbf{A}}_n \boldsymbol{Q}(\boldsymbol{u}'^+) + \lambda_m \left(\boldsymbol{Q}^- - \boldsymbol{Q}^+ \right) \right) \tag{3.18}$$

where λ_m is the maximum, in absolute value, of the eigenvalues of the Euler Jacobian $\bar{\mathbf{A}}_n = \partial \mathbf{F}_n / \partial \mathbf{U}$ from mean flow $\bar{\boldsymbol{u}}$.

For the boundary condition implementation for the linear calculation in DG, far field (inflow/outflow) and wall boundary, we always set the boundary condition for $\boldsymbol{u}'$ first, then form the boundary condition for $\boldsymbol{Q}$ by $\boldsymbol{Q} = \bar{\mathbf{M}} \boldsymbol{u}'$. At far-field boundaries $\boldsymbol{u}'$ is usually set to zero unless there is inflow disturbance. At wall boundaries, we evaluate $\boldsymbol{Q}_{bc}$ for the convective fluxes. Let $q_1 = (u'^- n_y - v'^- n_x) n_y$ and $q_2 =$

$(v'^{-}n_x - u'^{-}n_y)n_x$ then the reconstructed $\boldsymbol{u}'$ at a wall is

$$\boldsymbol{u}'_{bc} = \begin{Bmatrix} \rho'^{-} \\ q_1 \\ q_2 \\ T'^{-} \end{Bmatrix} . \tag{3.19}$$

Primitive Form

For the primitive formulation (2.13), its weak formulation is

$$\int_{\Omega_e} \left(\boldsymbol{W}^T \boldsymbol{u}'_{,t} + \boldsymbol{W}^T_{,i} \mathbf{G}_i \boldsymbol{u}' \right) d\mathbf{x} + \int_{\partial\Omega_e} \boldsymbol{W}^T \mathbf{G}_i n_i \boldsymbol{u}' \, d\mathbf{s} = \int_{\Omega_e} \boldsymbol{W}^T \mathbf{S} \, d\mathbf{s} \tag{3.20}$$

Introducing numerical fluxes and summing over all elements yields the similar formulation for (3.20)

$$\sum_{e=1}^{N} \int_{\partial\Omega_e} \boldsymbol{W}^T \widehat{\mathbf{G}_n \boldsymbol{u}'}(\boldsymbol{u}'^{-}, \boldsymbol{u}'^{+}) \, d\mathbf{s} + \sum_{e=1}^{N} \int_{\Omega_e} \left(\boldsymbol{W}^T \boldsymbol{u}'_{,t} - \boldsymbol{W}^T_{,i} \mathbf{G}_i \boldsymbol{u}' \right) d\mathbf{x} = \sum_{e=1}^{N} \int_{\Omega_e} \boldsymbol{W}^T \mathbf{S} \, d\mathbf{s} \tag{3.21}$$

All interface and boundary conditions are set through the numerical fluxes. The implementation of the boundary conditions is very similar to that of conservative formulation, but for $\boldsymbol{u}'$ directly.

3.2.4 Wave

In a similar manner, we solve the isentropic wave equation in the same formulation of linearized Euler.

The weak formulations for its conservative and primitive form are

$$\int_{\Omega_e} \left(\boldsymbol{W}^T \boldsymbol{Q}_{,t} + \boldsymbol{W}^T_{,i} \bar{\mathbf{A}}_i \boldsymbol{Q} \right) d\mathbf{x} + \int_{\partial\Omega_e} \boldsymbol{W}^T \bar{\mathbf{A}}_i n_i \boldsymbol{Q} \, d\mathbf{s} = 0 \tag{3.22}$$

$$\int_{\Omega_e} \left(\boldsymbol{W}^T \boldsymbol{u}'_{,t} + \boldsymbol{W}^T_{,i} \mathbf{G}_i \boldsymbol{u}' \right) d\mathbf{x} + \int_{\partial\Omega_e} \boldsymbol{W}^T \mathbf{G}_i n_i \boldsymbol{u}' \, d\mathbf{s} = \int_{\Omega_e} \boldsymbol{W}^T \mathbf{S} \, d\mathbf{s} \tag{3.23}$$

The boundary implementation of (3.22) and (3.23) is very similar to that of (3.16) and (3.20), respectively.

3.2.5 Remarks

Considering the similarity of (3.3),(3.12), (3.15) and (3.22), we are able to solve those problems in a unified framework, which provides us great convenience for the following multi-model simulation to build on the single-grid framework and element level modeling.

3.3 Multi-domain/Multi-model simulations

The goal of multi-domain/model simulation is to reduce the overall time and memory required to simulate the flow by using the locally selected cheaper and more computational efficient physical models without sacrificing the global fidelity of the simulation.

As mentioned in §3.1, one of the great advantages from DG is the local conservation that supports the multi-physics modeling. In this section, we present a multi-domain multi-model formulation for the state simulation and later optimal control computation using a discontinuous Galerkin formulation for its flexility, locality and high accuracy. In this approach, the coupling of multi-domain (near field and far field) and multi-model is achieved by weakly enforcing continuity of normal fluxes across a coupling surface.

3.3.1 Motivation

Compressible fluid flow simulations can be modeled with different physics equations. The simplest model is the full potential equation when inviscid, irrotatioanl and isentropic flows is assumed. For the inviscid compressible flows, usually the Euler equations are used to describe the behavior of the inviscid flows. To include the viscous effects needed for accurate modeling of boundary layer, the Navier–Stokes equations is the choice, although it is very expensive because of high resolution required in the viscous regions. Furthermore, for high Reynolds number flows, turbulence model needs to be used to get accurate results. In the linear case, for example, the acoustics propagation and receptivity problem, the linearized version of Euler or Navier–Stokes equations are applied. Due to the tremendous computational time needed for the numerical solution of the complex flows, multi-domain/model methods are usually favored, which usually decompose the flow field domain into multiple zones characterized by different physical properties of the flow, to reduce the memory requirement and to improve the accuracy of the solution. It is also called the heterogeneous domain decomposition method in [98], which must include the physically and mathematically justified transmission conditions at the artificial interface to get quite accurate approximate solution. For the mathematical description of coupling heterogeneous models for the compressible flows, more details are given in [98].

In fact, there is long history of using such multi-model approach for the computational efficiency issue. Boundary layer coupling or thin layer Navier–Stokes coupling have been widely used, although such approaches do not include all the physics required for the complex flows. For the transonic flows, the multi-model approach is applied in [10, 102] for the three-dimensional rotor flows in forward flight and shows that the computational cost can be reduced by a factor of two for a Navier–Stokes/full potential coupling. Such efficiency is justified by the fact that a larger percent of

computational domain is in the full potential region, resulted from its cheap cost. The overall solution strategy is solving the different equations alternatively in each region through the overlapping domain decomposition, similar to a sub-domain iterative method. Contrary to the sub-domain iterative approach, Cai [91, 92] developed multi-model, Euler/full potential coupling for the steady flow computation of three dimensional transonic flow, using the explicit and implicit approach based on the general finite volume. The coupled system is solved simultaneously. A finite volume based conservative interpolation is used for the coupling of the full potential equation and the Euler equation so that the flux will remain conservative at the discrete level. There is also some other work using the heterogeneous domain decomposition. Coclici *et al.* [27] have used coupling of Navier–Stokes and linearized Euler equations for steady viscous two-dimensional flow around airfoil base in an iterative manner by constructing the suitable artificial boundary conditions at the coupling surface. They also considered the formal asymptotic expansions to construct appropriate boundary layer corrections of the coupled problem modeling the viscous-inviscid interaction using one dimensional analysis in [28]. Beyond it, Coclici extended their work for the complex compressible magneto-plasma flow using the heterogeneous domain decomposition [26].

Computational Aeroacoustics implies the direct simulation of acoustic fields generated by flows and of the interaction of acoustic fields with flows. Due to the multi-scale/physics nature of near-field fluid flow and far-field acoustics field, the near-field fluid flow is characterized by small spatial fluid structures with slow propagating convective velocity, such as small vortices in a turbulent flow, the far-field acoustics is small amplitude fluctuations with long wavelength and fast propagating sound speed. As reviewed in §1.2, besides the traditional direct acoustics simulation,

the more extensively used is the zone approach (near-field sound source and far-field acoustics) after taking advantage of the multiple scale nature of aeroacoustics phenomena. Such zone approach may be handled by acoustics analogy [75] and its derivative [42,48,76,95,122], Kirchhoff method [79] or the Euler equations which may very often be the linearized Euler equation [43, 44, 51, 120]. Among those methods, nonlinear near-field CFD calculation plus the far-field linearized Euler solver seems to give better insight into the mechanisms of the sound generation and propagation in the vicinity of the flow region and allow the feedback from acoustics to the fluid flow, the latter of which is extremely important for the adjoint simulation for the optimal control work. The key in such approach is to use the high order method, in particular the numerical scheme with low dispersion and dissipation in the far field.

As the recent rapid development of discontinuous Galerkin for it is easy to handle the complex geometry, high-order and compact, it has gotten strong interest, many implementations have been proposed and several studies have been performed on its dissipation and dispersion properties. All these studies indicate that it offers clear advantages in terms of accuracy when applied to wave propagation problems as in [45, 101, 111].

Here we propose that in the near field, the Navier–Stokes equation is solved and the linearized Euler equation or its simplified case (isentropic wave) is used for the far field. The two are solved through the heterogeneous non-overlapping domain decomposition approach based on the discontinuous Galerkin framework, which posses several good features useful for our application. First, they easily allow for varying the polynomial order of approximation from one element to the next. They also allow for very general meshes. Finally, the methods are locally conservative, that is, they are based on satisfying conservation principles element-by-element. Considering the above features, a multi-domain, multi-model framework is constructed by achieving

coupling transmission condition through the weakly enforcement using the numerical flux. Our goal is to reduce the overall time and memory required to capture the far field acoustics by using locally selected and more computational efficient physical models without sacrificing the global fidelity of the simulation. In fact, this approach can be generalized for more complicated heterogeneous domain decomposition if the corresponding coupling condition is formulated.

In this section, we first give the formulation for the multi-model coupling, then present the implementation details based on DG. In the BVI problem we are interested in, solving the linearized Euler or isentropic wave equation in the far field, it not only brings the computational saving, but also is more efficient for the acoustics propagation. All those models or solvers calculate the inviscid fluxes through the coupling edges. As mentioned before, the discontinuous Galerkin formulation is adopted to adequately interface these different solvers at different domains. An explicit approach is first considered to validate the spatial discretization, in the future the implicit implementation will also be explored. Here we focus on the description of the two-model formulation, although more models coupling can also be addressed if the corresponding coupling condition is given. For convenience, the slightly different formulation is used for the model description.

3.3.2 Formulation

The computational domain Ω is split into two sub-domains as shown in Figure 3.2, Ω_{near} for the near field and Ω_{far} for the far field. The interface between Ω_{near} and Ω_{far} is denoted by Γ_c.

In the near-field, the flow is modeled using the compressible Navier–Stokes equations (3.1a) which, in conservative form, are given by

$$\mathbf{U}_{,t}(\mathbf{Y}) + \left(\mathbf{F}_{i,i}(\mathbf{Y}) - \mathbf{F}^v_{i,i}(\mathbf{Y}, \nabla\mathbf{Y})\right) = \mathbf{0} \tag{3.24a}$$

in $(t_0, t_f) \times \Omega_{\text{near}}$ with boundary conditions

$$\mathbf{B}_{\text{near}}(\mathbf{Y}, g) = \mathbf{0} \quad \text{on } (t_0, t_f) \times \partial\Omega_{\text{near}}\,, \tag{3.24b}$$

where $\mathbf{B}_{\text{near}}$ includes the coupling between near- and far-field subdomains and the transpiration boundary condition on the control boundary. The initial conditions in the near-field are

$$\mathbf{Y}(t_0, \mathbf{x}) = \mathbf{Y}_0(\mathbf{x}) \quad \text{in } \Omega_{\text{near}} \tag{3.24c}$$

where $\mathbf{Y}_0$ is typically a steady-state solution of the Navier–Stokes equations over the rotor blade with a superimposed vortex upstream of the blade in the BVI control problem. In equations (3.24), $\mathbf{n}$ is the unit outward normal vector, $\mathbf{Y} = (\rho, u_1, u_2, T)^{\mathcal{T}}$ is the vector of primitive flow variables, and the conservation variables, expressed as functions of the primitive variables, are given by $\mathbf{U}(\mathbf{Y}) = (\rho, \rho u_1, \rho u_2, \rho E)^{\mathcal{T}}$.

The far-field flow in Ω_{far} is modeled using the linearized Euler equations (3.25). We assume that $\mathbf{Y} = \overline{\mathbf{Y}} + \mathbf{y}$ where $\overline{\mathbf{Y}}$ are mean-flow primitive variables and $\mathbf{y}$ are fluctuations in the primitive variables. With this notation, the linearized Euler equations are

$$\overline{\mathbf{M}}\mathbf{y}_{,t} + \left(\overline{\mathbf{A}}_i \overline{\mathbf{M}}\mathbf{y}\right)_{,i} = \mathbf{0} \quad \text{in } (t_0, t_f) \times \Omega_{\text{far}} \tag{3.25}$$

where

$$\begin{aligned} \overline{\mathbf{M}}(\overline{\mathbf{Y}}) &= \left.\frac{\partial \mathbf{U}}{\partial \mathbf{Y}}\right|_{\overline{\mathbf{Y}}} \\ \overline{\mathbf{A}}_i(\overline{\mathbf{Y}}) &= \left.\frac{\partial \mathbf{F}_i}{\partial \mathbf{U}}\right|_{\mathbf{U}(\overline{\mathbf{Y}})} \end{aligned}$$

In order to discretize this equation using discontinuous Galerkin, we introduce the quasi-conservative variables $\boldsymbol{Q}(\mathbf{y}; \overline{\mathbf{Y}}) = \overline{\mathbf{M}}(\overline{\mathbf{Y}})\mathbf{y}$ and recast the linearized Euler equations in the form

$$\boldsymbol{Q}_{,t}(\mathbf{y}) + \mathbf{F}'_{i,i}(\mathbf{y}) = \mathbf{0} \quad \text{in } (t_0, t_f) \times \Omega_{\text{far}} \tag{3.26a}$$

where the flux is given by $\mathbf{F}'_i(\mathbf{y}) = \overline{\mathbf{A}}_i \boldsymbol{Q}(\mathbf{y})$. Equation (3.26a) is solved subject to appropriate boundary conditions of the form

$$\mathbf{B}_{\text{far}}(\mathbf{y}) = \mathbf{0} \quad \text{ on } (t_0, t_f) \times \partial\Omega_{\text{far}} \,. \tag{3.26b}$$

For the problems presented here, the far-field equations are not explicitly dependent on the control variables g which live on the near-field control surface. However, $\mathbf{B}$ does represent the coupling between the near- and far-field subdomains as well as nonreflecting boundary conditions on the outer far-field boundary. Initial conditions for the far-field problem are of the form

$$\mathbf{y}(t_0, \mathbf{x}) = \mathbf{y}_0(\mathbf{x}) \quad \text{ in } \Omega_{\text{far}} \tag{3.26c}$$

where $\mathbf{y}_0$ is typically zero and $\overline{\mathbf{Y}}$ is typically a uniform flow. In the following, we suppress the explicit dependence of far-field quantities on $\overline{\mathbf{Y}}$ unless necessary for clarity.

Given the similarity of (3.24) and (3.26), we are able to solve these equations in a unified discontinuous Galerkin framework that is particularly convenient for multi-model simulation and optimization.

3.3.3 Implementation

The DG method for the near-field is obtained by starting from the strong form of the compressible Navier–Stokes equations (3.24a). Consider a single element, Ω_e, multiply by a weighting function $\boldsymbol{W}$ that is continuous in Ω_e, integrate the flux terms by parts, replace the actual flux terms by appropriate numerical fluxes, and sum over

all elements $\Omega \in \Omega_{\text{near}}$. Doing so results in the discontinuous Galerkin weak form

$$\sum_{e=1}^{N} \left\{ \int_{\Omega_e} (\boldsymbol{W} \cdot \mathbf{U}_{,t} + \boldsymbol{W}_{,i} \cdot (\mathbf{F}_i^v - \mathbf{F}_i) - \boldsymbol{W} \cdot \mathbf{S}) \, d\mathbf{x} + \int_{\partial\Omega_e} \boldsymbol{W} \cdot \left(\widehat{\mathbf{F}}_n(\mathbf{U}^-, \mathbf{U}^+) - \widehat{\mathbf{F}}_n^v(\mathbf{U}^-, \nabla\mathbf{U}^-, \mathbf{U}^+, \nabla\mathbf{U}^+) \right) d\mathbf{s} \right\} = 0 \quad (3.27)$$

where the $\mathbf{U}^+$ and $\mathbf{U}^-$ states are defined in Figure 3.1. For an element edge on the subdomain boundary $\partial\Omega_{\text{near}}$, $\mathbf{U}^+ = \mathbf{U}_{bc}$ for an edge coincident with a prescribed boundary condition or, in the case of the coupling boundary between Ω_{near} and Ω_{far}, $\mathbf{U}^+ = \mathbf{U}(\overline{\mathbf{Y}} + \mathbf{y})$ on Γ_c where $\overline{\mathbf{Y}}$ is the mean field and $\mathbf{y}$ is the far-field (perturbation) solution at that edge. Likewise, for inter-element boundaries, $\mathbf{U}^+$ comes from the neighboring element. Thus, all interface and boundary conditions are set through the numerical fluxes.

The far-field linearized Euler equations (2.12) are also discretized in space using discontinuous Galerkin with the weighting function on element Ω_f denoted by $\boldsymbol{V}$. This leads to the DG weak form

$$\sum_{f=1}^{M} \left\{ \int_{\Omega_f} \left(\boldsymbol{V} \cdot \boldsymbol{Q}_{,t} - \boldsymbol{V}_{,i} \cdot \mathbf{A}_i \boldsymbol{Q} - \boldsymbol{V} \cdot \mathbf{S} \right) d\mathbf{x} + \int_{\partial\Omega_f} \boldsymbol{V} \cdot \widehat{\mathbf{F}}'_n(\mathbf{y}^-, \mathbf{y}^+) \, d\mathbf{s} \right\} = 0 \quad (3.28)$$

where, again, all interface and boundary conditions are set through the numerical flux. For the outer far-field boundary, $\mathbf{y}^+ = 0$ which is a first-order nonreflecting condition. On the coupling boundary Γ_c, $\mathbf{y}^+ = \mathbf{Y}(\mathbf{U}) - \overline{\mathbf{Y}}$ where $\mathbf{Y}(\mathbf{U})$ is the primitive solution vector corresponding to the conservative state vector $\mathbf{U}$ at the near-field edge.

The coupling between near-field NS and far-field LEE comprises the inviscid and viscous coupling based on the weak form and numerical flux formulations. Here we base our multi-domain multi-model coupling on the non-overlapping partition and describe the construction of coupling condition for our two model formulation as in Figure 3.3.

For the inviscid coupling, coupling will be achieved by an approximate Riemann (an upwind flux) solver at different domains. The solutions are weakly coupled through the numerical flux. Exploiting the locality of discontinuous Galerkin method, for the near-field NS element Ω_e, the normal numerical flux $\widehat{\mathbf{F}}_n(\mathbf{U})$ at Γ_c using the simple Lax-Friedrichs numerical flux (3.6) is defined as

$$\widehat{\mathbf{F}}_n(\mathbf{U}) = \frac{1}{2}\left(\mathbf{F}_n(\mathbf{U}) + \mathbf{F}_n{}'(\mathbf{U}(\overline{\mathbf{Y}}, \mathbf{y})) + \lambda_m(\mathbf{U} - \mathbf{U}(\overline{\mathbf{Y}}, \mathbf{y}))\right)$$

where the conversion $\mathbf{U}(\overline{\mathbf{Y}}, \mathbf{y})$ is the variable transformed from the quasi-conservative variable $\boldsymbol{Q}$ in the LEE element and

$$\lambda_m = \max[\frac{\partial \mathbf{F}_n(\mathbf{U})}{\partial \mathbf{U}}, \frac{\partial \mathbf{F}_n{}'(\mathbf{U}(\overline{\mathbf{Y}}, \mathbf{y}))}{\partial \bar{\mathbf{U}}}]$$

. For the far-field LEE element Ω_f,

$$\widehat{\mathbf{F}}'_n(\boldsymbol{Q}) = \frac{1}{2}\left(\mathbf{F}'_n(\boldsymbol{Q}) + \mathbf{F}'_n{}'(\boldsymbol{Q}(\overline{\mathbf{Y}}, \mathbf{Y})) + \lambda_m(\boldsymbol{Q} - \boldsymbol{Q}(\overline{\mathbf{Y}}, \mathbf{Y}))\right)$$

where the conversion $\boldsymbol{Q}(\overline{\mathbf{Y}}, \mathbf{Y})$ is the variable transformed from $\mathbf{Y}$ in the NS element and

$$\lambda_m = \max[\frac{\partial \mathbf{F}'_n(\boldsymbol{Q})}{\partial \boldsymbol{Q}}, \frac{\partial \mathbf{F}'_n{}'(\boldsymbol{Q}(\overline{\mathbf{Y}}, \mathbf{Y}))}{\partial \boldsymbol{Q}}]$$

Besides the inviscid coupling, there is also the viscous coupling. Consistent with our implementation for the state calculation, the Bassi–Rebay numerical viscous flux [8, 9], defined in (3.7),(3.9) is used for the illustration.

Following (3.7), first a "jump savvy" gradient of the state, $\boldsymbol{\sigma} \sim \nabla \mathbf{U}$ is computed

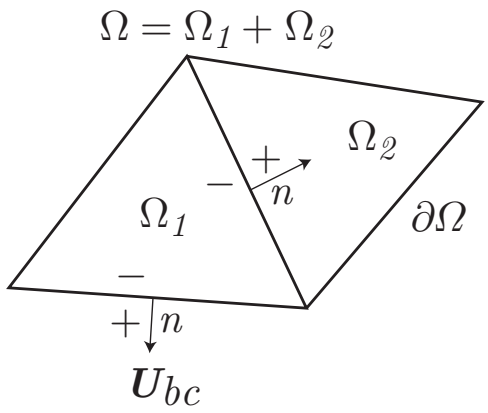

Figure 3.1: Schematic of DGM discretization [31], the solution and weighting functions discontinuous across element interfaces

by solving

$$\sum_{n=1}^{N} \int_{\Omega_n} \boldsymbol{V}^T \boldsymbol{\sigma}_j \, d\mathbf{x} = -\sum_{n=1}^{N} \int_{\Omega_n} \boldsymbol{V}_{,j}^T \mathbf{U} \, d\mathbf{x} + \sum_{n=1}^{N} \int_{\partial\Omega_n/\Gamma_c} \boldsymbol{V}^T \widehat{\mathbf{U}} n_j \, d\mathbf{s} + \int_{\Gamma_c} \boldsymbol{V}^T \widehat{\mathbf{U}(\overline{\mathbf{Y}}, \mathbf{y})} n_j$$

$\forall \boldsymbol{V} \in \mathcal{V}(\mathcal{P}_h)$ and for j from 1 to d, where

$$\widehat{\mathbf{U}} = \frac{1}{2}\left(\mathbf{U}^- + \mathbf{U}^+\right) . \qquad \forall \partial\Omega_e/\Gamma_c$$

$$\widehat{\mathbf{U}(\overline{\mathbf{Y}}, \mathbf{y})} = \frac{1}{2}\left(\mathbf{U}^- + \mathbf{U}^+(\overline{\mathbf{Y}}, \mathbf{y})\right) . \qquad \forall \Gamma_c$$

where $\mathbf{U}^+(\overline{\mathbf{Y}}, \mathbf{y})$ is related with the LEE element edge and $\mathbf{U}^-$ is from the NS element edge.

Our final Bassi–Rebay viscous flux $\widehat{\mathbf{F}}_n^v$ is then computed using

$$\widehat{\mathbf{F}}_n^v(\mathbf{U}^-, \boldsymbol{\sigma}^-, \mathbf{U}^+, \boldsymbol{\sigma}^+) = \frac{1}{2}\left(\mathbf{F}_n^v(\mathbf{U}^-, \boldsymbol{\sigma}^-) + 0\right) . \tag{3.29}$$

where $\mathbf{F}_n^v(\mathbf{U}^+, \boldsymbol{\sigma}^+) = 0$ is the flux contribution from the edge in the linearized Euler domain, *i.e.,* here the viscous effect is negligible in the linearized Euler domain.

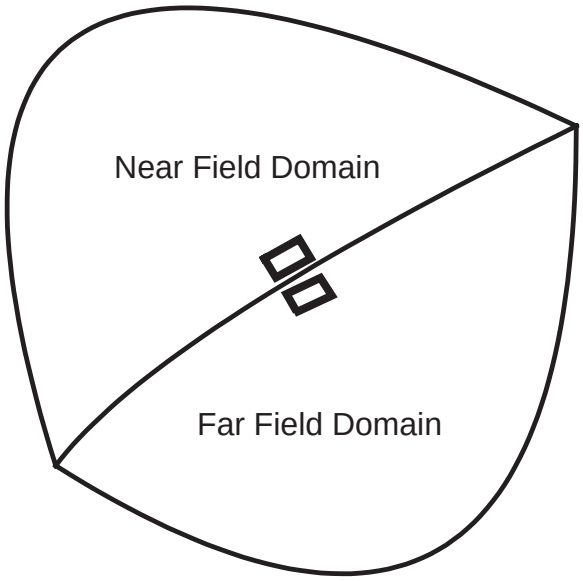

Figure 3.2: Coupling of different fidelity models in the multi-domain, near-field and far-field

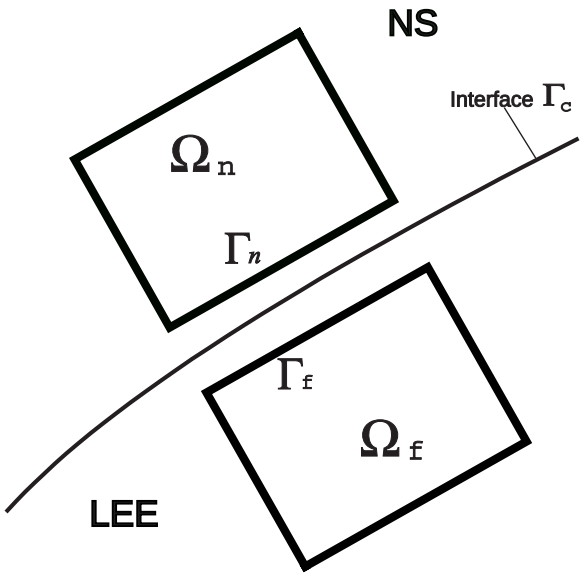

Figure 3.3: Coupling NS and LEE at two element edges

Chapter 4

Optimal Control Formulations

The coupling of accurate computational fluid dynamics analysis with optimal control theory has the potential to advance active flow-control for complex flows. Application of optimal control theory directly to the flow governing equations provides a rigorous framework for the active flow control and systematic method to derive control laws for the most efficient distribution of control effect to achieve a desired objective. Since our control varies over part of the boundary and in time, the number of control variables obtained after discretization is huge. Therefore we use adjoint based gradient method for the solution of the discretization of the optimal system and the gradient of the objective functional with-respect-to the control is evaluated efficiently using the adjoints. In general, there are two approaches to adjoint-based gradient evaluation: the optimize-then-discretize approach (continuous adjoint) and discretize-then-optimize approach (discrete adjoint). One of the goals of our research is to evaluate and compare these two approaches for formulating and solving optimal control problems using DGM. In this chapter, we focus on the optimize-then-discretize approach by presenting a discussion of the problem formulation, implementation.

4.1 The Objective Functional

Following [37, 38], all optimal control problems treated in this thesis are of the form

$$\min_{\mathbf{g}\in\mathcal{G}_{ad}} \quad J(\mathbf{g}) \stackrel{\text{def}}{=} J_{\text{obs}}(\mathbf{U}(\mathbf{g})) + J_{\text{reg}}(\mathbf{g}), \tag{4.1}$$

where $\mathbf{g}$ is the control, $\mathcal{G}_{ad}$ is the set of admissible controls, $\mathbf{U}(\mathbf{g})$ is the solution of the state governing equations (NS/Euler/LEE/Wave/Burgers/Advection–Diffusion), J_{obs}

is the part of the cost function that represents our flow control objective and $J_{\text{reg}}(\mathbf{g})$ is a regularization term, typically some weighted norm of the control as in [1, 64]. For the discussion of the existence of $\mathbf{g}$ and the well-posedness of the optimal control problem, [37, 38] gives more details.

4.1.1 Cost Functional

Because we are mostly interested in the noise control of aeroacoustics which intends to minimize the acoustics pressure fluctuation in the far field, we define

$$J_{obs} = \int_{t_0}^{t_f} \int_{\Omega_{\text{obs}}} \frac{\alpha_0}{2}(p - p_a)^2 d\mathbf{x}dt \tag{4.2}$$

as a measure of aeroacoustic noise to be reduced, where p_a is the ambient or steady mean flow pressure distribution.

Besides the acoustics control problems, there are also other control problems we are interested in, such as the cylinder vortex shedding suppressing, the Terminal Kinetic Energy (TKE) control of vortex rebound. The following objective functionals are also defined

$$J_{obs} = \frac{1}{2}\int_t \int_{\Omega_{obs}} ((\rho - \rho_o)^2 + (\rho u - \rho_o u_o)^2 + (\rho v - \rho_o v_o)^2 + (\rho E - \rho_o E_o)^2) d\mathbf{x}dt \tag{4.3}$$

and

$$J_{obs} = \frac{1}{2}\int_{\Omega_{obs}} (\rho \boldsymbol{u}^2)_{t=t_f} d\mathbf{x}dt \tag{4.4}$$

4.1.2 Regularization

Regarding the regularization $J_{reg}(\mathbf{g})$, it is usually defined as

$$J_{reg}(\mathbf{g}) = \int_{t_0}^{t_f} \int_{\Gamma_c} \Big(\frac{\alpha_1}{2}\|\mathbf{g}_t\|_2^2 + \frac{\alpha_2}{2}\|\nabla \mathbf{g}\|_2^2 + \frac{\alpha_3}{2}\|\mathbf{g}\|_2^2 \Big) d\mathbf{x}dt. \tag{4.5}$$

where $\alpha_1, \alpha_2, \alpha_3 > 0$. For the treatment of those penalty terms $\mathbf{g}_t$, $\nabla\mathbf{g}$ and $\mathbf{g}$, [37, 38] give very good discussion.

4.2 Adjoint equations

All the following adjoint formulations are obtained through continuous adjoint approach, the detailed derivation is given in Appendix A.

4.2.1 Adjoint Euler

For the adjoint Euler, it is

$$-\boldsymbol{\lambda}_{,t} - \mathbf{A}_i{}^T \boldsymbol{\lambda}_{,x_i} = \mathbf{S} \tag{4.6}$$

where the $\mathbf{S}$ is dependent on the objective functional. For the derivation details, it is in Appendix A.1.1.

4.2.2 Adjoint Navier–Stokes

With the additional viscous flux term $\mathbf{F}^v$, it becomes more complicated to derive the viscous adjoint governing equations and the boundary condition. The derivation details are given in Appendix A.1.2. After transformation in Appendix B.1, the adjoint Navier–Stokes equations is

$$\boldsymbol{\lambda}_{,t} + (\mathbf{F}_i^a)_{,x_i} - (\boldsymbol{G}_i^a)_{,x_i} + (\boldsymbol{G}_i^{av})_{,x_i} = \widetilde{\mathbf{S}} \tag{4.7}$$

where $\mathbf{F}_i^a$, $\boldsymbol{G}_i^a$ and $\boldsymbol{G}_i^{av}$ are defined in Appendix B.1.

4.2.3 Adjoint Linearized Euler

For the linearized Euler equation, its adjoint formulation is very similar to that of adjoint Euler except that the coefficient matrix $\bar{\mathbf{A}}$ is from mean flow $\bar{\boldsymbol{u}}$.

$$-\boldsymbol{\lambda}_{,t} - \bar{\mathbf{A}}_i^{\,T} \boldsymbol{\lambda}_{,x_i} = \mathbf{S} \tag{4.8}$$

where

$$\bar{\mathbf{A}}_i = \frac{\partial F_i}{\partial \mathbf{U}} \Big|_{\mathbf{U}(\bar{\boldsymbol{u}})}$$

and $\mathbf{S}$ is dependent on the objective functional as the variation of $\boldsymbol{Q}$ instead of $\mathbf{U}$.

4.2.4 Adjoint Wave

From the similar adjoint analysis, the formulation for adjoint wave equation is

$$-\boldsymbol{\lambda}_{,t} - \bar{\mathbf{A}}_i^{\,T} \boldsymbol{\lambda}_{,x_i} = \mathbf{S} \tag{4.9}$$

where $\bar{\mathbf{A}}$, $\mathbf{S}$ are given in the appendix.

For linearized Euler and isentropic wave equations, their adjoint equations (4.8), (4.9) are transpose of their state equations (2.13) and (2.17), respectively, except the adjoint source term from the objective functional (4.1).

4.3 Adjoint Formulations for Multi-Model System

As in our typical problem, blade-vortex interaction in Figure 4.3, the compressible Navier–Stokes equation is used in the near-field Ω_{near} and the linearized Euler or isentropic wave equation in the far-field Ω_{far}. For the illustration, the abstract interface is given in Figure 4.1. The objective functional J is defined in the observation domain Ω_{obs} which is inside far-field Ω_{far}. The control $\mathbf{g}$ is the on-blade control, which lies in Γ_c of near-field Ω_{near}. The coupling interface between near-field and far-field is Γ_{nf}. In

the following derivation of the adjoint coupling condition, we assume the mean flow in the far field is not affected by the near-field control(*i.e.,* boundary blowing/suction) and use the same formulation in §3.3.2

4.3.1 State Coupling

Consider the coupling of NS and LEE or Wave, the transmission operator is defined between $\mathbf{U}$ and $\boldsymbol{Q}$. Because of the far-field linearization based on the primitive variables, the transformation uses the primitive variables $\mathbf{Y}$ and $\mathbf{y}$.

NS/LEE

Due to the linearization in the far field, the conversion from $\mathbf{y}$ of LEE to $\mathbf{Y}$ of NS is,

$$\mathbf{Y} = \mathbf{I}\overline{\mathbf{Y}} + \mathbf{I}\mathbf{y} \tag{4.10}$$

and that from NS to LEE is,

$$\mathbf{y} = \mathbf{I}\mathbf{Y} - \mathbf{I}\overline{\mathbf{Y}} \tag{4.11}$$

where $\mathbf{I}$ is the identity matrix.

By weakly coupling through the numerical flux, we achieve the *inviscid flux* coupling for the state solution coupling between LEE and NS besides the *viscous flux* coupling formulated in §3.3.3.

$$\int_{\Gamma_{nf}} \boldsymbol{W} \cdot \widehat{\mathbf{N}_n}\big(\underbrace{\mathbf{I}\overline{\mathbf{Y}} + \mathbf{I}\mathbf{y}}_{\text{LEE}}, \underbrace{\mathbf{Y}}_{\text{NS}}\big)\, d\Gamma\,, \qquad \int_{\Gamma_{nf}} \boldsymbol{W}' \cdot \widehat{\mathbf{F}_n}\big(\underbrace{\mathbf{I}\mathbf{Y} - \mathbf{I}\overline{\mathbf{Y}}}_{\text{NS}}, \underbrace{\mathbf{y}}_{\text{LEE}}\big)\, d\Gamma \tag{4.12}$$

NS/Wave

For the coupling of Wave and NS, $\mathbf{y}$ is defined as

$$\mathbf{y} = [\rho' \quad u' \quad v']^T$$

considering the isentropic acoustics, $p' = c^2\rho'$, where $c = \sqrt{\bar{T}}$ is the local sound speed,

$$\begin{aligned} T' &= T - \bar{T} = \gamma\frac{p+p'}{\rho+\rho'} - \gamma\frac{\bar{p}}{\bar{\rho}} \\ &\approx (\gamma-1)\frac{\bar{T}}{\bar{\rho}}\rho' \end{aligned}$$

The transmission operator from $\mathbf{y}$ of Wave to $\mathbf{Y}$ of NS is

$$\begin{aligned} \mathbf{Y} &= \mathbf{I}\overline{\mathbf{Y}} + \begin{pmatrix} 1 & 0 & 0 \\ 0 & 1 & 0 \\ 0 & 0 & 1 \\ \frac{(\gamma-1)\bar{T}}{\bar{\rho}} & 0 & 0 \end{pmatrix} \begin{pmatrix} \rho' \\ u' \\ v' \end{pmatrix} \\ &= \mathbf{I}\overline{\mathbf{Y}} + \mathbf{W}\mathbf{y} \end{aligned} \tag{4.13}$$

and from $\mathbf{Y}$ of NS to $\mathbf{y}$ of Wave is

$$\begin{aligned} \mathbf{y} &= \begin{pmatrix} 1 & 0 & 0 & 0 \\ 0 & 1 & 0 & 0 \\ 0 & 0 & 1 & 0 \end{pmatrix} (\mathbf{Y} - \overline{\mathbf{Y}}) \\ &= \mathbf{N}\mathbf{Y} - \mathbf{N}\overline{\mathbf{Y}} \end{aligned} \tag{4.14}$$

The convective flux coupling between Wave and NS is

$$\int_{\Gamma_{nf}} \boldsymbol{W} \cdot \widehat{\mathbf{N}_n}\big(\underbrace{\mathbf{I}\overline{\mathbf{Y}} + \mathbf{W}\mathbf{y}}_{\text{Wave}}, \underbrace{\mathbf{Y}}_{\text{NS}}\big)\, d\Gamma\,, \qquad \int_{\Gamma_{nf}} \boldsymbol{W}' \cdot \widehat{\mathbf{F}_n}\big(\underbrace{\mathbf{N}\mathbf{Y} - \mathbf{N}\overline{\mathbf{Y}}}_{\text{NS}}, \underbrace{\mathbf{y}}_{\text{Wave}}\big)\, d\Gamma \tag{4.15}$$

Besides the inviscid flux coupling, there is also the viscous flux coupling described in §3.3.3.

4.3.2 Adjoint Coupling

We use a gradient-based optimization procedure to solve the optimal control problem represented by minimizing (7.1) subject to the state equations (3.24) in the near-field and (3.26) in the far-field. The gradient is computed using a continuous adjoint method (i.e. the optimize-then-discretize approach). For the adjoint coupling, we introduce the following assumption that the mean flow in the far field is not affected by the near-field control(*i.e.,* boundary blowing/suction), which is reasonable if the coupling interface is faraway from the near field. Therefore, variation of the mean flow in the far field $\overline{\mathbf{Y}}' = 0$. Due to the linearization in the far field, variation of $\mathbf{y}$ also leads to $\mathbf{y} = \mathbf{y}'$.

The variation of two operators (4.10), (4.11) becomes

$$\mathbf{Y}' = \mathbf{I}\mathbf{y} \tag{4.16}$$

$$\mathbf{y} = \mathbf{I}\mathbf{Y}' \tag{4.17}$$

and variation of (4.13) and (4.14) becomes

$$\mathbf{Y}' = \mathbf{W}\mathbf{y} \tag{4.18}$$

$$\mathbf{y} = \mathbf{N}\mathbf{Y}' \tag{4.19}$$

We begin by introducing the adjoint variables $\boldsymbol{\lambda}$ for the near-field Navier–Stokes equations and $\boldsymbol{\xi}$ for the linearized Euler equations in the far-field. We then define an

augmented Lagrangian as

$$\begin{aligned} & L(\mathbf{U}(\mathbf{Y}), \boldsymbol{Q}(\mathbf{y}), \mathbf{g}, \boldsymbol{\lambda}, \boldsymbol{\xi}) \\ & \quad = J(\boldsymbol{Q}(\overline{\mathbf{Y}}, \mathbf{y}), g) + \int_{t_0}^{t_f} \int_{\Omega_{\text{near}}} \boldsymbol{\lambda}^T (\mathbf{U}(\mathbf{Y})_t + \mathbf{F}_{i,i} - \mathbf{F}^v_{i,i}) d\mathbf{x} \\ & \quad + \quad \int_{t_0}^{t_f} \int_{\Omega_{\text{far}}} \boldsymbol{\xi}^T (\boldsymbol{Q}(\overline{\mathbf{Y}}, \mathbf{y})_t + (\bar{\mathbf{A}}_i \boldsymbol{Q})_{,i}) d\mathbf{x} \\ & \quad + \quad \int_{\Omega_{\text{near}}} (\boldsymbol{\lambda}_0)^T (\mathbf{U} - \mathbf{U}_0) d\mathbf{x} + \int_{\Omega_{\text{far}}} (\boldsymbol{\xi}_0)^T (\boldsymbol{Q} - \boldsymbol{Q}_0) d\mathbf{x} \end{aligned} \tag{4.20}$$

Assuming $J(\boldsymbol{Q}(\overline{\mathbf{Y}}, \mathbf{y}), g)$ is only defined inside far-field Ω_f, variation over (4.20),

$$\begin{aligned} & L'(\mathbf{U}(\mathbf{Y}), \boldsymbol{Q}(\overline{\mathbf{Y}}, \mathbf{y}), \mathbf{g}, \boldsymbol{\lambda}, \boldsymbol{\xi}) \\ & \quad = J' + \int_{t_0}^{t_f} \int_{\Omega_{\text{near}}} \boldsymbol{\lambda}^T (\mathbf{U}'_{,t} + \mathbf{F}_{i,i}{}' - \mathbf{F}^v_{i,i}{}') d\mathbf{x} + \int_{\Omega_{\text{near}}} (\boldsymbol{\lambda}_0)^T \mathbf{U}' d\mathbf{x} \\ & \quad + \quad \int_{t_0}^{t_f} \int_{\Omega_{\text{far}}} \boldsymbol{\xi}^T (\boldsymbol{Q}'(\overline{\mathbf{Y}}, \mathbf{y})_{,t} + (\bar{\mathbf{A}}_i \boldsymbol{Q}')_{,i}) d\mathbf{x} + \int_{\Omega_{\text{far}}} (\boldsymbol{\xi}_0)^T \boldsymbol{Q}' d\mathbf{x} \\ & \quad = J' + \int_{t_0}^{t_f} \int_{\Omega_{\text{near}}} (\boldsymbol{\lambda}^T \mathbf{U}'_{,t} + \boldsymbol{\lambda}_{,i}{}^T \mathbf{F}^{v\prime}_i - \boldsymbol{\lambda}_{,i}{}^T \mathbf{F}_i{}') d\mathbf{x} \\ & \quad + \int_{t_0}^{t_f} \int_{\partial\Omega_{\text{near}}} (\boldsymbol{\lambda}^T \mathbf{F}_n{}' - \boldsymbol{\lambda}^T \mathbf{F}^{v\prime}_n) d\mathbf{x} + \int_{\Omega_{\text{near}}} (\boldsymbol{\lambda}_0)^T \mathbf{U}' d\mathbf{x} \\ & \quad + \int_{t_0}^{t_f} \int_{\Omega_{\text{far}}} (\boldsymbol{\xi}^T \boldsymbol{Q}'(\overline{\mathbf{Y}}, \mathbf{y})_t - \boldsymbol{\xi}_i{}^T \bar{\mathbf{A}}_i \boldsymbol{Q}') d\mathbf{x} \\ & \quad + \int_{t_0}^{t_f} \int_{\partial\Omega_{\text{far}}} \boldsymbol{\xi}^T \bar{\mathbf{A}}_n \boldsymbol{Q}' d\mathbf{x} + \int_{\Omega_{\text{far}}} (\boldsymbol{\xi}_0)^T \boldsymbol{Q}' d\mathbf{x} \\ & \quad = J_{\boldsymbol{Q}} \boldsymbol{Q}' + \int_{t_0}^{t_f} \int_{\Omega_{\text{near}}} -\mathbf{U}^{T\prime} (\boldsymbol{\lambda}_{,t} + (\mathbf{F}^a_i)_{,x_i} - (\boldsymbol{G}^a_i)_{,x_i} + (\boldsymbol{G}^{av}_i)_{,x_i} - \widetilde{\mathbf{S}}) d\mathbf{x} \\ & \quad + \int_{t_0}^{t_f} \int_{\partial\Omega_{\text{near}}/\Gamma_{nf}} (\boldsymbol{\lambda}^T \widehat{\mathbf{F}_n}' - \boldsymbol{\lambda}^T \widehat{\mathbf{F}^v_n}') d\mathbf{x} + \int_{t_0}^{t_f} \int_{\Gamma_{nf}} (\boldsymbol{\lambda}^T \widehat{\mathbf{F}_n}' - \boldsymbol{\lambda}^T \widehat{\mathbf{F}^v_n}') d\mathbf{x} \\ & \quad + \int_{t_0}^{t_f} \int_{\Omega_{\text{far}}} \boldsymbol{Q}^{T\prime} (-\boldsymbol{\xi}_{,t} - \bar{\mathbf{A}}_i{}^T \boldsymbol{\xi}_{,x_i}) d\mathbf{x} \\ & \quad + \int_{t_0}^{t_f} \int_{\partial\Omega_{\text{far}}/\Gamma_{nf}} \boldsymbol{\xi}^T \widehat{\bar{\mathbf{A}}_n \boldsymbol{Q}}' d\mathbf{x} + \int_{t_0}^{t_f} \int_{\Gamma_{nf}} \boldsymbol{\xi}^T \widehat{\bar{\mathbf{A}}_n \boldsymbol{Q}}' d\mathbf{x} \\ & \quad + \int_{\Omega_{\text{near}}} \mathbf{U}^{T\prime} \boldsymbol{\lambda}|_{t_f} d\mathbf{x} + \int_{\Omega_{\text{near}}} \mathbf{U}^{T\prime} (\boldsymbol{\lambda}_0 - \boldsymbol{\lambda})|_{t_0} d\mathbf{x} \\ & \quad + \int_{\Omega_{\text{far}}} \boldsymbol{Q}^{T\prime} \boldsymbol{\xi}|_{t_f} d\mathbf{x} + \int_{\Omega_{\text{far}}} \boldsymbol{Q}^{T\prime} (\boldsymbol{\xi}_0 - \boldsymbol{\xi})|_{t_0} d\mathbf{x} \end{aligned} \tag{4.21}$$

where the last several terms represent the adjoint initial conditions for the near/far-field, and more derivation details are given in Appendix A, B.

From the variation $\mathbf{U}'$ in Ω_{near}, we get the near-field adjoint Navier–Stokes equation (B.8), where there is no contribution from J, given that J is only defined inside far-field. In the same manner, the adjoint linearized Euler (4.8) in the far field is obtained. Next we will focus on the derivation of the adjoint transmission condition at Γ_{nf}.

Adjoint inviscid coupling

Similar to the state coupling, the adjoint coupling will be divided into the adjoint inviscid and adjoint viscous coupling. We will treat the two terms $\boldsymbol{\lambda}^T\widehat{\mathbf{F}_n}'$ and $\boldsymbol{\lambda}^T\widehat{\mathbf{F}_n^v}'$, separately. For the numerical flux of $\widehat{\mathbf{F}_n}'$ and $\widehat{\bar{\mathbf{A}}_n\boldsymbol{Q}}'$, both use the Lax–Friedrichs flux (3.6) as

$$\begin{aligned}
\boldsymbol{\lambda}^T\widehat{\mathbf{F}_n}' &= \boldsymbol{\lambda}^T\frac{1}{2}\left(\mathbf{F}_n(\mathbf{Y})' + \mathbf{F}_n(\mathbf{I}\overline{\mathbf{Y}}+\mathbf{F}\mathbf{y})' + \lambda_m\left(\mathbf{U}' - \mathbf{U}'(\mathbf{I}\overline{\mathbf{Y}}+\mathbf{F}\mathbf{y})\right)\right)\\
&= \boldsymbol{\lambda}^T\frac{1}{2}\Big(\frac{\partial\mathbf{F}_n}{\partial\mathbf{Y}}\mathbf{Y}' + \frac{\partial\mathbf{F}_n(\overline{\mathbf{Y}}+\mathbf{F}\mathbf{y})}{\partial\mathbf{Y}}(\overline{\mathbf{Y}}'+\mathbf{F}\mathbf{y}')\\
&\quad +\lambda_m\left(\frac{\partial\mathbf{U}}{\partial\mathbf{Y}}\mathbf{Y}' - \frac{\partial\mathbf{U}(\overline{\mathbf{Y}}+\mathbf{F}\mathbf{y})}{\partial\mathbf{Y}}(\overline{\mathbf{Y}}'+\mathbf{F}\mathbf{y}')\right)\Big)\\
&= \frac{1}{2}\mathbf{Y}'^T\left(\frac{\partial\mathbf{F}_n}{\partial\mathbf{Y}}^T\boldsymbol{\lambda} + \lambda_m\frac{\partial\mathbf{U}}{\partial\mathbf{Y}}^T\boldsymbol{\lambda}\right)\\
&\quad +\frac{1}{2}(\mathbf{F}\mathbf{y}')^T\left(\frac{\partial\mathbf{F}_n(\overline{\mathbf{Y}}+\mathbf{F}\mathbf{y})}{\partial\mathbf{Y}}^T\boldsymbol{\lambda} - \lambda_m\frac{\partial\mathbf{U}(\overline{\mathbf{Y}}+\mathbf{F}\mathbf{y})}{\partial\mathbf{Y}}^T\boldsymbol{\lambda}\right)
\end{aligned}$$

$$\begin{aligned}
\boldsymbol{\xi}^T\widehat{\bar{\mathbf{A}}_n\boldsymbol{Q}}' &= \boldsymbol{\xi}^T\frac{1}{2}\big(\bar{\mathbf{A}}_n\boldsymbol{Q}'(\overline{\mathbf{Y}},\mathbf{y}) + \mathbf{A}_n\boldsymbol{Q}'(\overline{\mathbf{Y}},\mathbf{N}(\mathbf{Y}-\overline{\mathbf{Y}}))\\
&\quad +\overline{\lambda_m}\left(\boldsymbol{Q}'(\overline{\mathbf{Y}},\mathbf{y}) - \boldsymbol{Q}'(\overline{\mathbf{Y}},\mathbf{N}(\mathbf{Y}-\overline{\mathbf{Y}}))\right)\big)\\
&= \frac{1}{2}\mathbf{y}'^T\left(\frac{\partial\boldsymbol{Q}}{\partial\overline{\mathbf{Y}}}^T\mathbf{A}_n{}^T\boldsymbol{\xi} - \overline{\lambda_m}\frac{\partial\boldsymbol{Q}}{\partial\overline{\mathbf{Y}}}^T\boldsymbol{\xi}\right)\\
&\quad +\frac{1}{2}(\mathbf{N}\mathbf{Y}')^T\left(\frac{\partial\boldsymbol{Q}}{\partial\mathbf{y}}^T\mathbf{A}_n{}^T\boldsymbol{\xi} + \overline{\lambda_m}\frac{\partial\boldsymbol{Q}}{\partial\mathbf{y}}^T\boldsymbol{\xi}\right)
\end{aligned}$$

In the above derivation, we assume that the far field mean flow $\overline{\mathbf{Y}}$ is steady and not affected by the control so that $\overline{\mathbf{Y}}' = 0$.

So

$$\begin{aligned}
&\int_{t_0}^{t_f}\int_{\Gamma_{nf}} \boldsymbol{\lambda}^T \widehat{\mathbf{F}_n}' d\mathbf{x} + \int_{t_0}^{t_f}\int_{\Gamma_{nf}} \boldsymbol{\lambda}^T \widehat{\mathbf{A}_n \boldsymbol{Q}}' d\mathbf{x} \\
= &\int_{t_0}^{t_f}\int_{\Gamma_{nf}} \frac{1}{2}\mathbf{Y}'^T \Big((\frac{\partial \mathbf{F}_n}{\partial \mathbf{Y}}^T + \lambda_m \frac{\partial \mathbf{U}}{\partial \mathbf{Y}}^T)\boldsymbol{\lambda} - \mathbf{N}^T (\frac{\partial \boldsymbol{Q}}{\partial \mathbf{y}}^T \mathbf{A}_n{}^T + \overline{\lambda_m} \frac{\partial \boldsymbol{Q}}{\partial \mathbf{y}}^T)\boldsymbol{\xi} \Big) \\
&-\frac{1}{2}\mathbf{y}'^T \big((\frac{\partial \boldsymbol{Q}}{\partial \mathbf{y}}^T \mathbf{A}_n{}^T - \overline{\lambda_m} \frac{\partial \boldsymbol{Q}}{\partial \mathbf{y}}^T)\boldsymbol{\xi} \\
&-\mathbf{F}^T (\frac{\partial \mathbf{F}_n(\overline{\mathbf{Y}} + \mathbf{F}\mathbf{y})}{\partial \mathbf{Y}}^T - \lambda_m \frac{\partial \mathbf{U}(\overline{\mathbf{Y}} + \mathbf{F}\mathbf{y})}{\partial \mathbf{Y}}^T)\boldsymbol{\lambda} \big)
\end{aligned}$$

and consider the following transformation

$$\begin{aligned}
\mathbf{M} &= \frac{\partial \mathbf{U}}{\partial \mathbf{Y}} \\
\overline{\mathbf{M}} &= \frac{\partial \boldsymbol{Q}}{\partial \mathbf{y}} \\
\frac{\partial \boldsymbol{Q}}{\partial \mathbf{y}}^T \mathbf{A}_n{}^T &= \overline{\frac{\partial \mathbf{U}}{\partial \mathbf{Y}}}^T \overline{\frac{\partial \mathbf{F}_n}{\partial \mathbf{U}}}^T = \overline{\frac{\partial \mathbf{F}_n}{\partial \mathbf{Y}}}^T
\end{aligned}$$

we obtain the adjoint operator between the near-field and far-field

- From far-field $\boldsymbol{\xi}$ to near-field $\boldsymbol{\lambda}$,

$$(\frac{\partial \mathbf{F}_n}{\partial \mathbf{Y}}^T + \lambda_m \mathbf{M}^T)\boldsymbol{\lambda} = \mathbf{N}^T (\overline{\frac{\partial \mathbf{F}_n}{\partial \mathbf{Y}}}^T + \overline{\lambda_m \mathbf{M}}^T)\boldsymbol{\xi} \qquad \forall \Gamma_{nf} \tag{4.22}$$

- From near-field $\boldsymbol{\lambda}$ to far-field $\boldsymbol{\xi}$,

$$(\overline{\frac{\partial \mathbf{F}_n}{\partial \mathbf{Y}}}^T - \overline{\lambda_m \mathbf{M}}^T)\boldsymbol{\xi} = \mathbf{F}^T (\frac{\partial \mathbf{F}_n(\overline{\mathbf{Y}} + \mathbf{F}\mathbf{y})}{\partial \mathbf{Y}}^T - \lambda_m \mathbf{M}(\overline{\mathbf{Y}} + \mathbf{F}\mathbf{y})^T)\boldsymbol{\lambda} \quad \forall \Gamma_{nf} \tag{4.23}$$

The implementation details for the adjoint inviscid coupling are shown in Figure 4.4. It is very similar to the state inviscid coupling in §3.3.3.

NS/LEE Consider the state coupling condition (4.10), (4.11), both $\mathbf{N}$ and $\mathbf{F}$ are identity matrix, so (4.22), (4.23) becomes

$$(\frac{\partial \mathbf{F}_n}{\partial \mathbf{Y}}^T + \lambda_m \mathbf{M}^T)\boldsymbol{\lambda} = (\overline{\frac{\partial \mathbf{F}_n}{\partial \mathbf{Y}}}^T + \overline{\lambda_m \mathbf{M}}^T)\boldsymbol{\xi} \qquad \forall \Gamma_{nf} \qquad (4.24)$$

and

$$(\overline{\frac{\partial \mathbf{F}_n}{\partial \mathbf{Y}}}^T - \overline{\lambda_m \mathbf{M}}^T)\boldsymbol{\xi} = (\frac{\partial \mathbf{F}_n(\overline{\mathbf{Y}} + \mathbf{y})}{\partial \mathbf{Y}}^T - \lambda_m \mathbf{M}(\overline{\mathbf{Y}} + \mathbf{y})^T)\boldsymbol{\lambda} \qquad \forall \Gamma_{nf} \qquad (4.25)$$

(4.24) and (4.25) can be approximate as

$$\begin{aligned} \boldsymbol{\lambda} &= \boldsymbol{\xi} \\ \boldsymbol{\xi} &= \boldsymbol{\lambda} \quad \text{at} \quad \Gamma_{nf} \end{aligned}$$

NS/Wave Consider the state coupling condition (4.13), (4.14),

$$(\frac{\partial \mathbf{F}_n}{\partial \mathbf{Y}}^T + \lambda_m \mathbf{M}^T)\boldsymbol{\lambda} = \mathbf{N}^T(\overline{\frac{\partial \mathbf{F}_n}{\partial \mathbf{Y}}}^T + \overline{\lambda_m \mathbf{M}}^T)\boldsymbol{\xi} \qquad \forall \Gamma_{nf} \qquad (4.26)$$

and

$$(\overline{\frac{\partial \mathbf{F}_n}{\partial \mathbf{Y}}}^T - \overline{\lambda_m \mathbf{M}}^T)\boldsymbol{\xi} = \mathbf{W}^T(\frac{\partial \mathbf{F}_n(\overline{\mathbf{Y}} + \mathbf{y})}{\partial \mathbf{Y}}^T - \lambda_m \mathbf{M}(\overline{\mathbf{Y}} + \mathbf{y})^T)\boldsymbol{\lambda} \qquad \forall \Gamma_{nf} \qquad (4.27)$$

Two linear equations (4.26), (4.27) need to be solved to get $\boldsymbol{\lambda}|_{\text{NS}} = N(\boldsymbol{\xi}|_{\text{Wave}})$ and $\boldsymbol{\lambda}|_{\text{Wave}} = F(\boldsymbol{\xi}|_{\text{NS}})$ at coupling interface Γ_{nf}.

Adjoint viscous coupling

Besides the adjoint inviscid flux coupling, there is also the viscous coupling for $-\boldsymbol{\lambda}^T \widehat{\mathbf{F}_n^v}'$, which can be transformed into the two terms, adjoint viscous convection term $-\mathbf{U}'\widehat{\boldsymbol{G}_n^a}$ and adjoint diffusion term $\mathbf{U}'\widehat{\boldsymbol{G}_n^{av}}$. More details are given in Appendix B.1. Here those two terms are only from the adjoint Navier–Stokes equations.

Adjoint viscous convective flux $\widehat{\boldsymbol{G}_n^a}$ For the coupling at Γ_{nf}, the numerical flux $\widehat{\boldsymbol{G}_n^a}$, we are using the central flux as in B.1.1. Because of the coupling, there is no contribution from LEE/Wave side Ω_f, so

$$\widehat{\boldsymbol{G}}_n^a(\boldsymbol{\lambda}^-, \boldsymbol{\lambda}(\boldsymbol{\xi})^+) = \frac{1}{2}\left(\boldsymbol{G}_n^a(\boldsymbol{\lambda}^-) + 0\right) \qquad \forall \Gamma_{nf} \tag{4.28}$$

Adjoint viscous diffusive flux $\widehat{\boldsymbol{G}_n^{av}}$ For the coupling at Γ_{nf}, the numerical flux $\widehat{\boldsymbol{G}_n^{av}}$, we are using the Bassi–Rebay flux as in §3.3.3. Because of the coupling, there is no flux contribution from LEE/Wave side Ω_f.

Following (3.7), first a "jump savvy" gradient of the state, $\boldsymbol{\sigma} \sim \nabla\boldsymbol{\lambda}$ is computed by solving

$$\begin{aligned}\sum_{e=1}^{N} \int_{\Omega_e} \boldsymbol{V}^T \boldsymbol{\sigma}_j \, d\mathbf{x} \;&=\; -\sum_{e=1}^{N} \int_{\Omega_e} \boldsymbol{V}_{,j}^T \boldsymbol{\lambda} \, d\mathbf{x} + \sum_{e=1}^{N} \int_{\partial\Omega_e/\Gamma_{ef}} \boldsymbol{V}^T \widehat{\boldsymbol{\lambda}} n_j \, d\mathbf{s} \\ &\quad + \int_{\Gamma_{ef}} \boldsymbol{V}^T \widehat{\boldsymbol{\lambda}(\boldsymbol{\xi})} n_j\end{aligned}$$

$\forall \boldsymbol{V} \in \mathcal{V}(\mathcal{P}_h)$ and for j from 1 to d, where

$$\begin{aligned}\widehat{\boldsymbol{\lambda}} \;&=\; \frac{1}{2}\left(\boldsymbol{\lambda}^- + \boldsymbol{\lambda}^+\right) \,. \qquad \forall \partial\Omega_e/\Gamma_{nf} \\ \widehat{\boldsymbol{\lambda}} \;&=\; \frac{1}{2}\left(\boldsymbol{\lambda}^- + \boldsymbol{\lambda}^+(\boldsymbol{\xi})\right) \,. \qquad \forall \Gamma_{nf}\end{aligned}$$

where $\boldsymbol{\lambda}^+(\boldsymbol{\xi})$ is related with the linearized Euler element edge and $\boldsymbol{\lambda}^-$ is from the NS element edge.

Our final Bassi–Rebay viscous flux $\widehat{\boldsymbol{G}}_n^{av}$ is then computed using

$$\widehat{\boldsymbol{G}}_n^{av}(\boldsymbol{\lambda}^-, \boldsymbol{\sigma}^-, \boldsymbol{\lambda}^+, \boldsymbol{\sigma}^+) = \frac{1}{2}\left(\boldsymbol{G}_n^{av}(\boldsymbol{\lambda}^-, \boldsymbol{\sigma}^-) + 0\right) \,. \qquad \forall \Gamma_{nf} \tag{4.29}$$

where $\boldsymbol{G}_n^{av}(\boldsymbol{\lambda}^+, \boldsymbol{\sigma}^+) = 0$ is the flux contribution from the edge in the linearized Euler

domain, which is zero in our adjoint formulation.

4.3.3 Optimal Control of Multi-model System

Our optimization strategy for the multi-model system is shown in Figure 4.2. Combining the multi-model solver for the state and adjoint, we get our gradient information for the multi-model system. With the suitable gradient-based optimization algorithms, we are able to solve the optimal control problem for the multi-model system.

4.4 Optimization Algorithm

4.4.1 Conjugate Gradient

The control is updated using a gradient based algorithm. Solution of the optimality equations yields the gradient of the objective functional with respect to the control which should be equal to zero at the optimum. We use a nonlinear conjugate gradient method to solve this optimization problem as in [20, 22, 33, 35, 38]. After the state and adjoint equations are solved, the gradient of the cost functional can be obtained. Following the optimization method, an iterative update method based on the Polak-Ribiere conjugate gradient algorithm [97] is used in our work. It is given by

$$\overline{\Phi}^{k+1} = \overline{\Phi}^{k} + \alpha^{k}\mathbf{h}^{k} \tag{4.30}$$

where the update direction $\mathbf{h}^k = -\mathbf{g}^k + \beta^k \mathbf{h}^{k-1}$, $\mathbf{g}^k$ is the gradient obtained from (A.28), (A.32) or (A.33), $\beta^k = (\mathbf{g}^k - \mathbf{g}^{k-1}) \cdot \mathbf{g}^k / (\mathbf{g}^{k-1} \cdot \mathbf{g}^{k-1})$. The step-size α^k determines how far one moves in the direction $\mathbf{h}^k$ to obtain the new control. At each iteration, the value of α^k is calculated by using several test α^k to minimize $\overline{\mathcal{J}}^{k+1}$ in the direction of $\mathbf{h}^k$ using line minimization, which is a testing procedure to find the

minimum value of α in the function $\overline{\mathcal{J}}(\overline{\Phi}^k + \alpha \mathbf{h}^k)$, where $\overline{\Phi}^k$ and $\mathbf{h}^k$ are known and α is the independent variable [97].

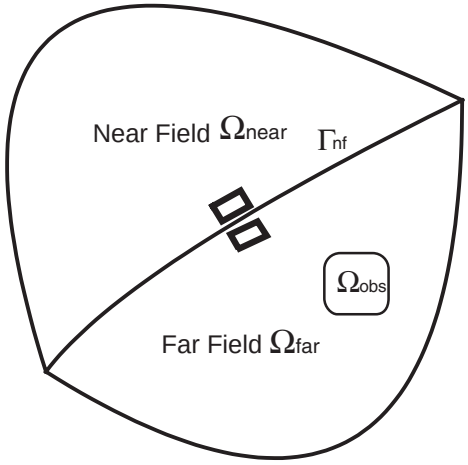

Figure 4.1: Schematic of optimal control problem for coupled system

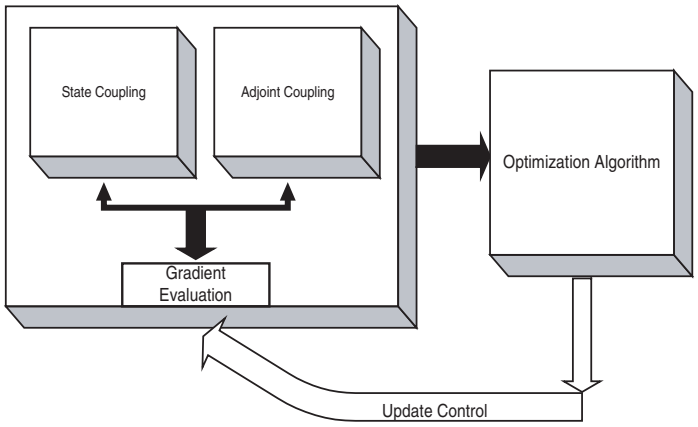

Figure 4.2: Optimization strategy for the multi-model system using the adjoint approach

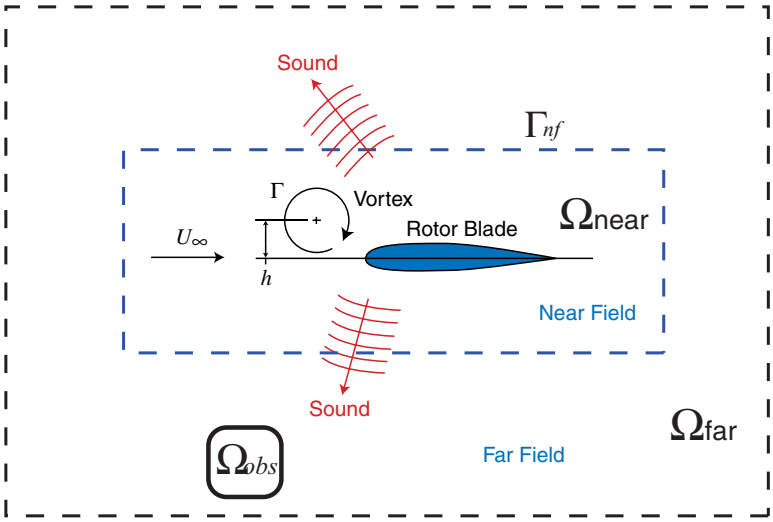

Figure 4.3: Schematic of multi-domain/model for blade-vortex interaction

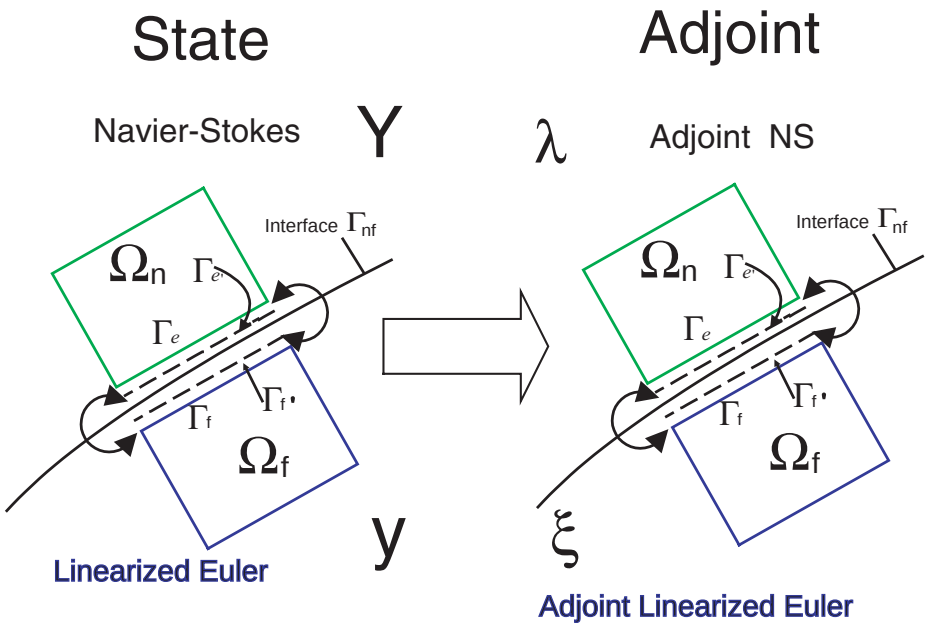

Figure 4.4: Adjoint coupling for the multi-model implementation

Chapter 5

State Validation

In this chapter, we give results of state solution without control based on the single model and multi-model to validate our state solver, especially the linearized acoustics solvers. Such validation for accurate state solution is crucial for evaluating the control strategies. This chapter begins with two validation results for the linear solvers, linearized Euler and isentropic wave solver, by presenting one dimensional planar acoustics propagation and the benchmark problem of the acoustics scattering. Results are presented and compared to the existent analytical solution.

To validate the multi-model multi-domain algorithm, the second part of this chapter presents the acoustic results from three cases with different model coupling: acoustics scattering, inviscid vortex cylinder interaction and viscous vortex rotor-blade interaction, along with comparisons to the available analytical results or the solutions from direct full-field acoustics solver.

5.1 Planar Acoustic Waves

To validate our linearized Euler or isentropic Wave equation solver, we consider a linear planar acoustics problem as our first validation case. Based on the characteristic

relations for the Euler equations [57]

$$\begin{aligned} \delta w_1 &= \delta\rho - \frac{\delta p}{c^2} \\ \delta w_2 &= n_y\delta u - n_x\delta v \\ \delta w_3 &= \overrightarrow{n}\overrightarrow{u} + \frac{\delta p}{\rho c} \\ \delta w_4 &= -\overrightarrow{n}\overrightarrow{u} + \frac{\delta p}{\rho c} \end{aligned} \tag{5.1}$$

In (5.1), the four equations correspond to the entropic, vortical, and two acoustic wave. If considering the isentropic and isvorticity acoustics, the first two characteristic variables will be zero. Given the acoustics distribution, we can get the initial acoustic formulation.

5.1.1 1D Gaussian Acoustics

In this case, an initial condition of Gaussian pulse $\exp(-\frac{(x-x_0)^2}{\lambda^2})$ is used, the wave propagates toward the x axle direction.

$$\begin{aligned} \delta p &= \frac{\varepsilon\exp(-\frac{(x-x_0)^2}{2\lambda^2})}{2} \\ \delta\rho &= \frac{\varepsilon\exp(-\frac{(x-x_0)^2}{2\lambda^2})}{2c^2} \\ \delta u &= \frac{\varepsilon\exp(-\frac{(x-x_0)^2}{2\lambda^2})}{2\rho c} \\ \delta v &= 0 \end{aligned} \tag{5.2}$$

It is one dimensional problem, however we solve it in two dimensional setting with both periodical boundary condition for left/right and top/bottom boundary. There is no mean flow $\bar{u} = 0, \bar{v} = 0$. For this acoustics setting, the reference $M = 0.3$ and the local sound speed $c = 3.3333$. From the planar acoustics physics, in theory we know the planar acoustics will travel to $f(x - c * t)$ at time t for a right propagating

planar acoustics as

$$\begin{aligned} p &= \bar{p} + \frac{\varepsilon \exp(-\frac{(x-ct-x_0)^2}{2\lambda})}{2} \\ \rho &= \bar{\rho} + \frac{\varepsilon \exp(-\frac{(x-ct-x_0)^2}{2\lambda})}{2c^2} \\ u &= \frac{\varepsilon \exp(-\frac{(x-ct-x_0)^2}{2\lambda})}{2\rho c} \\ v &= 0 \end{aligned}$$

where $\varepsilon = 0.001$, $x_0 = 1.5$. Considering $c = 3.33333$ and the periodical boundary condition, at $t = 12.0$ after 60000 steps with time step $\delta t = 0.0002$, the acoustics is supposed to be back to the initial position, which is also our analytical solution at $t = 12$. We solve this problem with three solvers, linearized Euler, isentropic Wave and full Euler solvers, all in the conservative form (2.12), (2.16) and (2.1). The whole domain includes 25 elements with $p = 5$ in each element as in Figure 5.3. Through this numerical experiment, we want to study the dispersion and dissipation property of the our linear acoustics solver at different resolution after traveling 40 wave length.

Numerical Result

Figure 5.4 shows the numerical and theoretical result for density fluctuation ρ' at $t = 12$. At $p = 3$, there is around 7 points per wave length, it is well below the resolution required to resolve the acoustic pulse. As expected, at $p = 3$ even the initial condition is not smooth at all in Figure 5.4. There is also some jumps in the middle at so low resolution. After travelling 40 wave length, because of the numerical dissipation at the low resolution, there is some obvious change for the wave amplitude. All those are desirable at the low resolution for acoustic computation. Increasing $p = 3$ to $p = 5$, now there is 9 points per wave length. We get much better agreement between the analytical and numerical solution in Figure 5.5, although there

is still some noticeable errors. Increasing to $p = 8$, the agreement becomes perfect in Figure 5.6. We also solve this problem using the isentropic wave solver. Due to the isentropic property of this problem, in theory both solvers (LEE and Wave) should give the same accuracy, which is shown in Figures 5.7. It is also shown in Figure 5.9 where the relative error from LEE and Wave is the same. Solving this problem with the nonlinear Euler solver, we still get excellent solution in Figures 5.8 and 5.9. The error is comparable to that from LEE and Wave solvers at most of state resolution, however at high resolution the relative error is not as good as those from the linear solvers, which might be from its nonlinear effect as in Figure 5.9.

5.2 Acoustic Scattering from Cylinder

For the blade-vortex interaction problem, one very important aspect is to accurately capture the resulting acoustic wave propagating away from the blade. To ensure our acoustics solver accurately capture such acoustics, we have validated our code for the classical benchmark problem of planar acoustics scattering from a circular cylinder, because of the known analytical solution. This interaction results the scattered wave propagating away from the cylinder. This problem has also been computed by Collis [29] in frequency domain for the validation for the leading-edge receptivity problems. We have validated this case of planar acoustics scattered from a stationary circular cylinder of radius $a = 0.5$ subject to a plane acoustic-wave travelling perpendicular to the cylinder axis. In this case, the reference length is the cylinder diameter, the reference velocity is the uniform mean flow speed $U_\infty = 1.0$ and all other reference quantities are based on the far field values.

The incident plane-wave is expressed as

$$p_i = P_0 e^{ik(x-ct)} \tag{5.3}$$

$$k = \frac{2\pi}{\lambda} \tag{5.4}$$

where the direction of propagation is along the positive x-axis and P_0 is the incident pressure amplitude, here it is 0.01. Under these conditions, the scattered pressure wave is expressed by the following Bessel Function expansion as defined in [87],

$$P_s = \sum_{m=0}^{\infty} A_m \cos(m\theta)[J_m(kr) + iN_m(kr)]e^{-i\omega t} \tag{5.5}$$

where (r, θ) are the usual cylindrical coordinates, $\omega = \frac{2\pi c}{\lambda}$ and

$$A_m = -\varepsilon_m P_0 i^{m+1} e^{-i\gamma_m} \sin\gamma_m$$

$$\tan\gamma_0 = -\frac{J_1(k)}{N_1(k)}$$

with $\varepsilon_0 = 1$ and $\varepsilon_m = 2$ for all m larger than zero. J_m and N_m are Bessel functions of first- and second-kind, respectively.

The simulation is conducted for an incident acoustic wave with wave number $k = 2.5$. The whole domain Ω is quite large $[-30, 30] \times [-30, 30]$ with sponge layer enforced around the perimeter of the domain to approximate a nonreflecting boundary [39, 40].

Since the computational domain is very large, at the left boundary, locally the plane acoustic wave is forced for the acoustics propagation. Over the region $\Omega \backslash [-20, 20] \times [-20, 20]$, an outflow sponge term is added to damp only the scattered field with the incident wave unaffected. This is accomplished by the sponge term

$$W(q) = -f_d(\vec{x})(q - q_i) \tag{5.6}$$

where q_i is the vector of the conservative variables corresponding to the incident plane acoustic wave, which is a reference state of a spatial coordinates and of time. The sponge function for our case is designed to vary smoothly from zero in the interior to a finite value A_s on the boundary and given by

$$f_d(\vec{x}) = \begin{cases} A_s(\frac{x+20}{-30+20})^{N_s} & x \in [-30, -20] \\ A_s(\frac{x-20}{30-20})^{N_s} & x \in [20, 30] \\ A_s(\frac{y-20}{30-20})^{N_s} & y \in [20, 30] \\ A_s(\frac{y+20}{-30+20})^{N_s} & y \in [-30, -20] \\ 0 & \text{otherwise} \end{cases}$$

with $A_s = 100$ and $N_s = 3$. Such implementation for the far field boundary is pretty effective, as in Figure 5.11, the scattered acoustics is damped very smoothly and cleanly in the sponger layer around the boundary.

For this simulation, the incident acoustic wave length is $\lambda = 2.51327$. In Figure 5.10 the computational domain comprises 6832 quadrilateral elements with per element size around $h = 0.8$, polynomial order $p = 6$ for each element. There are at least 18 nodes per wave length.

This problem is solved with the full Euler, linearized Euler and Wave solvers. Here we present some results from linearized Euler solver. Figure 5.11 shows contours of the instantaneous, scattered pressure field from the simulation demonstrating the damping of the scattered field in the sponge region. The scattered pressure RMS P_{rms} along the ray $\theta = \pi$ is shown in Figure 5.12[a] compared to the theoretical solution (5.5). As expected, the acoustic intensity approaches constant far from the cylinder which confirms the expected $1/r$ decay of the scattered acoustics. In the sponge, the intensity of the scattered wave is smoothly damped to zero. Furthermore, we also validate the directionality of the scattered acoustics, which is very important for our future BVI acoustics simulation and its control. Figure 5.12[b] shows a polar plot of the scattered pressure P_{rms} at $r = 10.0$. It shows excellent agreement between the

theory and simulation. Both the two plots show that our linear acoustics solver can accurately predict the intensity and directionality of acoustic wave scattered from a solid body.

5.2.1 Euler/Wave

As validation of our multi-model approach, this classical acoustics benchmark problem using Euler/Wave coupling is also presented for the validation. In Figure 5.13, it can be seen that a very arbitrary interface is selected that separates the Euler domain in the near field from the wave equation domain in the far field. The pressure field shown in Figure 5.13 from the simulation also demonstrates the damping of the scattered wave in the sponge region. Note that this mesh is also partitioned into multiple domains for the parallel computation.

Figures 5.14 and 5.15 show contours of the instantaneous, total and scattered pressure field from the simulation and very smooth solutions are obtained near the coupling surface. In Figure 5.16, the RMS pressure from the scattered wave is compared with the analytical solution from inviscid theory and both ray and polar RMS pressure agree with the theoretical results with no indication of inaccuracies near the coupling interface. This test case demonstrates that our multi-model approach can accurately predict the intensity and directionality of acoustic wave scattered from a solid body and gives us confidence in our multi-model formulation.

5.3 Vortex-Cylinder Interaction

The flexibility of our coupling approach is demonstrated from the following simulation results for a vortex interacting with a circular cylinder in a uniform flow $M = 0.3$ as in Figure 5.1. The simulation results from heterogeneous domain decomposition approach will be compared with that from direct Euler solver. In this problem, the

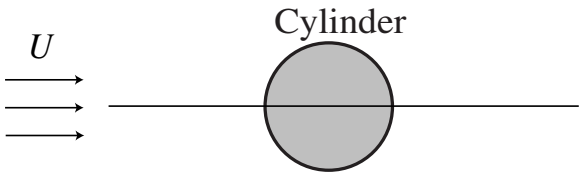

Figure 5.1: Inviscid vortex cylinder interaction

domain is decomposed into two domains, a linearized Euler (LEE) or isentropic Wave domain outside and Euler domain inside as in Figure 5.17. The collocation mesh, shown in Figure 5.18 shows that the dense mesh is used along the vortex trajectory. With this approach, the discontinuous Galerkin method can accurately capture the evolution of the inviscid vortex while efficiently resolving the acoustic field away from the cylinder. Such model problem has been used as the prototype for the Blade-Vortex-Interaction noise capture and its optimal control [33].

For the multi-model simulation, both Euler/LEE and Euler/Wave have been applied. To validate the solution from our multi-model solver, we place several observation points P_0, P_1 and P_2 in the computational domain as in Figure 5.17, so we can compare the ρ, p, u and v history at those observation from direct Euler, Euler/LEE and Euler/Wave. Furthermore, we also define two coupling interface in Figure 5.17 to investigate the effect of the coupling interface location.

In Figure 5.19, the pressure contours at $t = 15.0$ from direct Euler and Euler/LEE coupled solver looks extremely similar, both of which are in the same contour levels. Furthermore, in Figure 5.20, around the coupling interface the pressure contour is also quite smooth without any discontinuities. Figures 5.21, 5.22 and 5.23 are the time history of ρ, p, u and v at the observation of P_0, P_1 and P_2, using the smaller coupling interface. From those figures, the solution from Euler, Euler/LEE and Euler/Wave has excellent agreement at the observation inside or outside the coupling interface. As expected, increasing the Euler domain inside, we still get the excellent time history

at P_0, P_1 and P_2 as in Figures 5.24, 5.25, and 5.26. Both the small and big coupling surface is far away from the vortex trajectory, which make it reasonable to assume the linear far-field. All those indicate that the solution from multi-model approach (Euler/LEE, Euler/Wave) agrees very well with that from direct Euler solver at the observation inside or outside the coupling interface.

To investigate the effect from the multi-model formulation, Figure 5.27 shows the pressure error history $p - p_{\text{Euler}}$ from Euler/LEE and Euler/Wave at P_0. The errors from Euler/Wave and Euler/LEE are quite small using the small and large coupling interface. The difference of using Euler/Wave and Euler/LEE is very small and the result of Euler/LEE is slightly better. As expected, making Euler domain inside bigger does make the solution slightly better for both Euler/Wave and Euler/LEE coupling. However, under the small coupling interface, the error from both Euler/Wave and Euler/LEE after $t = 24.0$ becomes significant. The peak error at $t = 24.5$ is around 0.1, which is quite large. Check the vortex trajectory in Figure 5.17, at that time the vortex has passed the small coupling interface and entered the LEE or Wave domain. The error due to the vortex in a linear domain will propagate to P_0. Such error has also been noticed by Brentener for the Kirchhoff method when the vortex passed the Kirchhoff surface [16, 17].

Figure 5.27 is the pressure error history at P_0 inside both coupling surfaces. If there was no feedback from the far field acoustics to the inside fluid flow, the pressure history at P_0 should have been the same as that from direct Euler solver. On the contrary, the pressure error history in Figure 5.27 indicates that the far-field linear modelling gives the feedback to the near-field fluid flow and eventually affects the near-field state solution. However, such feedback is quite small as shown in Figure 5.27. Figure 5.28 shows the pressure error history at the observation P_1, which is between the big and small coupling interfaces. There is very little difference between Euler/Wave and

Euler/LEE coupling. With larger coupling interface, the error is less. In Figure 5.29 it is the error history for the far field pressure at P_2. Compared with that from direct Euler solver, both Euler/Wave and Euler/LEE gives excellent pressure history using the small and large coupling interface. Larger coupling interface gives better solution. Check the pressure error history at P_2 in Figure 5.29, it is similar to P_1. Both Euler/Wave and Euler/LEE give excellent solution, the solution using the larger coupling interface is better.

In summary, for this specific problem, we conclude that the both Euler/Wave and Euler/LEE coupling gives very excellent agreement with the solution from direct Euler solver. The difference between the two multi-model coupling is very small, Euler/LEE coupling does give slightly better solution. The solution is more sensitive to the location of the coupling interface. To get the accurate far field pressure, the location of the coupling interface is very important. Too small interface will bring the nonlinearity into the linear domain and makes the far field modelling inaccurate. The location of both coupling interface are far away from the vortex trajectory which makes it contain the nonlinear interaction inside as in Figure 5.17. As expected, we get excellent time history of p,u and v for P_1 for all the three observation locations. However, there is slight error in Figure 5.28 when the vortex passes the small coupling interface. Considering the extra cost from LEE and limited improvement, we conclude that for the far field, the isentropic Wave equation with the reasonable domain partition should be adequate for the far-field acoustics computation.

5.4 Vortex-Rotor Interaction

In this section, a model BVI problem is presented in Figure 5.2, where the rotor is Bell AH-1 rotor blade, the vortex is the compressible Oseen vortex. The Oseen vortex is advected towards the rotor blade in the uniform flow of $M = 0.3$. For this kind of BVI

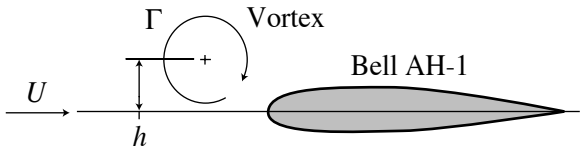

Figure 5.2: Schematic of Bell AH1 rotorblade vortex interaction

problem, where the impulsive noise is usually generated by the rotating machinery, the simplified model, an Euler [70] or even a full potential model [63] may be adequate because the turbulence is not so important. Because of our interest in applying the blowing/suction on the surface of the rotor blade for the on-blade control, which may introduce vorticity at the blade surface to alleviate the interaction between the vortex and the blade, we decide to use the Navier–Stokes (NS) equations in the near field to capture the viscous phenomenon. In the far field, the nonlinearity and viscosity is very weak, the linearized Euler or isentropic Wave equations is adequate for the acoustics propagation. Such domain partition is to make the inside domain better resolve the viscous effect where the very dense mesh is used and the sparser mesh is used outside to capture the BVI noise.

For this multi-model simulation in Figure 5.30, in the near field, the viscous NS equations are used and the linearized Euler or isentropic wave equations are applied in the far field to capture the BVI noise. To study the effect of the multi-model coupling, we place several observation points P_0, P_1, P_2 and P_3 in the computational domain as in Figure 5.31 so that we can compare the pressure and velocity history at those observation from direct NS, NS/LEE and NS/Wave.

This problem setup follows Lee's work [70] using the completely structured mesh. Reynolds number $Re = 1000$ is used for this viscous BVI problem. The problem of wakes forming and hitting the right boundary in [70] is fixed using the sponger layer defined in $[3.72, 6.5] \times [-1, 1]$ in the NS domain. The reference state $\mathbf{U}_{ref}$ in the sponge is obtained by solving a steady flow of freestream passing the Bell AH-1 rotor

with free stream as the reference state in the sponge layer.

In Figure 5.32, the scattered pressure contours at $t = 68.4$ from direct NS and NS/LEE coupled solver looks very similar, both of which are in the same contour levels. However, for the scattered pressure contour from direct NS solver, there is two additional pressure acoustics in the far field. It appears to be from the viscous effect in the far field. Around the coupling interface, the scattered pressure contour is also quite smooth without any discontinuities in Figure 5.32[b].

Figure 5.33 shows the time history of p, u and v at the observation of P_0, which is located outside the coupling interface. All show that the solution from direct NS, NS/Wave and NS/LEE have excellent agreement. The same happens for that of P_1, P_2 and P_3 as in Figures 5.34, 5.35 and 5.36. It indicates that the solution from multi-model approach(NS/LEE, NS/Wave) have excellent agreement with that from direct NS solver at the observation inside or outside the coupling interface, although there is some slight error for u and v from coupled solver compared with that from NS at the end of time history in Figures 5.34, 5.35 and 5.36.

Compared with the pressure from direct NS, the difference from multi-model solver is more obvious in Figure 5.37 for P_0 which is in the linear domain above the blade. NS/Wave and NS/LEE give similar pressure history with very little difference. The peak error is between 10^{-4} and 10^{-3}. For P_1, it is inside NS domain. The difference from multi-model solver is small, but not negligible. It indicates that the current coupling is dual communication, *i.e.,* the near-field and far-field affects each other, which is contrary to the traditional coupling, such as FW-H equation and Kirchhoff method, both of which assume that the far-field acoustics won't reflect back. Because of the similar location, the pressure history of P_2 is also similar to that of P_0 in Figure 5.39, the difference between NS/Wave and NS/LEE is extremely small.

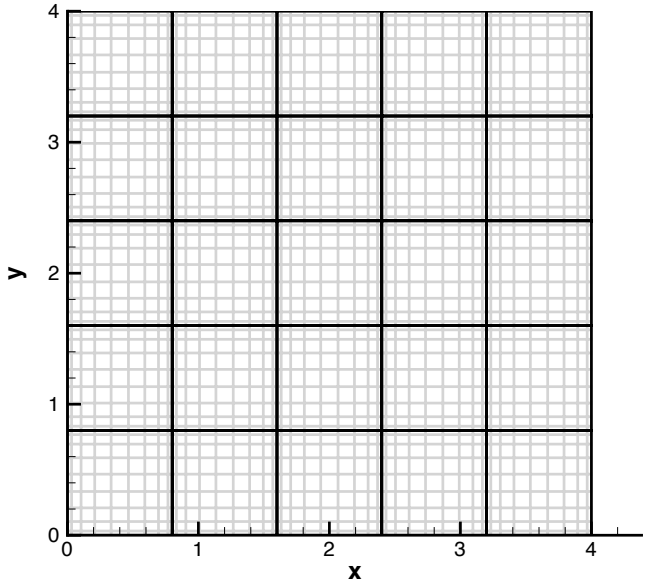

Figure 5.3: One-dimensional Gaussian pulse propagation using 25 elements with polynomial order $p = 5$, quadrilateral mesh

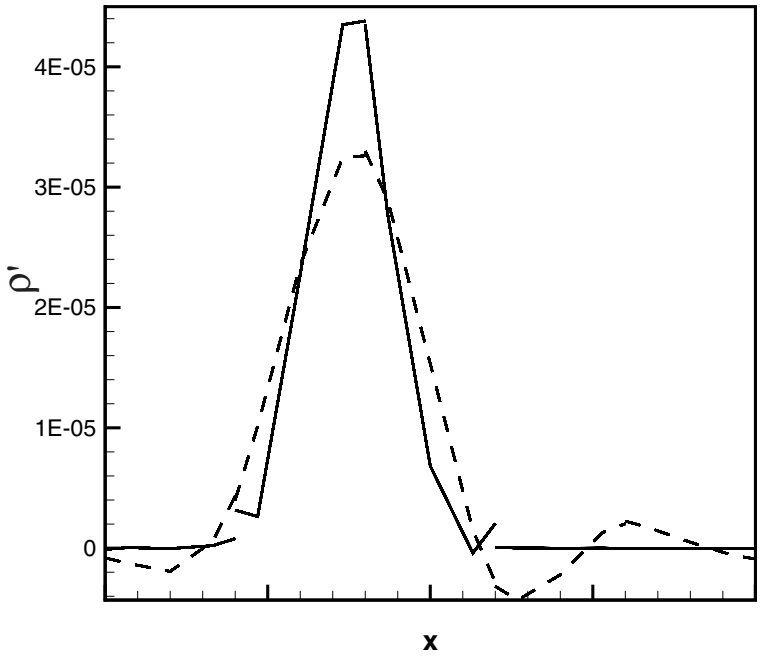

Figure 5.4: LEE: density fluctuation ρ' with polynomial order $p = 3$: —— initial profile; ---- the profile at $t = 12$;

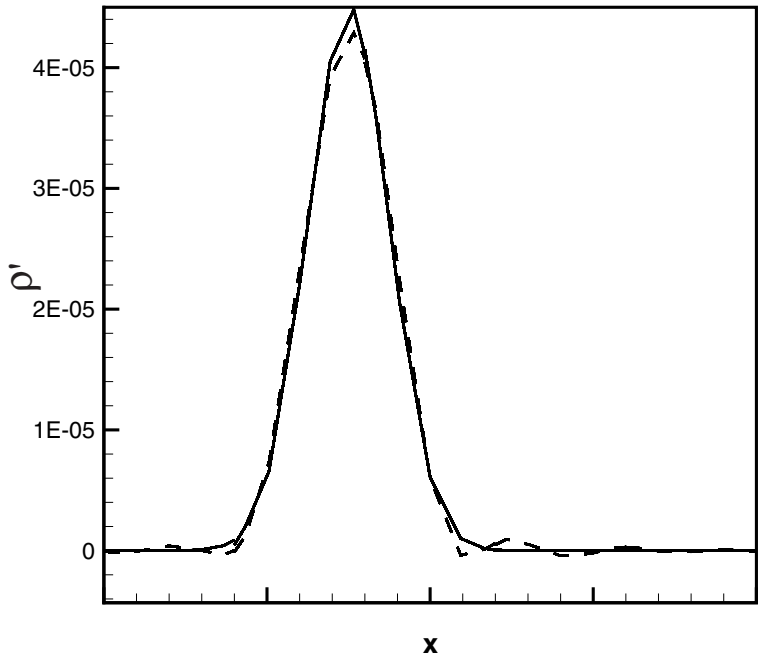

Figure 5.5: LEE: density fluctuation ρ' with polynomial order $p = 5$: —— initial profile; ---- the profile at $t = 12$;

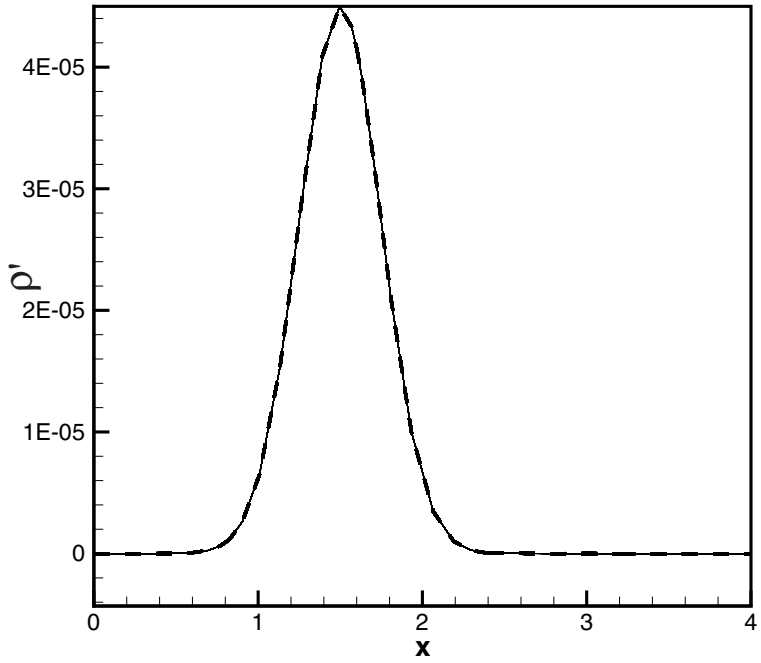

Figure 5.6: LEE: density fluctuation ρ' with polynomial order $p = 8$: —— initial profile; ---- the profile at $t = 12$;

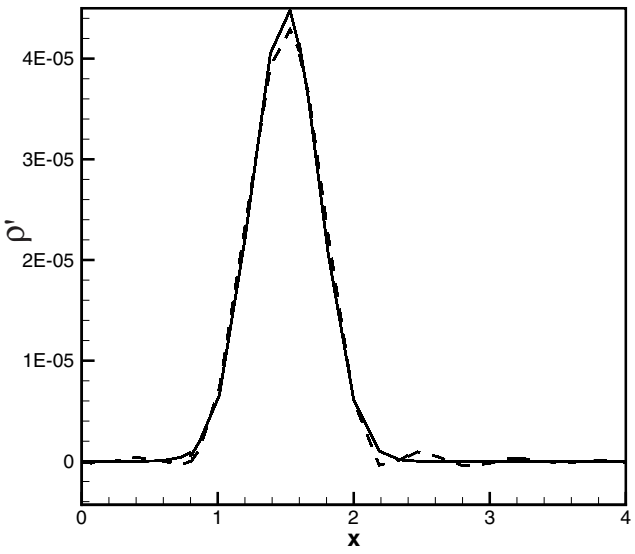

Figure 5.7: Wave: density fluctuation ρ' with polynomial order $p = 5$: —— initial profile; ---- the profile at $t = 12$;

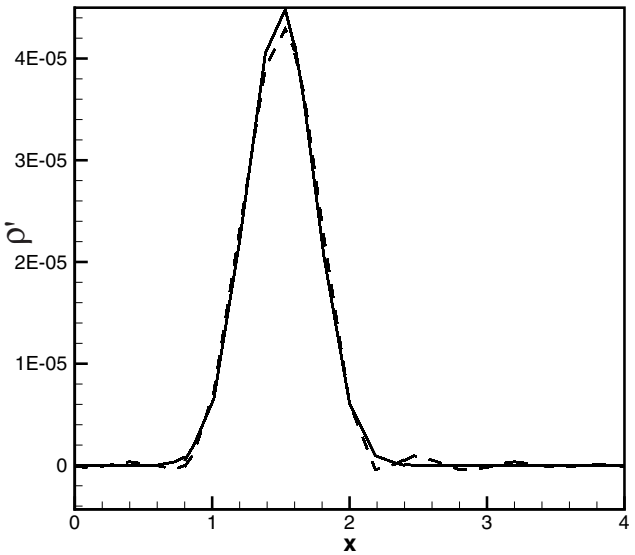

Figure 5.8: Euler: density fluctuation ρ' with polynomial order $p = 5$: —— initial profile; ---- the profile at $t = 12$;

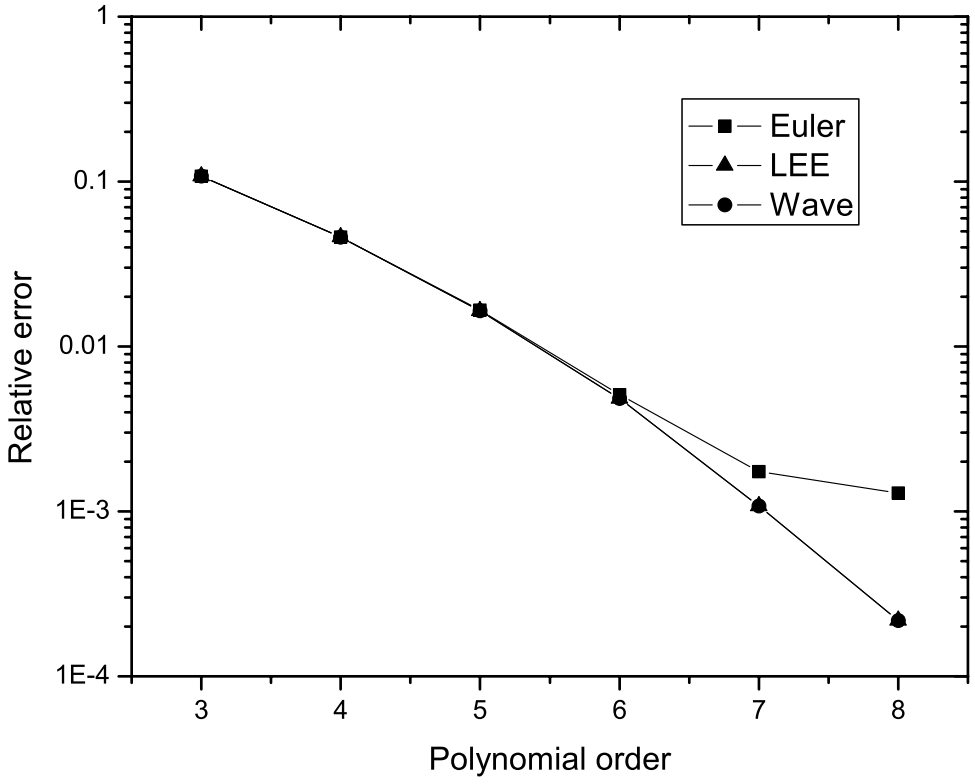

Figure 5.9: Relative error Vs. Polynomial order p

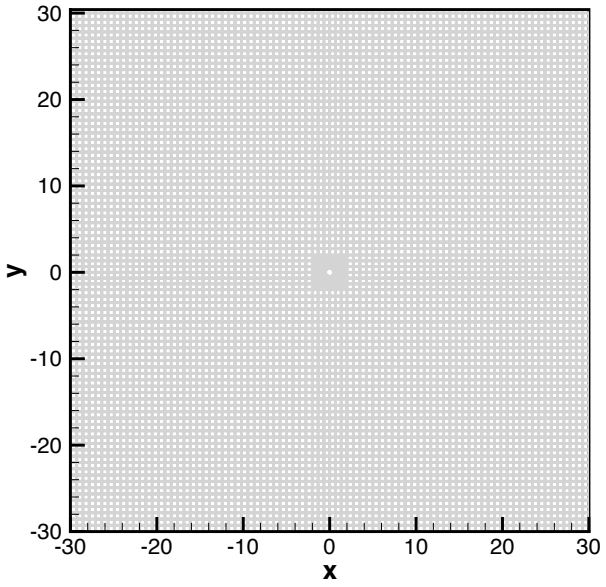

Figure 5.10: Mesh for the planar acoustics scattering

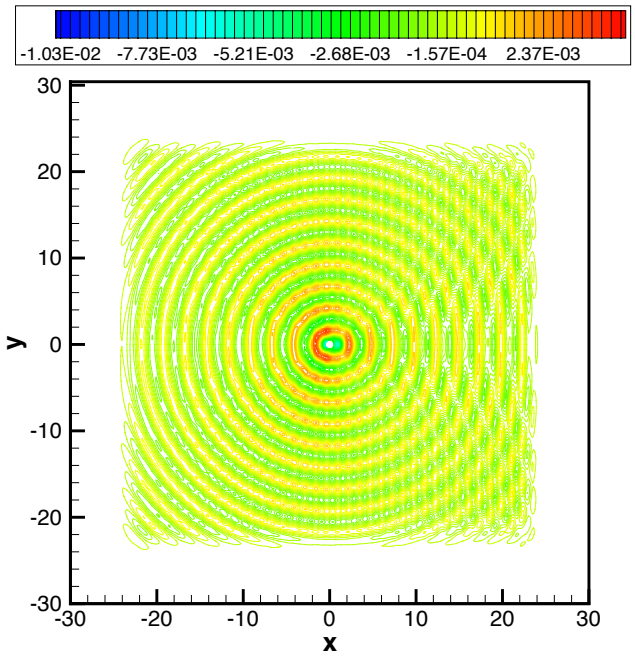

Figure 5.11: Scattered pressure

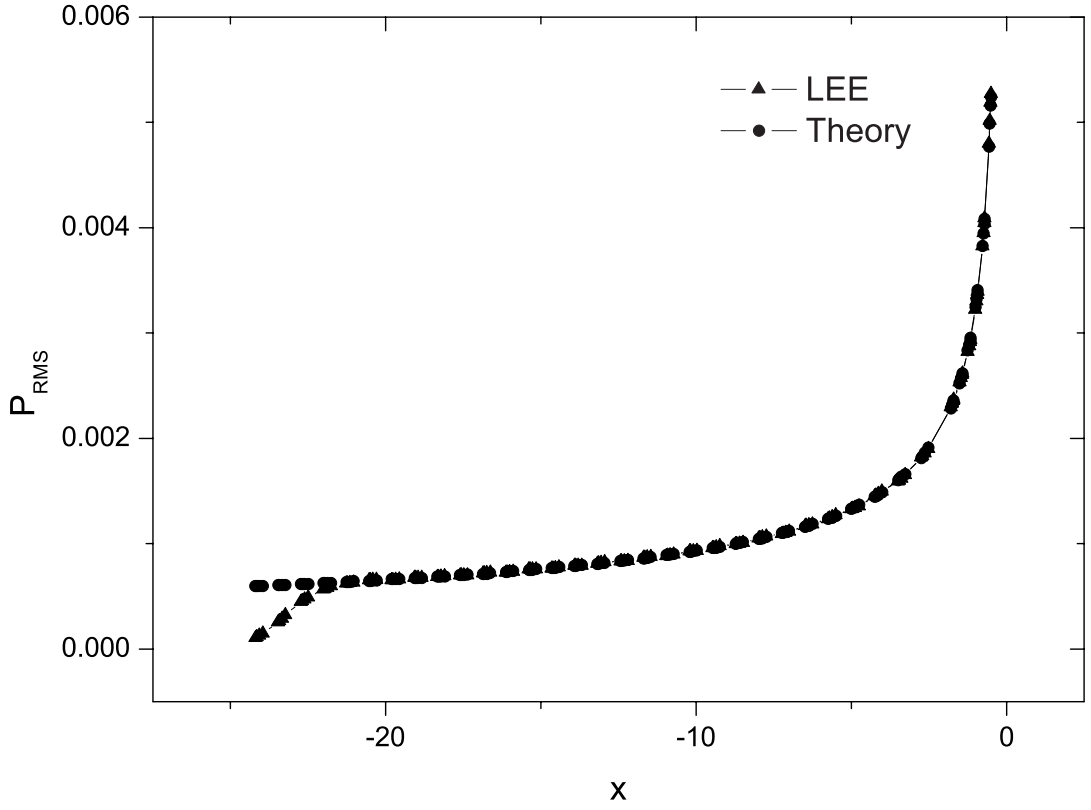

(a)

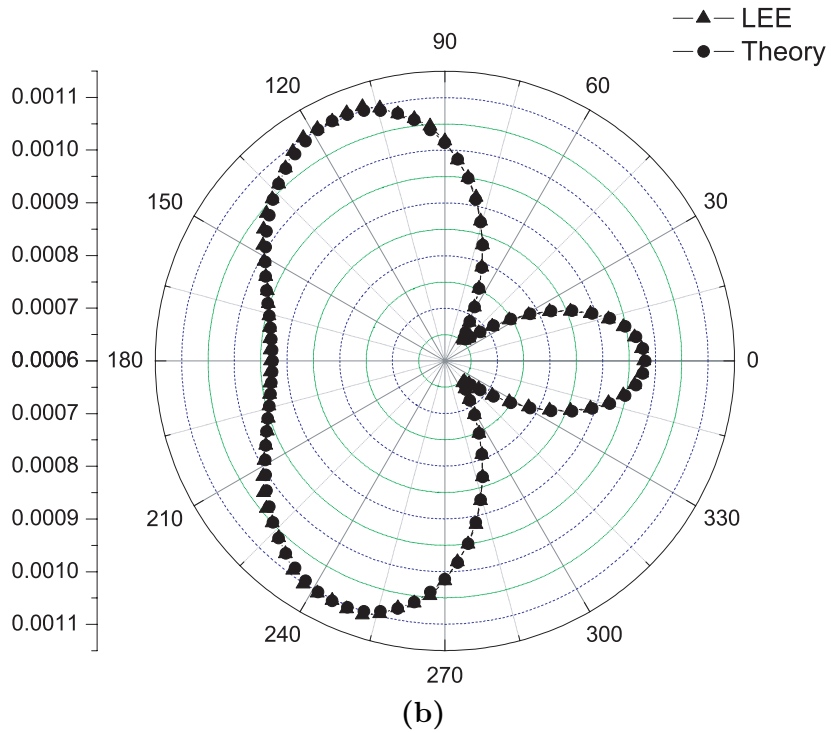

(b)

Figure 5.12: (a) Comparison of RMS pressure along the ray $\theta = \pi$, (b) Comparison of RMS pressure along radius $r = 10$

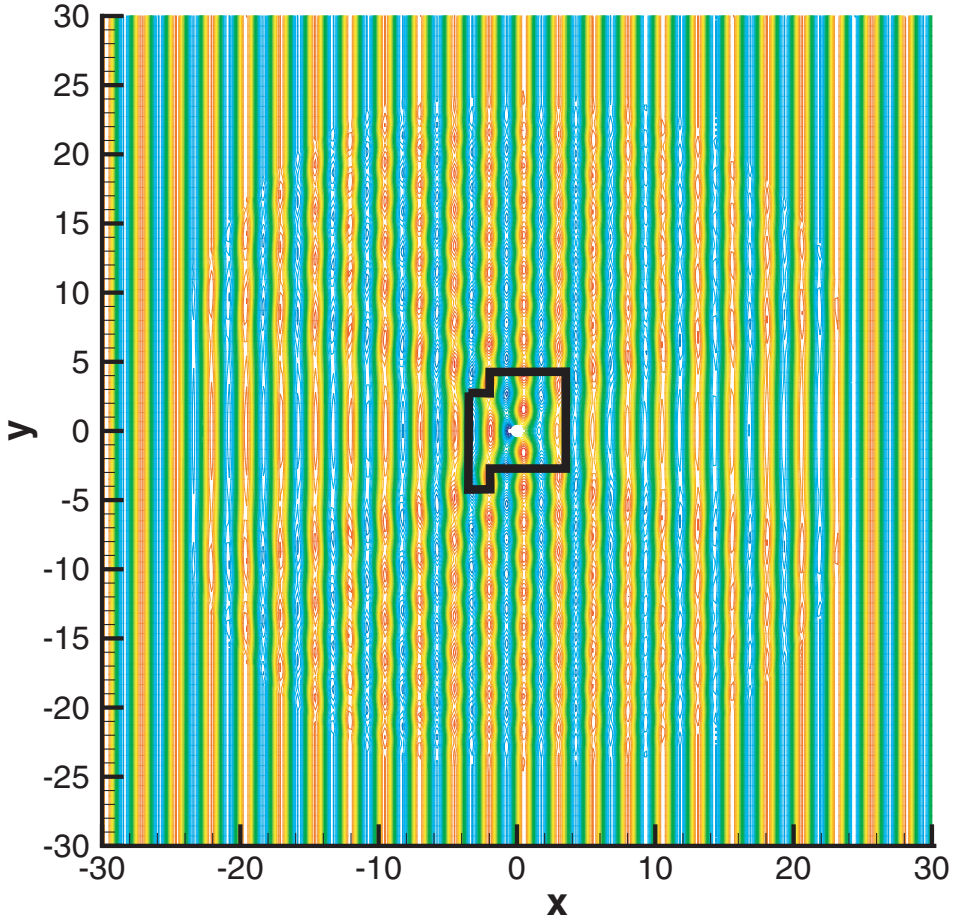

Figure 5.13: Acoustic scattering from a circular cylinder: incident and scattered pressure on the full domain. The irregular solid line denotes the interface between the Euler region in the near field and the wave equation region in the far field

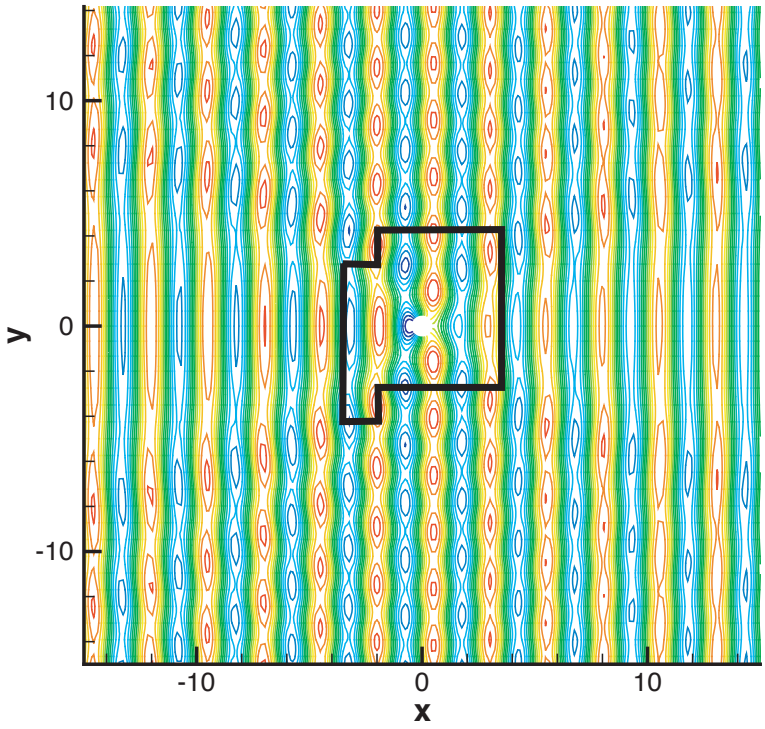

Figure 5.14: Incident and scattered pressure near the cylinder

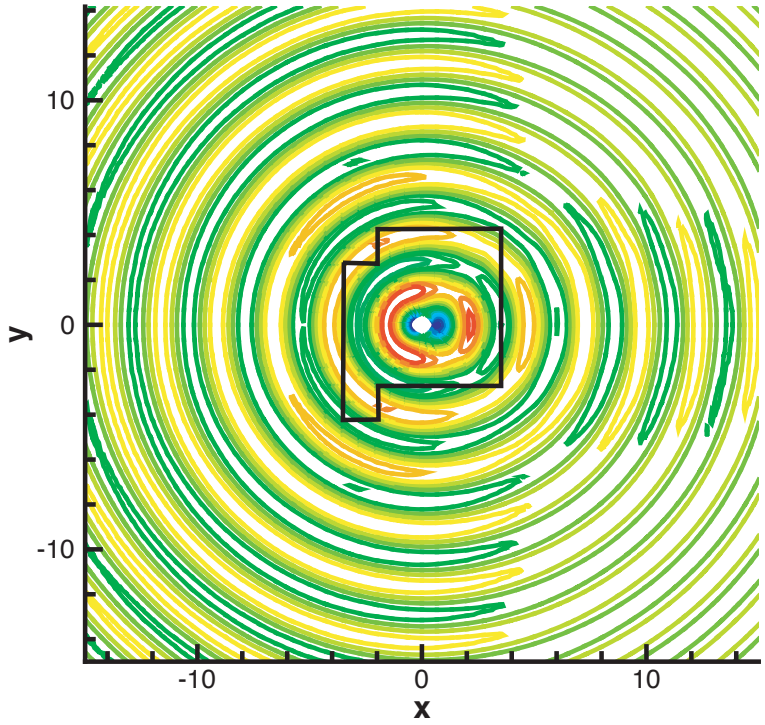

Figure 5.15: Scattered pressure near the cylinder

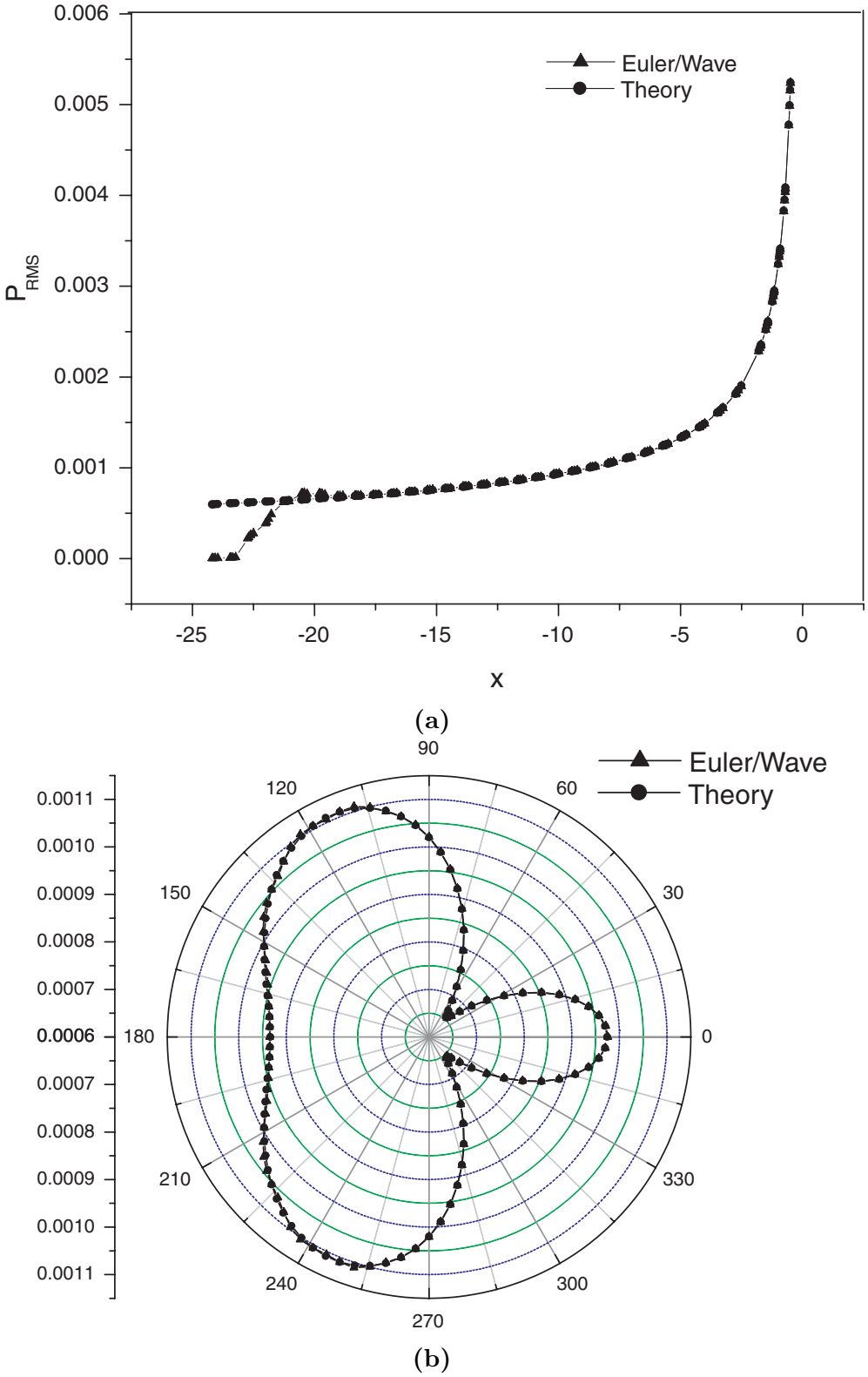

Figure 5.16: (a) Comparison of RMS pressure along the ray $\theta = \pi$, (b) Comparison of RMS pressure along radius $r = 10$ (that is outside the coupling interface).

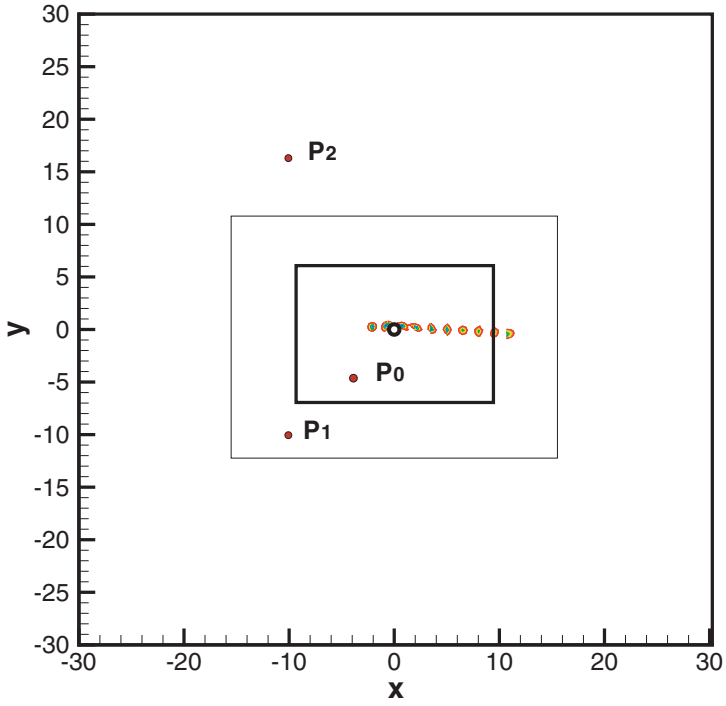

Figure 5.17: Domain/model decomposition for inviscid vortex cylinder interaction

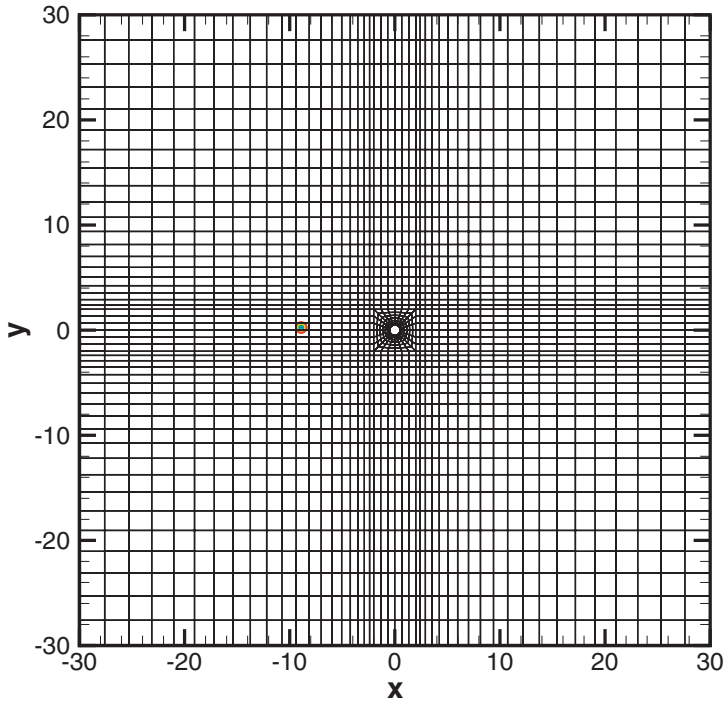

Figure 5.18: Mesh for inviscid vortex cylinder interaction

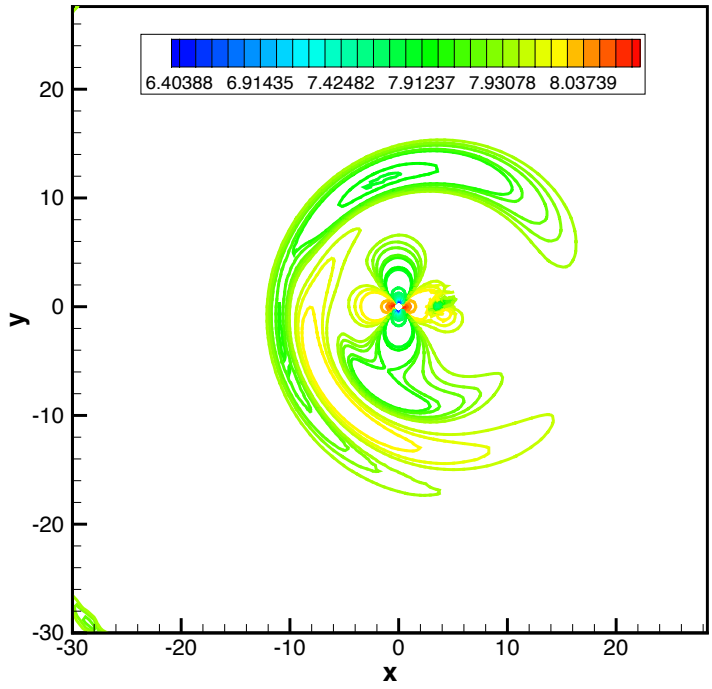

(a)

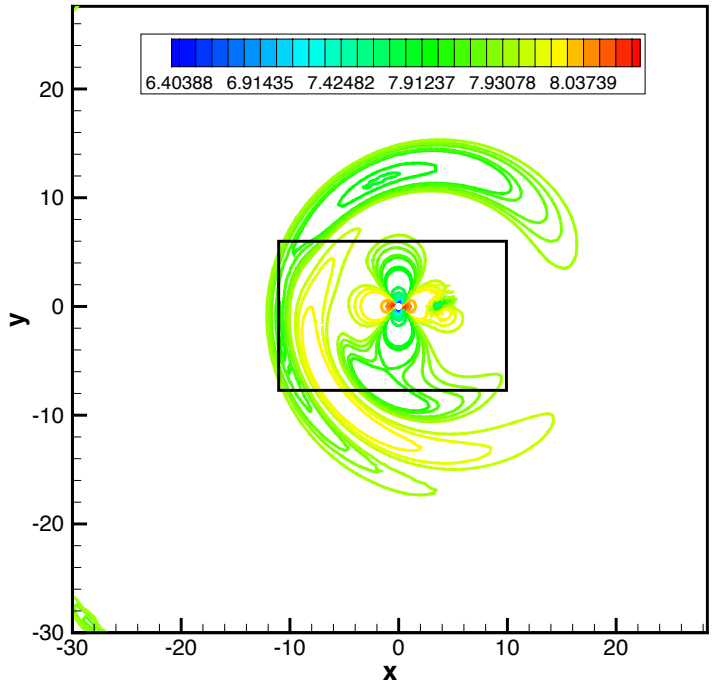

(b)

Figure 5.19: Pressure contours from direct Euler and Euler/Wave coupled solver, both are in the same contour levels: (a) Pressure contour from direct Euler solver at $t = 15.0$, (b) Pressure contour from coupled Euler/Wave solver at $t = 15.0$.

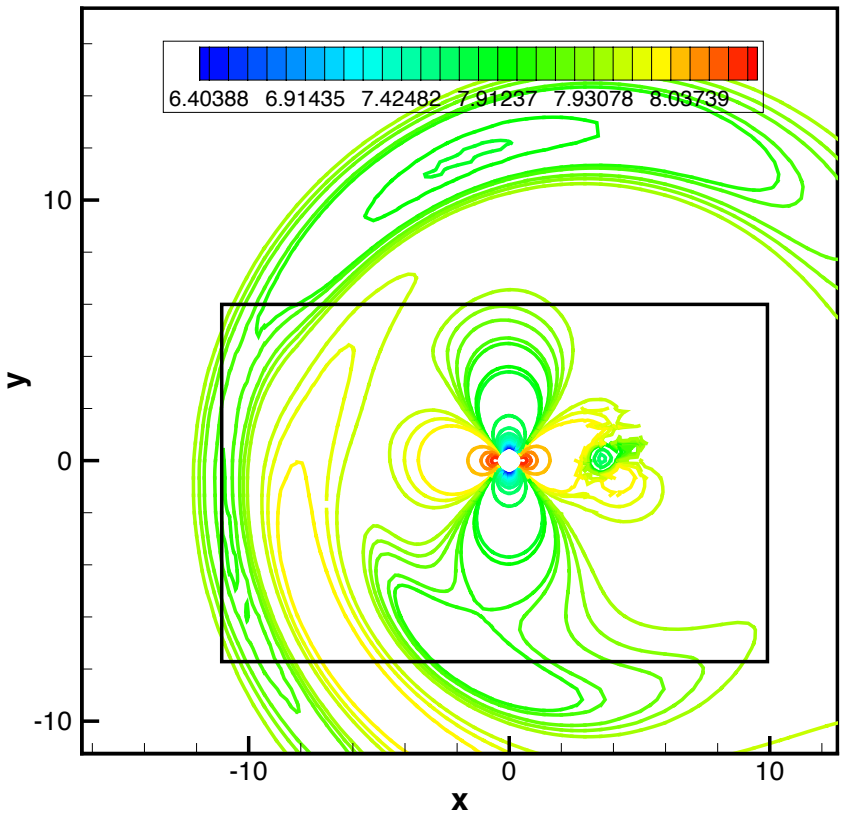

Figure 5.20: Pressure closeup around the coupling interface

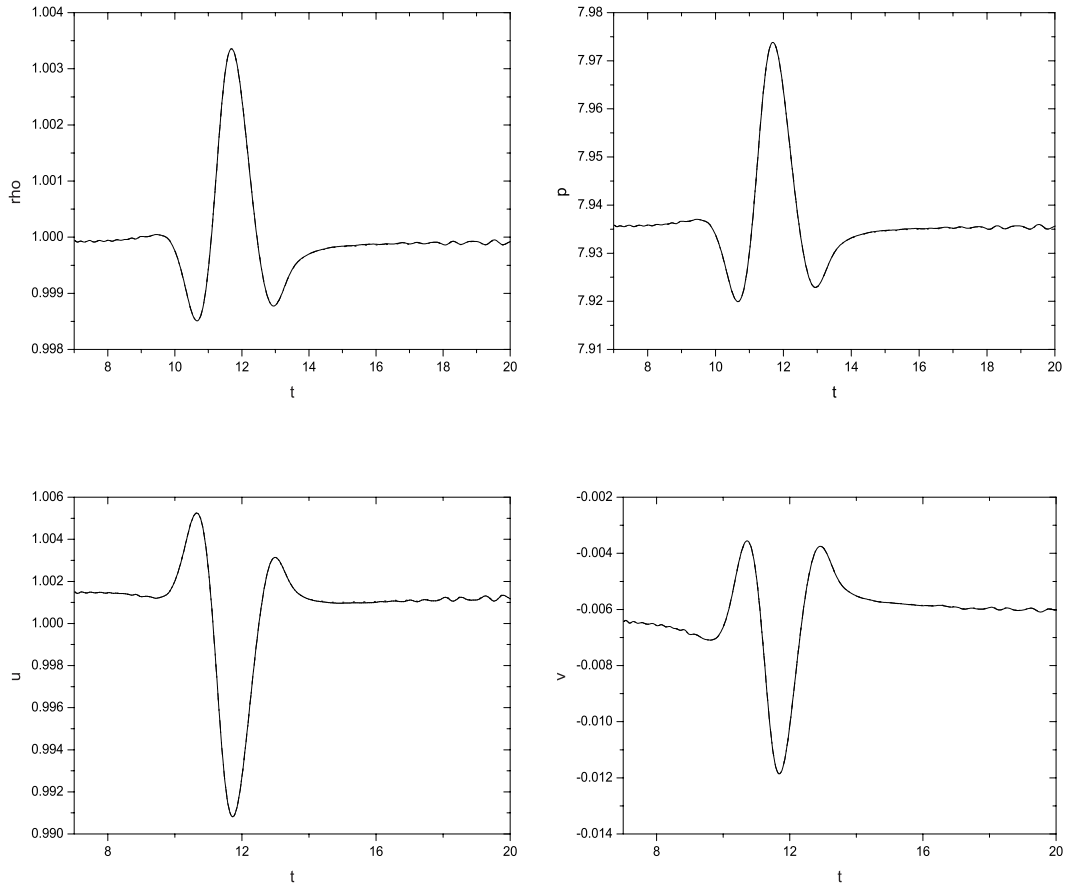

Figure 5.21: Time history at P_0 using the smaller coupling interface: (a) Density ρ, (b) Pressure p, (c) Velocity u (d) Velocity v. —— Euler/Wave; ---- Euler/LEE; ····· Euler.

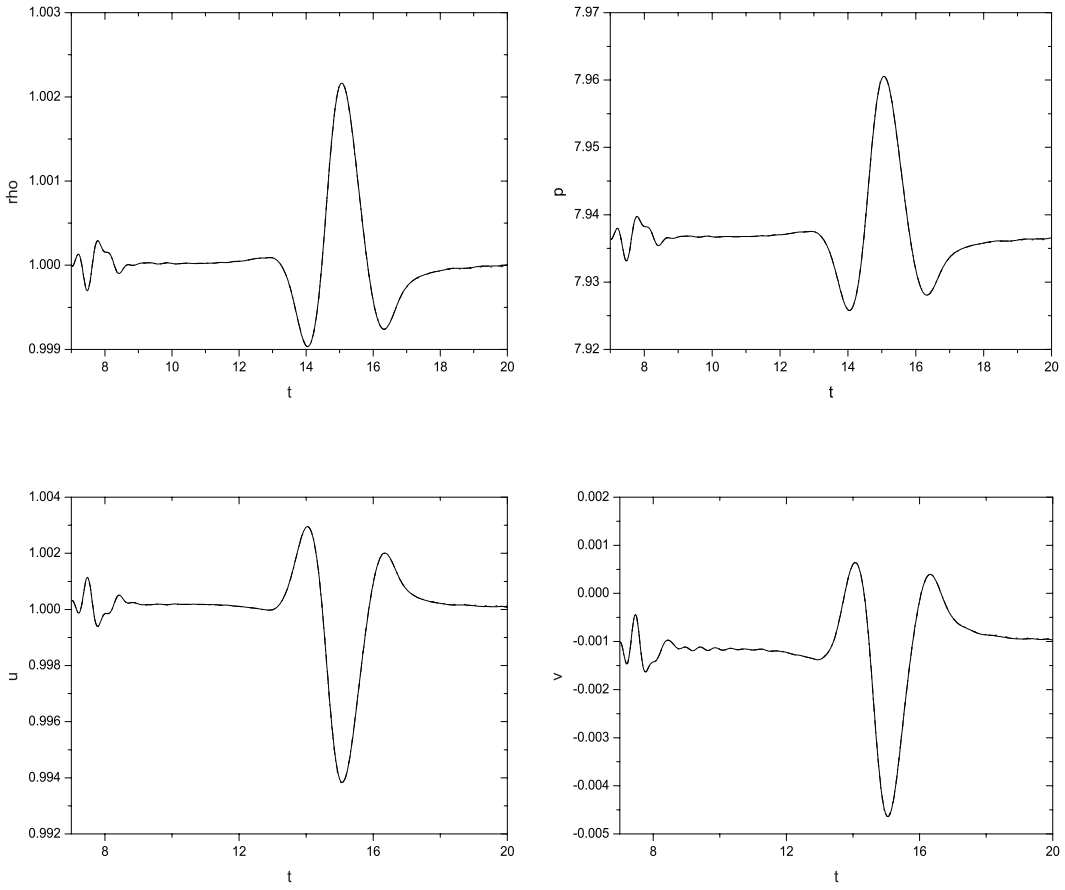

Figure 5.22: Time history at P_1 using the smaller coupling interface: (a) Density ρ, (b) Pressure p, (c) Velocity u (d) Velocity v. —— Euler/Wave; ---- Euler/LEE; ····· Euler.

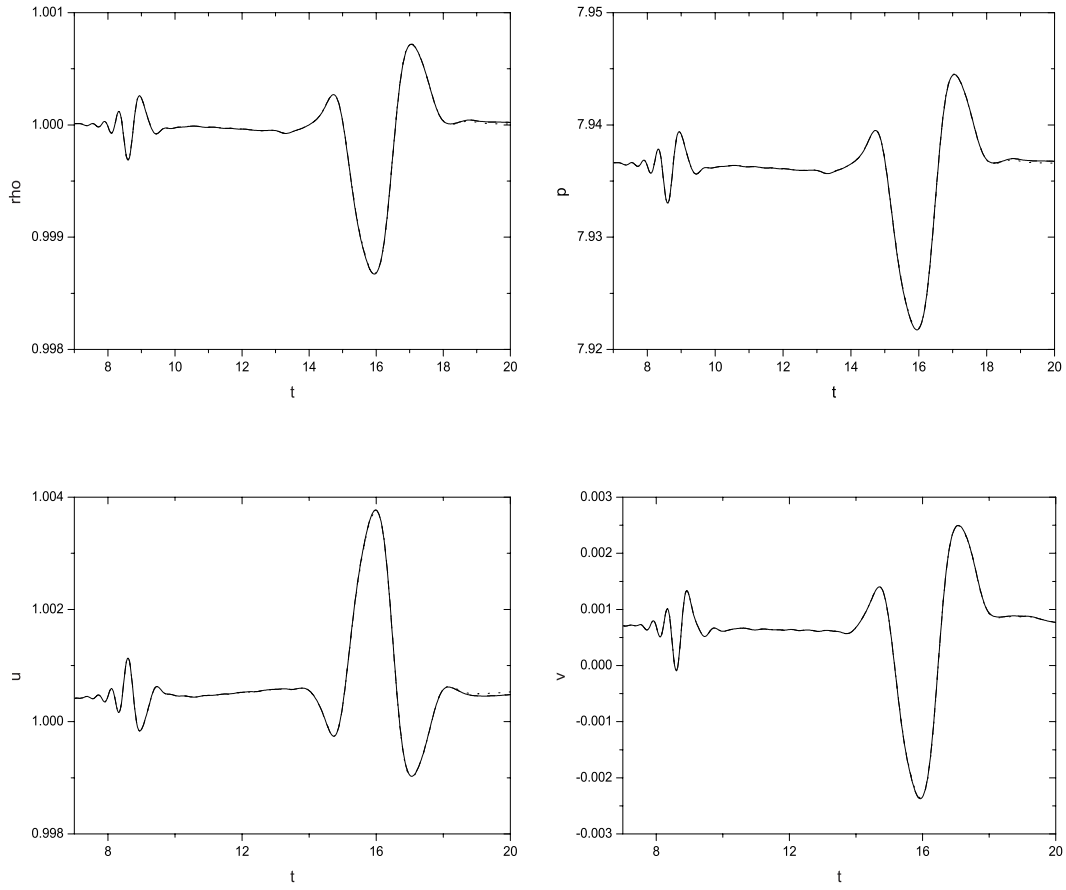

Figure 5.23: Time history at P_2 using the smaller coupling interface: (a) Density ρ, (b) Pressure p, (c) Velocity u (d) Velocity v. —— Euler/Wave; ---- Euler/LEE; ····· Euler.

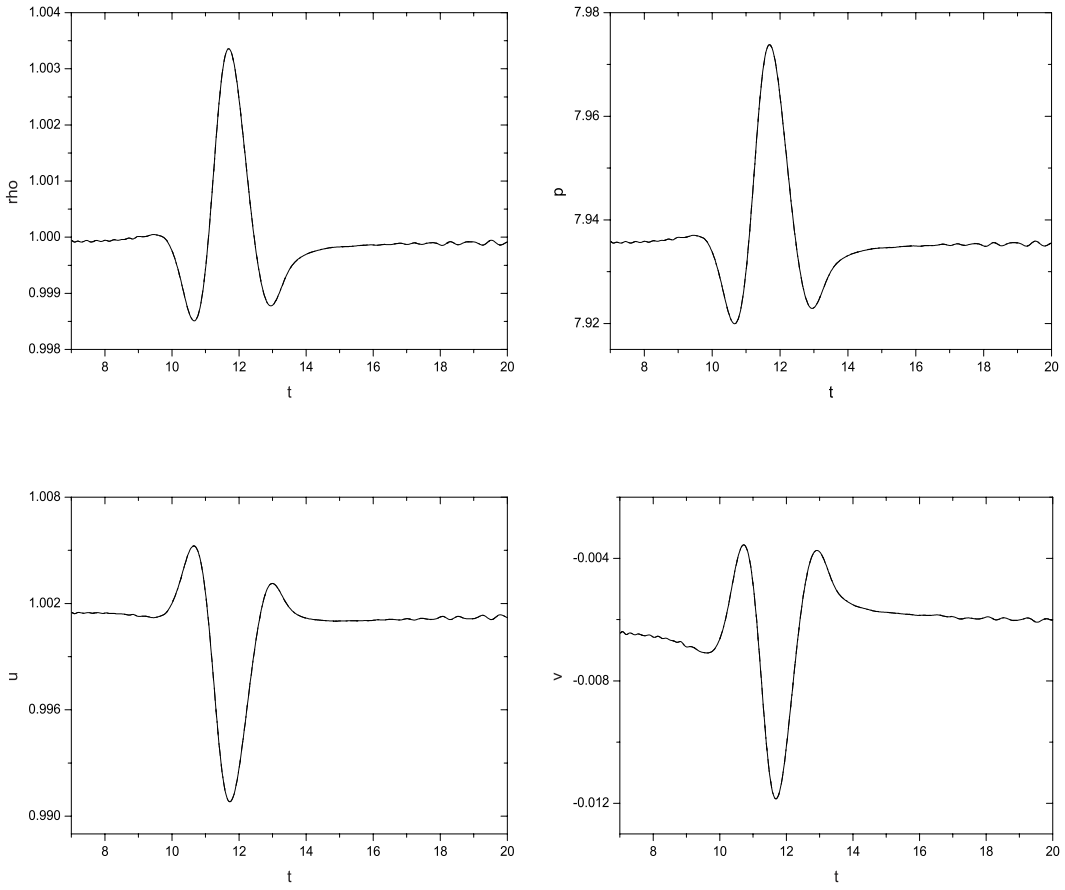

Figure 5.24: Time history at P_0 using the larger coupling interface: (a) Density ρ, (b) Pressure p, (c) Velocity u (d) Velocity v. —— Euler/Wave; ---- Euler/LEE; ····· Euler.

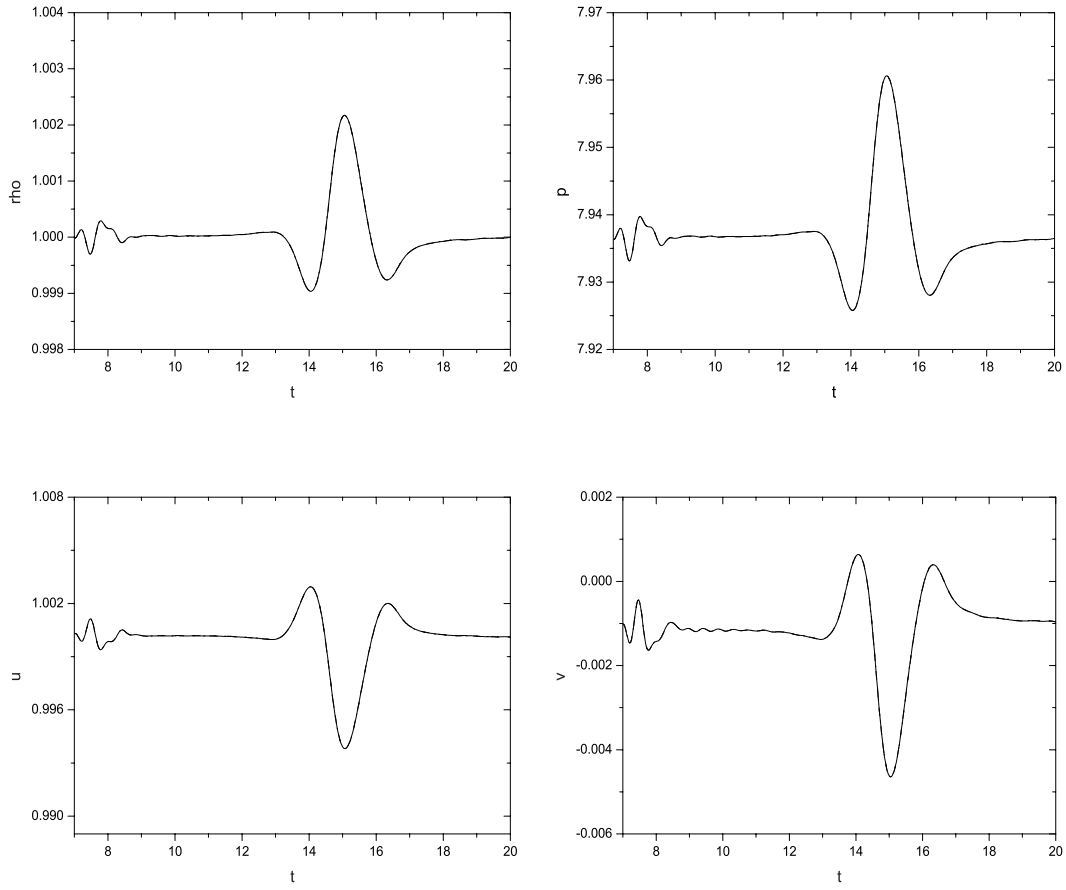

Figure 5.25: Time history at P_1 using the larger coupling interface: (a) Density ρ, (b) Pressure p, (c) Velocity u (d) Velocity v. —— Euler/Wave; ---- Euler/LEE; ····· Euler.

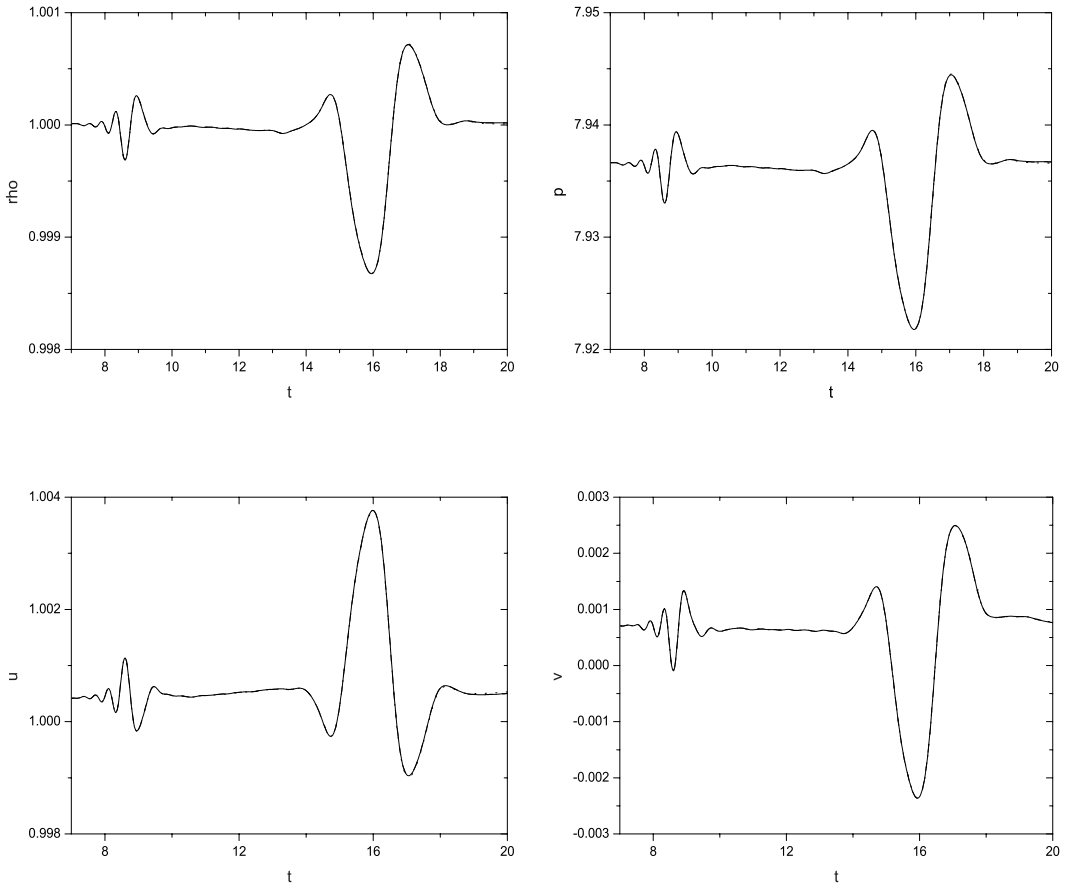

Figure 5.26: Time history at P_2 using the larger coupling interface: (a) Density ρ, (b) Pressure p, (c) Velocity u (d) Velocity v. —— Euler/Wave; ---- Euler/LEE; ····· Euler.

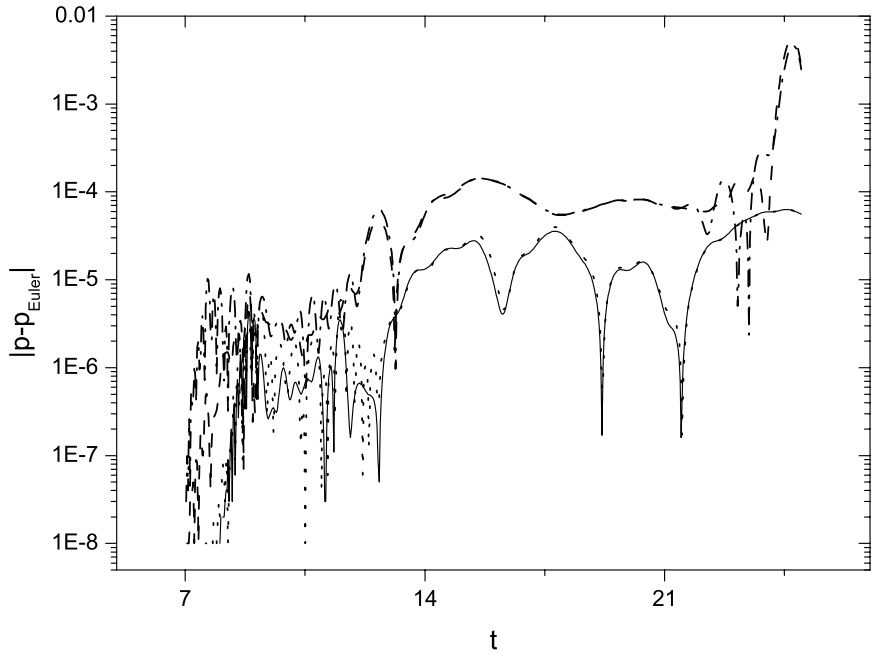

Figure 5.27: Pressure error history $|p - p_{\text{Euler}}|$ at P_0: —— Euler/LEE with large surface; ---- Euler/LEE with small surface; ····· Euler/Wave with large surface; —·— Euler/Wave with small surface.

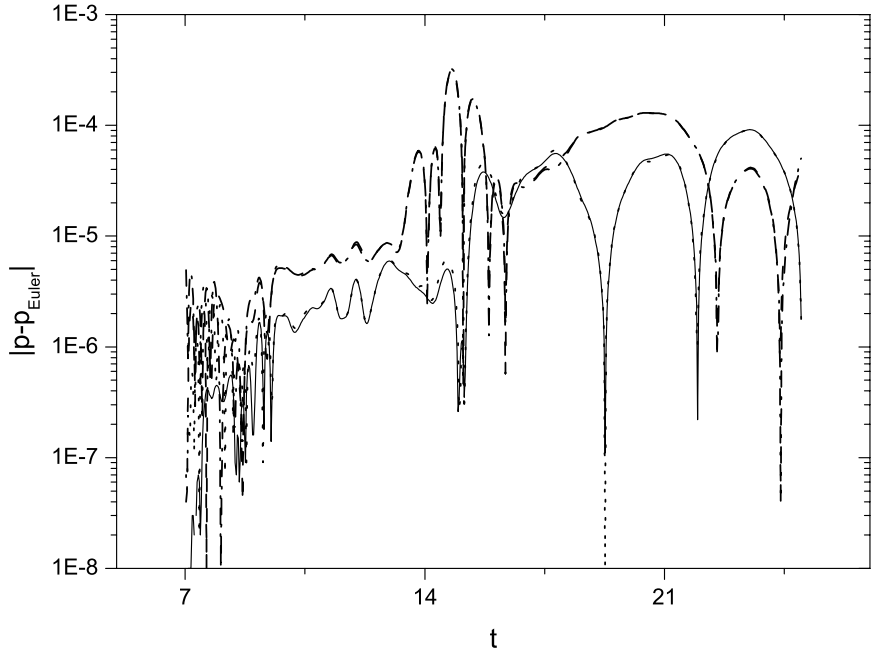

Figure 5.28: Pressure error history $|p - p_{\text{Euler}}|$ at P_1: —— Euler/LEE with large surface; ---- Euler/LEE with small surface; ····· Euler/Wave with large surface; —·— Euler/Wave with small surface.

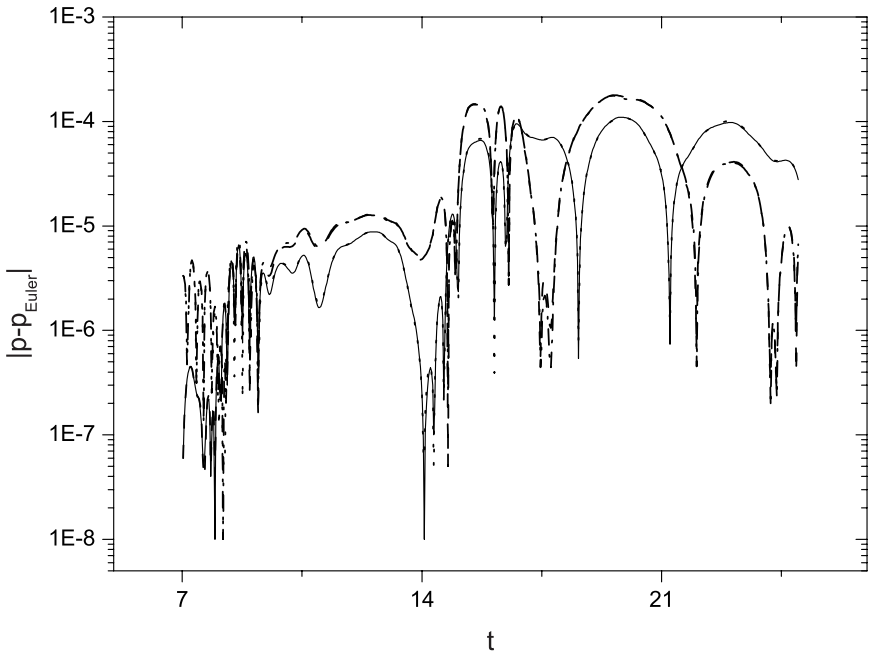

Figure 5.29: Pressure error history $|p - p_{\text{Euler}}|$ at P_2: —— Euler/LEE with large surface; - - - - Euler/LEE with small surface; ····· Euler/Wave with large surface; —·— Euler/Wave with small surface.

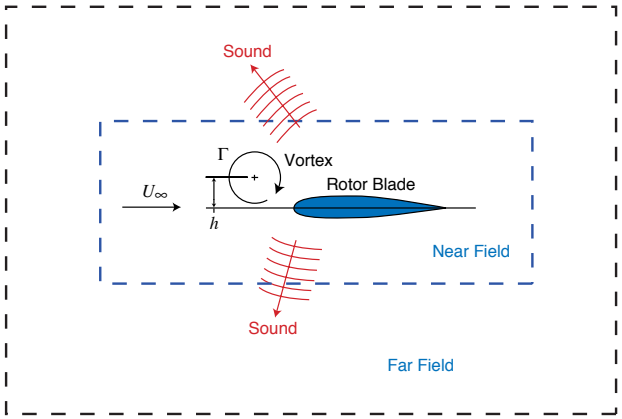

Figure 5.30: Bell AH1 rotorblade vortex interaction: Motivation

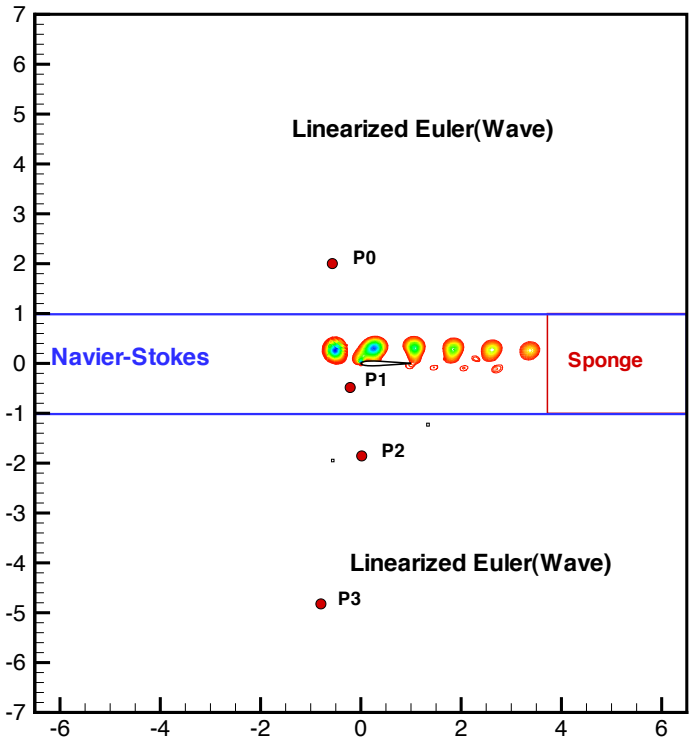

Figure 5.31: Bell AH1 rotorblade vortex interaction: scattered pressure evolution

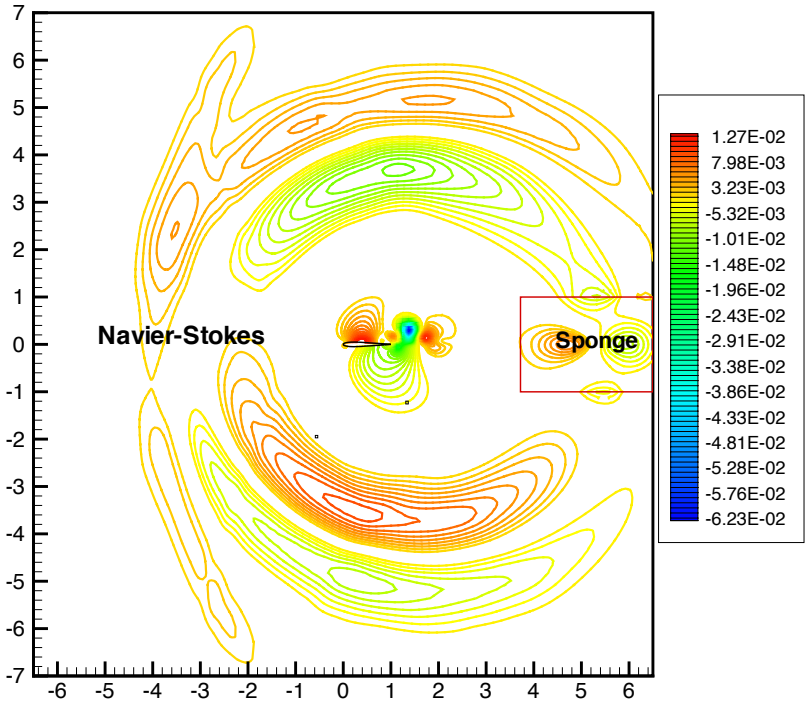

(a)

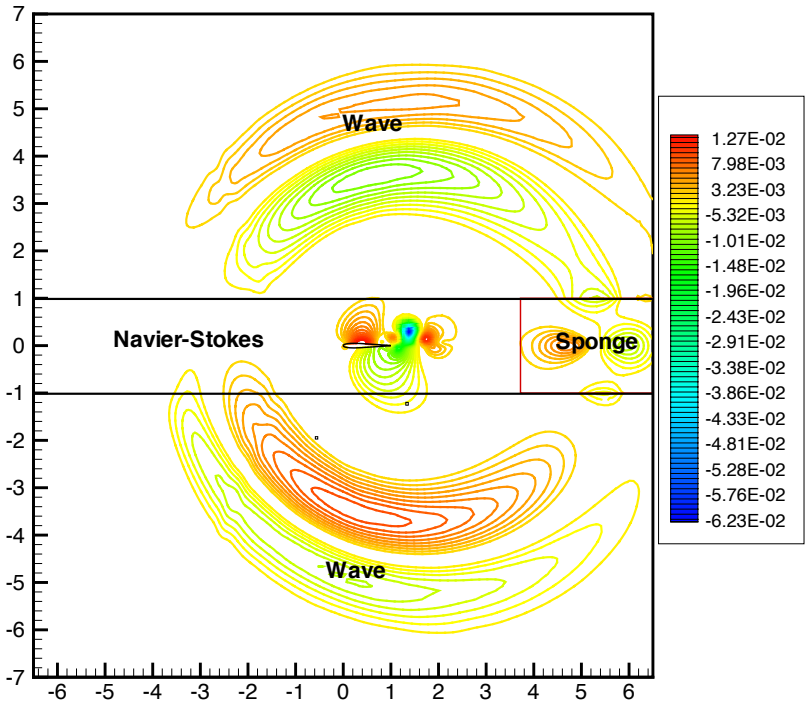

(b)

Figure 5.32: Scattered pressure contours from direct NS and NS/Wave coupled solver, both are in the same contour levels: (a)Scattered pressure contour from direct NS solver at $t = 68.4$, (b)Scattered pressure contour from coupled NS/Wave solver at $t = 68.4$.

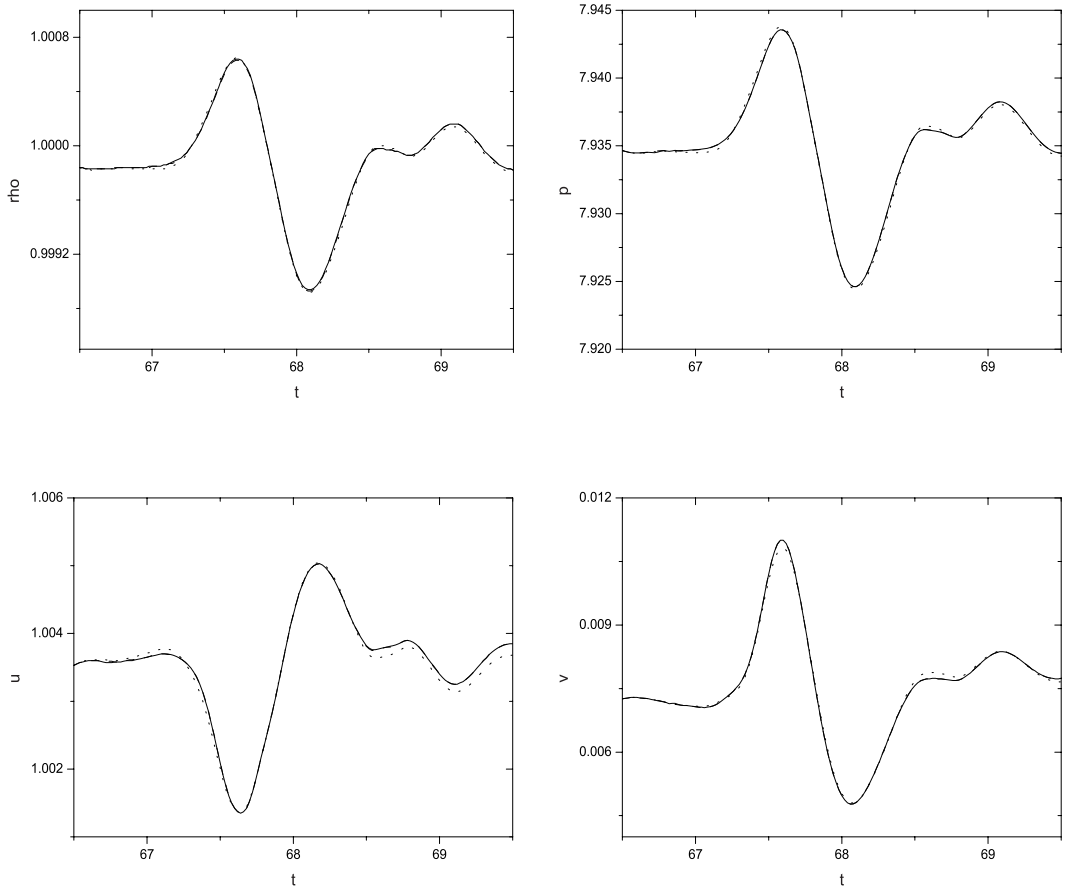

Figure 5.33: Time history at P_0: (a) Density ρ, (b) Pressure p, (c) Velocity u (d) Velocity v. —— NS/Wave; - - - - NS/LEE; ····· NS.

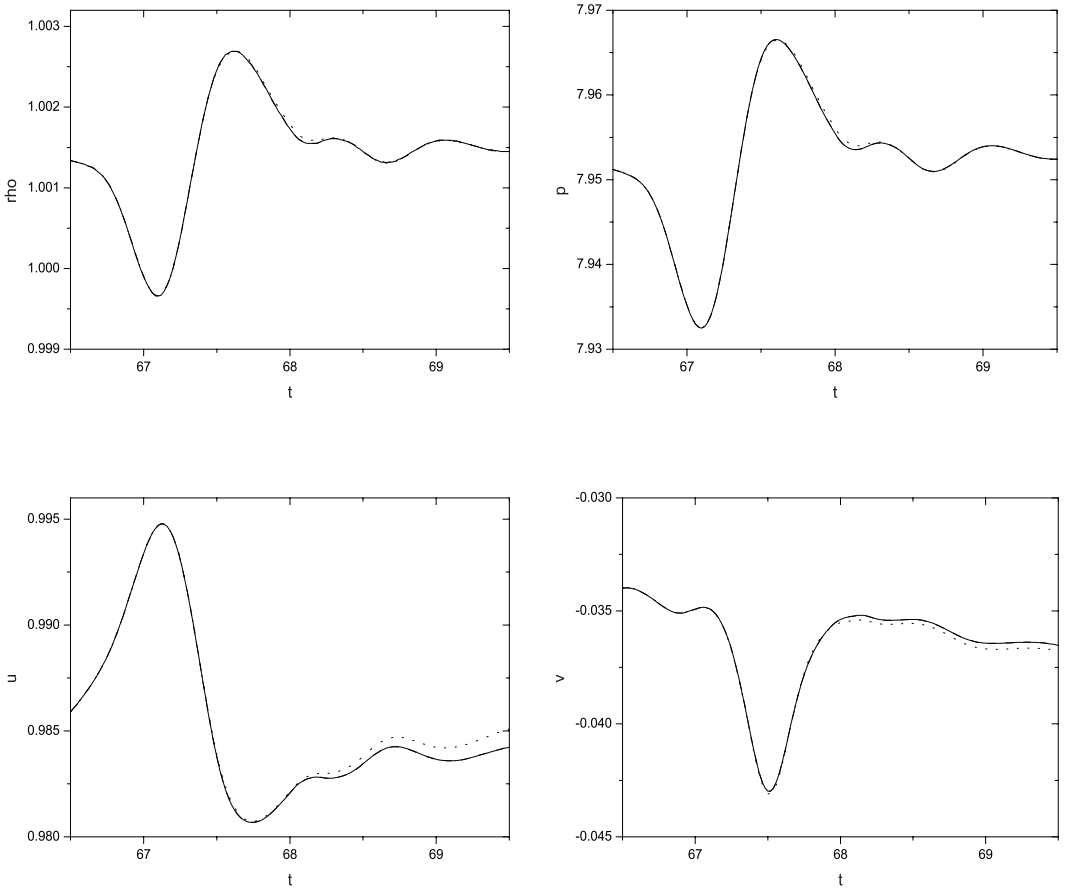

Figure 5.34: Time history at P_1: (a) Density ρ, (b) Pressure p, (c) Velocity u (d) Velocity v. —— NS/Wave; - - - - NS/LEE; ····· NS.

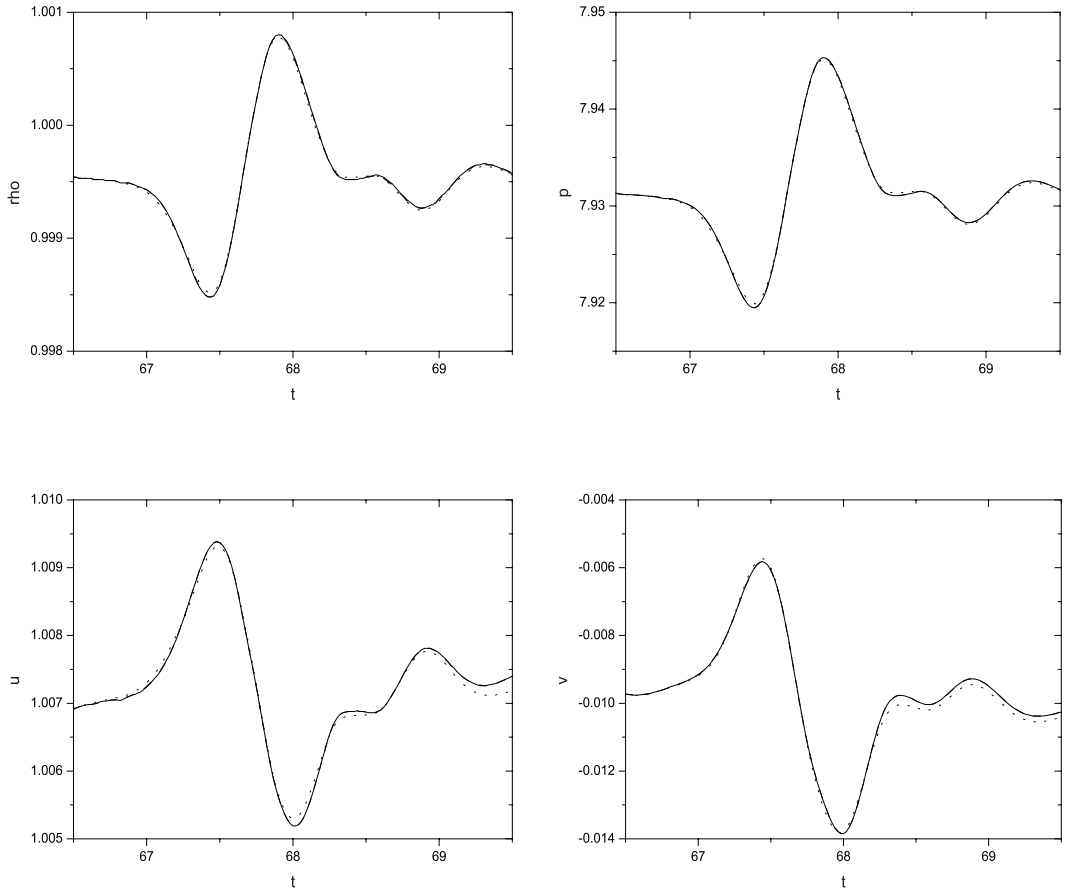

Figure 5.35: Time history at P_2: (a) Density ρ, (b) Pressure p, (c) Velocity u (d) Velocity v. —— NS/Wave; - - - - NS/LEE; ····· NS.

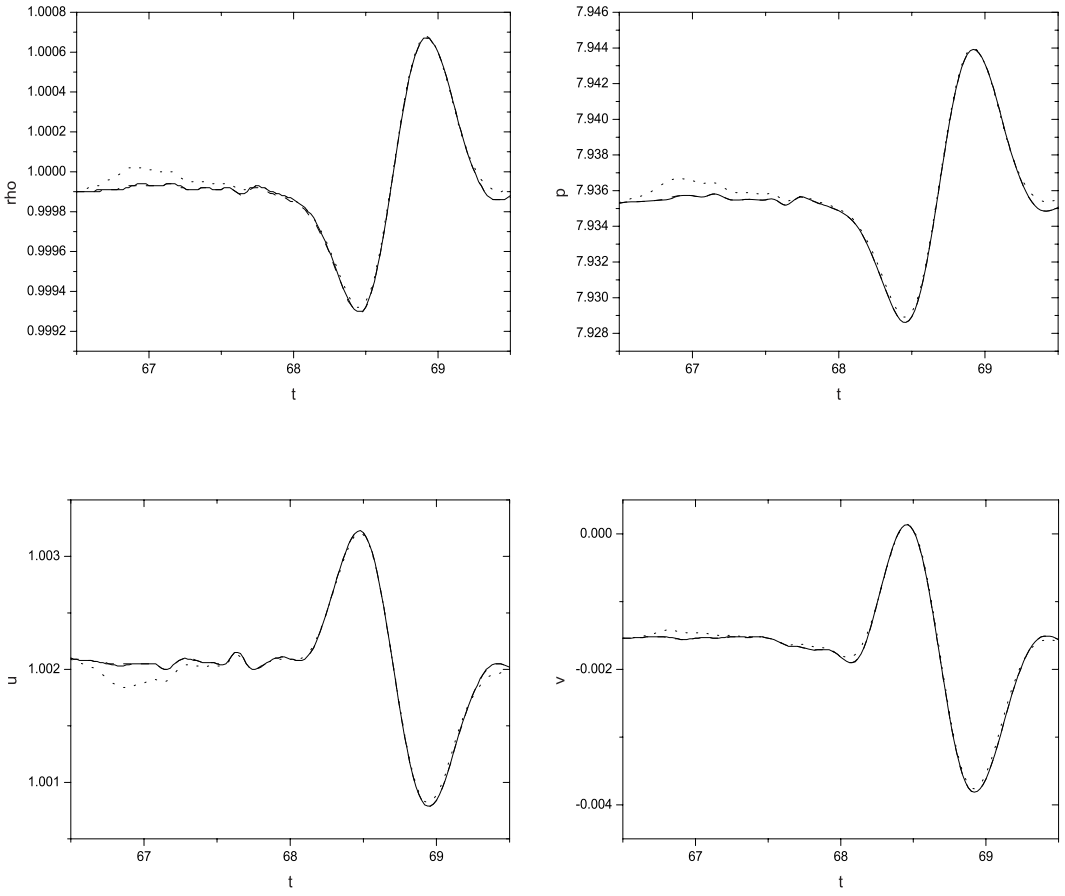

Figure 5.36: Time history at P_3: (a) Density ρ, (b) Pressure p, (c) Velocity u (d) Velocity v. —— NS/Wave; - - - - NS/LEE; ····· NS.

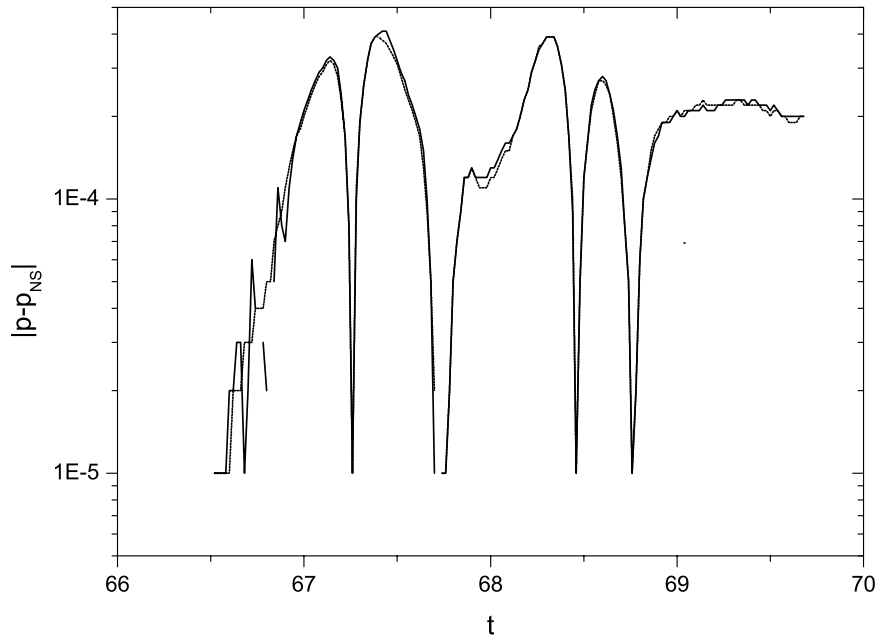

Figure 5.37: Pressure error history $|p - p_{NS}|$ at P_0: —— NS/LEE; ---- NS/Wave.

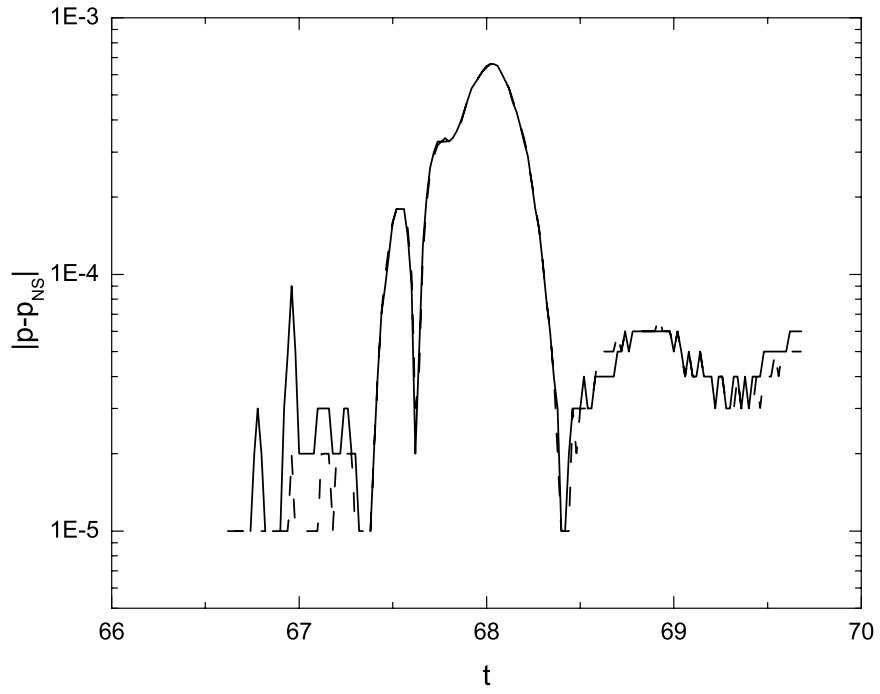

Figure 5.38: Pressure error history $|p - p_{NS}|$ at P_1: —— NS/LEE; ---- NS/Wave.

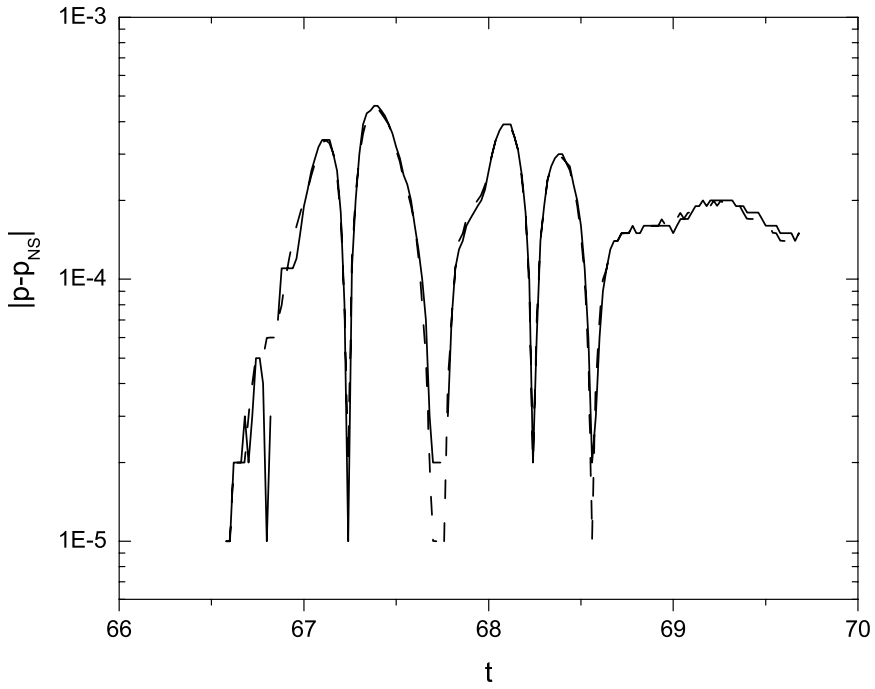

Figure 5.39: Pressure error history $|p - p_{NS}|$ at P_2: —— NS/LEE; ---- NS/Wave.

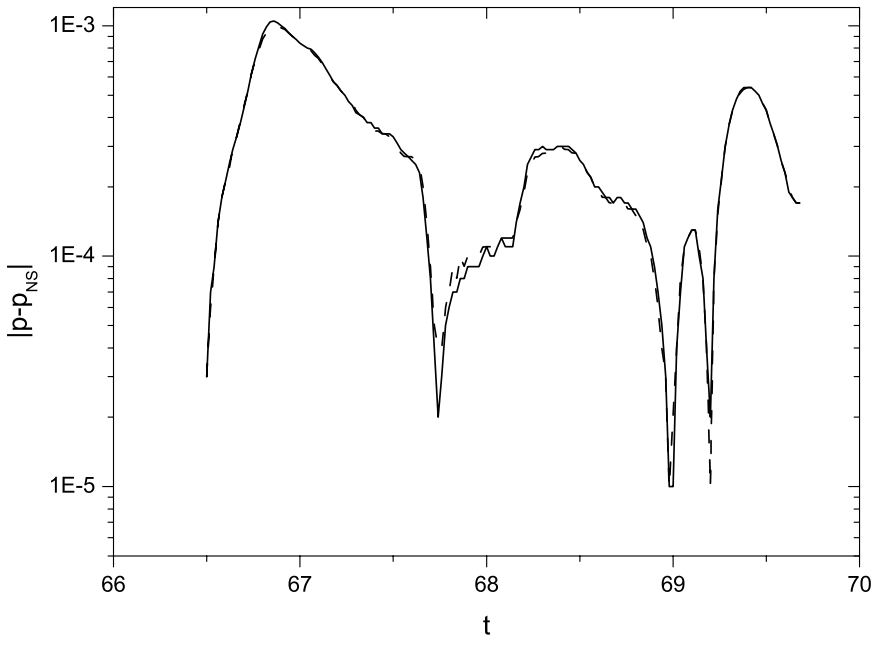

Figure 5.40: Pressure error history $|p - p_{NS}|$ at P_3: —— NS/LEE; ---- NS/Wave.

Chapter 6

Optimal Control of Fluids Problem

In this chapter, we present some results for several optimal control cases with different objective functionals. In §6.1, results are presented for the inviscid boundary control of acoustic pulse reflection problem. In §6.2, we present some results for the viscous boundary control of vortex rebound problem. The control objective is to minimize the terminal kinetic energy (TKE). In §6.3, we present another classical viscous control case, vortex shedding suppressing using the steady and unsteady boundary control.

6.1 Acoustic Pulse Reflection

In this section, we follow the third test case in Collis *et al.* [35], which focuses on the optimal transpiration boundary control with high order finite difference method. In this problem, a Gaussian acoustic pulse propagates towards the wall, then reflects back into the observation region from the solid wall. The control objective is to minimize the reflected acoustics in the observation region by using wall-normal suction/blowing at the wall. It is defined as

$$\begin{aligned} J(g) &= \tfrac{1}{2}\int_{t_0}^{t_f}\int_{\Omega_{\text{obs}}} \alpha_0 (p-p_a)^2 d\mathbf{x}\, dt \\ &\quad +\tfrac{1}{2}\int_{t_0}^{t_f}\int_{\Gamma_c} \Big(\alpha_1 g_t^2 + \alpha_2 g^2\Big) d\Gamma\, dt. \end{aligned} \tag{6.1}$$

where $\alpha_0 = 10^6$, $\alpha_1 = 10^{-3}$, $\alpha_2 = 10^{-4}$. The problem setup is very similar to that in [35]. The computational domain is $\Omega = [-12, 12] \times [0, 14]$ with periodic boundary conditions enforced in the horizontal direction and a sponge nonreflecting boundary treatment [40] in the vicinity of the top boundary. The control objective is identical

as defined over $\Omega_{\text{obs}} = [-5, 5] \times [5, 9]$ and time horizon $[2, 9]$ comprised of 700 uniform time-steps $\Delta t = 0.01$. The spatial domain is made up of 336 uniform Quad elements with polynomial order $p = 6$ for each element. The control is only allowed over the entire bottom boundary. The initial condition is a Gaussian acoustic pulse of amplitude $\varepsilon = 10^{-3}$ with standard deviation $\sigma = 0.25$, centered at mean height $x_2^* = 8$ above the wall,

$$\begin{aligned} v_1 =& 0, \\ v_2 =& -\frac{\varepsilon}{2} e^{-\frac{1}{2}\left(\frac{x_2 - x_2^*}{\sigma}\right)^2}, \\ p - p_a =& -\rho_a c_a v_2, \\ \rho - \rho_a =& \frac{p - p_a}{c_a^2}. \end{aligned} \tag{6.2}$$

In (6.2), the subscript 'a' denotes the ambient condition assumed to be a uniform quiescent flow where $\rho_a = T_a = 1$ and $c_a = 2$. The acoustic pulse propagates at the ambient speed of sound $c_a = 2$ towards the wall and at t_0, the beginning of the optimization horizon, it is located at $x_2 = 4$. For the no control simulation, the pulse reflects off the solid wall, passes through Ω_{obs}, and reaches $x_2 = 10$ at the final time t_f as in Figure 6.1.

6.1.1 Boundary Implementation

We take advantage of the linearity of this problem, the state boundary is enforced using the linear characteristic variable formulation. Inspired by the idea in [35] using the isentropic/is-vorticity blowing for the boundary control, the characteristic variables (5.1) are formed at the control boundary for the state and adjoint formulation. For the state control boundary, depending on whether blowing or suction, the boundary conditions are different. For the subsonic blowing $\vec{u}\vec{n} < 0$, which is similar to the inflow boundary condition, three physical boundary conditions plus a

numerical boundary condition are required for the subsonic blowing. Here the isentropic, iso-vorticity blowing is enforced on the control boundary. For the subsonic suction, it is similar to the outflow boundary, only one physical boundary plus three numerical boundaries are used. For the implementation for the boundary blowing and suction, it is different from that in [35], which is based on the approach originally formulated by J.Sesterhenn [106], who expresses the inviscid part of the equations as a decomposition into several plane waves aligned with the numerical grid in an attempt to merge finite difference with schemes based on compatibility equations. Our approach is very similar to the Riemann variable extrapolation for the boundary treatment as Thompson [116,117], Poinsot and Lele [96], where we actually define an extra boundary side as in §3.2.2 and extrapolate the Riemann variable depending on whether blowing or suction. For the adjoint boundary implementation, it basically follows [35] using the adjoint characteristic variable formulation, where the adjoint characteristic variables are formed at the boundary and extrapolated depending on whether blowing or suction.

6.1.2 Results Analysis

Without control, Figure 6.1 shows the Gaussian acoustic pulse travelling history, propagating towards the wall and reflecting back from the solid wall. The observation region is very quiet except for the passing of the reflecting pulse. Both the state solution from high order finite difference [35] and the DG look very good with very low dispersion and dissipation as expected. After the optimal control using the boundary blowing/suction, the reflection from the wall is reduced in several orders as in Figures 6.2. Significant acoustic reflection is reduced from both FD and DG. As described in [35], this optimization does make the controlled wall transparent to the incident acoustic pulse, where the central portion of the acoustic pulse between

$[-5, 5]$ has passed through the wall without noticeable reflection as in Figure 6.2. Checking the optimization history in Figure 6.3, the optimization history from DG looks much better than that of FD. Especially for the first several iterations, the objective functional J decreases more steeply. It is a very good feature for the future engineering application, which pays more attention to the first several optimization loops. It might be attributed to the high accuracy from DG implementation, which makes both state and adjoint solvers more accurate and leads better gradient information. In order to investigate the performance of boundary control in minimicking the nonreflecting boundary condition, we follow [35] and compare the different effects from the three boundary treatments: 1)far field boundary, 2)sponge, and 3)boundary control. We also compute $J_{obs} = \frac{1}{2}\int_{t_0}^{t_f}\int_{\Omega_{\text{obs}}}\alpha_0(p-p_a)^2 d\mathbf{x}dt$ for each case to estimate the acoustics reflection. As in Table 6.1, we get slightly different quantities from FD [35]. The amount of reflections in the observation region from sponge treatment is smallest followed by the Riemann boundary treatment. Both two significantly reduce the acoustics reflection amount, compared with the optimal boundary control. However, our optimal boundary control is still very effective, reducing the reflection from 1.1031 to 2.6336×10^{-05}. In [35], both the acoustics reflection from sponge and Riemann extrapolation treatments is small, but not as good as ours. Our implementation with DG is more effective. Look at the time history of pressure fluctuations $\int_{\Omega_{\text{obs}}}\alpha_0(p-p_a)^2 d\mathbf{x}$ in Figure 6.4, which is consistent with Table 6.1.

6.2 TKE control of Vortex Rebound

The optimal control problem in this section is the minimization of kinetic energy at final time for a model problem consisting of two counter-rotating viscous vortices above an infinite wall. Due to the self-induced velocity field, the two vortices propagate downward and interact with the wall. For this vortex rebound model problem, wall

normal suction and blowing is used to minimize cost functionals of Terminal Kinetic Energy (TKE). As a model problem for viscous flow control, it has been investigated extensively by Collis *et al.* [36, 38] using the two approaches: optimize-discretize and discretize-optimize. We choose this model problem as our validation case. The problem setup follows [36], the initial flow field is determined by the superposition of two compressible viscous vortices [41] with some initial running to get rid of the transients because of the sudden superimposing of two vortices that doesn't satisfy the NS equations. Same as in [36], the computational domain is $[-15, 15] \times [0, 15]$. The side and top boundaries are assumed to be located far enough from the main flow region, which are treated as the simple state boundary. This computational domain is made up with 450 quadrilateral elements with polynomial $p = 5$ for each element. For convergence study, we also increase $p = 5$ to $p = 7$, the overall optimization history is similar, but both the state and adjoint solution get better resolved and we get better gradient. Our control time window $t_0 = 5, t_f = 40$ and the control $\mathbf{g}$ is the wall normal velocity along the bottom wall Γ_c. Our objective functional is defined as

$$\begin{aligned} \min_{\mathbf{g}\in\mathcal{G}_{ad}} \quad J(\mathbf{g}) &\stackrel{\text{def}}{=} J_{\text{obs}}(\mathbf{U}(\mathbf{g})) + J_{\text{reg}}(\mathbf{g}) \\ &= \frac{1}{2}\int_{\Omega_{obs}} \alpha(\rho \boldsymbol{u}^2)_{t=t_f} d\mathbf{x}dt + \int_{t_0}^{t_f}\int_{\Gamma_c} \Big(\frac{\alpha_1}{2}\|\mathbf{g}_t\|_2^2 + \frac{\alpha_2}{2}\|\mathbf{g}\|_2^2\Big) d\mathbf{x}dt \end{aligned}$$

where $\alpha = 0.5$, $\alpha_1 = 0.002$ with temporal regularization , and $\alpha_2 = 0.005$.

In all cases the optimization is started with zero control. We have done three runs, the first is for $p = 5$ without temporal regularization $\alpha_1 = 0$, the second is for $p = 5$ with temporal regularization $\alpha_1 = 0.002$ and the third is for $p = 7$ with temporal regularization $\alpha_1 = 0.002$.

Figure 6.5 shows the contours of kinetic energy for the uncontrolled flow and the controlled flow from run using $p = 5$ without temporal regularization. For the uncontrolled flow, the vortices propagate toward the wall and interact with the solid wall,

the vortices strength also becomes weak because of the viscous diffusion. Figure 6.6 is the contour of vorticity for the controlled and uncontrolled flow. It shows that vortex trajectory more clearly. The effect of the optimal control almost completely sucks the vortices along the wall and reduces the kinetic energy by more than two orders of magnitude.

As found in [36, 38], for TKE control in this case, without temporal regularization, there is strong oscillation along the temporal direction in the control profile. Figure 6.7(a) shows the control profile for our first run at $p = 5$ without temporal regularization. Including the temporal regularization, two runs at $p = 5$ with $\alpha_1 = 0.002$ and $\alpha_1 = 0.05$ are used. The control profiles in Figure 6.7(b) and 6.7(c) becomes quite smooth, especially along the temporal direction. Increasing $\alpha_1 = 0.002$ to $\alpha_1 = 0.05$ for $p = 5$, there is slight difference in the control profile in the two figures. It indicates that small temporal regularization term makes difference for transient optimization problem. However, with the temporal regularization term, the optimization converges more slowly than without it as shown in Figure 6.8 in the first several iterations. Overall the optimization history is pretty close. For the optimization convergence study, the polynomial order has also been increased from $p = 5$ to $p = 7$ to check whether increasing the state resolution will improve the optimization performance. From the control profile in Figure 6.7(d) for $p = 7$ with temporal regularization, the control profile is very similar to that at $p = 5$. Look at the optimization history at $p = 7$ in Figure 6.8 and 6.9, it is almost identical to $p = 5$. It indicates that for this problem current resolution at $p = 5$ is adequate. To further validate our optimization solver, we do a detailed comparison with the results in Collis *et al.* [36, 38] in Table 6.2. Our optimization result is much better with lower resolution at $p = 5$.

6.3 Cylinder Wake Control

In this section, optimal control of the unsteady wake behind a circular cylinder at low Reynolds numbers is presented. Considerable research has been conducted for cylinder wake control using a variety of approaches including distributed controls, boundary control, and cylinder rotation (see e.g., Refs. [58, 74, 93, 109, 110]).

6.3.1 Steady Control

We consider steady suction/blowing on the entire cylinder surface as the control and find an optimal spatial distribution of the control to drive the unsteady wake at $Re = 100$ to match the steady wake at $Re = 20$, both at a freestream Mach number of 0.3. Our problem setup is similar to that of Li *et al.* [74], although we consider compressible flow with somewhat different boundary conditions, a slightly modified objective function (described below), and our control is distributed over the entire cylinder surface. The domain (see Figure 6.10) is rectangular $\Omega = [-3, 19] \times [-3, 3.1]$ with the cylinder center located at $(0, 0)$. A block structured mesh using 576 quadrilaterals was generated using a special purpose grid generator [115] and each quadrilateral has polynomial order $p = 4$.

While the problem geometry described above is similar to that in Ref. [74], we use non-reflecting boundary conditions on the top and bottom boundaries, while slip walls were imposed in [74]. Since our formulation is compressible, we must also prescribe a thermal boundary condition at the cylinder surface and the results presented here use an adiabatic wall boundary condition. Additional details regarding the problem setup, discretization, and state solutions can be found in [32].

Objective functionals

Similar to that in [74], the objective functional for the current problem is defined as a full flow field tracking problem where the controlled flow is driven toward the steady laminar flow at $Re = 20$. Thus, our objective is to control the unsteady flow at $Re = 100$ so that it approaches the steady flow at $Re = 20$ and we define our objective function as

$$\begin{aligned} \mathcal{J} &= \frac{1}{2}\int_t\int_\Omega((\rho-\rho_o)^2+(\rho u-\rho_o u_o)^2 \\ &+ (\rho v-\rho_o v_o)^2+(\rho E-\rho_o E_o)^2)d\Omega dt \\ &+ \frac{\omega_1}{2}\int_t\int_{\Gamma_c} g^2 d\Gamma dt \end{aligned} \tag{6.3}$$

where $\rho_o, \rho_o u_o, \rho_o v_o, \rho_o E_o$ are the conservation variables of the target flow field (steady flow at $Re = 20$) and g is the steady control (blowing/suction velocity) on the cylinder surface, Γ_c. Due to our compressible formulation, our objective function targets differences in the conservation variables while Li *et al.* [74]target differences in the velocity components. Similar to Li *et al.* [74] we define our time window, T, as one shedding period. After obtaining an adequately converged optimal control distribution, we then continue advancing the solution using this steady control profile to observe its long time influence on the flow.

Adjoint formulation

The gradient computation is based on the continuous adjoint formulation for the Navier–Stokes equations described in [21, 33, 35, 36] and these adjoint equations are discredited using DGM. Details of the formulation and implementation is in Appendix A. The adjoint solution is used to compute the gradient of the objective functional with respect to the control and a nonlinear conjugate gradient method in §4.4.1 is used to update the control.

Results

Figure 6.11 presents streamwise momentum contours for the steady laminar flow state at $Re = 20$, which is our target solution. Figure 6.12 shows snapshots of the uncontrolled flow at $Re = 100$ during one vortex shedding period which takes the typical form of the Káramán vortex street.

Starting from the fully developed Káramán vortex street at $Re = 100$, we then proceed to solve the optimal control problem described above and the convergence history of the objective functional and norm of the gradient of the objective function are shown in Figure 6.13. The majority of the reduction in J occurs in the first 4 iterations which is similar to observed in [74]. However, gradient of the objective function continues to decrease with additional iterations and drops by more than two orders of magnitude after 20 iterations (recall that it is the square of the gradient norm that is plotted in Figure 6.13.)

Taking the control distribution after 20 iterations as the optimal solution, we then continued the simulation for an additional 20 vortex shedding periods and snapshots of streamwise momentum are shown in Figure 6.14. Clearly, the vortex shedding is nearly suppressed by $t = 40$ (and computations for longer times verifies that shedding is completely suppressed). These results are qualitatively similar to the incompressible results of Li *et al.* [74].

The interests of practical applications of optimal control for flow around the cylinder usually involve the drag reduction C_D. For a viscous flow, the total drag forces comprise the pressure and skin friction resulted from the viscous stress along the surface. Figure 6.15 shows the time history of the drag coefficient C_D in the time interval $[50, 53]$(one shedding period $1T$). It shows that drag history for $Re = 20$ that is flat because it is the steady flow and the flow practically remains attached. In the center of Figure 6.15, it is the drag history for $Re = 100$ without steady control,

which shows the typical periodical shedding phenomenon under the low Re number. With the optimal control, the drag for the flow at $Re = 100$ is reduced significantly. With the optimal control profile obtained after the optimization converges, the flow continues advancing $40T$, its drag get further reduction as in Figure 6.16. Those results presented demonstrate the effectiveness in improving the drag performance by using the steady boundary blowing/suction around the cylinder. Besides the drag reduction, Figure 6.17 also shows the lift coefficient for $Re = 20.0$ and $Re = 100.0$ with and without control, where the lift is mainly from the pressure difference on the cylinder surface. From the figure, the lift fluctuation of the cylinder is reduced successfully. Interestingly, the flow continues advancing with the optimal control, the lift fluctuations becomes negative and flat, which seems to be from the steady control profile that is not symmetric around the X axile as in Figure 6.19. We are really interested in how the boundary control affects the cylinder wake. The flow pattern displays the expected revolution as the Reynolds number increases. At higher viscosity ($Re < 40$), the flow remains attached as in Figure 6.11, the wake behind the cylinder comprises a steady recirculation region with two vortices symmetrically attached to the cylinder. With the Reynolds number increasing, the size of the vortices grows. When Re reaches less than 60, the trailing vortex street becomes unstable. For Re is larger than 60, the vortex shedding occurs behind the cylinder because of the flow instability. The attached vortices becomes asymmetric and are shed alternatively at $Re > 60$. In Figure 6.19, it is the optimal steady control profile, most of the control around the cylinder is the blowing except some suction at bottom of the cylinder. Around the top and bottom of the cylinder, the blowing becomes very weak. At the leading edge, it is very flat and the blowing strength is low. Most of the blowing happens around the trailing edge and makes the vortex suppression effective. Such boundary profile is different from that reported by Li *et al.* [74] where

the blowing mixed suction around the trailing edge. However, both show that the control is most effective around the trailing edge. Actually, our steady control profile in Figure 6.19 is pretty close to the control profile in the Min *et al.* [85] for their pressure tracking problem, although their work is based on the suboptimal feedback control procedure. Blowing is applied to the rear part and suction is to the upper and lower parts of the cylinder surface.

6.3.2 Unsteady Control

In this section, we further consider the unsteady boundary control for this flow tracking problem. The objective functional is defined as

$$\begin{aligned} \mathcal{J} &= \frac{1}{2}\int_t\int_\Omega((\rho-\rho_o)^2+(\rho u-\rho_o u_o)^2 \\ &+ (\rho v-\rho_o v_o)^2+(\rho E-\rho_o E_o)^2)d\Omega dt \\ &+ \frac{\omega_1}{2}\int_t\int_{\Gamma_c} g^2 d\Gamma dt+\frac{\omega_2}{2}\int_t\int_{\Gamma_c} {g_{,t}}^2 d\Gamma dt \end{aligned} \tag{6.4}$$

Without temporal regularization $g_{,t}$, $\omega_2 = 0$. To better suppress the cylinder shedding, we increase the optimal time window from $1T$ for steady control to $2T$ for unsteady control in this case. In this study, we are interested in the effects of the unsteady boundary control and the drag reduction. The problem formulation and derivation is very similar to 6.3.1, except that the control g is defined in $[t_0, t_f] \times \Gamma_c$.

Looking at the snapshots with control and without control in Figure 6.20 and 6.21, the shedding suppression is not so obvious, which is also shown in the optimization history in Figure 6.22. After several optimization loop, there is about 25% reduction for $\mathcal{J}$. If excluding the penalty terms, the reduction is slightly bigger for J_o. Although the reduction of the objective functional is not so significant, the drag reduction is quite impressive as in Figure 6.23 that is the drag history of the cylinder shedding at $Re = 100$ without control and with control (with/without temporal regularization).

From the figure, it shows that after the control, the drag is reduced significantly. With the temporal regularization term $g_{,t}$ included in the penalty, the drag get further reduction. For the evolution of the lift coefficient in Figure 6.24, the lift fluctuation becomes smaller after the unsteady boundary control. With temporal regularization for the control, the fluctuation becomes much smaller.

Method	Control	Riemann	Sponge
FD	4.0e-05	6.4e-05	1.0e-05
DG	2.6e-05	6.6e-10	3.7e-10

Table 6.1: Comparison of acoustics reflection $J_{obs} = \frac{1}{2}\int_{t_0}^{t_f}\int_{\Omega_{\text{obs}}}\alpha_0(p-p_a)^2 d\mathbf{x}dt$ using optimal control, Riemann boundary and sponge. Data for FD is from [35]

Run	α_1	α_2	α_3	J_0	J_{final}	$\text{TKE}_{\text{final}}$
FD cont.	0.5	0.005	0.005	12.43	0.48	0.42
FD cont	0.05	0.005	0.005	12.43	0.37	0.32
FD cont	0	0.005	0.005	12.43	0.24	0.20
FD disc	0.05	0.005	0.005	12.43	0.25	0.20
FD disc	0	0.005	0.005	12.43	0.24	0.20
DG p5	0	0.005	0	11.65	0.092	0.053
DG p5	0.002	0.005	0	11.65	0.11	0.078
DG p7	0.002	0.005	0	11.65	0.13	0.096

Table 6.2: Comparison of objective function values for boundary control of terminal kinetic energy with [36, 38]

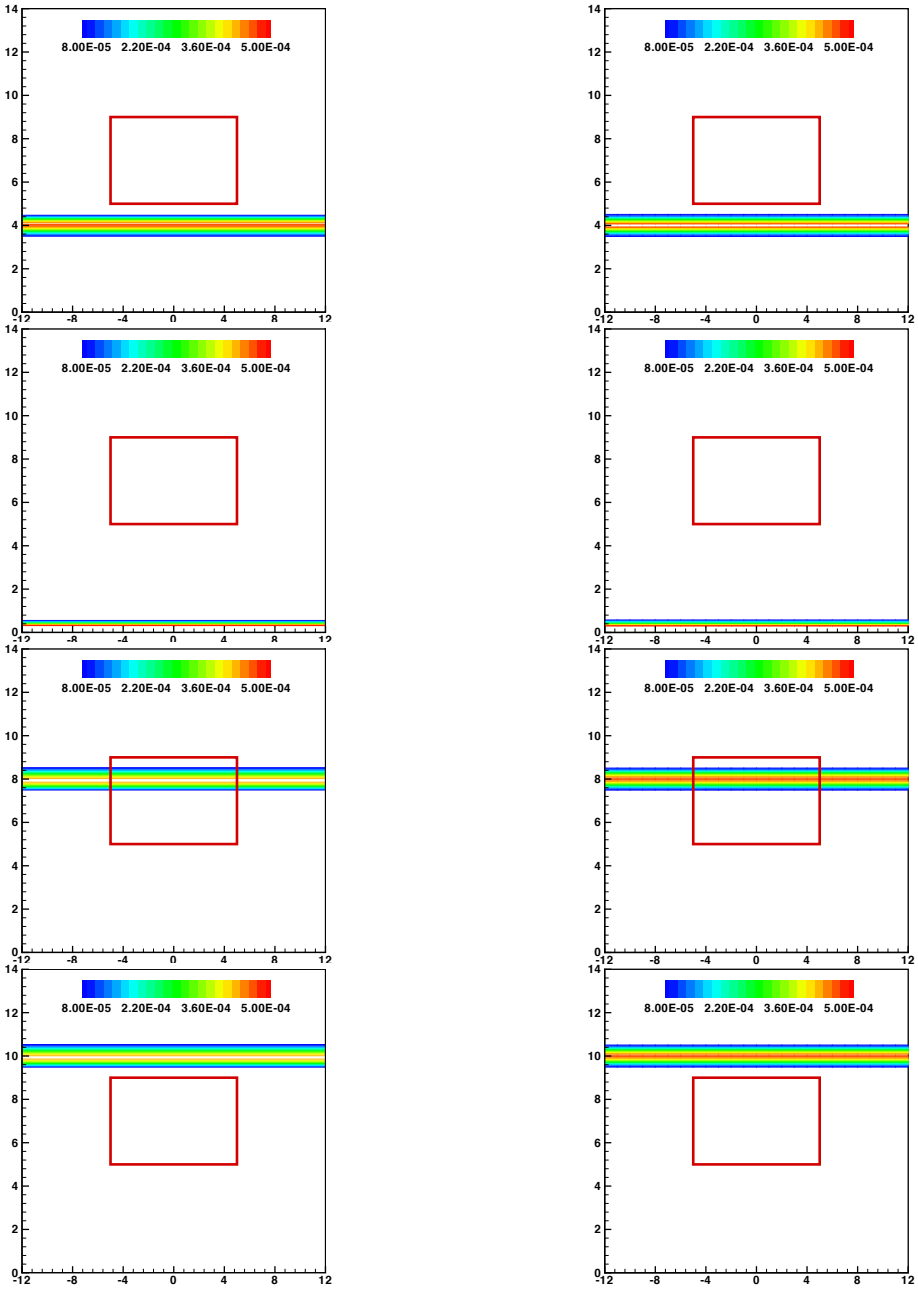

(a) FD **(b)** DG

Figure 6.1: Contours of $p - p_a$ at instants $t = 2, 4, 8, 9$ without control, FD (left) and DG (right). Data of FD is from [35]

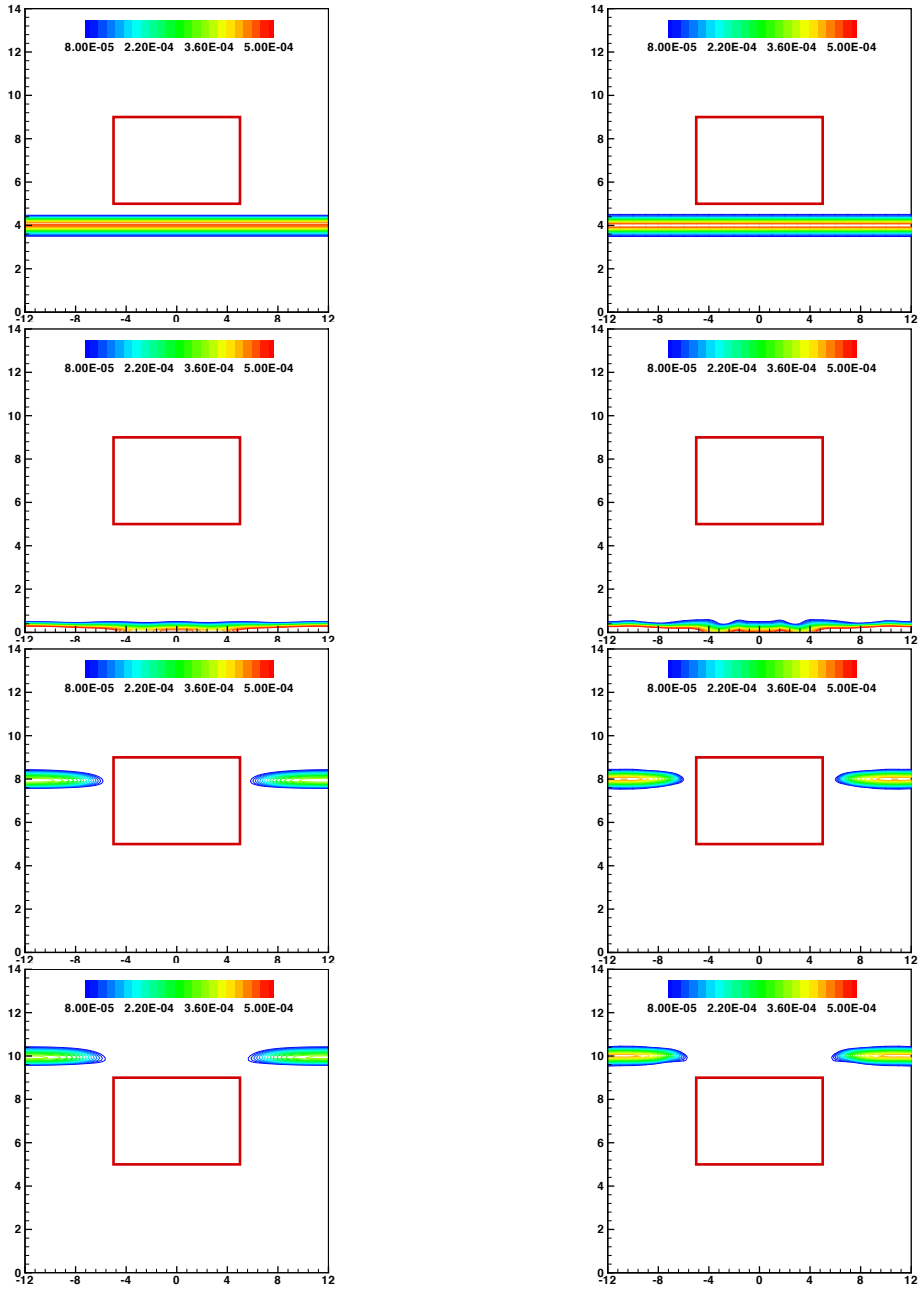

(a) FD **(b)** DG

Figure 6.2: Contours of $p - p_{\mathrm{a}}$ at instants $t = 2, 4, 8, 9$ with optimal control, FD(left) and DG (right). Data for FD is from [35]

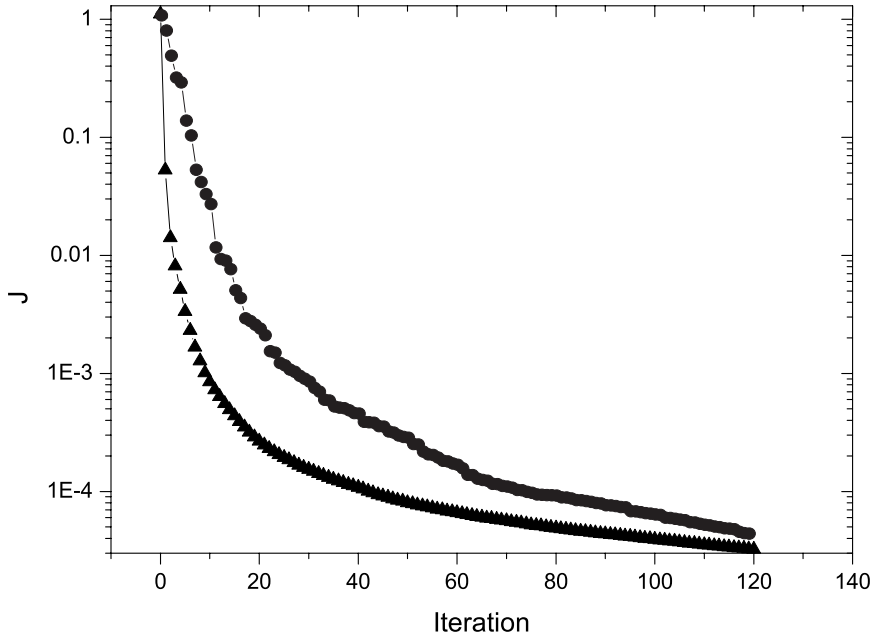

Figure 6.3: Evolution of the Objective functional J from FD and DG: • result from FD; ▲ result from DG.

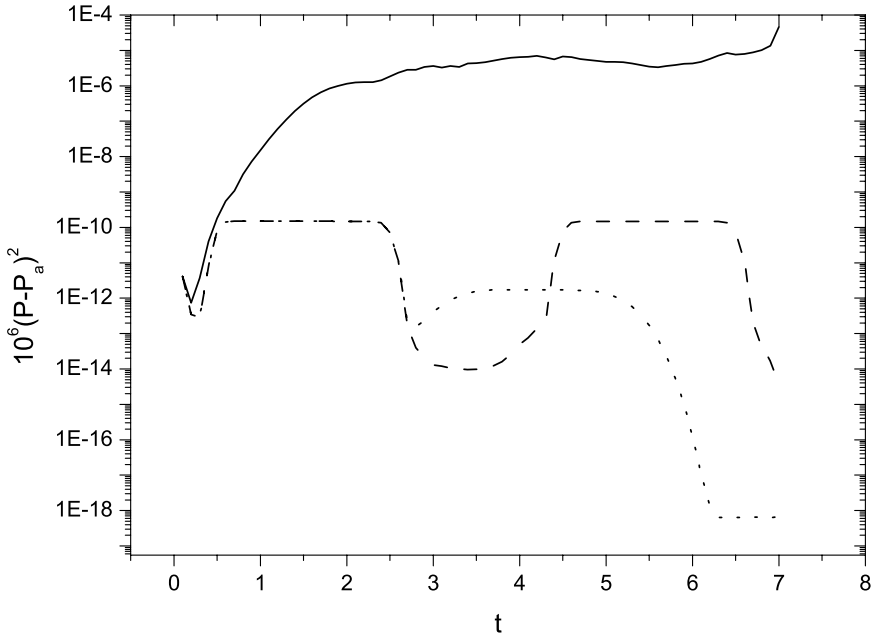

Figure 6.4: Time history of pressure reflection: —— reflection from optimal control; - - - - reflection using the Riemann boundary treatment; ····· reflection using the sponge.

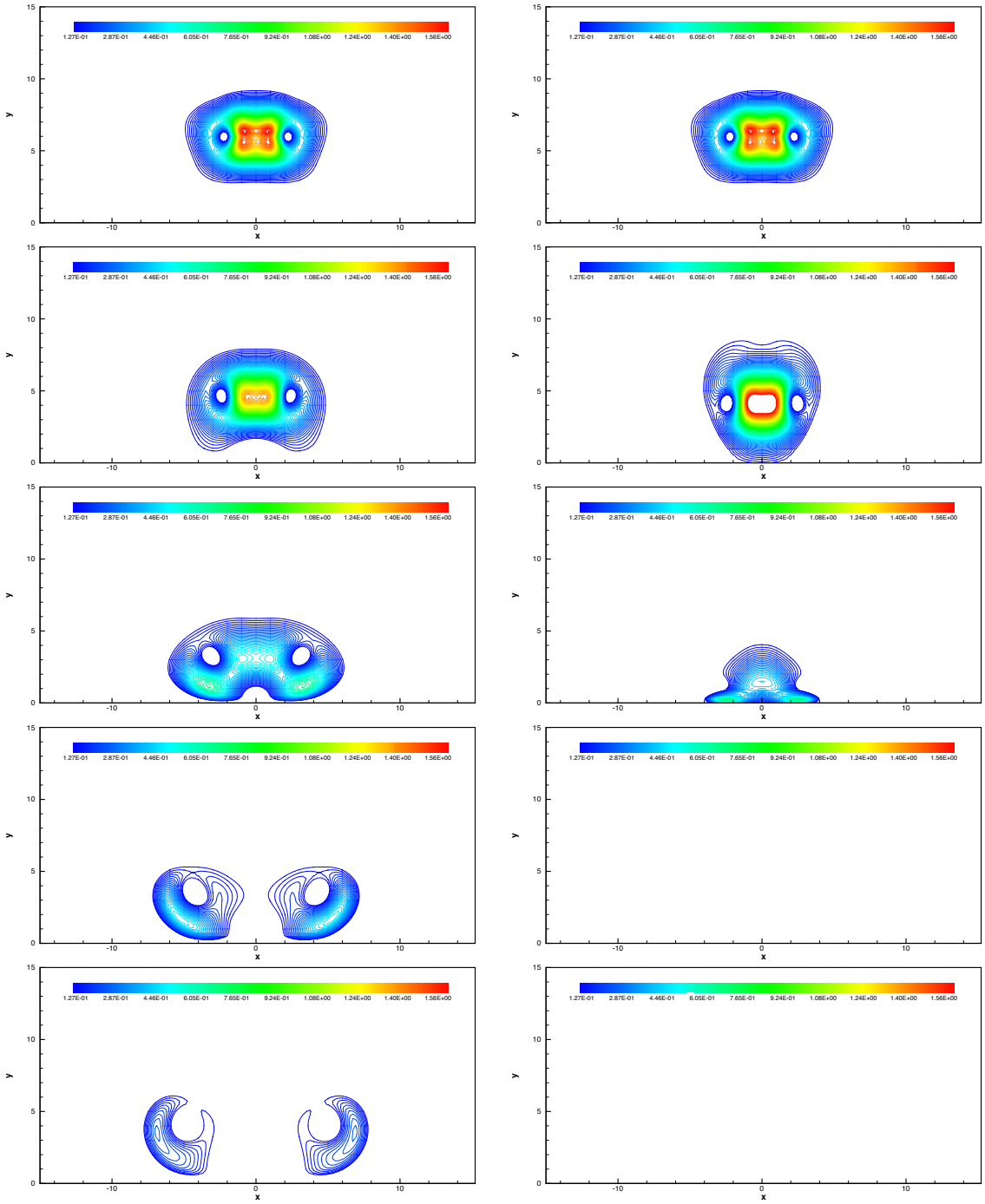

(a) No control **(b)** Optimal control

Figure 6.5: Contours of KE at instants $t = 0, 10, 20, 30, 40$ without and with control, No control (left) and Optimal control(right).

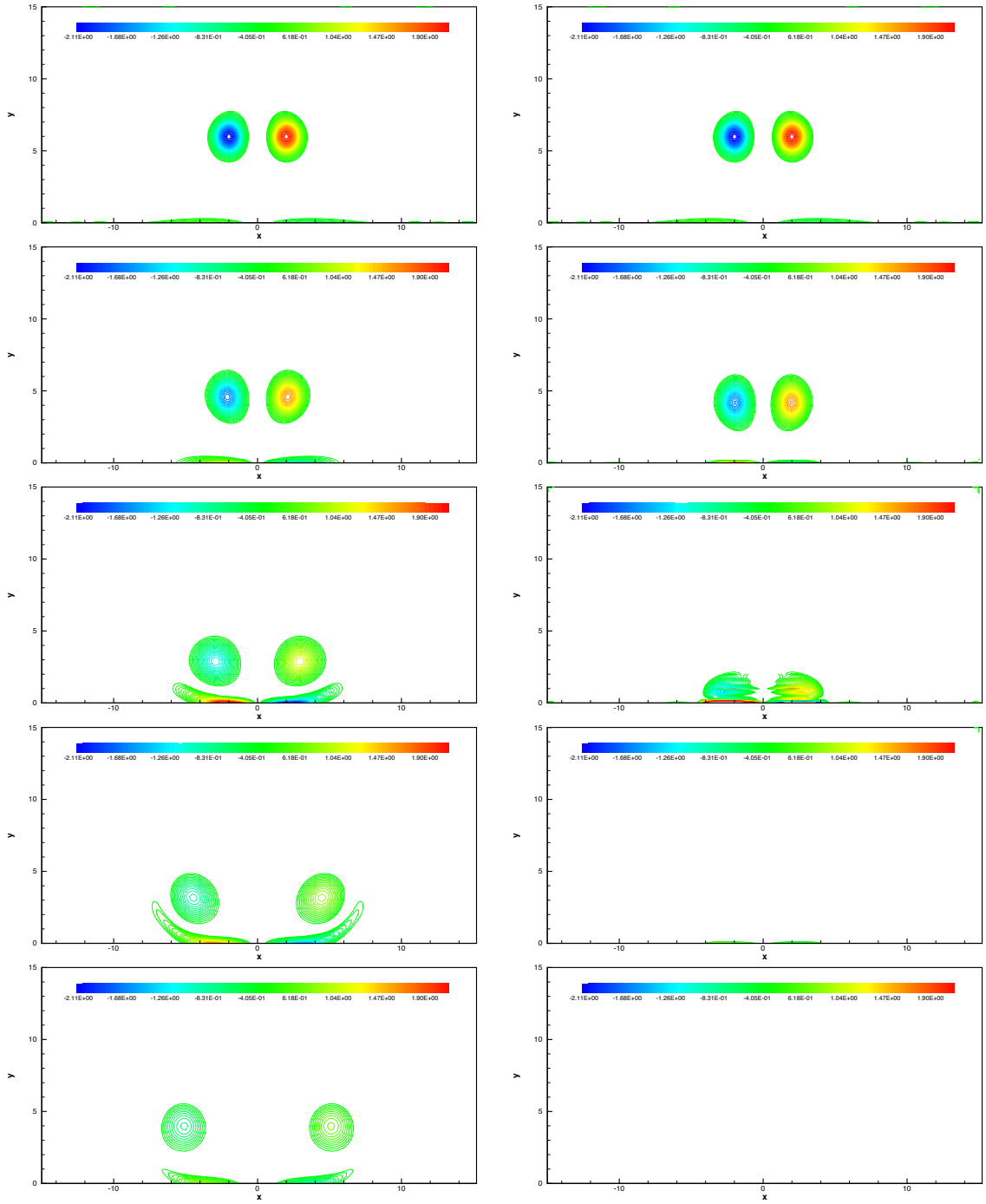

(a) No control **(b)** Optimal control

Figure 6.6: Contours of vorticity at instants $t = 0, 10, 20, 30, 40$ without and with control, No control (left) and Optimal control(right).

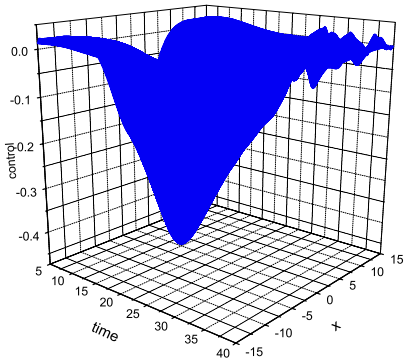

a) $\alpha_1 = 0$, $\alpha_2 = 0.005$, $p = 5$.

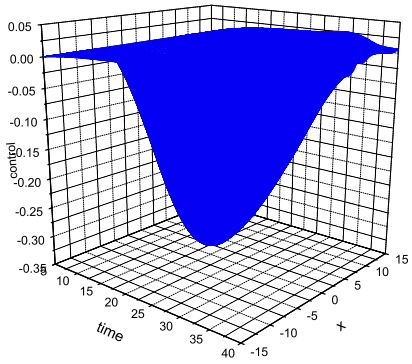

b) $\alpha_1 = 0.002$, $\alpha_2 = 0.005$, $p = 5$.

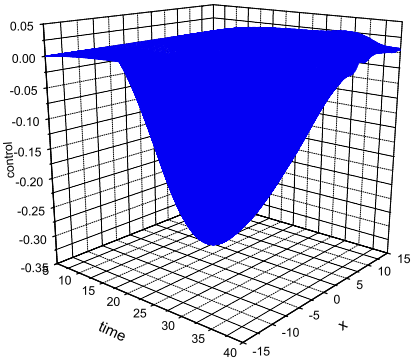

c) $\alpha_1 = 0.05$, $\alpha_2 = 0.005$, $p = 5$.

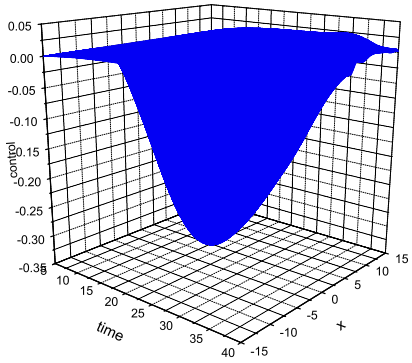

d) $\alpha_1 = 0.002$, $\alpha_2 = 0.005$, $p = 7$.

Figure 6.7: Optimal wall-normal velocity distributions for TKE control.

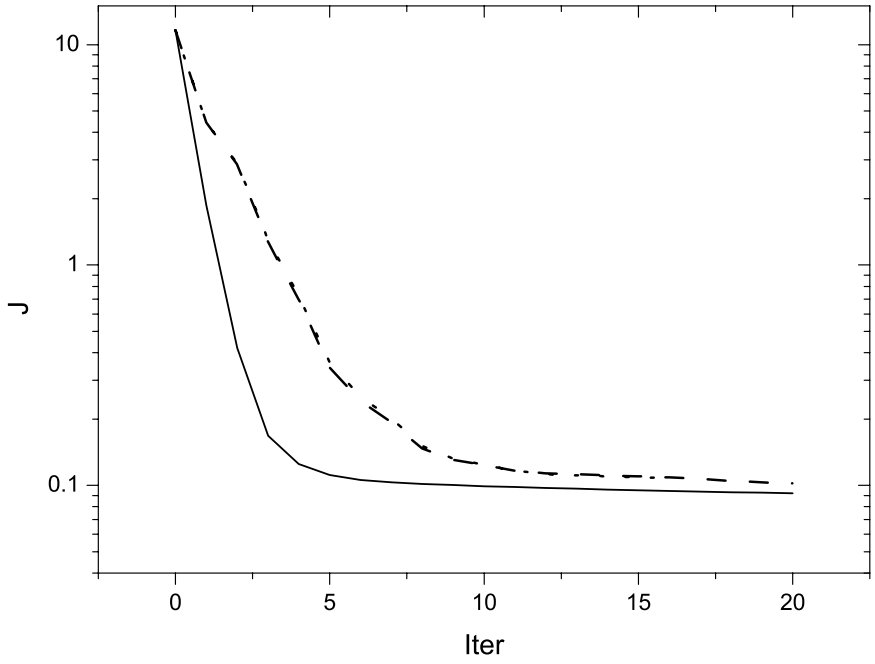

Figure 6.8: Evolution of the objective functional J: —— J at $p = 5$, $\alpha_1 = 0.005$ and $\alpha_2 = 0$, ---- J at $p = 5$, $\alpha_1 = 0.005$ and $\alpha_2 = 0.002$, ····· J at $p = 7$, $\alpha_1 = 0.005$ and $\alpha_2 = 0.002$.

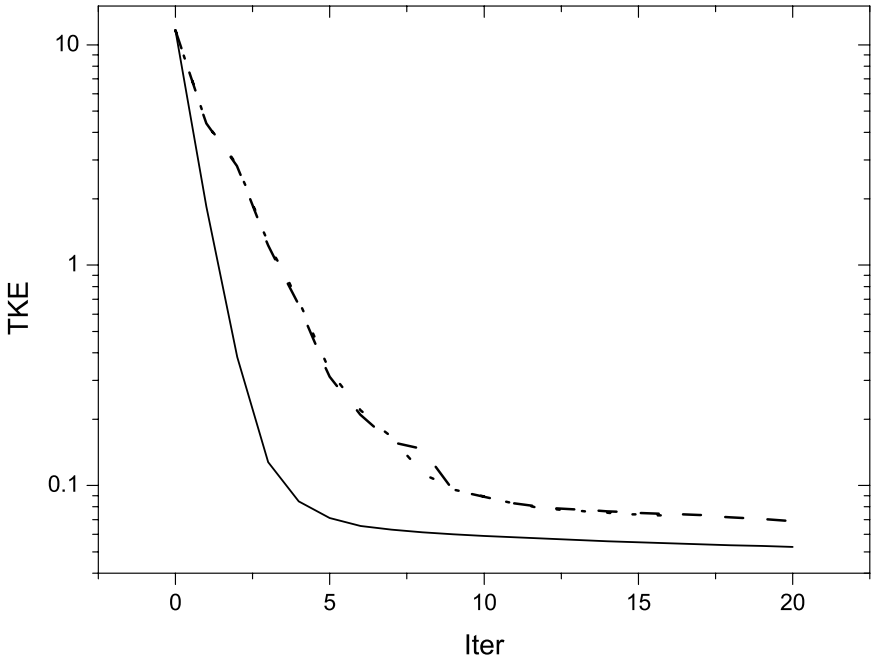

Figure 6.9: Evolution of the objective functional J_{obs}: —— J_{obs} at $p = 5$, $\alpha_1 = 0.005$ and $\alpha_2 = 0$, ---- J_{obs} at $p = 5$, $\alpha_1 = 0.005$ and $\alpha_2 = 0.002$, ····· J_{obs} at $p = 7$, $\alpha_1 = 0.005$ and $\alpha_2 = 0.002$.

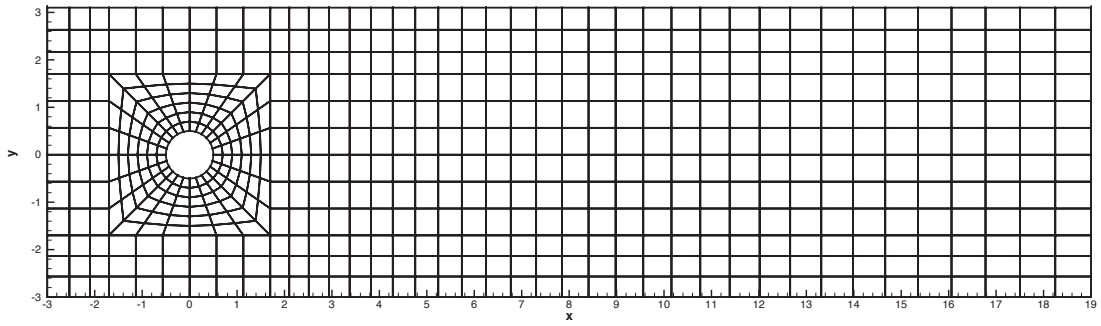

Figure 6.10: Element mesh for cylinder wake control.

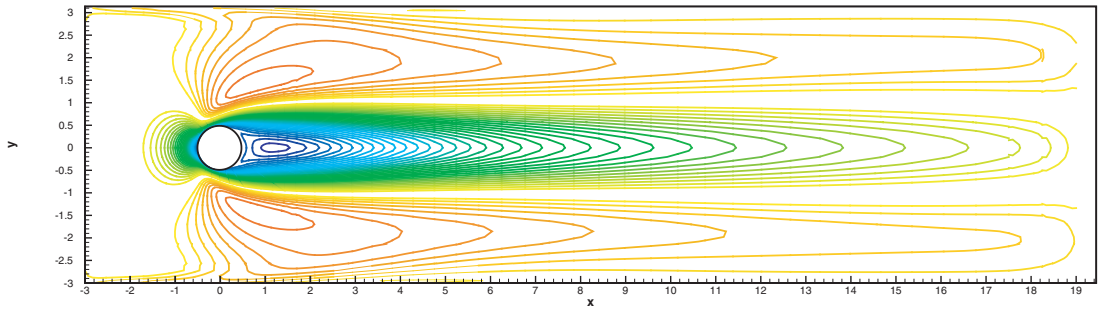

Figure 6.11: Contours of streamwise momentum, ρu, for the uncontrolled steady-state solution at $Re = 20$.

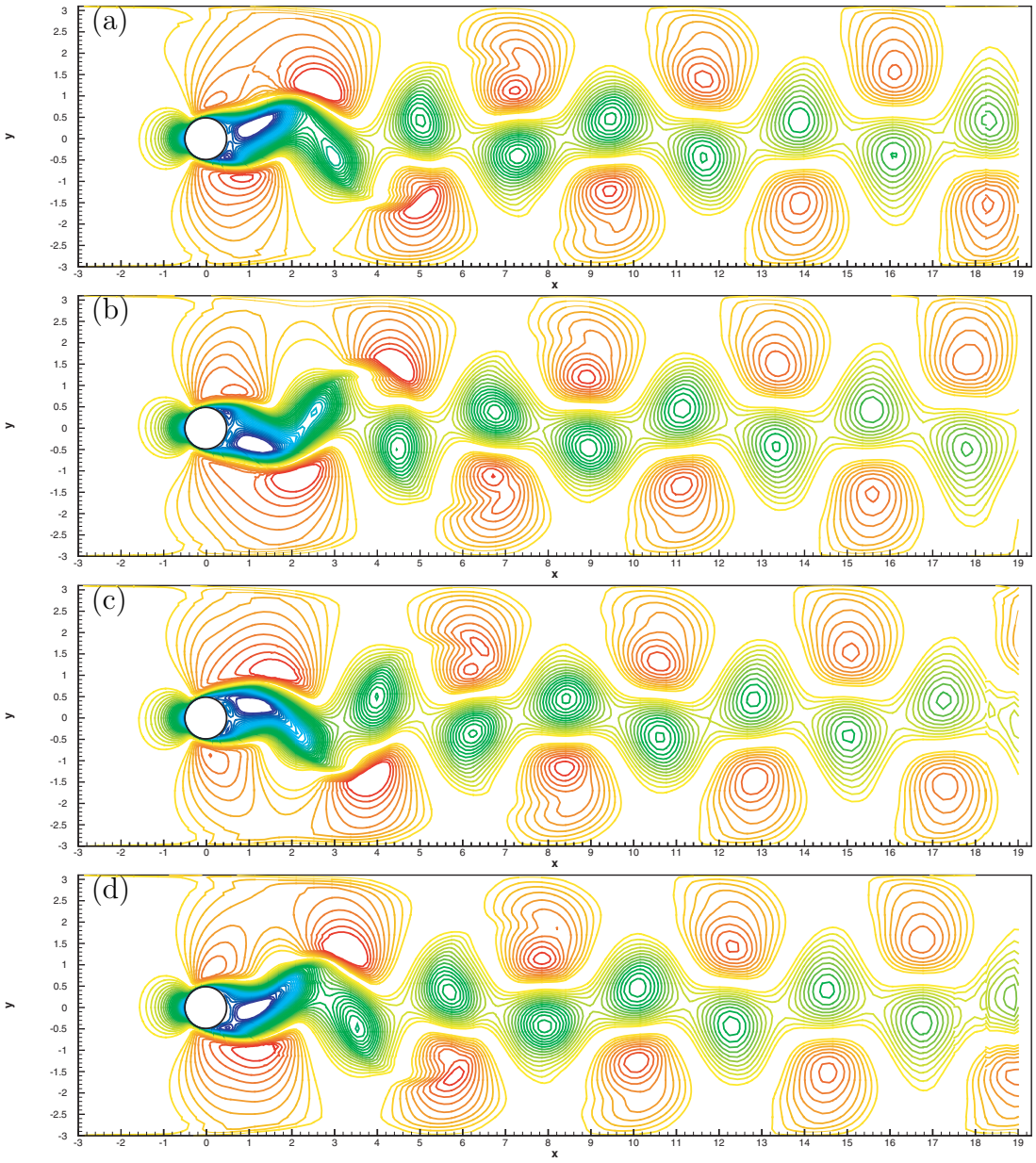

Figure 6.12: Contours of streamwise momentum, ρu, for one vortex shedding period for the uncontrolled flow at $Re = 100$: (a) $t = 0.2$, (b) $t = 0.8$, (c) $t = 1.4$, and (d) $t = 2$.

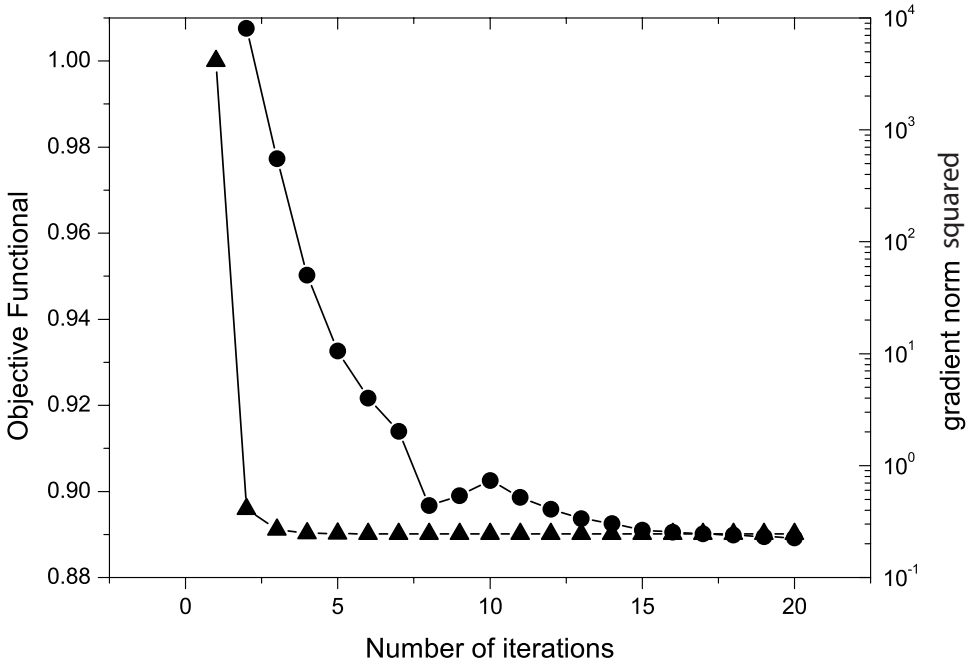

Figure 6.13: Optimization history for the objective functional and the norm of the gradient of the objective functional squared. The optimization time window is one shedding period which corresponds to 2 time units: • gradient norm squared; ▲ objective functional.

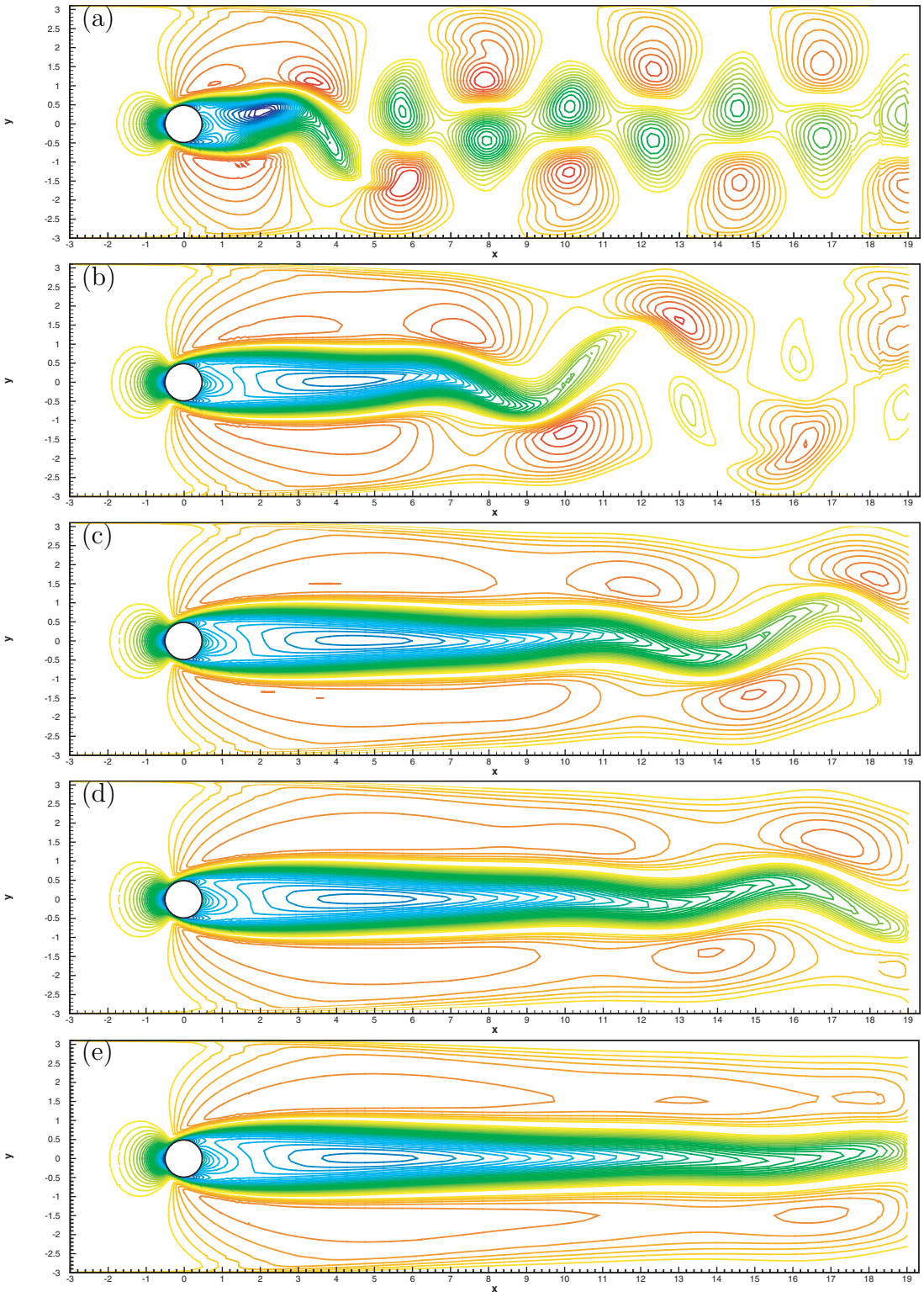

Figure 6.14: Contours of streamwise momentum, ρu, for the controlled flow at $Re = 100$: (a) $t = 2$, (b) $t = 14$, (c) $t = 26$, (d) $t = 30$, (e) $t = 40$. Note that the steady optimal control is obtained over the first two time units, but is then used throughout the remainder of the computation.

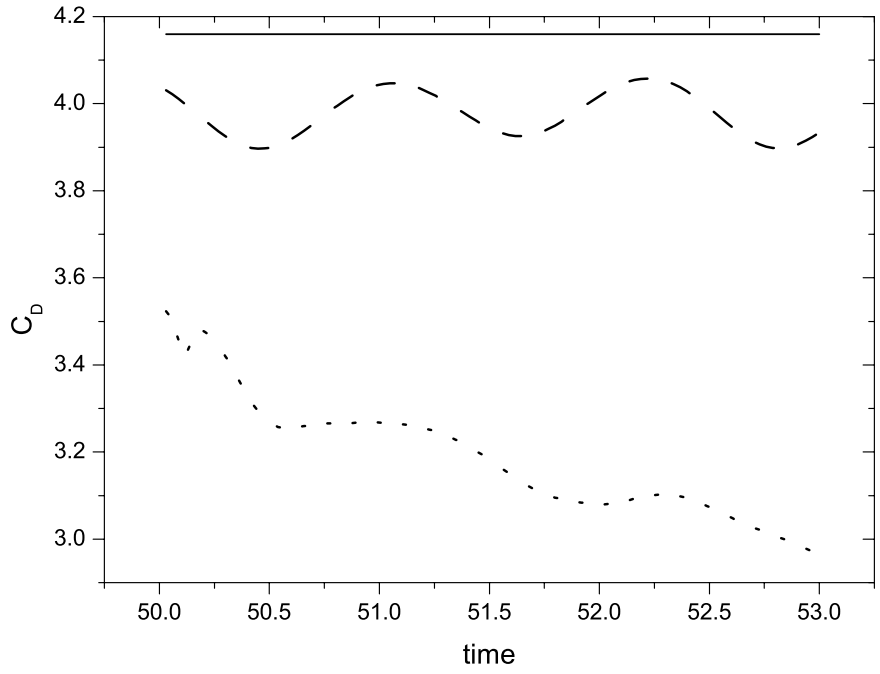

Figure 6.15: Time history of drag coefficients for $Re = 20$ and $Re = 100$ with/ without steady control: —— $Re = 20$ without control; ---- $Re = 100$ without control; ····· $Re = 100$ with control.

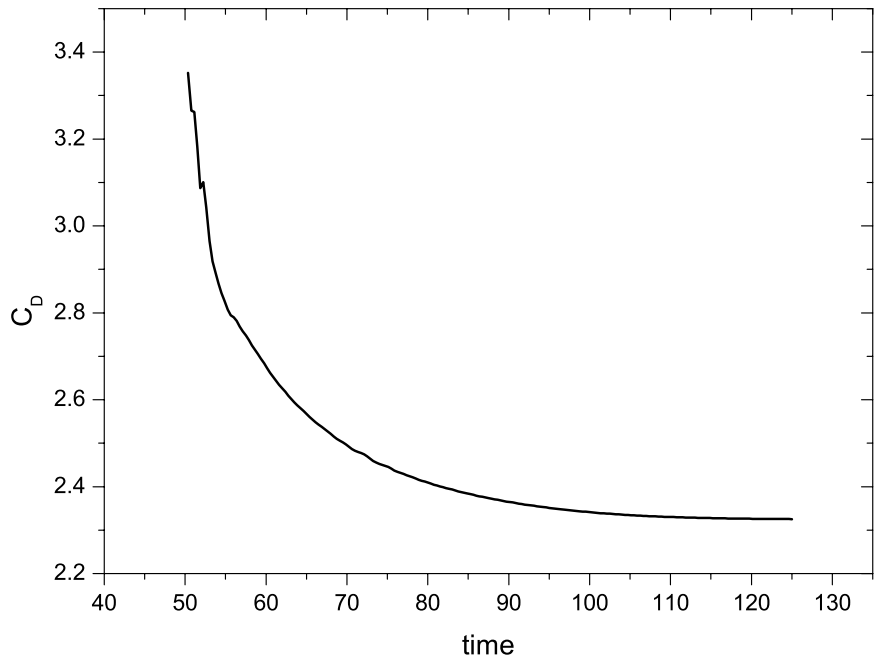

Figure 6.16: Time history of drag coefficients with the flow advancing using the optimal control.

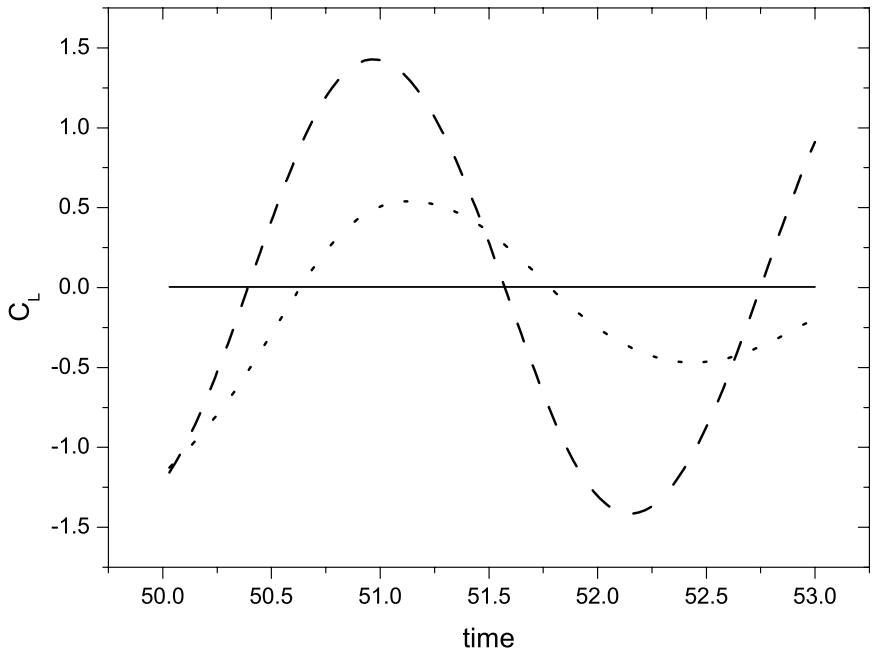

Figure 6.17: Time history of lift coefficients for $Re = 20$ and $Re = 100$ with without steady control: —— $Re = 20$ without control; ---- $Re = 100$ without control; ····· $Re = 100$ with control.

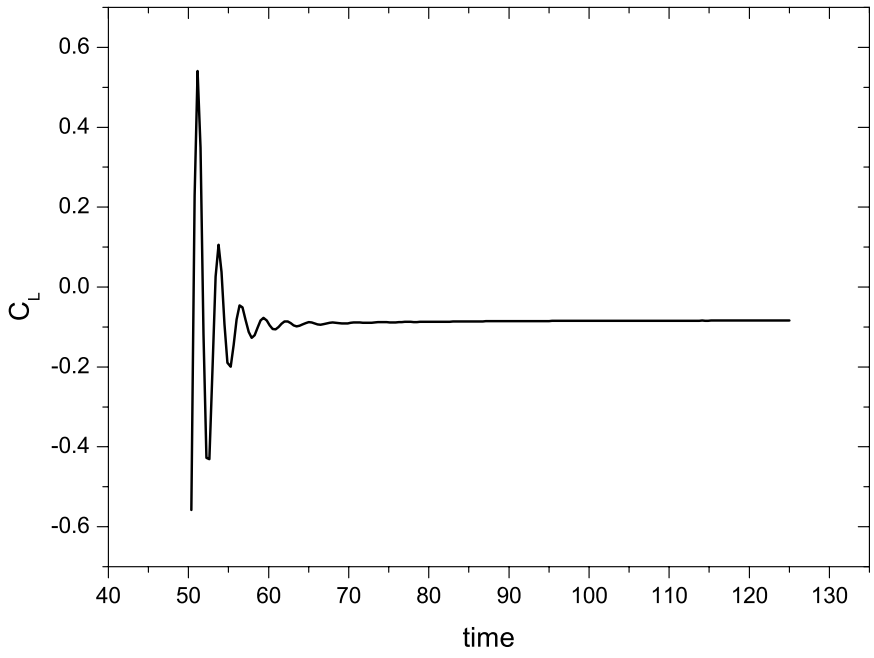

Figure 6.18: Time history of lift coefficients with the flow advancing using the optimal boundary

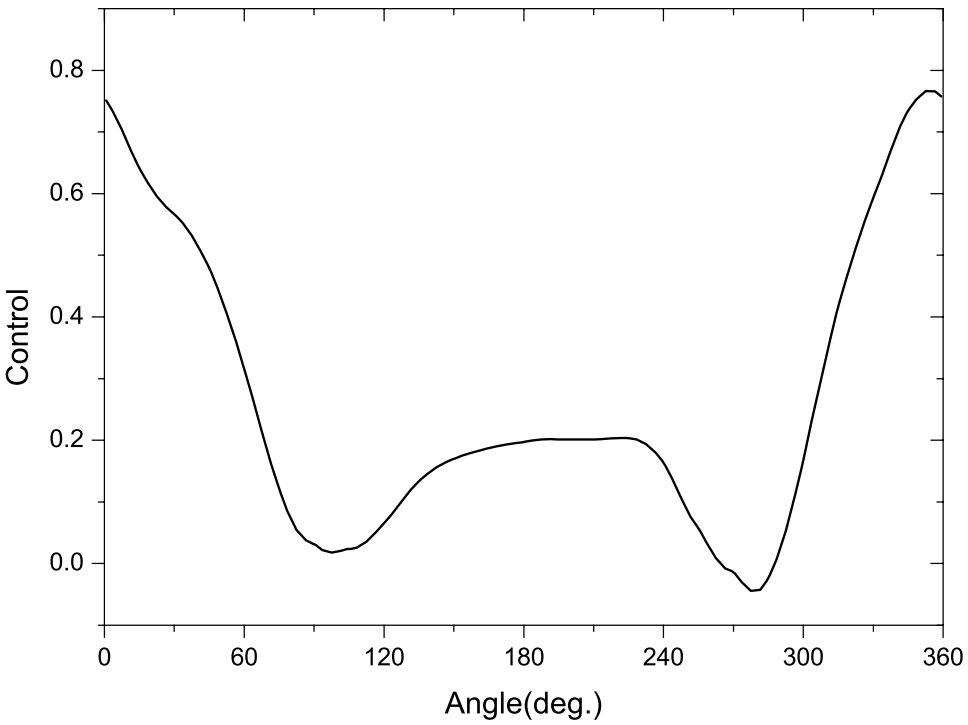

Figure 6.19: Optimal boundary control profile after 16 control iterations

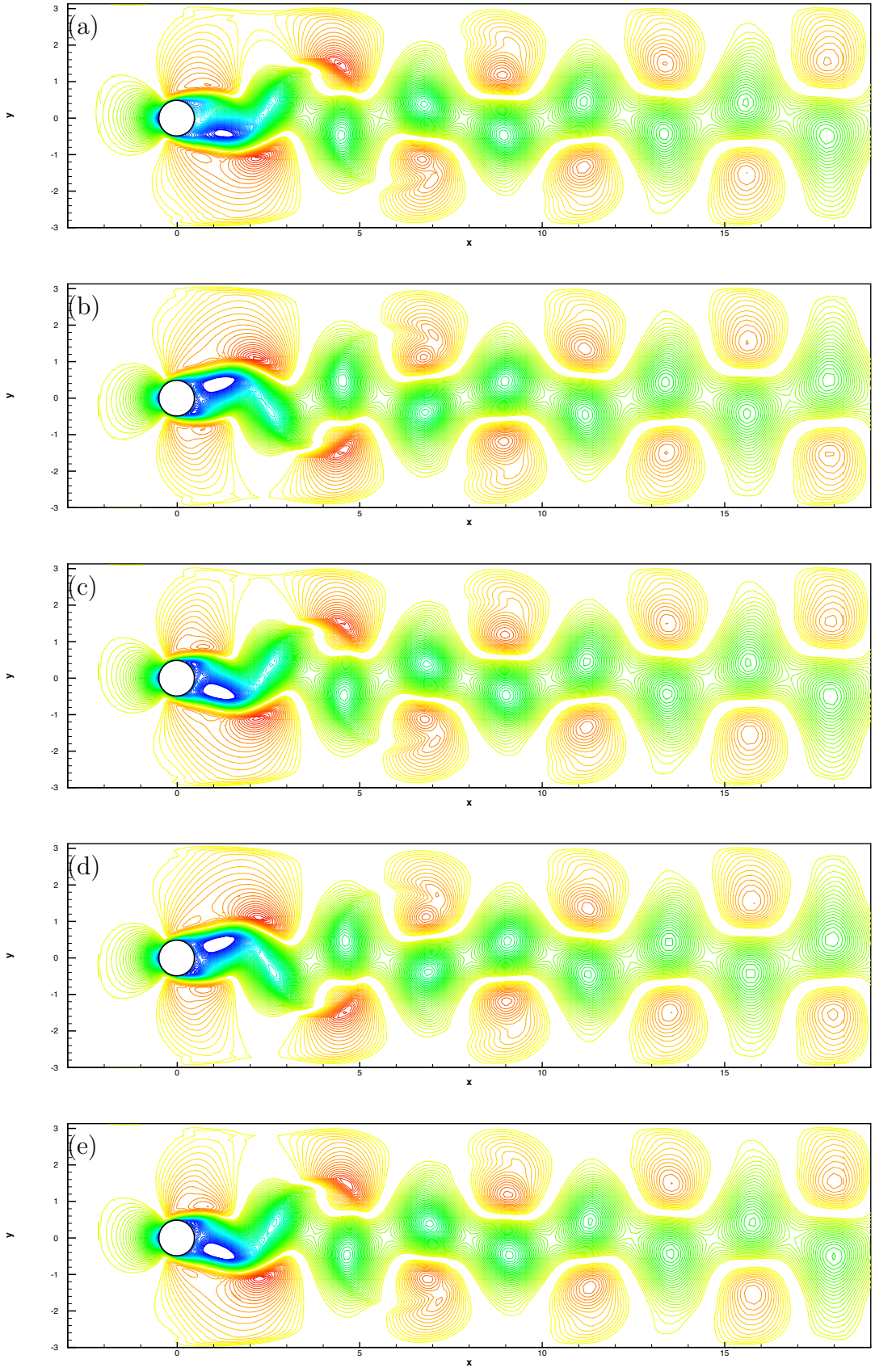

Figure 6.20: Contours of streamwise momentum, ρu, for the uncontrolled flow at $Re = 100$: (a) $t = 1.2$, (b) $t = 2.4$, (c) $t = 3.6$, (d) $t = 4.8$, (e) $t = 6.0$.

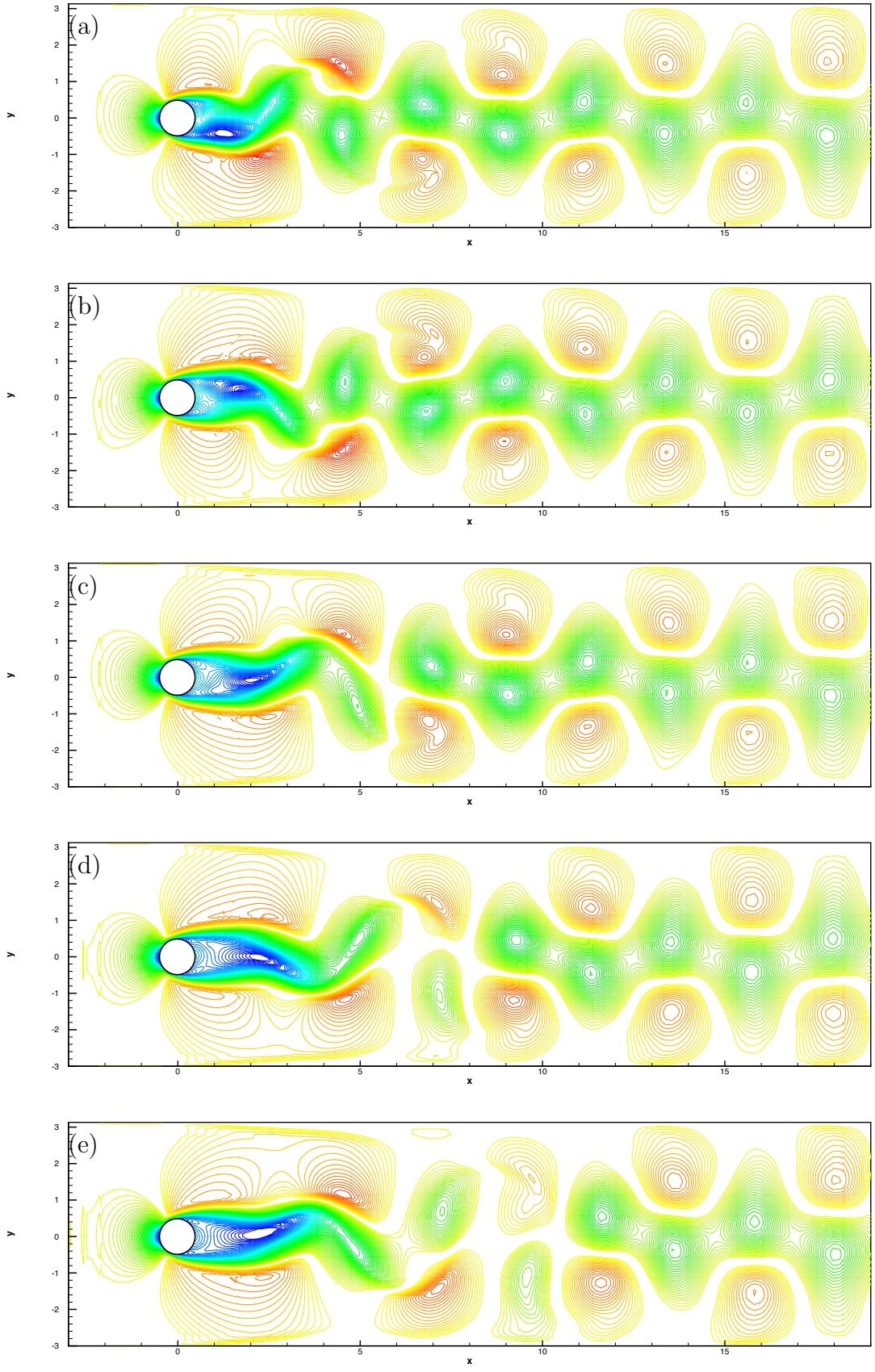

Figure 6.21: Contours of streamwise momentum, ρu, for the controlled flow with temporal regularization at $Re = 100$: (a) $t = 1.2$, (b) $t = 2.4$, (c) $t = 3.6$, (d) $t = 4.8$, (e) $t = 6.0$.

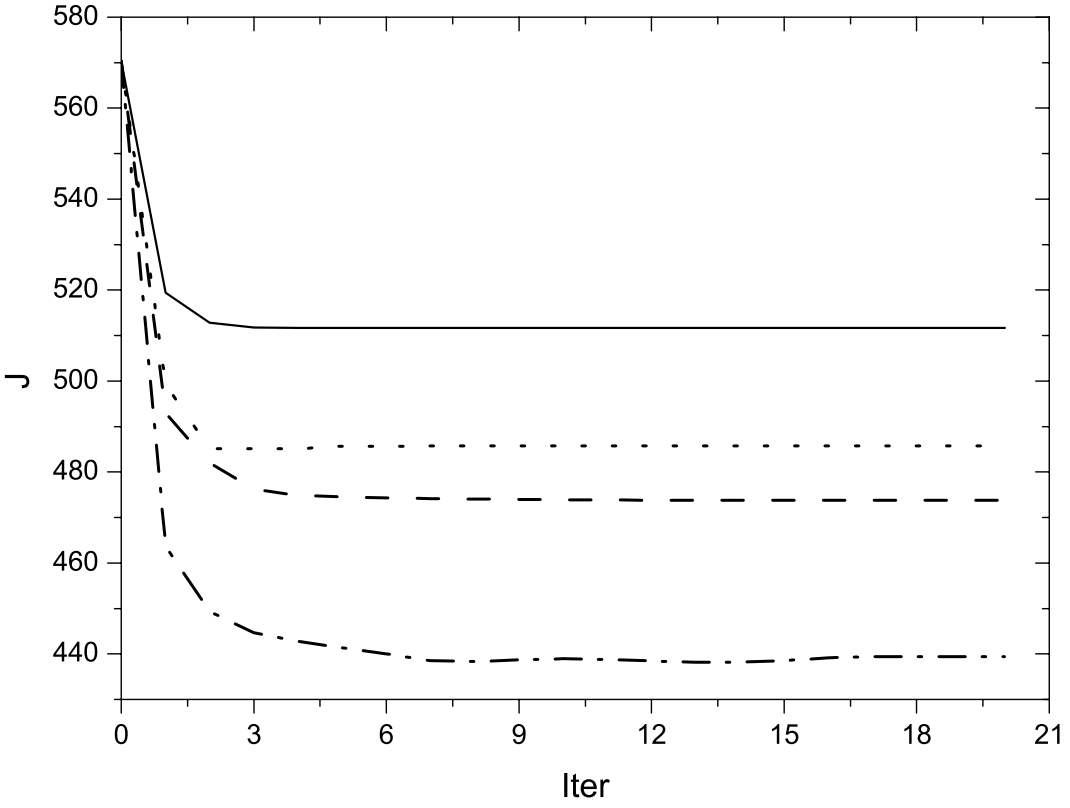

Figure 6.22: Optimization history for the objective functional J and the pure objective J_{obs}, the optimization time window is two shedding period which corresponds to 6 time units: —— J_{obs} without g_t, ····· J_{obs} with g_t, - - - - J without g_t, —-— J with g_t

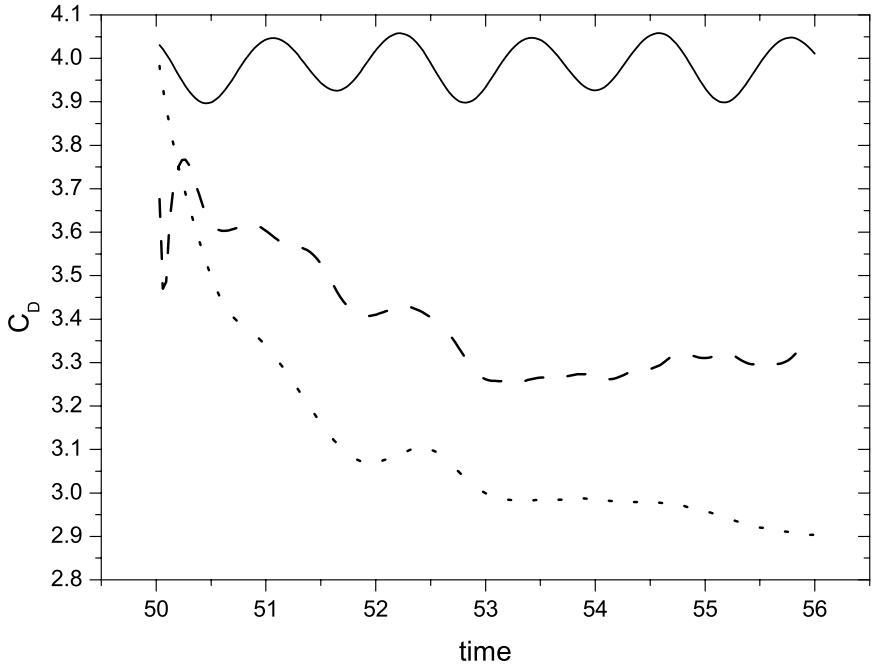

Figure 6.23: Time history of drag coefficients for $Re = 100$ with/without control: —— $Re = 100$ without control; ---- $Re = 100$ with control, $\omega_1 = 360$, $\omega_2 = 0$; ····· $Re = 100$ with control, $\omega_1 = 30$, $\omega_2 = 60$.

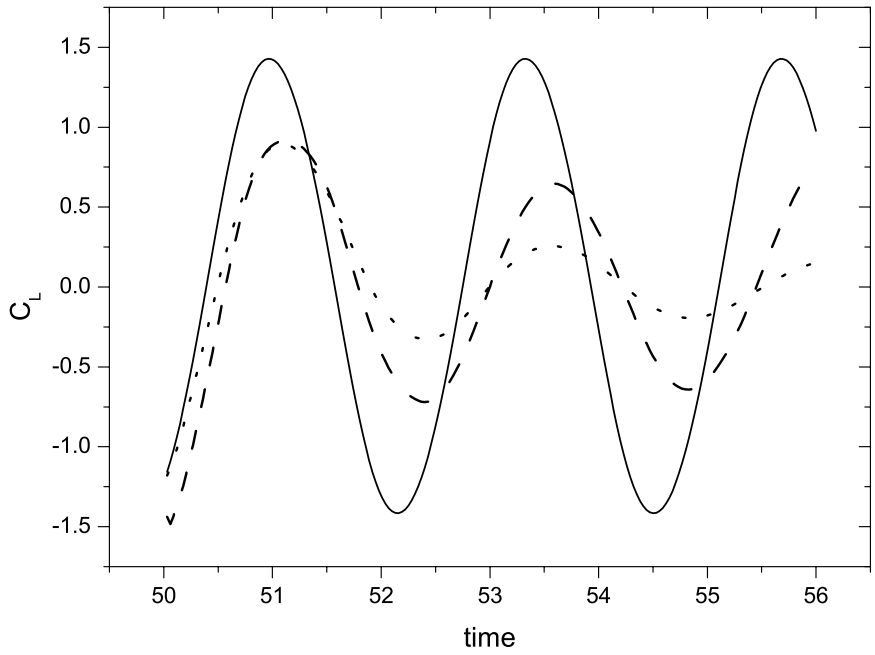

Figure 6.24: Time history of lift coefficients for $Re = 100$ with/without control: —— $Re = 100$ without control; ---- $Re = 100$ with control, $\omega_1 = 360$, $\omega_2 = 0$; ····· $Re = 100$ with control, $\omega_1 = 30$, $\omega_2 = 60$.

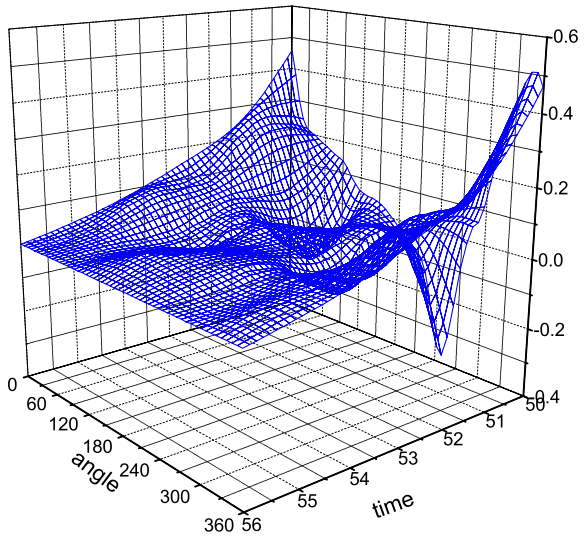

Figure 6.25: Optimal boundary control profile after 13 control iterations without $g_{,t}$

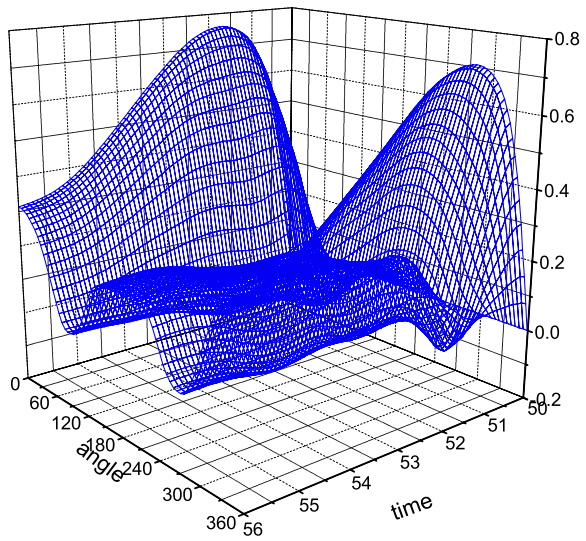

Figure 6.26: Optimal boundary control profile after 20 control iterations with $g_{,t}$

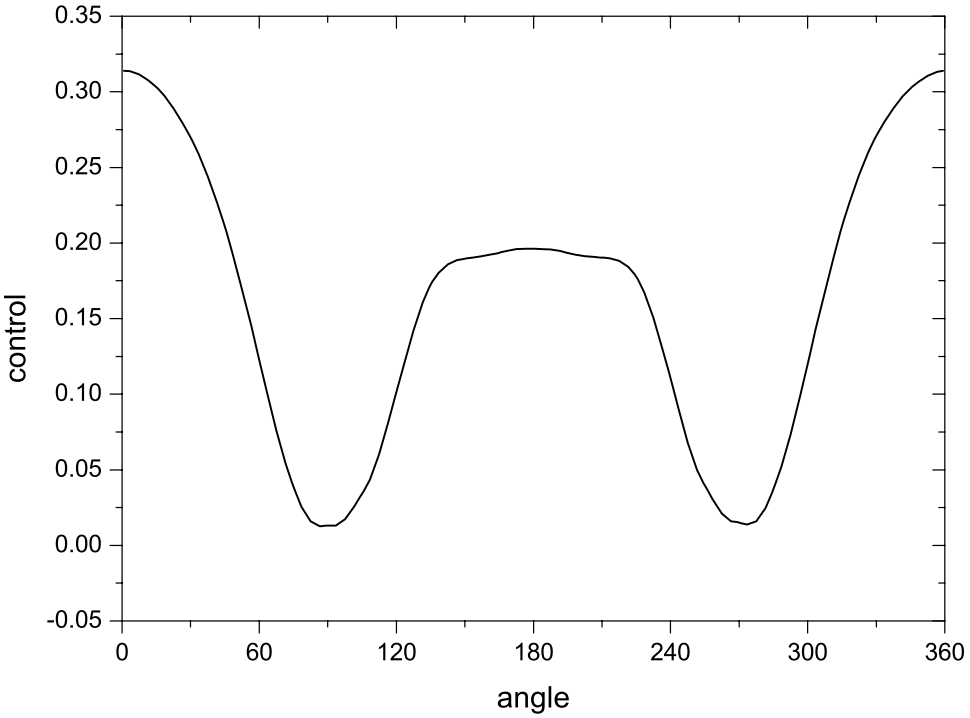

Figure 6.27: Optimal boundary control profile after 20 control iterations with $g_{,t}$ at $t = 6.0$

Chapter 7

Optimal Control for the Coupling Systems

In Chapter 6, we successfully applied optimal control to several model problems: Gaussian acoustic pulse reflection, TKE control of vortex rebounding and the vortex shedding suppressing. However, these problems are all based on the single domain/model formulation. For complex flow problem including the multi-physics inside, such as BVI noise control problem we are interested in, single model implementations might not be so efficient. As formulated in §4.3, we have developed a novel multi-domain/model framework for the optimal control of aeroacoustics problem. In this chapter, we apply this multi-model framework to our interested BVI phenomena to explore boundary control strategies for BVI noise reduction.

7.1 Problem Setup

The state solution for the BVI noise produced by the interaction of a vortex with a Bell AH1 rotor blade in a uniform stream is presented in §5.4. It is solved with the full field Navier–Stokes equations, multi-model NS/LEE and NS/Wave coupling, all of which give good solution and have excellent agreement. It shows that our multi-model simulation is quite feasible for this BVI problem with excellent accuracy for the far field acoustics capturing. To extend such approach to our interested BVI control problem in Figure 7.1, the computational domain is decomposed into three parts. In the middle the viscous Navier–Stokes equations are applied to model the nonlinear interaction between the vortex and rotor blade. In the upper and lower region the linearized Euler equations are used to capture the scattered acoustics. Motivated by the success of Collis *et al.* [33] using the boundary blowing/suction for the optimal

control of aeroacoustic noise generated by cylinder vortex interaction, we use the time- and space-dependent distribution of rotor surface normal velocity (suction/blowing) as our control mechanism. Nakamura's work [89] indicates that the leading edge of the rotor blade plays a very important role in the interaction process. Through the CFD simulation, Romuald Morvant [88] also shows that BVI is primarily leading-edge phenomenon and the compressibility waves which propagate upstream below and above the rotor are generated from the large flow deflection at the leading edge. He also pointed out that compressibility waves tend to dominate the overall noise in the subsonic flow. Given the computational expense for optimal control of such complex problem, we devise our optimization problem only to capture and reduce the noise from the interaction at the leading edge. The initial condition is well defined in §5.4. It is important to start the optimization time window at a time when the initial transient has left the domain and the local mesh resolution is adequate to resolve the vortex. We run the computation after the vortex superposition for 69000 steps to $t = 1.36$ to make sure that the transients associated with the superposition has left the domain. The optimal time window is defined as $t_0 = 1.36$ when the vortex is near the leading edge, $t_f = 2.96$ when the vortex has just passed the trailing edge. Since the BVI noise is strongest at 30^o from the negative x-axis, our observation region Ω_{obs} in our objective functional is defined in the upstream below the rotor blade as in Figure 7.1. We are primarily interested in reducing the amplitude of the noise in region of Ω_o and our control objective is defined as

$$\begin{aligned} J(g) &= \tfrac{1}{2}\int_{t_0}^{t_f}\int_{\Omega_{\text{obs}}} \alpha_0 (p - p_a)^2 d\mathbf{x}\, dt \\ &\quad + \tfrac{1}{2}\int_{t_0}^{t_f}\int_{\Gamma_c} \Big(\alpha_1 g_t^2 + \alpha_2 g^2\Big) d\Gamma\, dt. \end{aligned} \tag{7.1}$$

where p_a is the ambient or steady mean-flow pressure distribution, the wights $\alpha_0 = 10000.0$, $\alpha_1 = 0$ and $\alpha_2 = 1.0$. Our objective is to minimize the acoustic pressure

intensity in the rectangle area depicted in Figure 7.1 within some reasonable time window. The control is exerted on the surface of the rotor blade and is chosen to be the time and position dependent wall–normal velocity. In this problem setup, our control is along the whole blade. Following [33], four stations are placed above and below the rotor blade to record the time history of pressure fluctuations. Stations P_1 and P_2 are located in the LEE domain above the blade to capture the upward acoustics. Stations P_3 and P_4 are defined inside the observation region Ω_o.

7.2 Result and Analysis

7.2.1 Noise Reduction

Figure 7.2 shows the pressure contours at different time levels. The intensity of acoustic pressure inside the observation region has been clearly reduced. It is seen more clearly in Figure 7.2 at $t = 2.16$ and $t = 2.56$. Quantitatively after 3 iterations, J is reduced from 0.91 to 0.058 and the sound level in the observation region is reduced about 12dB. However, the sound level above the rotor blade upstream seems to get strengthened as in Figure 7.2. Those are more clearly shown in Figure 7.3, which is the pressure fluctuation history at stations P_1, P_2, P_3 and P_4. Compared with the uncontrolled pressure fluctuation at those four stations, the pressure fluctuation amplitude for P_3 and P_4 inside the observation region Ω_o is noticeably reduced. However, at the end of the pressure fluctuation history at P_4, the pressure fluctuation amplitude slightly increased. It might be from the trailing edge waves when the control has not been able to take effect because of our small optimization window. The pressure fluctuation amplitude in P_1 and P_2 above the blade becomes larger. Such finding has also been reported in [33]. Look at the pressure fluctuations at those sensing stations for the no-control and controlled flow in Figure 7.3, the control only takes effect after the certain time period as in all stations. For station P_1, the effect

of the control is not felt until $t = 1.76$. It takes slightly longer for station P_2 feel the effect of the control. The same are also true for stations P_3 and P_4. The reason is that the information travels at the speed of the sound relative to the fluid and there is a delay between the start of control at $t = 1.36$ and any corresponding change at the stations.

7.2.2 Adjoint Analysis

To better understand the control process, the evolution of adjoint variable λ_4 is shown in Figure 7.4, which contributes to the gradient information for the control update. This adjoint quantity is like an adjoint wave and contributed by the pressure fluctuation in the objective functional. As the adjoint wave moves the upward and interacts with the rotor blade, eventually takes effect on the control region along the blade surface. Such adjoint wave interacts with the rotor blade and dominates the gradient around the rotor blade. Given this qualitative behavior of the adjoint solution, such interaction between the control and the flow field alters the far-field acoustics delicately by changing the near-field acoustic source. Figure 7.4 also shows that the adjoint solution around the coupling surface is quite smooth, indicating that our coupling approach for the adjoint equations is working properly.

7.2.3 Discussion

In order to understand the underlying mechanism of noise reduction, several important BVI parameters are checked carefully. Interestingly, the most important two characteristic for BVI noise: vortex strength and miss distance, are barely changed as shown in Figure 7.5. Without control, the vortex strength changes from -5.0144 to -4.12657 after passing the blade. With control, the vortex strength changes from -5.0144 to -4.10883. It indicates that the control doesn't appear to change the vortex

trajectory or vortex strength. It is not certain whether it follows the same control mechanism found by Collis *et al.* [33] from the study of the cylinder vortex interaction that the acoustics from the control interactions with the mean flow conceals the BVI. However, it is very wise to look at its vorticity field. The vorticity field with the control is deducted with the one without control and the difference of vorticity field around the rotor blade is shown in Figure 7.6. Figure 7.6 shows that the boundary blowing/scution along the blade does introduce the vorticity to the flow field, especially the flow field around the blade. Such vorticity is not negligible, which may be the major source contributing to our control mechanism. Checking the unsteady drag coefficient which usually comprises the pressure and skin friction resulted from the viscous stress along the surface as in Figure 7.7, the drag gets slight increase in the first half optimization time window, which seems to be mainly from the viscous stress because of the control exerted along the rotor blade. In the second half window, the drag is recovering back as the control becomes weaker. We are more interested in the lift coefficient C_l, which is mainly from the pressure difference on the blade surface. As reviewed by Peake and Crighton [94], the reduction of the unsteady lift on the blade during the interaction would consequently, at least at low Mach number, also reduce the noise. Such mechanism has led to the use of the oscillating trailing edge flaps to reduce the unsteady lift on the blade as in [65, 90, 107] and incorporating the suction/blowing on the blade surface [56, 71]. Look at the lift history in Figure 7.8, the lift does get noticeably reduction, although there is slight increase in the end. The lift fluctuations caused by blade vortex interaction are responsible for the impulsive noise. Such reduction in the lift fluctuations implies the noise reduction. There is a significant reduction in the temporal gradient of lift leading to a reduction in BVI sound levels.It is quite consistent with our control result in Figure 7.3.

7.3 Summary

We believe that our work is the first model-based effort to use optimal control theory to attempt the BVI noise control based on the relatively realistic BVI configuration. Our numerical simulation and its control is also based on an efficient and novel multi-domain/model method. As we have found, such approach works quite well for our state calculation and its adjoint computation. The results obtained in the present work appear to be quite promising. It suggests that the boundary blowing and suction is quite feasible means to reduce blade-vortex interaction (BVI) noise and also shows that optimal distributions of wall-normal suction and blowing can reduce the BVI noise significantly. In our current case, when the objective functional is set to target only the forward scattered BVI sound, a 12dB reduction is obtained. The vortex strength and trajectory get barely changed. However, as we observed, the optimal control does alter the interaction of the vortical and potential fields, which is the source of BVI noise. One of the impact from such interaction is the slight increase of drag in the first half of the optimization window and lift reduction all over the time window. Although those preliminary results are quite promising, further investigation is required. As our first attempt, the control is distributed all over the blade surface. It is not a good practice because of the cost and the singularity around the trailing edge. As we know that BVI is primarily leading-edge phenomenon, our further work is to investigate the control mechanism around the leading edge.

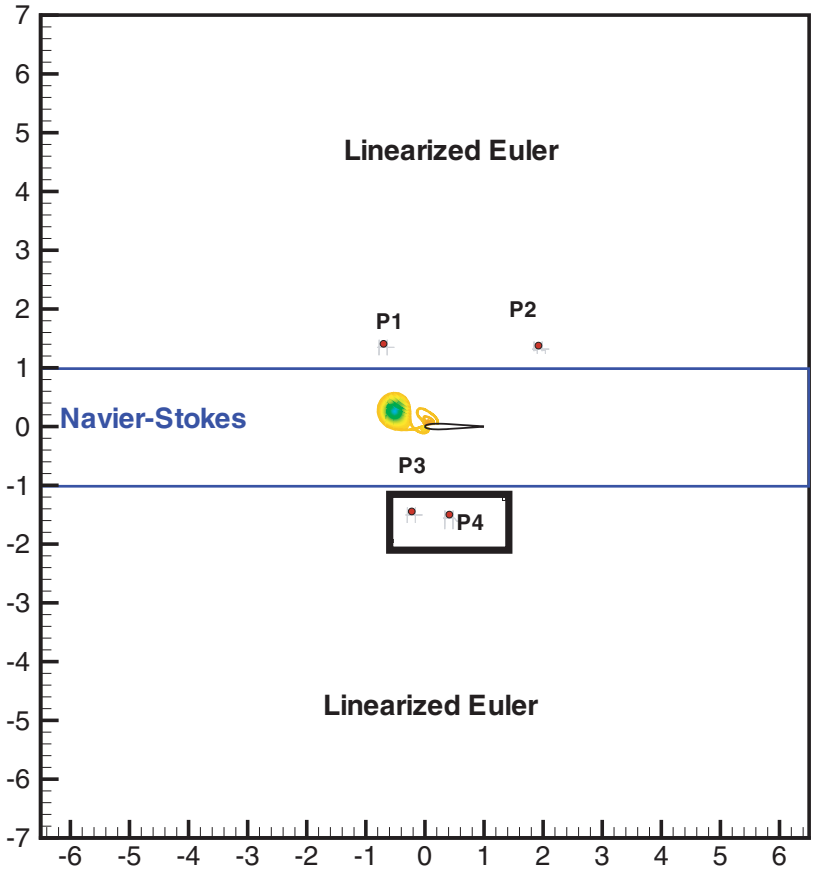

Figure 7.1: Problem setup for BVI

x

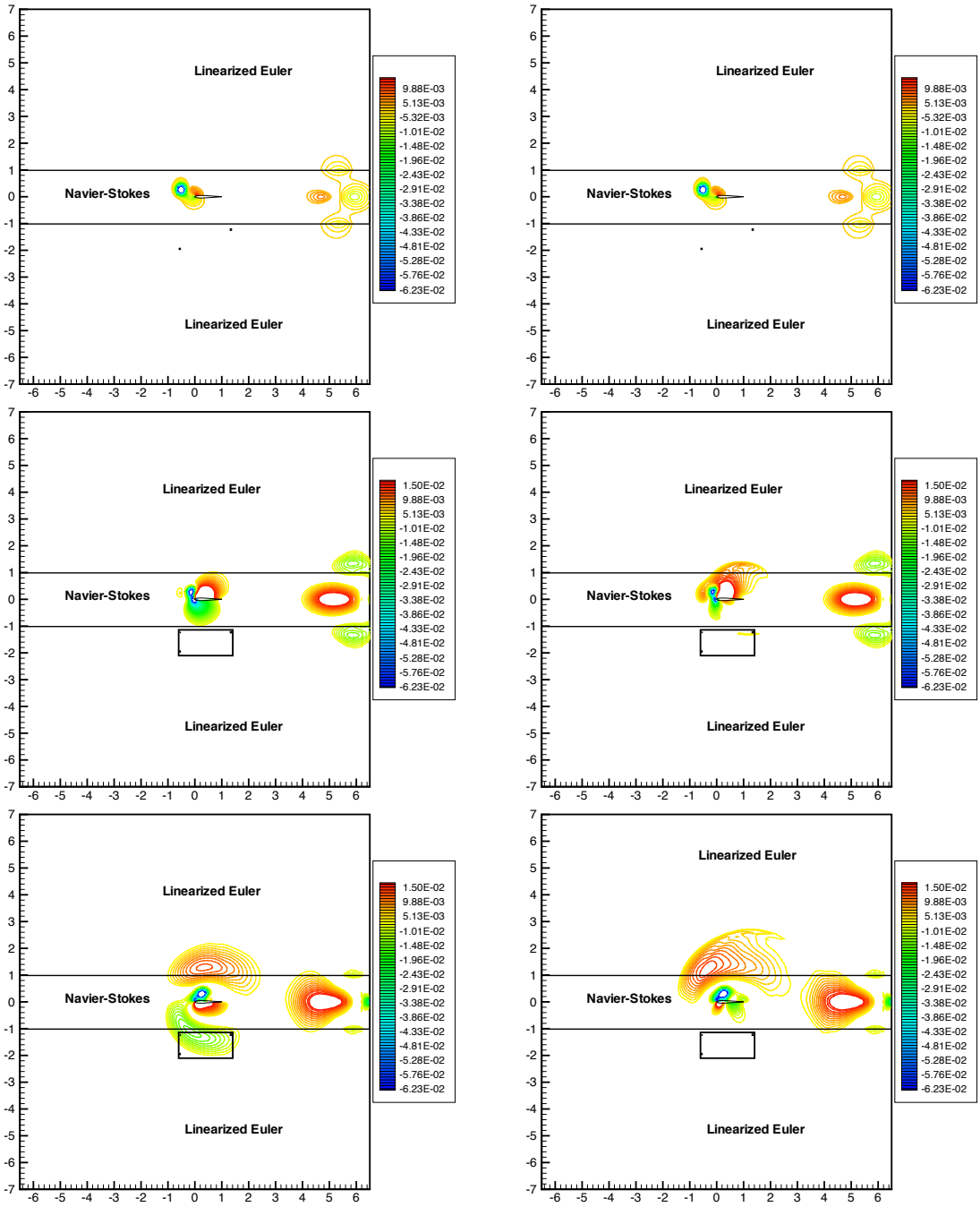
Linearized Euler
Navier-Stokes
Linearized Euler
9.88E-03
5.13E-03
-5.32E-03
-1.01E-02
-1.48E-02
-1.96E-02
-2.43E-02
-2.91E-02
-3.38E-02
-3.86E-02
-4.33E-02
-4.81E-02
-5.28E-02
-5.76E-02
-6.23E-02
1.50E-02
9.88E-03
5.13E-03
-1.01E-02
-1.48E-02
-1.96E-02
-2.43E-02
-2.91E-02
-3.38E-02
-3.86E-02
-4.33E-02
-4.81E-02
-5.28E-02
-5.76E-02
-6.23E-02

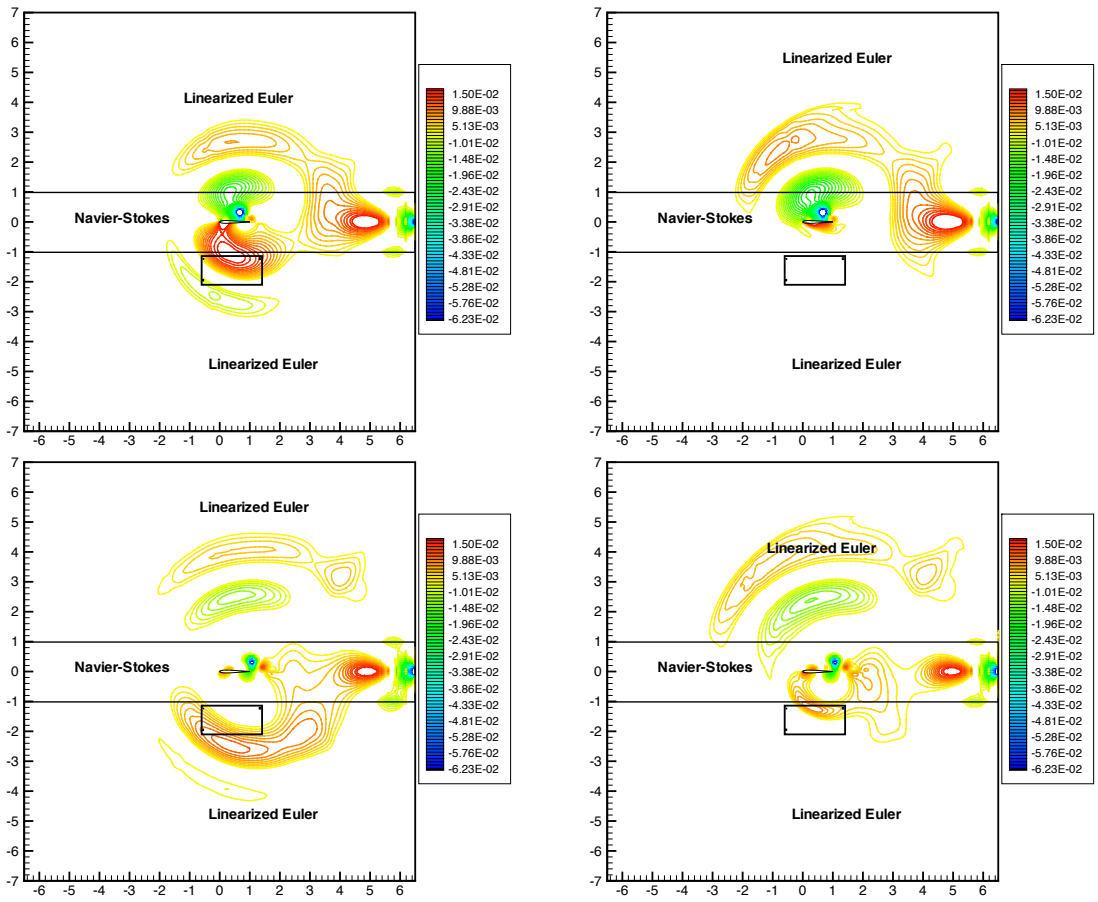

(a) No control **(b)** Optimal control

Figure 7.2: Contours of scattered pressure $p - p_a$ at instants $t = 1.36$, 1.76, 2.16, 2.56, 2.96 for no control (left) and optimal control (right).

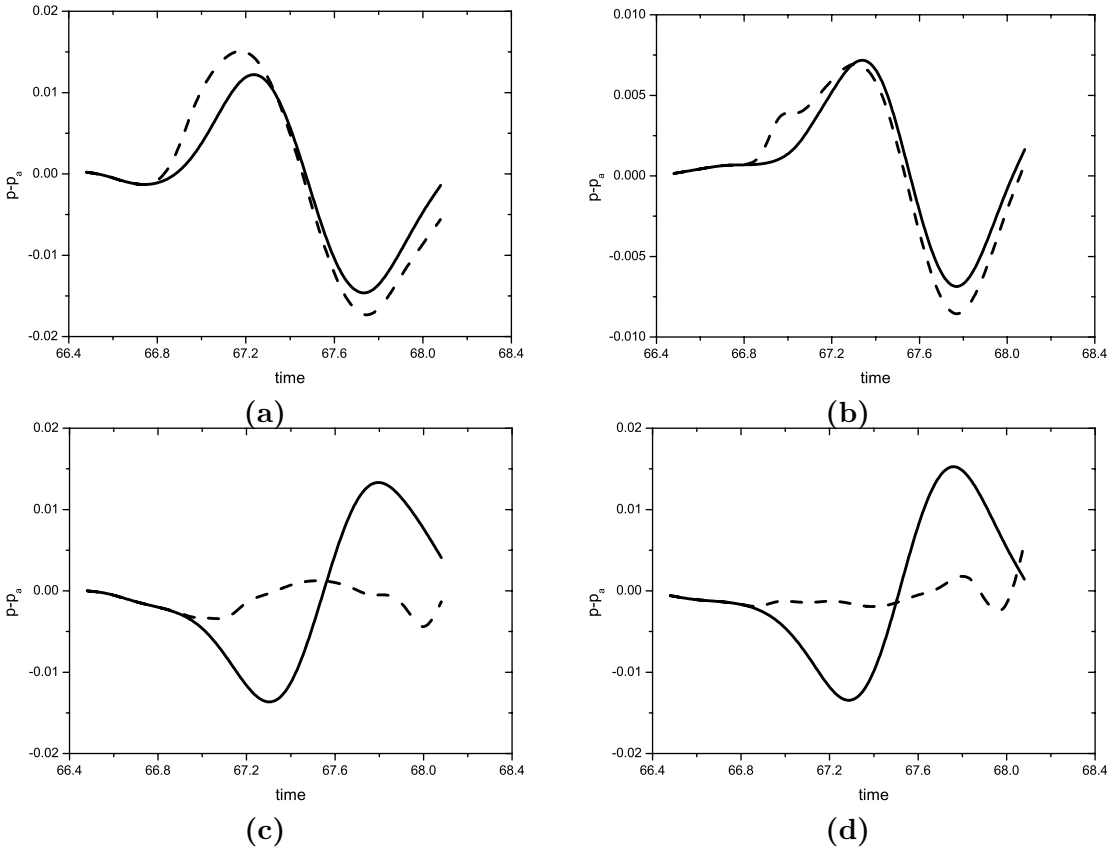

Figure 7.3: Time history of pressure at observations (a) station 1, (b) station 2, (c) station 3, (d) station 4: —— no control; ---- optimal control.

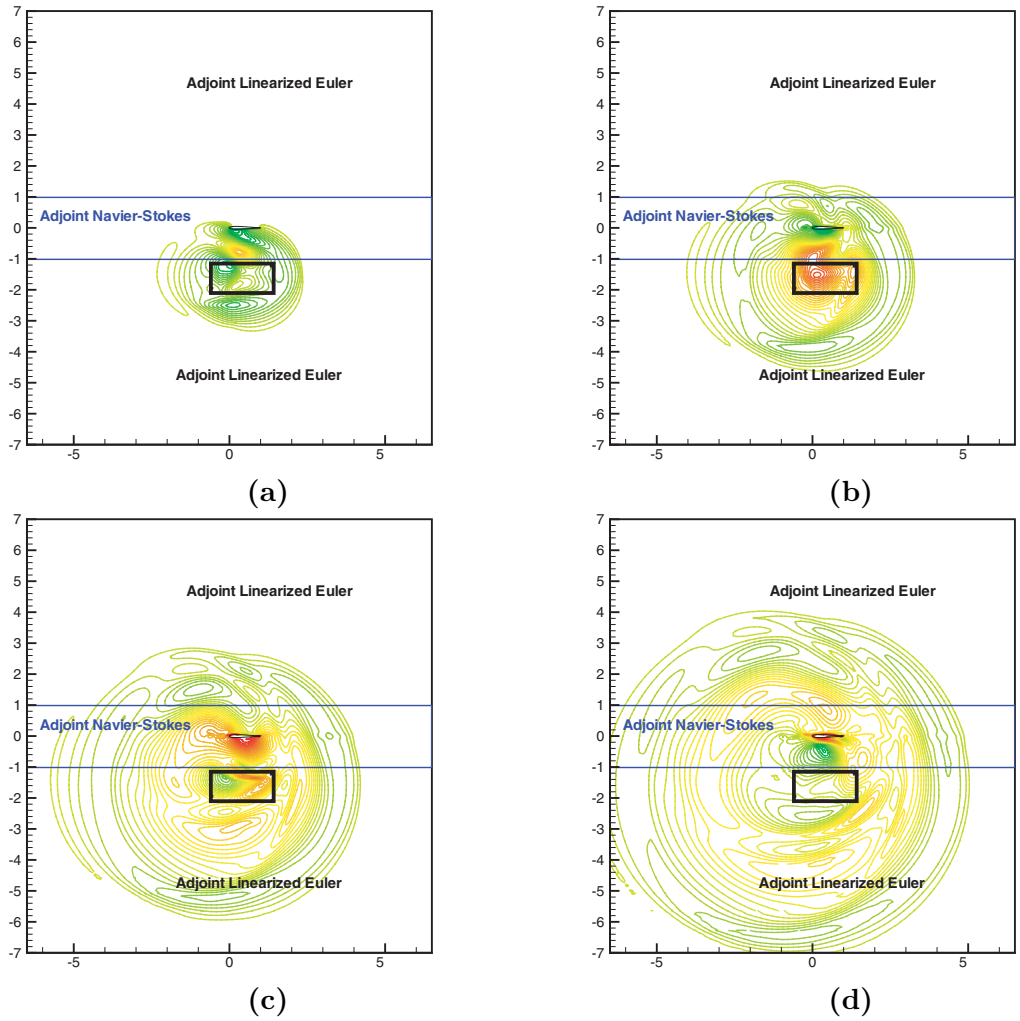

Figure 7.4: Adjoint variable λ_4, the time goes backward in the adjoint solution (a) t=2.56, (b) t=2.16, (c) t=1.76, (d) t=1.40

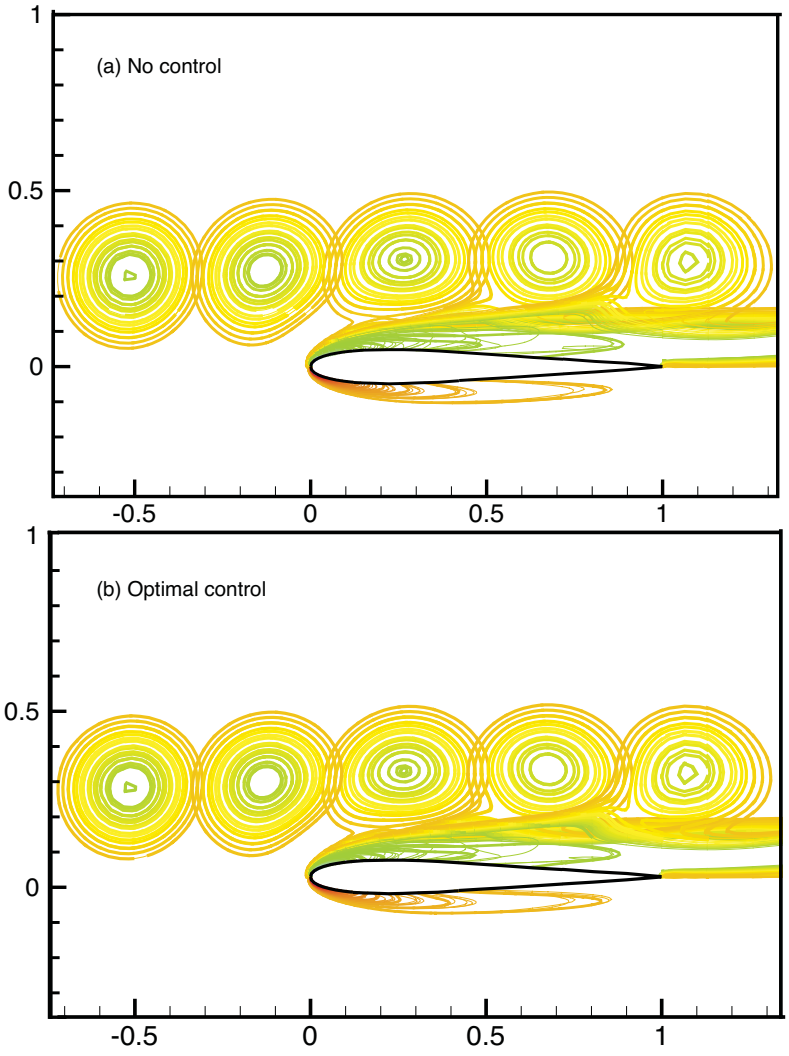

Figure 7.5: Vortex trajectories with/without control during the interaction.

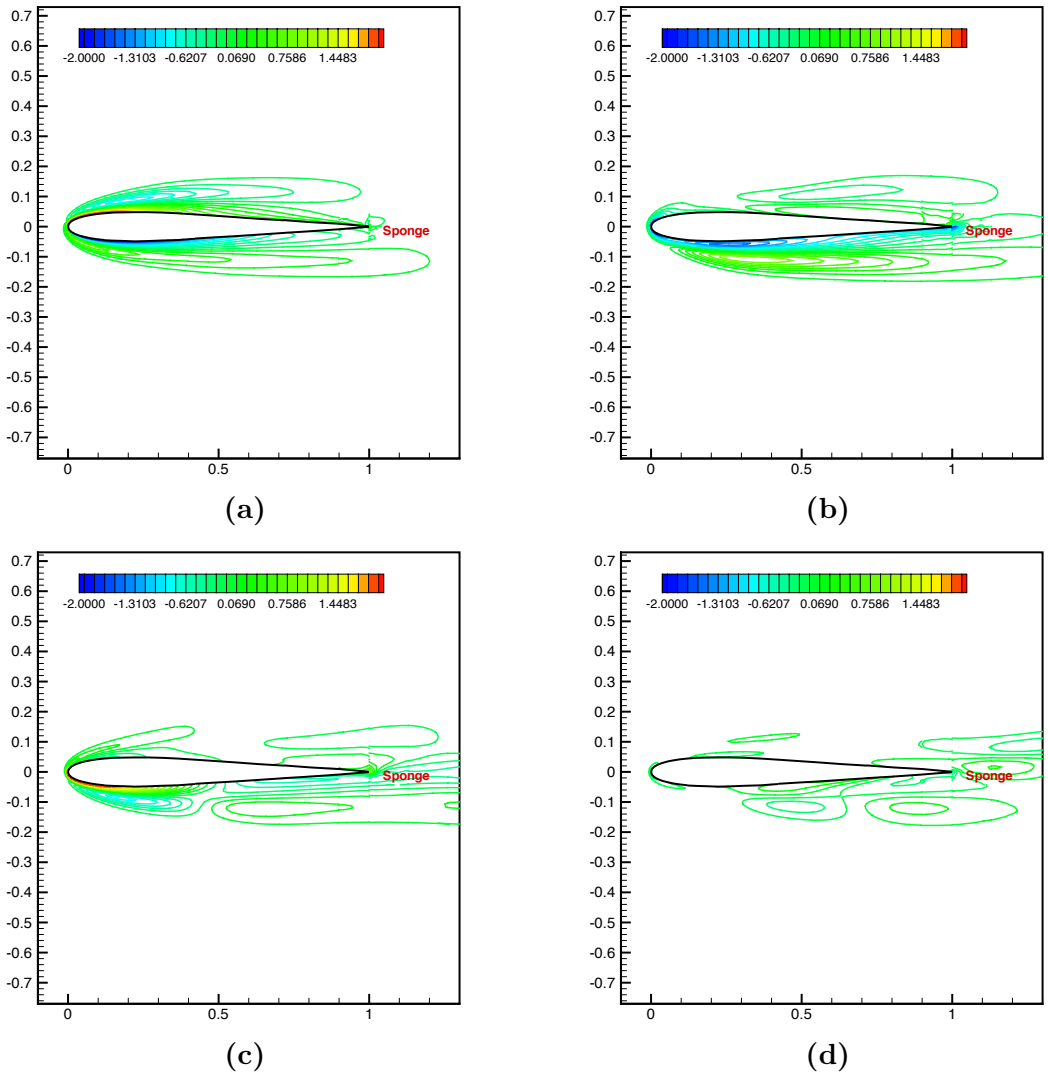

Figure 7.6: Vorticity field $w - w_0$(a) t=1.76, (b) t=2.16, (c) t=2.56, (d) t=2.96

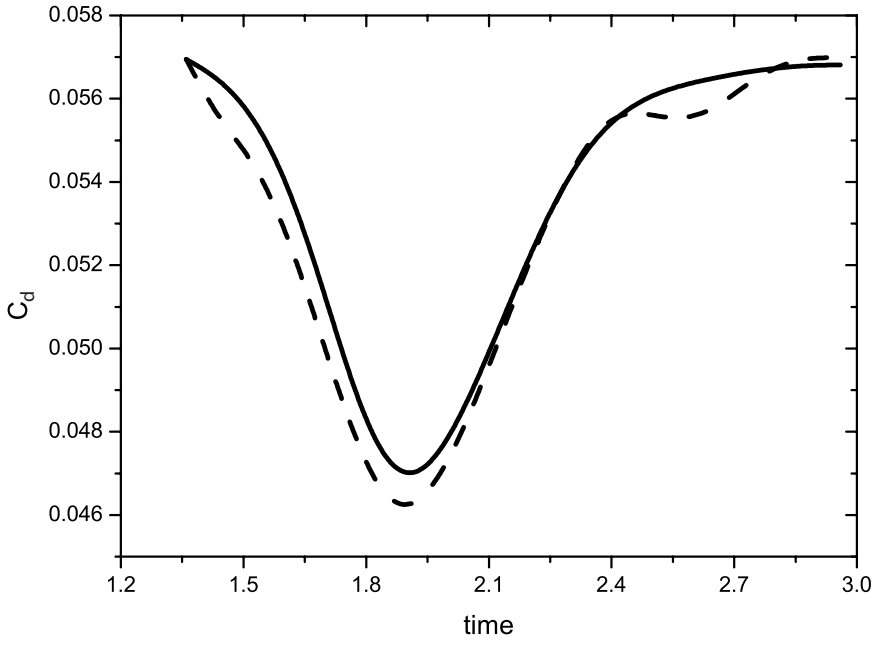

Figure 7.7: Time history of drag coefficients for BVI noise control with/ without control: —— no control; ---- optimal control.

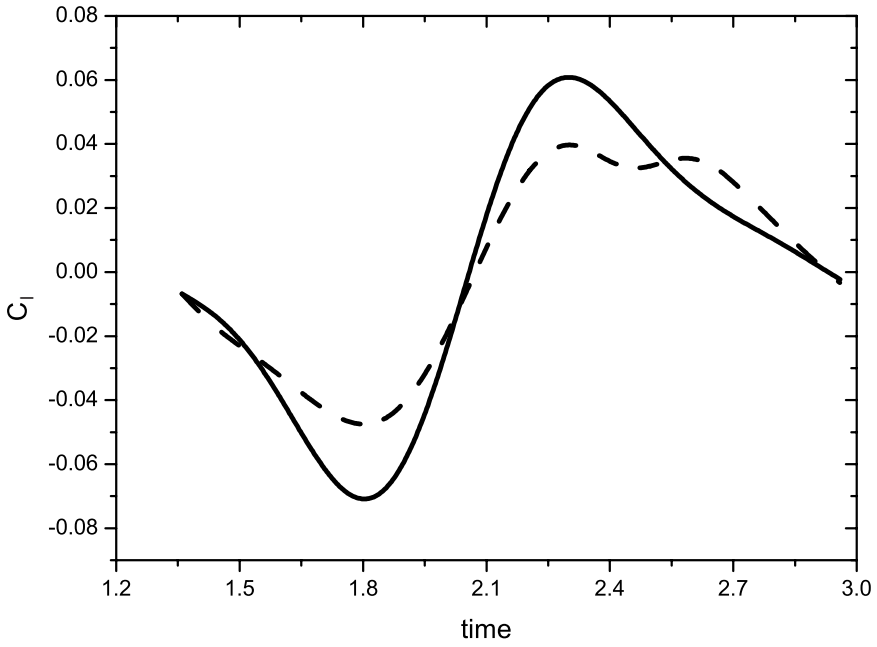

Figure 7.8: Time history of lift coefficients for BVI noise control with/ without control: —— no control; ---- optimal control

Chapter 8

Conclusions and Future Work

8.1 Conclusions

The use of on-blade normal velocity actuation for controlling the impulsive noise arising from blade-vortex interaction (BVI) has been investigated using the novel multi-domain multi-model method. Exploiting the multiphysics structure of this problem, nonlinear acouqstics source plus linear acoustics propagation, we have explored and developed a discontinuous Galerkin (DG) based multi-domain multi-model method for optimal control of aeroacoustics. In this approach the coupling of multi-domains (near-field and far-field) and multi-models is achieved by weakly enforcing continuity of normal fluxes across a coupling surface. We have developed this approach for different multi-model coupling problems for a single-grid framework. Also, we have extended the multi-model approach to the control framework. To be more explicit, in solving our adjoint equations, we now weakly enforce the continuity of normal adjoint fluxes across a coupling surface.

Our numerical method has been validated using a suite of model acoustics and optimal control problems. Excellent agreement with reference computations and/or analytical solutions have been obtained (refer to Chapters 5 and 6).

Given the success of validation of both the state calculation and model flow control problems, we extend the multi-domain, multi-model framework for the optimal control of complex acoustics problems, namely, the BVI phenomena. In doing so, we explore boundary control strategies for BVI noise reduction. Our results demonstrate that DG based multi-model method is a viable tool for obtaining quantitatively accurate results for acoustics control using wall normal blowing/suction. Here, for the current

BVI problem, we couple the near field and far field with a NS and LEE, respectively. And, we employ boundary blowing/suction around the rotor blade as our control mechanism.

For the conditions described in Chapter 7, we obtain a 12dB reduction in sound pressure level when the objective function targets the downward radiated BVI noise. Interestingly, the optimal control has negligible effect on both the vortex strength and trajectory, however, it does alter the interaction of the vortical and potential fields that is the source of BVI noise. While this results in a slight increase in drag, there is a significant reduction in the temporal gradient of lift leading to a reduction in BVI noise levels.

8.2 Future Work

The use of high resolution in the near-wall region to resolve boundary layers imposes stringent restrictions on the time step size using explicit time advancement. Additionally, this limits our optimal time window to short intervals. Therefore, to reduce the computational cost and cover a reasonable optimal time window, an implicit time scheme is needed, at least for the viscous flux evaluation. Thus, we can employ larger time steps to advance the flow resulting in reduced computational cost.

Meanwhile, a practical way to reduce computational cost, in the interim, is to introduce instantaneous control following the approach of [12,20]. However, it will not lead to the same control that would be obtained by optimizing over the entire control time window. Furthermore, this introduces large discontinuous control inputs at the beginning of the each control window. Alternatively, we can possibly overcome the time step restriction by resorting to inviscid boundary control as [35]. This approach [35] has severe physical constraints for the inviscid blowing. For the current BVI problem, besides viscous equations, inviscid equations and full potential equation have

also been successfully used to model the nonlinear interaction. However, whether this BVI noise control problem can be modeled using inviscid or full potential equations with the wall normal blowing and suction remains an open question.

As for our current multi-model coupling, in addition to the domain and model (equations) coupling, we can introduce time scale coupling [105]. Upon closer examination of the current multi-scale problem (BVI), the aeroacoustic wavelength in the far-field is in general much larger than the wavelength of the fluid flow phenomena in the near-field whose acoustics source are normally eddies with a much smaller structure. Moreover, these eddies in the near-field advect with the fluid flow, whose speed is usually slower than the far-field sound speed. As a result, the local CFL number in each domain is different. The Use of local time-stepping in the near-field and far-field may lead to improved computational efficiency.

Finally, during optimization, it is found that our current optimization algorithm (nonlinear conjugate gradient method) converges slowly. A significant portion of the computational effort is expended during the line search procedure. Here, the exploration of other quasi-Newton based optimizers as a means to improve convergence has the potential to reduce computational cost.

Appendix A

Derivation of Adjoint Equations

In this chapter, we derive the analytical adjoint equations for the optimal control of the inviscid and viscous flow. The optimal control framework is based on the adjoint methods for controlling the unsteady two-dimensional compressible Euler/Navier–Stokes equations. The adjoint problem formulation is from the continuous adjoint(i.e. optimize-discretize) approach, defining a Lagrange multiplier first, then getting the corresponding adjoint system and gradient information through the variation of $\boldsymbol{u}$, $\mathbf{U}$ and $\mathbf{g}$ as in [36, 108] and Jameson's work [61, 62]. The resulting adjoint system will be used to determine the sensitivity of the flow to the applied control, which is the center of control update with a gradient based optimization algorithm.

A.1 Adjoint Euler and Navier–Stokes Equations and Gradient Equations

The following derivation is based on the variation formulation,i.e., define a Lagrange multiplier, then variation of the state $\boldsymbol{u}$, $\mathbf{U}$ and control $\mathbf{g}$ to get the adjoint equation and the gradient equation. For the derivation purpose, the cost functional is defined as

$$J(\mathbf{U}) = J(\mathbf{U}, g) \tag{A.1}$$

and as the typical case, the compressible Navier–Stokes equations3.1a is used as the state governing equations.

We define the Lagrangian as

$$\begin{aligned} L(\mathbf{U},\mathbf{g},\boldsymbol{\lambda},\boldsymbol{\lambda}^0) &= J(\mathbf{U},g)+\int_{t_0}^{t_f}\int_{\Omega}\boldsymbol{\lambda}^T(\mathbf{U}(\boldsymbol{u})_t+\mathbf{F}_{i,i}-\mathbf{F}^v_{i,i})d\mathbf{x} \\ &\quad +\int_{\Omega}(\boldsymbol{\lambda}^0)^T(\mathbf{U}-\mathbf{U}_0)d\mathbf{x}. \end{aligned} \tag{A.2}$$

where inviscid flux $\mathbf{F}$, viscous flux $\mathbf{F}^v$ are defined in 2.

The final variational form becomes

$$\begin{aligned} L(\mathbf{U},\mathbf{g},\boldsymbol{\lambda},\boldsymbol{\lambda}^0) &= J'(\mathbf{U},g)+\int_{t_0}^{t_f}\int_{\Omega}\boldsymbol{\lambda}^T(\mathbf{U}'(\boldsymbol{u})_t+\mathbf{F}_{i,i}{}'-\mathbf{F}^v_{i,i}{}')d\mathbf{x} \\ &\quad +\int_{\Omega}(\boldsymbol{\lambda}^0)^T\mathbf{U}'d\mathbf{x}. \end{aligned} \tag{A.3}$$

We associate adjoint variables

$$\boldsymbol{\lambda}=\begin{pmatrix}\lambda_1\\ \lambda_2\\ \lambda_3\\ \lambda_4\end{pmatrix},$$

with the NS equations 2.4 or Euler equations 2.1.

Through the variation with $\mathbf{U}$ and $\mathbf{g}$ we will get the corresponding adjoint equation and gradient equation. From the equation formulation, especially the viscous flux term $\mathbf{F}^v$, the variation with primitive variables $\boldsymbol{u}$ will be easier for the derivation. To derive the adjoint equation, adjoint boundary condition and gradient equation, we use the variation of the primitive $\boldsymbol{u}$ for convenience, but in the end we write the adjoint equation based on the variation of conservative $\mathbf{U}$, which is consistent with the state discretization variable $\mathbf{U}$. It is very convenient to transform between $\boldsymbol{u}'$ and $\mathbf{U}'$ by using $\boldsymbol{u}'=\mathbf{M}^{-1}\mathbf{U}'$, where $\mathbf{M}$ is the Jacobian between $\boldsymbol{u}$ and $\mathbf{U}$.

Regarding the objective $J(\mathbf{U}, g)$, it is usually defined as

$$\widehat{J}(\mathbf{g}) = \frac{1}{2}\int_{\Omega_0} J_{t_f} d\mathbf{x} + \frac{1}{2}\int_{t_0}^{t_f}\int_{\Omega_0} J(t) d\mathbf{x} + \int_{t_0}^{t_f}\int_{\Gamma_c}\Big(\frac{\alpha_1}{2}\|\mathbf{g}_t\|_2^2 + \frac{\alpha_2}{2}\|\nabla\mathbf{g}\|_2^2 + \frac{\alpha_3}{2}\|\mathbf{g}\|_2^2\Big) d\mathbf{x}. \tag{A.4}$$

where $\alpha_1, \alpha_2, \alpha_3 > 0$. For the treatment of those penalty terms $\mathbf{g}_t$, $\nabla\mathbf{g}$ and $\mathbf{g}$, [37, 38] give very good discussion, which we will follow and discuss in other place.

For convenience, J is defined as

$$\widehat{J}(\mathbf{g}) = \frac{1}{2}\int_{t_0}^{t_f}\int_{\Omega_0} J(t) d\mathbf{x} + \int_{t_0}^{t_f}\int_{\Gamma_c}\frac{\alpha_3}{2}\|\mathbf{g}\|_2^2 d\mathbf{x}. \tag{A.5}$$

The variation form becomes

$$\delta L_{\mathbf{U}} = J' + \int_{t_0}^{t_f}\int_{\Omega} \boldsymbol{\lambda}^T(\mathbf{U}(\boldsymbol{u})'_t + \mathbf{F}_{i,i}{}' - \mathbf{F}^v_{i,i}{}') d\mathbf{x} + \int_{\Omega} \boldsymbol{\lambda}_0{}^T \mathbf{U}' d\mathbf{x} \tag{A.6}$$

$$\begin{aligned}
&\int_{\Omega} \boldsymbol{\lambda}^{0T}\mathbf{U}' d\mathbf{x} + \int_{t_0}^{t_f}\int_{\Omega} \boldsymbol{\lambda}^T(\mathbf{U}'_{,t} + \mathbf{F}_{i,i}{}' - \mathbf{F}^v_{i,i}{}') d\mathbf{x} \\
&= \int_{\Omega} \mathbf{U}'^T(\boldsymbol{\lambda}^0 - \boldsymbol{\lambda}|_{t_0}) d\mathbf{x} + \int_{\Omega} \mathbf{U}'^T \boldsymbol{\lambda}|_{t_f} d\mathbf{x} \\
&\quad - \int_{t_0}^{t_f}\int_{\Omega} \mathbf{U}'(\boldsymbol{\lambda}_{,t} + \mathbf{A}_1{}^T\boldsymbol{\lambda}_{,x} + \mathbf{A}_2{}^T\boldsymbol{\lambda}_{,y}) d\mathbf{x} \\
&\quad + \int_{t_0}^{t_f}\int_{\Omega} (\mathbf{F}_i^{vT\prime}\boldsymbol{\lambda}_{,x} + \mathbf{F}_2^{vT\prime}\boldsymbol{\lambda}_{,y}) d\mathbf{x} \\
&\quad + \int_{t_0}^{t_f}\int_{\Gamma} (n_1\mathbf{F}_1{}^{T\prime} + n_2\mathbf{F}_2{}^{T\prime})\boldsymbol{\lambda} d\mathbf{x} \\
&\quad - \int_{t_0}^{t_f}\int_{\Gamma} (n_1\mathbf{F}_1^{vT\prime} + n_2\mathbf{F}_2^{vT\prime})\boldsymbol{\lambda} d\mathbf{x}
\end{aligned} \tag{A.7}$$

where $\mathbf{A}_i = \frac{\partial \mathbf{F}}{\partial \mathbf{U}}$ as defined also in the following appendix.

To simplify A.7, the following terms are defined, respectively.

$$\boldsymbol{I}_1 = \int_{t_0}^{t_f}\int_{\Gamma}(n_1\mathbf{F}_1{}^{T'} + n_2\mathbf{F}_2{}^{T'})\boldsymbol{\lambda}d\mathbf{x}$$

$$\boldsymbol{I}_2 = \int_{t_0}^{t_f}\int_{\Omega}(\mathbf{F}_i^{vT'}\boldsymbol{\lambda}_{,x} + \mathbf{F}_2^{vT'}\boldsymbol{\lambda}_{,y})d\mathbf{x}$$

$$\boldsymbol{I}_3 = -\int_{t_0}^{t_f}\int_{\Gamma}(n_1\mathbf{F}_1^{vT'} + n_2\mathbf{F}_2^{vT'})\boldsymbol{\lambda}d\mathbf{x}$$

For $\boldsymbol{I}_1$,

$$\begin{aligned}
\boldsymbol{I}_1 &= \int_{t_0}^{t_f}\int_{\Gamma}(n_i\mathbf{F}_i{}^{T'})\boldsymbol{\lambda}d\mathbf{x} \\
&= \int_{t_0}^{t_f}\int_{\Gamma_\infty}(n_i\mathbf{F}_i{}^{T'})\boldsymbol{\lambda}d\mathbf{x} + \int_{t_0}^{t_f}\int_{\Gamma_c+\Gamma_s}(n_i\mathbf{F}_i{}^{T'})\boldsymbol{\lambda}d\mathbf{x} \\
&= \int_{t_0}^{t_f}\int_{\Gamma_\infty}\mathbf{U}^{T'}(n_i\mathbf{A}_i{}^{T}\boldsymbol{\lambda})d\mathbf{x} + \int_{t_0}^{t_f}\int_{\Gamma_c+\Gamma_s}(n_i\mathbf{F}_i{}^{T'})\boldsymbol{\lambda}d\mathbf{x} \qquad \text{(A.8)}
\end{aligned}$$

where Γ_∞ is the far field boundary, Γ_s is the solid wall(isoflux or isothermal), Γ_c is the control boundary, isoflux or isothermal wall.

Considering the boundary condition at the solid wall Γ_s where

$$\begin{aligned}
u_1 &= 0 \\
u_2 &= 0 \\
T &= T_0 \quad \text{or} \quad T_{,x_i}n_i = 0 \qquad \forall\Gamma_s \qquad \text{(A.9)}
\end{aligned}$$

and the control boundary condition

$$\begin{aligned}
V_s &= -u_1n_2 + u_2n_1 = 0 \\
V_n &= u_1n_1 + u_2n_2 \quad = \mathbf{g} \\
T &= T_0 \quad \text{or} \quad T_{,x_i}n_i = 0 \qquad \forall\Gamma_c \qquad \text{(A.10)}
\end{aligned}$$

so

$$\begin{aligned}
&\int_{t_0}^{t_f}\int_{\Gamma_c+\Gamma_s}(n_i{\mathbf{F}_i}^{T\prime})\boldsymbol{\lambda}d\mathbf{x}\\
&\quad=\int_{t_0}^{t_f}\int_{\Gamma_s}p'[0\quad n_1\quad n_2\quad 0]^T\boldsymbol{\lambda}d\mathbf{x}\\
&\qquad+\int_{t_0}^{t_f}\int_{\Gamma_c}\big(V_n[\rho\quad \rho u_1\quad \rho u_2\quad \rho E]^{T\prime}+{V_n}'[\rho\quad \rho u_1\quad \rho u_2\quad \rho E]^T\\
&\qquad\quad+p'[0\quad n_1\quad n_2\quad V_n]^T\big)\boldsymbol{\lambda}+p{V_n}'\lambda_4 d\mathbf{x}\\
&\quad=\int_{t_0}^{t_f}\int_{\Gamma_s}p'[0\quad n_1\quad n_2\quad 0]^T\boldsymbol{\lambda}d\mathbf{x}\\
&\qquad+\int_{t_0}^{t_f}\int_{\Gamma_c}\big(V_n\mathbf{U}^{T\prime}+{V_n}'\mathbf{U}^T+p'[0\quad n_1\quad n_2\quad V_n]^T\big)\boldsymbol{\lambda}+p{V_n}'\lambda_4 d\mathbf{x}\quad\text{(A.11)}
\end{aligned}$$

and

$$\begin{aligned}
\boldsymbol{I}_1\;=\;&\int_{t_0}^{t_f}\int_{\Gamma_\infty}(n_i{\mathbf{F}_i}'^T)\boldsymbol{\lambda}d\mathbf{x}\\
&+\int_{t_0}^{t_f}\int_{\Gamma_s}p'[0\quad n_1\quad n_2\quad 0]^T\boldsymbol{\lambda}d\mathbf{x}\\
&+\int_{t_0}^{t_f}\int_{\Gamma_c}\Big(V_n\mathbf{U}^{T\prime}+{V_n}'\mathbf{U}^T+p'[0\quad n_1\quad n_2\quad V_n]^T\Big)\boldsymbol{\lambda}+\rho{V_n}'\lambda_4 d\mathbf{x}\quad\text{(A.12)}
\end{aligned}$$

For $\boldsymbol{I}_2$

$$\boldsymbol{I}_2=\int_{t_0}^{t_f}\int_{\Omega}(\mathbf{F}_i^{vT\prime}\boldsymbol{\lambda}_{,x}+\mathbf{F}_2^{vT\prime}\boldsymbol{\lambda}_{,y})d\mathbf{x}\quad\text{(A.13)}$$

Taking advantage of the simplicity of viscous term using the primitive variable $\boldsymbol{u}$,

$$\mathbf{F}_1^{v\prime}=\mathbf{D}_1\boldsymbol{u}'+\mathbf{K}_1^1{\boldsymbol{u}_{x_1}}'+\mathbf{K}_2^1{\boldsymbol{u}_{x_2}}'\quad\text{(A.14)}$$

$$\mathbf{F}_2^{v\prime}=\mathbf{D}_2\boldsymbol{u}'+\mathbf{K}_1^2{\boldsymbol{u}_{x_1}}'+\mathbf{K}_2^2{\boldsymbol{u}_{x_2}}'\quad\text{(A.15)}$$

where $\mathbf{D}_i=\frac{\partial\mathbf{F}_i^v}{\partial\boldsymbol{u}}$ and $\mathbf{K}_j^i=\frac{\partial\mathbf{F}_i^v}{\partial\boldsymbol{u}_{x_j}}$.

$$\begin{aligned}
\boldsymbol{I}_2 &= \int_{t_0}^{t_f}\int_{\Omega}(\mathbf{F}_i^{vT\prime}\boldsymbol{\lambda}_{,x}+\mathbf{F}_2^{vT\prime}\boldsymbol{\lambda}_{,y})d\mathbf{x} \\
&= \int_{t_0}^{t_f}\int_{\Omega}\boldsymbol{u}^{T\prime}(\mathbf{D}_i{}^T\boldsymbol{\lambda}_{x_i})d\mathbf{x}+\int_{t_0}^{t_f}\int_{\Omega}(\mathbf{K}_j^i\boldsymbol{u}_{x_j}{}')^T\boldsymbol{\lambda}_{x_i}d\mathbf{x} \\
&= \int_{t_0}^{t_f}\int_{\Omega}\boldsymbol{u}^{T\prime}(\mathbf{D}_i{}^T\boldsymbol{\lambda}_{x_i})d\mathbf{x}-\int_{t_0}^{t_f}\int_{\Omega}\boldsymbol{u}^{T\prime}(\mathbf{K}_j^{i\,T}\boldsymbol{\lambda}_{x_i})_{x_j}d\mathbf{x} \\
&+ \int_{t_0}^{t_f}\int_{\Gamma}\boldsymbol{u}^{T\prime}(n_j\mathbf{K}_j^{i\,T}\boldsymbol{\lambda}_{x_i})d\mathbf{x} \qquad \text{(A.16)}
\end{aligned}$$

where

$$(\mathbf{K}_j^i\boldsymbol{u}_{x_j}{}')^T\boldsymbol{\lambda}_{x_i}=(\boldsymbol{u}^{T\prime}\mathbf{K}_j^{i\,T}\boldsymbol{\lambda}_{x_i})_{,x_j}-\boldsymbol{u}^{T\prime}(\mathbf{K}_j^{i\,T}\boldsymbol{\lambda}_{x_i})_{x_j}$$

For $\boldsymbol{I}_3$,

$$\begin{aligned}
\boldsymbol{I}_3 &= -\int_{t_0}^{t_f}\int_{\Gamma}(n_1\mathbf{F}_1^{vT\prime}+n_2\mathbf{F}_2^{vT\prime})\boldsymbol{\lambda}d\mathbf{x} \\
&= -\int_{t_0}^{t_f}\int_{\Gamma}\left(\boldsymbol{u}^{T\prime}n_i\mathbf{D}_i^T+\boldsymbol{u}_{x_j}^{T}{}'n_i\mathbf{K}_j^{i\,T}\right)\boldsymbol{\lambda}d\mathbf{x} \qquad \text{(A.17)}
\end{aligned}$$

Considering A.12, A.16 and A.17,

$$\begin{aligned}
&\int_{\Omega}\mathbf{U}'^T\boldsymbol{\lambda}^0d\mathbf{x}+\int_{t_0}^{t_f}\int_{\Omega}\boldsymbol{\lambda}^T(\mathbf{U}'_{,t}+\mathbf{F}_{i,i}{}'-\mathbf{F}_{,i}^{v}{}')d\mathbf{x} \\
&\quad=\int_{\Omega}\mathbf{U}'^T(\boldsymbol{\lambda}^0-\boldsymbol{\lambda}|_{t_0})d\mathbf{x}+\int_{\Omega}\mathbf{U}'^T\boldsymbol{\lambda}|_{t_f}d\mathbf{x} \\
&\quad-\int_{t_0}^{t_f}\int_{\Omega}\mathbf{U}^{T\prime}(\boldsymbol{\lambda}_{,t}+\mathbf{A}_i{}^T\boldsymbol{\lambda}_{x_i})d\mathbf{x}+\int_{t_0}^{t_f}\int_{\Omega}\boldsymbol{u}'^T[(\mathbf{D}_i{}^T\boldsymbol{\lambda}_{x_i})-[\mathbf{K}_j^{i\,T}\boldsymbol{\lambda}_{x_i}]_{x_j}]d\mathbf{x} \\
&\quad+\int_{t_0}^{t_f}\int_{\Gamma_\infty}(n_i\mathbf{F}_i{}^{T\prime})\boldsymbol{\lambda}d\mathbf{x}+\int_{t_0}^{t_f}\int_{\Gamma_s}p'[0\quad n_1\quad n_2\quad 0]^T\boldsymbol{\lambda}d\mathbf{x} \\
&\quad+\int_{t_0}^{t_f}\int_{\Gamma_c}\left(V_n\mathbf{U}'^T+V_n{}'\mathbf{U}^T+p'[0\quad n_1\quad n_2\quad V_n]^T\right)\boldsymbol{\lambda}+\rho V_n{}'\lambda_4d\mathbf{x} \\
&\quad+\int_{t_0}^{t_f}\int_{\Gamma_c+\Gamma_s}\boldsymbol{u}'^T\left(n_j\mathbf{K}_j^{i\,T}\boldsymbol{\lambda}_{x_i}\right)d\mathbf{x} \\
&\quad-\int_{t_0}^{t_f}\int_{\Gamma_c+\Gamma_s}\left(\boldsymbol{u}'^Tn_i\mathbf{D}_i^T+\boldsymbol{u}_{x_j}^{T}{}'n_i\mathbf{K}_j^{i\,T}\right)\boldsymbol{\lambda}d\mathbf{x} \qquad \text{(A.18)}
\end{aligned}$$

For the volume integra at Ω, from

$$\int_{\Omega} \mathbf{U}'^{T}(\boldsymbol{\lambda}^{0} - \boldsymbol{\lambda}|_{t_0})d\mathbf{x}$$

we get the adjoint final compatibility relation $\boldsymbol{\lambda}^{0} - \boldsymbol{\lambda}|_{t_0}$, and our adjoint initial condition $\boldsymbol{\lambda}|_{t_f}$, which is also be dependent on the variation of J.

Considering $\mathbf{U}' = \mathbf{M}\boldsymbol{u}'$, which leads to $\boldsymbol{u}'^{T} = \mathbf{U}'^{T}\mathbf{M}^{-T}$, the adjoint equation becomes

$$\begin{aligned} &-\int_{t_0}^{t_f}\int_{\Omega} \mathbf{U}^{T\prime}(\boldsymbol{\lambda}_{,t} + \mathbf{A}_i{}^{T}\boldsymbol{\lambda}_{x_i})d\mathbf{x} + \int_{t_0}^{t_f}\int_{\Omega} \boldsymbol{u}^{T\prime}\left((\mathbf{D}_i{}^{T}\boldsymbol{\lambda}_{x_i}) - (\mathbf{K}_j^{i\,T}\boldsymbol{\lambda}_{x_i})_{x_j}\right)d\mathbf{x} \\ &\quad = -\int_{t_0}^{t_f}\int_{\Omega} \mathbf{U}^{T\prime}\left(\boldsymbol{\lambda}_{,t} + \mathbf{A}_i{}^{T}\boldsymbol{\lambda}_{x_i} + \mathbf{M}^{-T}(-\mathbf{D}_i{}^{T}\boldsymbol{\lambda}_{x_i} + (\mathbf{K}_j^{i\,T}\boldsymbol{\lambda}_{x_i})_{x_j})\right)d\mathbf{x} \end{aligned} \tag{A.19}$$

The adjoint equation becomes

$$-\boldsymbol{\lambda}_{,t} - \mathbf{A}_i{}^{T}\boldsymbol{\lambda}_{x_i} - \mathbf{M}^{-T}(-\mathbf{D}_i{}^{T}\boldsymbol{\lambda}_{x_i} + (\mathbf{K}_j^{i\,T}\boldsymbol{\lambda}_{x_i})_{x_j}) = \mathbf{S} \tag{A.20}$$

The boundary terms

$$\begin{aligned}
\boldsymbol{I}_B &= \int_{t_0}^{t_f}\int_{\Gamma_\infty}(n_i\mathbf{F}_i{}^{T\prime})\boldsymbol{\lambda}d\mathbf{x} \\
&\quad + \int_{t_0}^{t_f}\int_{\Gamma_s} p'[0 \quad n_1 \quad n_2 \quad 0]^T\boldsymbol{\lambda}d\mathbf{x} \\
&\quad + \int_{t_0}^{t_f}\int_{\Gamma_c}\left(V_n\mathbf{U}^{T\prime} + V_n{}'\mathbf{U}^T + p'[0 \quad n_1 \quad n_2 \quad V_n]^T\right)\boldsymbol{\lambda} + pV_n{}'\lambda_4 d\mathbf{x} \\
&\quad + \int_{t_0}^{t_f}\int_{\Gamma}\boldsymbol{u}^{T\prime}(n_j\mathbf{K}_j^{i\,T}\boldsymbol{\lambda}_{x_i})d\mathbf{x} - \int_{t_0}^{t_f}\int_{\Gamma}\left(\boldsymbol{u}^{T\prime}n_i\mathbf{D}_i^T + \boldsymbol{u}_{x_j}^{T\,\prime}n_i\mathbf{K}_j^{i\,T}\right)\boldsymbol{\lambda}d\mathbf{x} \\
&= \int_{t_0}^{t_f}\int_{\Gamma_\infty}(n_i\mathbf{F}_i{}^{T\prime})\boldsymbol{\lambda}d\mathbf{x} \\
&\quad + \int_{t_0}^{t_f}\int_{\Gamma_s} p'[0 \quad n_1 \quad n_2 \quad 0]^T\boldsymbol{\lambda}d\mathbf{x} \\
&\quad + \int_{t_0}^{t_f}\int_{\Gamma_c}\left(V_n\mathbf{U}^{T\prime} + V_n{}'\mathbf{U}^T + p'[0 \quad n_1 \quad n_2 \quad V_n]^T\right)\boldsymbol{\lambda} + pV_n{}'\lambda_4 d\mathbf{x} \\
&\quad + \int_{t_0}^{t_f}\int_{\Gamma}\boldsymbol{u}^{T\prime}\left(n_j\mathbf{K}_j^{i\,T}\boldsymbol{\lambda}_{x_i} - n_i\mathbf{D}_i^T\right)\boldsymbol{\lambda} + \boldsymbol{u}_{x_j}^{T\,\prime}n_i\mathbf{K}_j^{i\,T}\boldsymbol{\lambda}d\mathbf{x} \\
&= \boldsymbol{I}_\infty + \boldsymbol{I}_c + \boldsymbol{I}_v
\end{aligned} \tag{A.21}$$

Assume that there is no viscous effect in the far field as in [108], which is reasonable, so the $\Gamma = \Gamma_c + \Gamma_s$ for the viscous boundary integral.

Define

$$\boldsymbol{I}_\infty = \int_{t_0}^{t_f}\int_{\Gamma_\infty}(n_i\mathbf{F}_i{}^{T\prime})\boldsymbol{\lambda}d\mathbf{x} \tag{A.22}$$

$$\begin{aligned}
\boldsymbol{I}_c &= \int_{t_0}^{t_f}\int_{\Gamma_s} p'[0 \quad n_1 \quad n_2 \quad 0]^T\boldsymbol{\lambda}d\mathbf{x} \\
&\quad + \int_{t_0}^{t_f}\int_{\Gamma_c}\left(V_n\mathbf{U}^{T\prime} + V_n{}'\mathbf{U}^T + p'[0 \quad n_1 \quad n_2 \quad V_n]^T\right)\boldsymbol{\lambda} + pV_n{}'\lambda_4 d\mathbf{x} \\
&= \int_{t_0}^{t_f}\int_{\Gamma_c} V_n{}'(\mathbf{U}^T\boldsymbol{\lambda} + p\lambda_4)d\mathbf{x} + \int_{t_0}^{t_f}\int_{\Gamma_s} p'(n_1\lambda_2 + n_2\lambda_3)d\mathbf{x} \\
&\quad + \int_{t_0}^{t_f}\int_{\Gamma_c} V_n\mathbf{U}'^T\boldsymbol{\lambda} + p'(n_1\lambda_2 + n_2\lambda_3 + V_n\lambda_4)d\mathbf{x}
\end{aligned} \tag{A.23}$$

Introduce

$$V_s = -u_1 n_2 + u_2 n_1$$

$$V_n = u_1 n_1 + u_2 n_2$$

we get

$$u_1 = V_n n_1 - V_s n_2$$

$$u_2 = V_n n_2 + V_s n_1$$

where the outward normal vector $\vec{n} = (n_1, n_2)$ and tangential vector $\vec{s} = (-n_2, n_1)$.

$$\begin{aligned}
V_n \mathbf{U}'^T \boldsymbol{\lambda} &= V_n \boldsymbol{u}'^T \mathbf{M}^T \boldsymbol{\lambda} \\
&= V_n \begin{pmatrix} \rho' \\ -n_2 {V_s}' + n_1 {V_n}' \\ n_1 {V_s}' + n_2 {V_n}' \\ T' \end{pmatrix}^T \begin{pmatrix} \lambda_1 + \lambda_2 u_1 + \lambda_3 u_2 + \lambda_4 E \\ \rho\lambda_2 + \rho u_1 \lambda_4 \\ \rho\lambda_3 + \rho u_2 \lambda_4 \\ \frac{\rho\lambda_4}{\gamma(\gamma-1)} \end{pmatrix} \\
&= V_n \begin{pmatrix} 0 \\ -n_2 {V_s}' + n_1 {V_n}' \\ n_1 {V_s}' + n_2 {V_n}' \\ 0 \end{pmatrix}^T \begin{pmatrix} \lambda_1 + \lambda_2 u_1 + \lambda_3 u_2 + \lambda_4 E \\ \rho\lambda_2 + \rho u_1 \lambda_4 \\ \rho\lambda_3 + \rho u_2 \lambda_4 \\ \frac{\rho\lambda_4}{\gamma(\gamma-1)} \end{pmatrix} \\
&\quad + V_n \begin{pmatrix} \rho' \\ 0 \\ 0 \\ T' \end{pmatrix}^T \begin{pmatrix} \lambda_1 + \lambda_2 u_1 + \lambda_3 u_2 + \lambda_4 E \\ \rho\lambda_2 + \rho u_1 \lambda_4 \\ \rho\lambda_3 + \rho u_2 \lambda_4 \\ \frac{\rho\lambda_4}{\gamma(\gamma-1)} \end{pmatrix}
\end{aligned} \tag{A.24}$$

where $E = \frac{T}{\gamma(\gamma-1)} + \frac{1}{2}({u_1}^2 + {u_2}^2)$.

Consider

$$\mathbf{U}^T \boldsymbol{\lambda} = \rho\lambda_1 + \rho V_s \lambda_s + \rho V_n \lambda_n + \rho E \lambda_4 \qquad \forall \Gamma_c$$

So

$$\begin{aligned}
\boldsymbol{I}_c &= \int_{t_0}^{t_f}\int_{\Gamma_c} V_n{}'(\mathbf{U}^T\boldsymbol{\lambda} + p\lambda_4)d\mathbf{x} + \int_{t_0}^{t_f}\int_{\Gamma_s} p'(n_1\lambda_2 + n_2\lambda_3)d\mathbf{x} \\
&\quad + \int_{t_0}^{t_f}\int_{\Gamma_c} V_n\mathbf{U}^{T'}\boldsymbol{\lambda} + p'(n_1\lambda_2 + n_2\lambda_3 + V_n\lambda_4)d\mathbf{x} \\
&= \int_{t_0}^{t_f}\int_{\Gamma_c} V_n{}'(\rho\lambda_1 + \rho V_s\lambda_s + 2\rho V_n\lambda_n + (p + \rho E + \rho {V_n}^2)\lambda_4)d\mathbf{x} \\
&\quad + \int_{t_0}^{t_f}\int_{\Gamma_c} V_s{}'(\rho V_s V_n\lambda_4 + \rho V_n\lambda_s)d\mathbf{x} + \int_{t_0}^{t_f}\int_{\Gamma_s} p'(n_1\lambda_2 + n_2\lambda_3)d\mathbf{x} \\
&\quad + \int_{t_0}^{t_f}\int_{\Gamma_c} p'(n_1\lambda_2 + n_2\lambda_3 + V_n\lambda_4)d\mathbf{x} \\
&\quad + \int_{t_0}^{t_f}\int_{\Gamma_c} \rho'(\lambda_1 + \lambda_2 u_1 + \lambda_3 u_2 + \lambda_4 E)V_n d\mathbf{x} \\
&\quad + \int_{t_0}^{t_f}\int_{\Gamma_c} T'\frac{\rho\lambda_4}{\gamma(\gamma-1)}V_n d\mathbf{x}
\end{aligned} \tag{A.25}$$

For convenience, here we use the simple objective functional with its variation as

$$\widehat{J}'(\mathbf{U},\mathbf{g}) = \int_{t_0}^{t_f}\int_{\Omega} \mathbf{U}'^T\mathbf{r}d\mathbf{x} + \int_{t_0}^{t_f}\int_{\Gamma_c} \mathbf{g}'\alpha_3\mathbf{g}d\mathbf{x} \tag{A.26}$$

A.1.1 Adjoint Equation and Boundary Condition for Euler

If ignoring the viscous terms $\mathbf{F}^v$, from A.20 we obtain

$$-\boldsymbol{\lambda}_{,t} - {\mathbf{A}_i}^T\boldsymbol{\lambda}_{x_i} = \mathbf{S} \tag{A.27}$$

From the Lagrangian A.3, cost functional A.26 and the convective boundary A.25,

we get

$$
\begin{aligned}
L'(\mathbf{U}, g, \boldsymbol{\lambda}, \boldsymbol{\lambda}^0) \;=\; & \int_\Omega \mathbf{U}'^T(\boldsymbol{\lambda}_0 - \boldsymbol{\lambda}|_{t_0})d\mathbf{x} + \int_\Omega \mathbf{U}'^T\boldsymbol{\lambda}|_{t_f}d\mathbf{x} \\
& + \int_{t_0}^{t_f}\int_\Omega \mathbf{U}^{T\prime} - \boldsymbol{\lambda}_{,t} - \mathbf{A}_i{}^T\boldsymbol{\lambda}_{x_i} + \mathbf{r}d\mathbf{x} \\
& + \int_{t_0}^{t_f}\int_{\Gamma_c} (\mathbf{g}'\alpha_3\mathbf{g})d\mathbf{x} \\
& + \int_{t_0}^{t_f}\int_{\Gamma_\infty} (n_i\mathbf{F}_i{}^{T\prime})\boldsymbol{\lambda}d\mathbf{x} \\
& + \int_{t_0}^{t_f}\int_{\Gamma_c} V_n'(\rho\lambda_1 + \rho V_s\lambda_s + 2\rho V_n\lambda_n \\
& \qquad + (p + \rho E + \rho V_n^2)\lambda_4)dx \\
& + \int_{t_0}^{t_f}\int_{\Gamma_c} V_s'(\rho\lambda_4 V_s V_n + \rho V_n\lambda_s)dx \\
& + \int_{t_0}^{t_f}\int_{\Gamma_s} p'(n_1\lambda_2 + n_2\lambda_3)d\mathbf{x} \\
& + \int_{t_0}^{t_f}\int_{\Gamma_c} p'(n_1\lambda_2 + n_2\lambda_3 + V_n\lambda_4)d\mathbf{x} \\
& + \int_{t_0}^{t_f}\int_{\Gamma_c} \rho'(\lambda_1 + \lambda_2 u_1 + \lambda_3 u_2 + \lambda_4 E)V_n d\mathbf{x} \\
& + \int_{t_0}^{t_f}\int_{\Gamma_c} T'\frac{\rho\lambda_4}{\gamma(\gamma-1)}V_n d\mathbf{x}
\end{aligned}
$$

Gradient

Assuming the control is the normal velocity V_n at the boundary Γ_c, with only contribution from regularization term in A.26, the gradient equation with-regard-to V_n is

$$
\begin{aligned}
\nabla J \;=\; & \alpha_3\mathbf{g} \\
& + (\rho\lambda_1 + \rho V_s\lambda_s + 2\rho V_n\lambda_n + (p + \rho E + \rho V_n^2)\lambda_4)
\end{aligned} \tag{A.28}
$$

Inviscid Solid Wall

For the adjoint wall boundary condition, because we only have one physical constraint, normal velocity $V_n = 0$, all other constraints, such as $V_s, \quad p, \quad \rho, \quad T$, are loose. We get the following adjoint wall boundary condition from p' at the wall Γ_s,

$$\lambda_n = n_1\lambda_2 + n_2\lambda_3 = 0 \tag{A.29}$$

Blowing/Suction on the Inviscid Wall

With regarding to subsonic boundary blowing and suction on the control boundary, we treat them as the inflow boundary for the blowing, outflow boundary for the suction as in [34,35]. According to the characteristic relationship for the Euler equation [57], three physical boundaries is required for the subsonic inflow boundary(blowing) and one physical boundary condition required for the outflow boundary(suction). 6.1 gives a successful case which is built on the linear characteristic boundary implementation due to its linear nature of that acoustics problem. However, We still have difficulty in finding the suitable physics constraints to make our optimization procedures stable using the boundary blowing/suction, which becomes our future research direction.

A.1.2 Adjoint Equation and Boundary Condition for Navier–Stokes

Assume no viscous effect at far field boundary Γ_∞, we focus on the viscous boundary derivation.

Introduce natural coordinate system (s, n) and

$$\lambda_s = -n_2\lambda_2 + n_1\lambda_3$$
$$\lambda_n = n_1\lambda_2 + n_2\lambda_3$$
$$\lambda_{s,s} = -n_2\lambda_{s,x_1} + n_1\lambda_{s,x_2}$$
$$\lambda_{s,n} = n_1\lambda_{s,x_1} + n_2\lambda_{s,x_2}$$
$$\lambda_{n,s} = -n_2\lambda_{n,x_1} + n_1\lambda_{n,x_2}$$
$$\lambda_{n,n} = n_1\lambda_{n,x_1} + n_2\lambda_{n,x_2}$$
$$\lambda_{4,s} = -n_2\lambda_{4,x_1} + n_1\lambda_{4,x_2}$$
$$\lambda_{4,n} = n_1\lambda_{4,x_1} + n_2\lambda_{4,x_2}$$
$$\tau_{sn} = \tau_{21}n_1^2 + \tau_{22}n_1n_2 - \tau_{11}n_1n_2 - \tau_{12}n_2^2$$
$$\tau_{nn} = \tau_{11}n_1^2 + \tau_{12}n_1n_2 + \tau_{21}n_1n_2 + \tau_{22}n_2^2$$

we get

$$
\begin{aligned}
L'(\mathbf{U}, g, \ \boldsymbol{\lambda}, \ \boldsymbol{\lambda}^0) &= \int_\Omega \mathbf{U'}^T(\boldsymbol{\lambda}_0 - \boldsymbol{\lambda}|_{t_0})d\mathbf{x} + \int_\Omega \mathbf{U'}^T\boldsymbol{\lambda}|_{t_f}d\mathbf{x} \\
&+ \int_{t_0}^{t_f}\int_\Omega \mathbf{U}^{T\prime} - \boldsymbol{\lambda}_{,t} - \mathbf{A}_i{}^T\boldsymbol{\lambda}_{x_i} - \mathbf{M}^{-T}(-\mathbf{D}_i{}^T\boldsymbol{\lambda}_{x_i} + \mathbf{K}_j^{iT}\boldsymbol{\lambda}_{x_{i_{x_j}}}) + \mathbf{r}d\mathbf{x} \\
&+ \int_{t_0}^{t_f}\int_{\Gamma_c}(\mathbf{g}'\mathbf{g})d\mathbf{x} + \int_{t_0}^{t_f}\int_{\Gamma_\infty}(n_i\mathbf{F}_i{}^{T\prime})\boldsymbol{\lambda}d\mathbf{x} \\
&+ \int_{t_0}^{t_f}\int_{\Gamma_c} V_n'(\rho\lambda_1 + \rho V_s\lambda_s + 2\rho V_n\lambda_n + (p + \rho E + \rho V_n^2)\lambda_4)dx \\
&+ \int_{t_0}^{t_f}\int_{\Gamma_c+\Gamma_s} V_n'\frac{1}{Re}(\lambda(\frac{\partial\lambda_s}{\partial s} - \frac{\lambda_n}{R} + V_s\frac{\partial\lambda_4}{\partial s}) \\
&\quad +(\lambda+2\mu)(\frac{\partial\lambda_n}{\partial n} + V_n\frac{\partial\lambda_4}{\partial n}) - \tau_{nn}\lambda_4)dx \\
&+ \int_{t_0}^{t_f}\int_{\Gamma_c+\Gamma_s} V_n'\frac{1}{Re}(\frac{\lambda}{R}(\lambda_n + V_n\lambda_4))dx \\
&+ \int_{t_0}^{t_f}\int_{\Gamma_c} V_s'(\rho\lambda_4 V_s V_n + \rho V_n\lambda_s)dx \\
&+ \int_{t_0}^{t_f}\int_{\Gamma_c+\Gamma_s} V_s'\frac{1}{Re}\mu(\frac{\partial\lambda_n}{\partial s} + \frac{\partial\lambda_s}{\partial n} + \frac{\lambda_s}{R} \\
&\quad +V_n\frac{\partial\lambda_4}{\partial s} + V_s\frac{\partial\lambda_4}{\partial n} - \frac{\tau_{sn}}{\mu}\lambda_4)dx \\
&+ \int_{t_0}^{t_f}\int_{\Gamma_c+\Gamma_s} V_s'\frac{1}{Re}\frac{-\mu}{R}(\lambda_s + V_s\lambda_4)dx \\
&+ \int_{t_0}^{t_f}\int_{\Gamma_c+\Gamma_s} \frac{\partial V_n'}{\partial s}\frac{-\mu}{Re}(\lambda_s + V_s\lambda_4)dx \\
&+ \int_{t_0}^{t_f}\int_{\Gamma_c+\Gamma_s} \frac{\partial V_n'}{\partial n}\frac{-(2\mu+\lambda)}{Re}(\lambda_n + V_n\lambda_4)dx \\
&+ \int_{t_0}^{t_f}\int_{\Gamma_c+\Gamma_s} \frac{\partial V_s'}{\partial s}\frac{-\lambda}{Re}(\lambda_n + V_n\lambda_4)dx \\
&+ \int_{t_0}^{t_f}\int_{\Gamma_c+\Gamma_s} \frac{\partial V_s'}{\partial n}\frac{-\mu}{Re}(\lambda_s + V_s\lambda_4)dx \\
&+ \int_{t_0}^{t_f}\int_{\Gamma_c} \rho'(V_n(\lambda_1 + V_s\lambda_s + V_n\lambda_n + \lambda_4 E) + \frac{T}{\gamma}(\lambda_n + V_n\lambda_4)dx \\
&+ \int_{t_0}^{t_f}\int_{\Gamma_s} \rho'\frac{T}{\gamma}\lambda_n dx \\
&+ \int_{t_0}^{t_f}\int_{\Gamma_c} T'(V_n\frac{\rho\lambda_4}{\gamma(\gamma-1)} + \frac{k}{RePr(\gamma-1)}\frac{\partial\lambda_4}{\partial n} + \frac{\rho}{\gamma}(\lambda_n + V_n\lambda_4))dx \\
&+ \int_{t_0}^{t_f}\int_{\Gamma_s} T'(\frac{k}{RePr(\gamma-1)}\frac{\partial\lambda_4}{\partial n} + \frac{\rho}{\gamma}\lambda_n)dx \\
&+ \int_{t_0}^{t_f}\int_{\Gamma_c+\Gamma_s} \frac{\partial T'}{\partial n}\frac{-k\lambda_4}{RePr(\gamma-1)}dx
\end{aligned}
$$

So we get our adjoint initial condition

$$\boldsymbol{\lambda}|_{t_f} = 0 \tag{A.30}$$

adjoint equation

$$-\boldsymbol{\lambda}_{,t} - \mathbf{A}_i{}^T \boldsymbol{\lambda}_{x_i} - \mathbf{M}^{-T}(-\mathbf{D}_i{}^T \boldsymbol{\lambda}_{x_i} + \mathbf{K}_j^{i\,T} \boldsymbol{\lambda}_{x_i x_j}) + \mathbf{r} = 0 \tag{A.31}$$

Next we will consider different control condition and application.

Blowing/suction on the adiabatic wall

Our control is V_n at the wall Γ_c, and the $T_{,n} = 0$ at the wall $\Gamma_c + \Gamma_s$. So we have the following constraints

$$\begin{aligned}
V_n' &= 0 \quad \text{at} \quad \Gamma_s \\
V_s' &= 0 \quad \text{at} \quad \Gamma_c + \Gamma_s \\
\frac{\partial V_n{}'}{\partial s} &= 0 \quad \text{at} \quad \Gamma_s \\
\frac{\partial V_s{}'}{\partial s} &= 0 \quad \text{at} \quad \Gamma_c + \Gamma_s \\
\frac{\partial T'}{\partial n} &= 0 \quad \text{at} \quad \Gamma_c + \Gamma_s
\end{aligned}$$

and those terms will be unconstrained,

$$\begin{aligned}
V_n' &\quad \text{at} \quad \Gamma_c \\
\frac{\partial V_n{}'}{\partial s} &\quad \text{at} \quad \Gamma_c \\
\frac{\partial V_n{}'}{\partial n} &\quad \text{at} \quad \Gamma_c + \Gamma_s \\
\frac{\partial V_s{}'}{\partial n} &\quad \text{at} \quad \Gamma_c + \Gamma_s \\
\rho' &\quad \text{at} \quad \Gamma_c \\
T' &\quad \text{at} \quad \Gamma_c + \Gamma_s
\end{aligned}$$

so we get

$$\begin{aligned}
\frac{-\mu}{Re}(\lambda_s + V_s\lambda_4)) &= 0 \quad \text{at} \quad \Gamma_c \\
\frac{-(2\mu+\lambda)}{Re}(\lambda_n + V_n\lambda_4)) &= 0 \quad \text{at} \quad \Gamma_c + \Gamma_s \\
\frac{-\mu}{Re}(\lambda_s + V_s\lambda_4)) &= 0 \quad \text{at} \quad \Gamma_c + \Gamma_s \\
V_n(\lambda_1 + V_s\lambda_s + V_n\lambda_n + \lambda_4 E) &= 0 \quad \text{at} \quad \Gamma_c \\
V_n\frac{\rho\lambda_4}{\gamma(\gamma-1)} + \frac{\kappa}{RePr(\gamma-1)}\frac{\partial\lambda_4}{\partial n} &= 0 \quad \text{at} \quad \Gamma_c \\
\frac{\kappa}{RePr(\gamma-1)}\frac{\partial\lambda_4}{\partial n} &= 0 \quad \text{at} \quad \Gamma_s
\end{aligned}$$

here we exclude those terms V_n', which is related with the gradient equation.

The adjoint boundary conditions at the solid wall Γ_s become

$$\begin{aligned}
\lambda_s + V_s\lambda_4 &= 0 \\
\lambda_n + V_n\lambda_4 &= 0 \\
\lambda_n &= 0 \\
\frac{\partial\lambda_4}{\partial n} &= 0 \quad \text{at} \quad \Gamma_s
\end{aligned}$$

At the control boundary Γ_c,

$$\begin{aligned}
\lambda_s + V_s\lambda_4 &= 0 \\
\lambda_n + V_n\lambda_4 &= 0 \\
(\lambda_1 + V_s\lambda_s + V_n\lambda_n + \lambda_4 E) &= 0 \\
V_n\frac{\rho\lambda_4}{\gamma} + \frac{\kappa}{RePr}\frac{\partial\lambda_4}{\partial n} &= 0 \quad \text{at} \quad \Gamma_c
\end{aligned}$$

With all those V_n' plus from the J', we get our gradient equation

$$\begin{aligned}
\nabla J &= \frac{\alpha_3}{2}\mathbf{g} \\
&\quad +(\rho\lambda_1 + \rho V_s\lambda_s + 2\rho V_n\lambda_n + (p + \rho E + \rho V_n^2)\lambda_4) \\
&\quad +\frac{1}{Re}(\lambda(\frac{\partial\lambda_s}{\partial s} - \frac{\lambda_n}{R} + V_s\frac{\partial\lambda_4}{\partial s}) + (\lambda + 2\mu)(\frac{\partial\lambda_n}{\partial n} + V_n\frac{\partial\lambda_4}{\partial n}) - \tau_{nn}\lambda_4) \\
&\quad +\frac{1}{Re}(\frac{\lambda}{R}(\lambda_n + V_n\lambda_4)) \\
&= \frac{\alpha_3}{2}\mathbf{g} \\
&\quad +(\rho\lambda_1 + \rho V_s\lambda_s + 2\rho V_n\lambda_n + (p + \rho E + \rho V_n^2)\lambda_4) \\
&\quad +\frac{1}{Re}(\lambda(\frac{\partial\lambda_s}{\partial s} - \frac{\lambda_n}{R} + V_s\frac{\partial\lambda_4}{\partial s}) \\
&\qquad +(\lambda + 2\mu)(\frac{\partial\lambda_n}{\partial n} + V_n\frac{\partial\lambda_4}{\partial n}) - \tau_{nn}\lambda_4) \qquad \text{(A.32)}
\end{aligned}$$

considering $\frac{\lambda}{R}(\lambda_n + V_n\lambda_4) = 0 \quad \text{at} \quad \Gamma_c$.

Blowing/suction on the isothermal wall

Our control is V_n at the wall Γ_c, and the $T = T_0$ at the wall $\Gamma_c + \Gamma_s$. So we have the following constraints

$$\begin{aligned} V_n' &= 0 \quad \text{at} \quad \Gamma_s \\ V_s' &= 0 \quad \text{at} \quad \Gamma_c + \Gamma_s \\ \frac{\partial {V_n}'}{\partial s} &= 0 \quad \text{at} \quad \Gamma_s \\ \frac{\partial {V_s}'}{\partial s} &= 0 \quad \text{at} \quad \Gamma_c + \Gamma_s \\ T' &= 0 \quad \text{at} \quad \Gamma_c + \Gamma_s \end{aligned}$$

and those terms will be unconstrained,

$$\begin{aligned} V_n' &\quad \text{at} \quad \Gamma_c \\ \frac{\partial {V_n}'}{\partial s} &\quad \text{at} \quad \Gamma_c \\ \frac{\partial {V_n}'}{\partial n} &\quad \text{at} \quad \Gamma_c + \Gamma_s \\ \frac{\partial {V_s}'}{\partial n} &\quad \text{at} \quad \Gamma_c + \Gamma_s \\ \rho' &\quad \text{at} \quad \Gamma_c \\ \frac{\partial T'}{\partial n} &\quad \text{at} \quad \Gamma_c + \Gamma_s \end{aligned}$$

so we get

$$\begin{aligned}
\frac{-\mu}{Re}(\lambda_s + V_s\lambda_4)) &= 0 \quad \text{at} \quad \Gamma_c \\
\frac{-(\mu+\lambda)}{Re}(\lambda_n + V_n\lambda_4)) &= 0 \quad \text{at} \quad \Gamma_c + \Gamma_s \\
\frac{-\mu}{Re}(\lambda_s + V_s\lambda_4)) &= 0 \quad \text{at} \quad \Gamma_c + \Gamma_s \\
V_n(\lambda_1 + V_s\lambda_s + V_n\lambda_n + \lambda_4 E) &= 0 \quad \text{at} \quad \Gamma_c \\
V_n\frac{\rho\lambda_4}{\gamma(\gamma-1)} + (\lambda_n + V_n\lambda_4)\frac{\rho}{\gamma} + \frac{\kappa}{RePr(\gamma-1)}\frac{\partial\lambda_4}{\partial n} &= 0 \quad \text{at} \quad \Gamma_c \\
\frac{\kappa}{RePr(\gamma-1)}\frac{\partial\lambda_4}{\partial n} + \frac{\rho}{\gamma}\lambda_n &= 0 \quad \text{at} \quad \Gamma_s \\
\frac{-\kappa\lambda_4}{RePr(\gamma-1)} &= 0 \quad \text{at} \quad \Gamma_s + \Gamma_c
\end{aligned}$$

here we exclude those terms V_n', which will be come our gradient.

Eventually we get our adjoint boundary conditions, at the solid wall Γ_s

$$\begin{aligned}
\lambda_s + V_s\lambda_4 &= 0 \\
\lambda_n + V_n\lambda_4 &= 0 \\
\lambda_4 &= 0 \quad \text{at} \quad \Gamma_s
\end{aligned}$$

at the control boundary Γ_c

$$\begin{aligned}
\lambda_s + V_s\lambda_4 &= 0 \\
\lambda_n + V_n\lambda_4 &= 0 \\
(\lambda_1 + V_s\lambda_s + V_n\lambda_n + \lambda_4 E) &= 0 \\
\lambda_4 &= 0 \quad \text{at} \quad \Gamma_c
\end{aligned}$$

With all those V_n' plus from the J', we get our gradient equation

$$\begin{aligned}
\nabla J &= \frac{\alpha_3}{2}\mathbf{g} \\
&\quad +(\rho\lambda_1 + \rho V_s\lambda_s + 2\rho V_n\lambda_n + (p + \rho E + \rho V_n^2)\lambda_4) \\
&\quad +\frac{1}{Re}(\lambda(\frac{\partial\lambda_s}{\partial s} - \frac{\lambda_n}{R} + V_s\frac{\partial\lambda_4}{\partial s}) + (\lambda + 2\mu)(\frac{\partial\lambda_n}{\partial n} + V_n\frac{\partial\lambda_4}{\partial n}) - \tau_{nn}\lambda_4) \\
&\quad +\frac{1}{Re}(\frac{\lambda}{R}(\lambda_n + V_n\lambda_4)) \\
&= \frac{\alpha_3}{2}\mathbf{g} \\
&\quad +(\rho\lambda_1 + \rho V_s\lambda_s + 2\rho V_n\lambda_n + (p + \rho E + \rho V_n^2)\lambda_4) \\
&\quad +\frac{1}{Re}(\lambda(\frac{\partial\lambda_s}{\partial s} - \frac{\lambda_n}{R} + V_s\frac{\partial\lambda_4}{\partial s}) + (\lambda + 2\mu)(\frac{\partial\lambda_n}{\partial n} + V_n\frac{\partial\lambda_4}{\partial n}) - \tau_{nn}\lambda_4) \\
&= \frac{\alpha_3}{2}\mathbf{g} \\
&\quad +\frac{2\mu + \lambda}{Re}(\frac{\partial\lambda_n}{\partial n} + V_n\frac{\partial\lambda_4}{\partial n})
\end{aligned} \tag{A.33}$$

considering the adjoint boundary condition at Γ_c

$$\begin{aligned}
\lambda_1 &= 0 \\
\lambda_2 &= 0 \\
\lambda_3 &= 0 \\
\lambda_4 &= 0 \\
\frac{\partial\lambda_n}{\partial s} &= 0 \\
\frac{\partial\lambda_s}{\partial s} &= 0
\end{aligned}$$

Isothermal slip wall

Compared with the isothermal nonslip wall, we will have one more unconstraints V_s. $T = T_0$ at the wall Γ_s. So we have the following constraints

$$\begin{aligned} V_n' &= 0 \quad \text{at} \quad \Gamma_s \\ \frac{\partial {V_n}'}{\partial s} &= 0 \quad \text{at} \quad \Gamma_s \\ T' &= 0 \quad \text{at} \quad \Gamma_s \end{aligned}$$

and those terms will be unconstrained,

$$\begin{aligned} {V_s}' &\quad \text{at} \quad \Gamma_s \\ \frac{\partial {V_n}'}{\partial n} &\quad \text{at} \quad \Gamma_s \\ \frac{\partial {V_s}'}{\partial n} &\quad \text{at} \quad \Gamma_s \\ \frac{\partial {V_s}'}{\partial s} &\quad \text{at} \quad \Gamma_s \\ \rho' &\quad \text{at} \quad \Gamma_s \\ \frac{\partial T'}{\partial n} &\quad \text{at} \quad \Gamma_s \end{aligned}$$

so we get

$$\begin{aligned}
(\rho\lambda_4 V_s V_n + \rho V_n \lambda_s) + \frac{1}{Re}\mu(\frac{\partial\lambda_n}{\partial s} + \frac{\partial\lambda_s}{\partial n} + \frac{\lambda_s}{R} & \\
+V_n\frac{\partial\lambda_4}{\partial s} + V_s\frac{\partial\lambda_4}{\partial n} - \frac{\tau_{sn}}{\mu}\lambda_4) + \frac{1}{Re}\frac{-\mu}{R}(\lambda_s + V_s\lambda_4)) &= 0 \quad \text{at} \quad \Gamma_s \\
\frac{-(2\mu+\lambda)}{Re}(\lambda_n + V_n\lambda_4)) &= 0 \quad \text{at} \quad \Gamma_s \\
\frac{-\lambda}{Re}(\lambda_n + V_n\lambda_4)) &= 0 \quad \text{at} \quad \Gamma_s \\
\frac{-\mu}{Re}(\lambda_s + V_s\lambda_4)) &= 0 \quad \text{at} \quad \Gamma_s \\
V_n(\lambda_1 + V_s\lambda_s + V_n\lambda_n + \lambda_4 E) &= 0 \quad \text{at} \quad \Gamma_s \\
\frac{-\kappa\lambda_4}{RePr(\gamma-1)} &= 0 \quad \text{at} \quad \Gamma_s
\end{aligned}$$

Eventually we get our adjoint boundary conditions, at the solid wall Γ_s

$$\begin{aligned}
\lambda_s + V_s\lambda_4 &= 0 \\
\lambda_n + V_n\lambda_4 &= 0 \\
\lambda_4 &= 0 \quad \text{at} \quad \Gamma_s
\end{aligned}$$

After simplifying, we get

$$\begin{aligned}
\lambda_2 &= 0 \\
\lambda_3 &= 0 \\
\lambda_4 &= 0 \quad \text{at} \quad \Gamma_s
\end{aligned}$$

Iso-flux slip wall

Compared with the iso-flux nonslip wall, we will have one more unconstraints V_s. $T_{,n} = 0$ at the wall Γ_s. So we have the following constraints

$$\begin{aligned} V_n' &= 0 \quad \text{at} \quad \Gamma_s \\ \frac{\partial V_n{}'}{\partial s} &= 0 \quad \text{at} \quad \Gamma_s \\ \frac{\partial T'}{\partial n} &= 0 \quad \text{at} \quad \Gamma_s \end{aligned}$$

and those terms will be unconstrained,

$$\begin{aligned} V_s' &\quad \text{at} \quad \Gamma_s \\ \frac{\partial V_n{}'}{\partial n} &\quad \text{at} \quad \Gamma_s \\ \frac{\partial V_s{}'}{\partial n} &\quad \text{at} \quad \Gamma_s \\ \frac{\partial V_s{}'}{\partial s} &\quad \text{at} \quad \Gamma_s \\ \rho' &\quad \text{at} \quad \Gamma_s \\ T' &\quad \text{at} \quad \Gamma_s \end{aligned}$$

so we get

$$\begin{aligned}
(\rho\lambda_4 V_s V_n + \rho V_n \lambda_s) + \frac{1}{Re}\mu(\frac{\partial\lambda_n}{\partial s} + \frac{\partial\lambda_s}{\partial n} + \frac{\lambda_s}{R} \\
+V_n\frac{\partial\lambda_4}{\partial s} + V_s\frac{\partial\lambda_4}{\partial n} - \frac{\tau_{sn}}{\mu}\lambda_4) + \frac{1}{Re}\frac{-\mu}{R}(\lambda_s + V_s\lambda_4)) &= 0 \quad \text{at} \quad \Gamma_s \\
\frac{-(2\mu+\lambda)}{Re}(\lambda_n + V_n\lambda_4)) &= 0 \quad \text{at} \quad \Gamma_s \\
\frac{-\lambda}{Re}(\lambda_n + V_n\lambda_4)) &= 0 \quad \text{at} \quad \Gamma_s \\
\frac{-\mu}{Re}(\lambda_s + V_s\lambda_4)) &= 0 \quad \text{at} \quad \Gamma_s \\
V_n(\lambda_1 + V_s\lambda_s + V_n\lambda_n + \lambda_4 E) &= 0 \quad \text{at} \quad \Gamma_s \\
V_n\frac{\rho\lambda_4}{\gamma(\gamma-1)} + \frac{\kappa}{RePr(\gamma-1)}\frac{\partial\lambda_4}{\partial n} &= 0 \quad \text{at} \quad \Gamma_s
\end{aligned}$$

In short, the adjoint boundary conditions, at the solid wall Γ_s

$$\begin{aligned}
\lambda_s + V_s\lambda_4 &= 0 \\
\lambda_n + V_n\lambda_4 &= 0 \\
\frac{\partial\lambda_4}{\partial n} &= 0 \\
\frac{\partial\lambda_s}{\partial n} - \lambda_4(\frac{\tau_{nn}}{\mu} + \frac{V_s}{R}) &= 0 \quad \text{at} \quad \Gamma_s
\end{aligned}$$

Considering

$$\frac{\partial\lambda_s}{\partial n} = -\frac{\partial V_s\lambda_4}{\partial n} = -\lambda_4\frac{\partial V_s}{\partial n} - V_s\frac{\partial\lambda_4}{\partial n} = -\lambda_4\frac{\partial V_s}{\partial n}$$

and

$$\frac{\partial\lambda_s}{\partial n} - \lambda_4(\frac{\tau_{nn}}{\mu} + \frac{V_s}{R}) = -\lambda_4(\frac{\partial V_s}{\partial n} + \frac{\tau_{nn}}{\mu} + \frac{V_s}{R}) = 0$$

we can see $\lambda_4 = 0$ at the Γ_s

So the final adjoint boundary condition for the iso-flux slip wall is

$$\begin{aligned} \lambda_2 &= 0 \\ \lambda_3 &= 0 \\ \lambda_4 &= 0 \\ \frac{\partial \lambda_4}{\partial n} &= 0 \quad \text{at} \quad \Gamma_s \end{aligned}$$

A.1.3 Adjoint Far Field Boundary

For the adjoint far field boundary, it is related with this term $\int_{t_0}^{t_f}\int_{\Gamma_\infty}(n_i \mathbf{F}_i{}^{T'})\boldsymbol{\lambda} d\mathbf{x}$. To be easy, in the implementation, we are using the following adjoint boundary condition for the far field, i.e. zero fluctuation, zero traction in the far field.

$$\begin{array}{lll} \lambda_1 = 0 & \lambda_{1,x} = 0 & \lambda_{1,y} = 0 \\ \lambda_2 = 0 & \lambda_{2,x} = 0 & \lambda_{2,y} = 0 \\ \lambda_3 = 0 & \lambda_{3,x} = 0 & \lambda_{3,y} = 0 \\ \lambda_4 = 0 & \lambda_{4,x} = 0 & \lambda_{4,y} = 0 \end{array}$$

Appendix B

Spatial Discretization of Adjoint Navier-Stokes Equations

B.1 Transformation of the Adjoint Equations

For the discontinuous Galerkin(DG) discretization, the adjoint equation(A.31) needs to be transformed into the conservative(flux) form. Since the state solution variable is the conservative variable $\mathbf{U}$, the adjoint equation(A.31) is transformed into the conservative form with all coefficient matrix from $\mathbf{U}$.

Here is the adjoint equation for the Navier–Stokes equations based on the variation of primitive $\boldsymbol{u}$ from (A.31).

$$-\boldsymbol{\lambda}_{,t} - \mathbf{A}_i{}^T \boldsymbol{\lambda}_{x_i} - \mathbf{M}^{-T}(-\mathbf{D}_i{}^T \boldsymbol{\lambda}_{x_i} + (\mathbf{K}_j^{i\,T} \boldsymbol{\lambda}_{x_i})_{x_j}) + \mathbf{S}_p = 0 \tag{B.1}$$

where

$$\mathbf{M} = \frac{\partial \mathbf{U}}{\partial \boldsymbol{u}} \qquad \mathbf{A}_i = \frac{\partial \mathbf{F}}{\partial \mathbf{U}}$$
$$\mathbf{D}_i = \frac{\partial \mathbf{F}_i^v}{\partial \boldsymbol{u}} \qquad \mathbf{K}_j^i = \frac{\partial \mathbf{F}_i^v}{\partial \boldsymbol{u}_{x_j}}$$

On the other hand, the adjoint equation can also be written based on the conservative $\mathbf{U}$. Its derivation is very similar to the procedures in A.

$$-\boldsymbol{\lambda}_{,t} - \mathbf{A}_i{}^T \boldsymbol{\lambda}_{x_i} - (-\widehat{\mathbf{D}}_i^T \boldsymbol{\lambda}_{x_i} + (\widehat{\mathbf{K}}_j^{i\,T} \boldsymbol{\lambda}_{x_i})_{x_j}) + \mathbf{S}_c = 0 \tag{B.2}$$

where

$$\mathbf{A}_i = \frac{\partial \mathbf{F}}{\partial \mathbf{U}}, \qquad \widehat{\mathbf{D}}_i = \frac{\partial \mathbf{F}_i^v}{\partial \mathbf{U}}, \qquad \widehat{\mathbf{K}}_j^i = \frac{\partial \mathbf{F}_i^v}{\partial \mathbf{U}_{x_j}}$$

Through the simple derivation, we can show that the two forms of (B.1) and (B.2) are equivalent.

For equation (B.1), it can be transformed to

$$\begin{aligned} -\boldsymbol{\lambda}_{,t} &- \mathbf{A}_i{}^T\boldsymbol{\lambda}_{x_i} - \mathbf{M}^{-T}(-\mathbf{D}_i{}^T\boldsymbol{\lambda}_{x_i} + (\mathbf{K}_j^{i\,T}\boldsymbol{\lambda}_{x_i})_{x_j}) + \mathbf{S}_p \\ &= -\boldsymbol{\lambda}_{,t} - \mathbf{A}_i{}^T\boldsymbol{\lambda}_{x_i} + (\mathbf{D}_i\mathbf{M}^{-1})^T\boldsymbol{\lambda}_{x_i} - ((\mathbf{K}_j^i\mathbf{M}^{-1})^T\boldsymbol{\lambda}_{x_i})_{x_j} + \mathbf{M}_{x_j}^{-T}\mathbf{K}_j^{i\,T}\boldsymbol{\lambda}_{x_i} + \mathbf{S}_p \\ &= -\boldsymbol{\lambda}_{,t} - \mathbf{A}_i{}^T\boldsymbol{\lambda}_{x_i} + (\mathbf{D}_i\mathbf{M}^{-1} + \mathbf{K}_j^i\mathbf{M}_{x_j}^{-1})^T\boldsymbol{\lambda}_{x_i} - ((\mathbf{K}_j^i\mathbf{M}^{-1})^T\boldsymbol{\lambda}_{x_i})_{x_j} + \mathbf{S}_p \quad \text{(B.3)} \end{aligned}$$

Comparing (B.2) and (B.3),

$$\begin{aligned} \mathbf{D}_i\mathbf{M}^{-1} + \mathbf{K}_j^i\mathbf{M}_{x_j}^{-1} &= \frac{\partial \mathbf{F}_i^v}{\partial \boldsymbol{u}}\frac{\partial \boldsymbol{u}}{\partial \mathbf{U}} + \frac{\partial \mathbf{F}_i^v}{\partial \boldsymbol{u}_{x_1}}(\frac{\partial \boldsymbol{u}}{\partial \mathbf{U}})_{x_1} + \frac{\partial \mathbf{F}_i^v}{\partial \boldsymbol{u}_{x_2}}(\frac{\partial \boldsymbol{u}}{\partial \mathbf{U}})_{x_2} \\ &= \frac{\partial \mathbf{F}_i^v}{\partial \boldsymbol{u}}\frac{\partial \boldsymbol{u}}{\partial \mathbf{U}} + \frac{\partial \mathbf{F}_i^v}{\partial \boldsymbol{u}_{x_1}}\frac{\partial \boldsymbol{u}_{x_1}}{\partial \mathbf{U}} + \frac{\partial \mathbf{F}_i^v}{\partial \boldsymbol{u}_{x_2}}\frac{\partial \boldsymbol{u}_{x_2}}{\partial \mathbf{U}} \\ &= \frac{\partial \mathbf{F}_i^v}{\partial \mathbf{U}} \end{aligned} \quad \text{(B.4)}$$

where we are using

$$\frac{\partial \mathbf{F}_i^v}{\partial \boldsymbol{u}_{x_i}}(\frac{\partial \boldsymbol{u}}{\partial \mathbf{U}})_{x_i} = \frac{\partial \mathbf{F}_i^v}{\partial \boldsymbol{u}_{x_i}}\frac{\partial \boldsymbol{u}_{x_i}}{\partial \mathbf{U}}$$

For the other terms

$$\begin{aligned} \mathbf{K}_j^i\mathbf{M}^{-1} &= \frac{\partial \mathbf{F}_i^v}{\partial \boldsymbol{u}_{x_j}}\frac{\partial \boldsymbol{u}}{\partial \mathbf{U}} \\ &= \frac{\partial \mathbf{F}_i^v}{\partial \boldsymbol{u}_{x_k}}\frac{\partial \boldsymbol{u}_{x_k}}{\partial \mathbf{U}_{x_j}} + \frac{\partial \mathbf{F}_i^v}{\partial \boldsymbol{u}}\frac{\partial \boldsymbol{u}}{\partial \mathbf{U}_{x_j}} \\ &= \frac{\partial \mathbf{F}_i^v}{\partial \mathbf{U}_{x_j}} \\ &= \widehat{\mathbf{K}}_j^i \end{aligned} \quad \text{(B.5)}$$

where we are using

$$\begin{aligned}
\frac{\partial \boldsymbol{u}}{\partial \mathbf{U}} &= \frac{\partial \boldsymbol{u}_{x_i}}{\partial \mathbf{U}_{x_i}} \qquad \text{no Einstein rule} \\
\frac{\partial \boldsymbol{u}_{x_j}}{\partial \mathbf{U}_{x_i}} &= 0 \qquad \text{i} \neq \text{j} \\
\frac{\partial \boldsymbol{u}}{\partial \mathbf{U}_{x_i}} &= 0
\end{aligned}$$

It indicates that both equation (B.1) and (B.2) are consistent. Since then, we will focus on the equation (B.2) and transform it into the conservative (flux) form.

$$\begin{aligned}
-\boldsymbol{\lambda}_{,t} &- \mathbf{A}_i{}^T \boldsymbol{\lambda}_{x_i} - (-\widehat{\mathbf{D}}_i^T \boldsymbol{\lambda}_{x_i} + (\widehat{\mathbf{K}}_j^{i\,T} \boldsymbol{\lambda}_{x_i})_{x_j}) + \mathbf{S}_c \\
&= -\boldsymbol{\lambda}_{,t} - (\mathbf{A}_i{}^T \boldsymbol{\lambda})_{x_i} + \mathbf{A}_i{}^T{}_{x_i} \boldsymbol{\lambda} + (\widehat{\mathbf{D}}_i^T \boldsymbol{\lambda})_{x_i} - \widehat{\mathbf{D}}_i^T{}_{x_i} \boldsymbol{\lambda} - (\widehat{\mathbf{K}}_i^{j\,T} \boldsymbol{\lambda}_{x_j})_{x_i} + \mathbf{S}_c \\
&= 0 \qquad \text{(B.6)}
\end{aligned}$$

Write it in the following form

$$\boldsymbol{\lambda}_{,t} + (\mathbf{A}_i{}^T \boldsymbol{\lambda})_{x_i} - (\widehat{\mathbf{D}}_i^T \boldsymbol{\lambda})_{x_i} + (\widehat{\mathbf{K}}_i^{j\,T} \boldsymbol{\lambda}_{x_j})_{x_i} = \mathbf{A}_i{}^T{}_{x_i} \boldsymbol{\lambda} - \widehat{\mathbf{D}}_i^T{}_{x_i} \boldsymbol{\lambda} + \mathbf{S}_c \qquad \text{(B.7)}$$

Combined with the adjoint initial condition, adjoint boundary defined in A.1.2, the whole adjoint system is obtained.

B.1.1 Spatial Discretization in DG

For the equation (B.7), there are four terms, adjoint convection term $(\mathbf{A}_i{}^T \boldsymbol{\lambda})_{x_i}$, which can be solved using the general Riemann approximate solver, $(\widehat{\mathbf{D}}_i^T \boldsymbol{\lambda})_{x_i}$ which is called adjoint viscous convection term, is discretized using the central flux, since the eigenvalues of coefficient matrix $\widehat{\mathbf{D}}_i^T$ is very difficult to evaluate. The third term $(\widehat{\mathbf{K}}_i^{j\,T} \boldsymbol{\lambda}_{x_j})_{x_i}$, which is called adjoint diffusion term, is discretized using the Bassi-Rebay flux formulation (3.7), (3.9). The procedure is very similar to that for the discretization of the diffusion term in the state solver. The last term $\mathbf{A}_i{}^T{}_{x_i} \boldsymbol{\lambda} - \widehat{\mathbf{D}}_i^T{}_{x_i} \boldsymbol{\lambda} + \mathbf{S}_c$ is our source

term. As to our temporal integration, it is discretized with the explicit Runge-Kutta 4 method as discussed in [54].

Here we discretize (B.7) based on the discontinuous Galerkin formulations. For this equation, the adjoint convective, adjoint viscous convective and adjoint diffusion flux vectors in the ith coordinate direction are ${\mathbf{A}_i}^T\boldsymbol{\lambda}$, $\widehat{\mathbf{D}}_i^T\boldsymbol{\lambda}$, and $\widehat{\mathbf{K}}_i^{j\,T}\boldsymbol{\lambda}_{x_j}$. ${\mathbf{A}_i}^T{}_{x_i}\boldsymbol{\lambda} - \widehat{\mathbf{D}}_i^T{}_{x_i}\boldsymbol{\lambda} + \mathbf{S}_c$ is a source term. Equation (B.7) is solved subject to appropriate adjoint boundary conditions.

Define

$$\begin{array}{ll} \mathbf{F}_i^a = {\mathbf{A}_i}^T\boldsymbol{\lambda} & \boldsymbol{G}_i^{av} = \widehat{\mathbf{K}}_i^{j\,T}\boldsymbol{\lambda}_{x_j} \\ \boldsymbol{G}_i^a = \widehat{\mathbf{D}}_i^T\boldsymbol{\lambda} \quad , & \widetilde{\mathbf{S}} = {\mathbf{A}_i}^T{}_{x_i}\boldsymbol{\lambda} - \widehat{\mathbf{D}}_i^T{}_{x_i}\boldsymbol{\lambda} + \mathbf{S} \end{array}$$

(B.7) becomes

$$\boldsymbol{\lambda}_{,t} + (\mathbf{F}_i^a)_{x_i} - (\boldsymbol{G}_i^a)_{x_i} + (\boldsymbol{G}_i^{av})_{x_i} = \widetilde{\mathbf{S}} \tag{B.8}$$

Similar to the state discretizations in 3.2, the weak form of (B.8) is

$$\begin{aligned} \int_{\Omega_e} \left(\boldsymbol{W}^T\boldsymbol{\lambda}_{,t} + \boldsymbol{W}_{,i}^T(\boldsymbol{G}_i^a - \boldsymbol{G}_i^{av} - \mathbf{F}_i^a)\right)\, d\mathbf{x} \;\; &+ \int_{\partial\Omega_e} \boldsymbol{W}^T\left(\mathbf{F}_n^a + \boldsymbol{G}_n^{av} - \boldsymbol{G}_n^a\right)\, d\mathbf{s} \\ &= \int_{\Omega_e} \boldsymbol{W}^T\widetilde{\mathbf{S}}\, d\mathbf{s} \end{aligned} \tag{B.9}$$

Introducing numerical fluxes and summing over all elements yields the similar formulation as (3.3),

$$\begin{aligned} &\sum_{e=1}^{N} \int_{\partial\Omega_e} \boldsymbol{W}^T\left(\widehat{\mathbf{F}}_n^a(\boldsymbol{\lambda}^-,\boldsymbol{\lambda}^+) + \widehat{\boldsymbol{G}}_n^{av}(\boldsymbol{\lambda}^-,\nabla\boldsymbol{\lambda}^-,\boldsymbol{\lambda}^+,\nabla\boldsymbol{\lambda}^+) - \widehat{\boldsymbol{G}}_n^a(\boldsymbol{\lambda}^-,\boldsymbol{\lambda}^+)\right)\, d\mathbf{s} \\ &+ \sum_{e=1}^{N} \int_{\Omega_e} \left(\boldsymbol{W}^T\boldsymbol{\lambda}_{,t} + \boldsymbol{W}_{,i}^T(\boldsymbol{G}_i^a - \boldsymbol{G}_i^{av} - \mathbf{F}_i^a)\right)\, d\mathbf{x} = \sum_{e=1}^{N} \int_{\Omega_e} \boldsymbol{W}^T\widetilde{\mathbf{S}}\, d\mathbf{s} \end{aligned} \tag{B.10}$$

For the adjoint convective flux $\widehat{\mathbf{F}}_n^a(\boldsymbol{\lambda}^-,\boldsymbol{\lambda}^+)$, we use a Lax–Friedrichs method (3.6)

$$\widehat{\mathbf{F}}_n^a(\boldsymbol{\lambda}^-,\boldsymbol{\lambda}^+) = \frac{1}{2}\left(\mathbf{F}_n^a(\boldsymbol{\lambda}^-) + \mathbf{F}_n^a(\boldsymbol{\lambda}^+) - \lambda_m\left(\boldsymbol{\lambda}^- - \boldsymbol{\lambda}^+\right)\right) \tag{B.11}$$

where λ_m is the maximum, in absolute value, of the eigenvalues of the Euler Jacobian $\boldsymbol{A}_n = \partial \mathbf{F}_n / \partial \mathbf{U}$ from the state.

For the adjoint viscous convective flux $\widehat{\boldsymbol{G}}_n^a(\boldsymbol{\lambda}^-, \boldsymbol{\lambda}^+)$, we use a central flux because of the complexity of $\widehat{\mathbf{D}}_i^T$

$$\widehat{\boldsymbol{G}}_n^a(\boldsymbol{\lambda}^-, \boldsymbol{\lambda}^+) = \frac{1}{2}\left(\boldsymbol{G}_n^a(\boldsymbol{\lambda}^-) + \boldsymbol{G}_n^a(\boldsymbol{\lambda}^+)\right) \tag{B.12}$$

For the numerical adjoint diffusion flux $\widehat{\boldsymbol{G}}_n^{av}(\boldsymbol{\lambda}^-, \nabla\boldsymbol{\lambda}^-, \boldsymbol{\lambda}^+, \nabla\boldsymbol{\lambda}^+)$, we use the Bassi–Rebay flux, which is very similar to (3.7) and (3.9).

Appendix C

Optimal Control of Burgers Equation

In this chapter, results for Burgers equations using both distributed and boundary control (Dirichlet and Neumann) are presented to validate our approach.The numerical solution of optimal control problems governed by the unsteady compressible Navier–Stokes equations is a challenging problem that requires careful mathematical formulation, accurate state solution, efficient gradient computation, and convergent optimization algorithms. As a simplified model of the Navier–Stokes (NS) equation, the one-dimensional Burgers equation represents many of the properties of NS equations, such as nonlinear convection and viscous diffusion leading to shock waves and boundary layers. Given this, the viscous Burgers equation has received significant attention [19, 23, 69] and recent research has focused on the control of Burgers flow as a model for control of Navier–Stokes flows [11, 23]. To meet the challenges associated with optimal control of unsteady flow, we have developed a new computational framework based on the discontinuous Galerkin method (DGM) that allows for spectral accuracy on unstructured grids with the ability to use local *hp*-refinement. These capabilities will be of particular importance for large-scale optimal control for complex fluid flows such as those encountered in aeroacoustic applications. This paper presents our efforts in this direction by applying DGM to the solution of optimal control problems for flows governed by the viscous Burgers equation Since the number of control variables is large in the problems that we target, an adjoint equation is utilized to efficiently evaluate the gradient of the objective functional with-respect-to the control. In general, there are two approaches to adjoint-based gradient evaluation: the optimize-then-discretize approach and discretize-then-optimize approach.

One of the goals of our research is to evaluate and compare these two approaches for formulating and solving optimal control problems using DGM. In this chapter, we focus on the optimize-then-discretize approach by presenting a discussion of the problem formulation, implementation, and results.

C.1 Problem Formulation

C.1.1 Governing Equations

The Burgers equation is given by

$$\frac{\partial u}{\partial t} + \frac{1}{2}\frac{\partial u^2}{\partial x} - \nu\frac{\partial^2 u}{\partial x^2} = f + \Phi \tag{C.1}$$

with boundary conditions

$$\begin{aligned} u(0,t) &= \phi_L \\ \mu u_{,n}(L,t) + \beta u\vec{n} &= \phi_R \end{aligned} \tag{C.2}$$

and initial condition

$$u(x,0) = u_0(x) \tag{C.3}$$

in which Φ is the distributed control, and ϕ_L and ϕ_R are the boundary controls, with the spatial domain $\Omega = [0, L]$. Here, we set the source term, $f = 0$. With $\beta = 0$, we will get the Neumann boundary control.

C.1.2 Objective Functional

For the Burgers control problems in this paper, the objective functional is defined as

$$\begin{aligned}\mathcal{J} &= \frac{\ell}{2}\int_{t_0}^{t_0+T}\int_0^L \Phi^2 dxdt + \frac{\ell_1}{2}\int_{t_0}^{t_0+T}\phi_L^2 dt \\ &+ \frac{\ell_2}{2}\int_{t_0}^{t_0+T}\phi_R^2 dt + \frac{\omega_1}{2}\int_{t_0}^{t_0+T}\int_0^L (u-\tilde{u})^2 dxdt \\ &+ \frac{\omega_2}{2}\int_0^L \left[u(x,t_f)-\bar{u}(x)\right]^2 dx. \end{aligned} \tag{C.4}$$

where $\tilde{u}$ and $\bar{u}$ are the distributed and terminal target states, respectively.

C.1.3 Optimality Equations

First, we form a L^2-inner product by introducing an adjoint variable λ as

$$\begin{gathered}\langle \mathcal{N}u, \lambda\rangle = \\ \int_{t_0}^{t_0+T}\int_0^L \left(\tfrac{\partial u}{\partial t} + \tfrac{1}{2}\tfrac{\partial u^2}{\partial x} - \nu\tfrac{\partial^2 u}{\partial x^2} - \Phi\right)\lambda\, dx\, dt\,, \end{gathered} \tag{C.5}$$

where $\mathcal{N}u = 0$ denotes the Burgers equation (C.1).

Computing the variation of (C.5) with respect to the state variable u, and integrating by parts yields

$$\begin{aligned}\langle u', \mathcal{N}^*\lambda\rangle &= \int_0^L u'\lambda\Big|_{t_f} dx + \int_{t_0}^{t_0+T} u\lambda u'\Big|_0^L dt \\ &- \int_{t_0}^{t_0+T}\nu\lambda\frac{\partial u'}{\partial x}\Big|_0^L dt + \int_{t_0}^{t_0+T}\nu\frac{\partial\lambda}{\partial x}u'\Big|_0^L dt \\ &- \int_{t_0}^{t_0+T}\int_0^L \lambda\Phi' dxdt\,, \end{aligned} \tag{C.6}$$

where $\mathcal{N}^*$ denotes the adjoint operator, defined as

$$\mathcal{N}^*\lambda = -\frac{\partial\lambda}{\partial t} - u\frac{\partial\lambda}{\partial x} - \nu\frac{\partial^2\lambda}{\partial x}\,. \tag{C.7}$$

The variation of the objective functional (C.4) with respect to the control is

$$\begin{aligned}
\mathcal{J}' &= \ell \int_{t_0}^{t_0+T} \int_0^L \Phi\Phi' \, dx \, dt \\
&+ \ell_1 \int_{t_0}^{t_0+T} \phi_L \phi_L' \, dt + \ell_2 \int_{t_0}^{t_0+T} \phi_R \phi_R' \, dt \\
&+ \omega_1 \int_{t_0}^{t_0+T} \int_0^L (u - \tilde{u}) u' \, dx \, dt \\
&+ \omega_2 \int_0^L (u_{t_f} - \bar{u}) u_{t_f}' \, dx \, . \qquad \text{(C.8)}
\end{aligned}$$

According to the theory of Lagrange multipliers,

$$\mathcal{J}' - \langle \mathcal{N} u, \lambda \rangle' = 0$$

gives the adjoint equation

$$-\frac{\partial \lambda}{\partial t} - u \frac{\partial \lambda}{\partial x} - \nu \frac{\partial^2 \lambda}{\partial x} = \omega_1 (u - \tilde{u}) \qquad \text{(C.9)}$$

with the boundary conditions

$$\begin{aligned}
\lambda(0, t) &= 0 \\
u\lambda(L, t) + \nu \lambda_{,x}(L, t) &= 0 \qquad \text{(C.10)}
\end{aligned}$$

and end condition

$$\lambda(x, t_f) = \omega_2 (u(x, t_f) - \bar{u}(x)) \, . \qquad \text{(C.11)}$$

The optimality conditions are the state-equation (C.1) with boundary conditions (C.2) and initial condition (C.3), the adjoint equation (C.9) with boundary conditions

(C.10) and end condition (C.11) and the gradient equations, given by

$$\begin{aligned} \nabla_{\Phi}\mathcal{J} &= l\Phi + \lambda, \\ \nabla_{\phi_L}\mathcal{J} &= l_1\phi_L + \nu \left.\frac{\partial\lambda}{\partial x}\right|_{x=0}, \\ \nabla_{\phi_R}\mathcal{J} &= l_2\phi_R + \nu\lambda_{x=L}\,. \end{aligned}$$

Solution of the optimality equations yields the gradient of the objective functional with respect to the control which should be equal to zero at the optimum. We use a nonlinear conjugate gradient method to solve this optimization problem and more details regarding optimal control of Burgers flows can be found in [20].

C.2 Numerical Method

The optimality equations are discretized with a discontinuous Galerkin method in space and fourth-order accurate Runge-Kutta time-integration.

C.2.1 Spatial Discretization

We denote the boundary of the domain Ω as $\partial\Omega = \Gamma_D \cup \Gamma_N$ where Γ_D is the portion of the boundary where Dirichlet conditions are specified and Γ_N is the portion of the boundary where Neumann conditions are set. The spatial domain Ω is partitioned into a set of non-overlapping elements Ω_e that each have a Lipschitz boundary $\partial\Omega_e$. The element boundary is denoted as $\Gamma = \{\Gamma_D, \Gamma_N, \Gamma_0\}$ where Γ_0 are the inter-element boundaries. Let Ω_1 and Ω_2 be two adjacent elements; let $\Gamma_{12} = \partial\Omega_1 \cap \partial\Omega_2$; and let $\mathbf{n}^{(1)}$ and $\mathbf{n}^{(2)}$ be the corresponding outward unit normal vectors at that point.

Let $u^{(e)}$ and $F^{(e)}$ be the trace of a state u and flux vector F, respectively, on Γ_{12} from the interior of sub-domain Ω_e. Then, we define the average $\langle\,\cdot\,\rangle$ and jump $[\cdot]$

operators on Γ_{12} as

$$[u] = u^{(1)}n^{(1)} + u^{(2)}n^{(2)} \tag{C.12a}$$

$$[F_n] = F^{(1)}n^{(1)} + F^{(2)}n^{(2)}, \tag{C.12b}$$

$$\langle u \rangle = \frac{1}{2}\left(u^{(1)} + u^{(2)}\right), \tag{C.12c}$$

$$\langle F \rangle = \frac{1}{2}\left(F^{(1)} + F^{(2)}\right), \tag{C.12d}$$

where $F_n = Fn$ and $n = -1$ on a left boundary and $n = 1$ on a right boundary. Defining the convective and viscous fluxes as

$$F = \frac{u^2}{2}, \qquad F^v = \nu u_{,x}\,,$$

the discontinuous Galerkin formulation for the Burgers equation is

$$\begin{aligned}
\sum_e \int_{\Omega_e} \Big\{ w(u_{,t} - \Phi) + w_{,x}(F^v - F) \Big\} d\Omega - \\
\int_{\Gamma_0} [wn] \left\langle \widehat{F}^v - F \right\rangle \, d\Gamma - \int_{\Gamma_0} \langle \nu w_{,x} \rangle \left[n(\widehat{u} - u) \right] \, d\Gamma \\
- \int_{\Gamma_D} (\nu w_{,n})(u - \phi_L) + w \left(F_n^v - \widehat{F}_n^v(u, \phi_L) \right) \, d\Gamma \\
- \int_{\Gamma_N} w(\nu \phi_R - \widehat{F}_n^v(u,u)) \, d\Gamma = 0
\end{aligned} \tag{C.13}$$

where $\widehat{F}$, $\widehat{F^v}$ and $\widehat{u}$ are numerical fluxes. For the convective numerical inviscid flux, we use the Lax-Friedrichs flux [24], which can be expressed as

$$\widehat{F}(u^-, u^+) = \frac{1}{2}\left[F(u^-) + F(u^+) + \lambda_m (u^- - u^+) \right]$$

where $\lambda_m = |\partial F / \partial u|$. For the numerical viscous flux, $\widehat{F}^v$, and solution flux, $\widehat{u}$, we use the Bassi-Rebay method [8, 9]. All boundary conditions are enforced weakly through the numerical fluxes and additional details regarding weak boundary condition enforcement can be found in [31, 32]

The DGM discretization for the adjoint equation (C.9) is similar to that of state (C.13),

$$\begin{aligned}\sum_e \int_{\Omega_e} \Big\{ w\left(\lambda_{,t} - \lambda u_{,x} + \omega_1(u-\tilde{u})\right) - \\ w_{,x}(G^v + G)\Big\} d\Omega + \\ \int_{\Gamma_0} [wn] \left\langle \widehat{G}^v + G \right\rangle \, d\Gamma + \int_{\Gamma_0} \langle \nu w_{,x} \rangle \left[n(\widehat{\lambda} - \lambda) \right] \, d\Gamma \\ - \int_{\Gamma_D} \left\{ \nu w_{,n} \lambda - w \left(G_n^v - \widehat{G}_n^v(\lambda, 0) \right) \right\} d\Gamma \\ + \int_{\Gamma_N} w(-u\lambda - \widehat{G}_n^v(\lambda, \lambda)) \, d\Gamma = 0 \end{aligned} \tag{C.14}$$

where $G \equiv u\lambda$ and $G^v \equiv \nu\lambda_{,x}$. Similar to the state discretization, we use the Lax–Freidrichs and Bassi–Rebay numerical fluxes and the adjoint boundary conditions (C.10) are applied in evaluating the numerical fluxes on the domain boundary.

C.2.2 Temporal Discretization

A fourth-order accurate explicit Runge-Kutta method is used, which is symmetric and therefore well-suited for optimal control problems [54].

C.3 Results

The following results all use the continuous adjoint approach presented above. For all cases, the initial condition is the same as that in Chang's Ph.D. thesis [20] and is given by

$$u_0(x) = \sin\left(m\pi \tan(c_s(2x-1)) \,/\, \tan(c_s)\right) \tag{C.15}$$

where c_s is a parameter that controls the stretching of the initial profile. This initial profile can lead to boundary layers near the domain ends. We choose $c_s = 1.3$. Our space and time domain are $0 \leq x \leq 1$ and $0 \leq t \leq 1$, respectively. The viscosity

for all cases is $\nu = 0.01$. For spatial discretization, the domain is divided into 40 equally sized elements. Unless otherwise specified, fourth-order ($p = 4$) polynomial representations are used on each element and the time-step is $\Delta t = 0.00025$.

C.3.1 Distributed Control

The first test case corresponds to that done in Ref. [20] and is used to validate our implementation. The control objective is to sustain the initial profile, so the objective functional is defined as

$$\begin{aligned} \mathcal{J} &= \frac{\ell}{2}\int_0^1\int_0^1 \Phi^2 dxdt \\ &+ \frac{1}{2}\omega_1\int_0^1\int_0^1 (u-u_0)^2\, dxdt \\ &+ \frac{1}{2}\omega_2\int_0^1 [u(x,1)-u_0]^2\, dx. \end{aligned} \tag{C.16}$$

In our simulations, $\omega_1 = 1$, $\omega_2 = 1$, and $\ell = 0.01$.

Figure C.1 shows that as the number of optimization iterations increases, the state solution at $t = t_f = 1$ becomes closer and closer to the target solution. The distributed optimal control profile, $\Phi(x)$, is shown in Fig. C.2 after four optimization iterations which demonstrates that the control has boundary layers near the left and right boundaries and that the control changes in time in order to drive the solution toward the target state.

The evolution of the objective function, J, as the number of optimization iterations increases is shown in Fig. C.3. From this figure, we see that the objective functional drops to a value of 8×10^{-3} with no significant decrease in J beyond about 3 iterations which is consistent with prior results [20]. Taking advantage of the ability to perform p-refinement in DGM, Fig. C.3 also shows results for both $p = 2$ and $p = 6$. Overall the optimal-control solutions are similar for all values of p which indicates that this

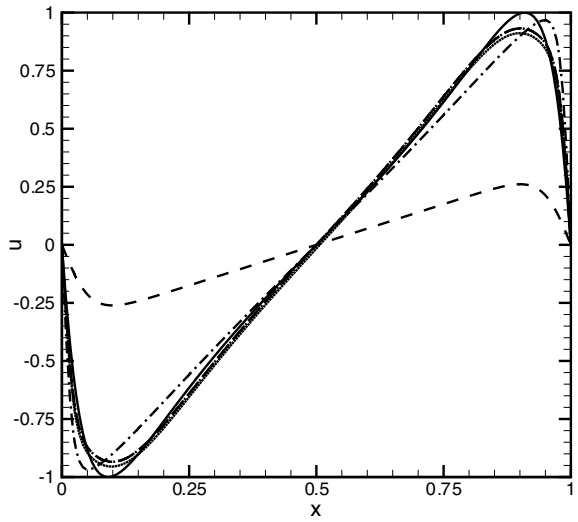

Figure C.1: Distributed control of Burgers equation for $p = 4$: —— initial profile; - - - - the profile without control at $t = 1$; —-— profile with control at $t = 1$ after first iteration; —·— profile with control at $t = 1$ after second iteration; ····· profile with control $t = 1$ after third iteration.

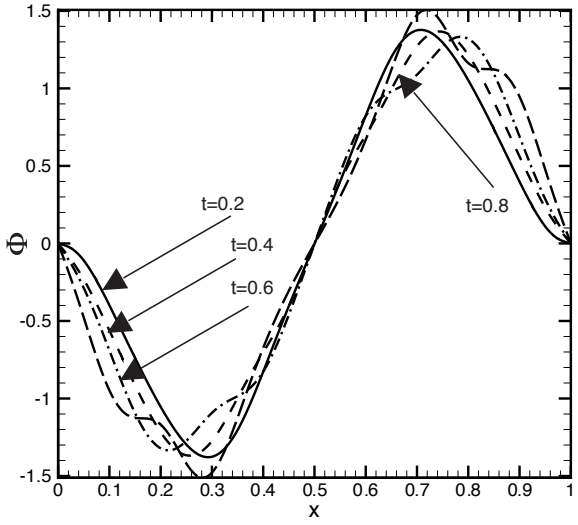

Figure C.2: Distributed control profile after fourth iteration at $t = 0.2$, 0.4, 0.6, and 0.8.

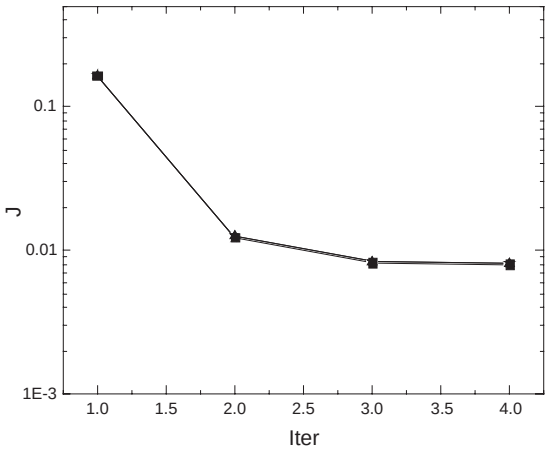

Figure C.3: Objective functional, J, at different iterations for distributed control: ▪ $p = 2$; △ $p = 4$; ◇ $p = 6$.

distributed control problem is well resolved, even at $p = 2$.

C.3.2 Boundary Control

In order to validate our implementation for boundary control, we formulate our test cases as inverse problems. Given a specified boundary condition, the corresponding state solutions are first obtained, which then become our objective solution $\tilde{u}$. Using this as our objective solution in the objective functional, we then solve the optimal control problem and compare the computed boundary values to the boundary condition that was originally prescribed.

Dirichlet Boundary Control

The initial condition is the same as that used for distributed control. Our control objective is to achieve the objective solution $\tilde{u}$, which is obtained using the prescribed

boundary condition $\phi_L^* = 2t^2$. Thus, the objective functional is

$$\begin{aligned} \mathcal{J} &= \frac{\ell_1}{2}\int_0^1 \phi_L^2 dt \\ &+ \frac{\omega_1}{2}\int_0^1\int_0^1 (u-\tilde{u})^2 dxdt \\ &+ \frac{1}{2}\omega_2 \int_0^1 \left[u(x,t_f)-\tilde{u}(x,t_f)\right]^2 dx \end{aligned} \tag{C.17}$$

where $\omega_1 = 1000$, $\omega_2 = 1$, and $\ell_1 = 0.001$. The initial guess for the boundary control is $\phi_L = 2t_f t$ so that the final boundary condition is satisfied at $t = 0$.

Comparing the target state and the optimal state solutions after 24 iterations (see Fig. C.5) shows that the agreement is excellent. It is also shown in Fig. C.6 that the control converges to the target boundary condition $\phi_L^* = 2t^2$. This can be seen more clearly in Fig. C.7 which shows the error in the computed control compared to the target boundary condition.

Figure C.8 presents the evolution of the objective functional showing that the value converges after about 20 optimization iterations for $p = 4$. Also shown in Fig. C.8 are convergence histories for other values of p. Improving resolution does appear to lead to a slightly smaller value of J although convergence is slightly slower for larger p.

Neumann Boundary Control

We now consider Neumann boundary control where the control variable is ϕ_R at $x = 1$. Our control objective is to sustain the target solution $\tilde{u}$ obtained using the prescribed boundary condition $\phi_R^* = -31.52(1 - 2\sqrt{t})$. The objective functional for

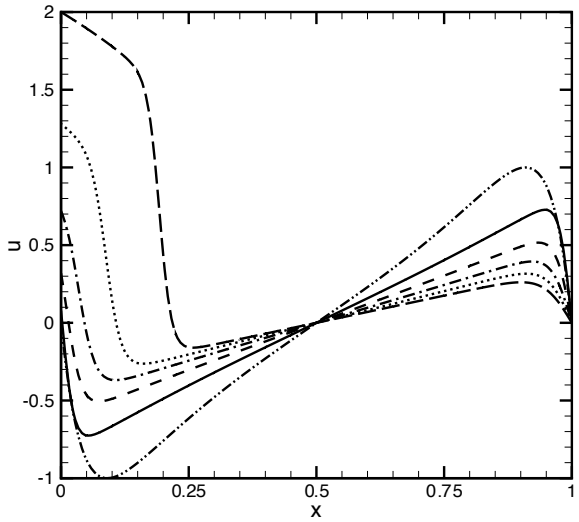

Figure C.4: State solution with prescribed Dirichlet boundary condition $\phi_L^* = 2t^2$ for $p = 4$: —·—·— initial profile; ——— the profile at $t = 0.2$; - - - - profile at $t = 0.4$; —·— profile at $t = 0.6$; ····· profile at $t = 0.8$; – – – profile at $t = 1$.

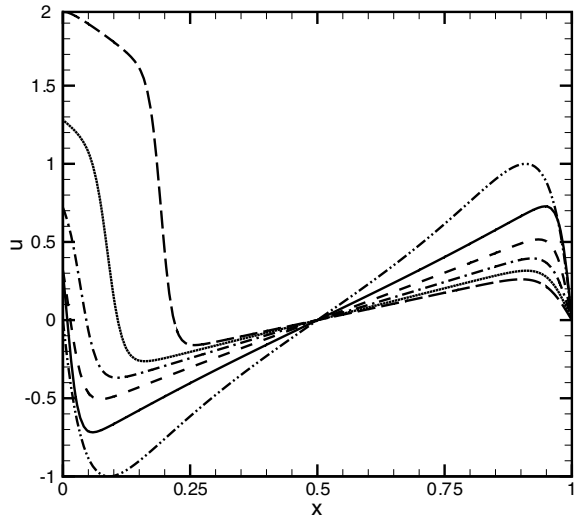

Figure C.5: Final optimal state solution using Dirichlet boundary control for $p = 4$: —·—·— initial profile; ——— the profile at $t = 0.2$; - - - - profile at $t = 0.4$; —·— profile at $t = 0.6$; ····· profile at $t = 0.8$; – – – profile at $t = 1$.

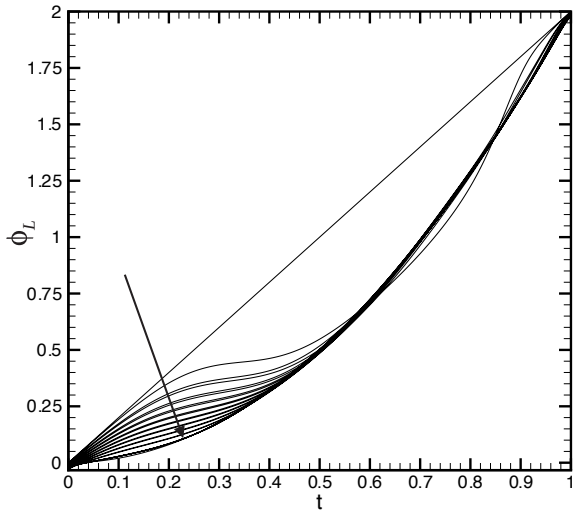

Figure C.6: Iteration history for Dirichlet optimal control with $p = 4$. The arrow shows the direction of increasing optimization iterations.

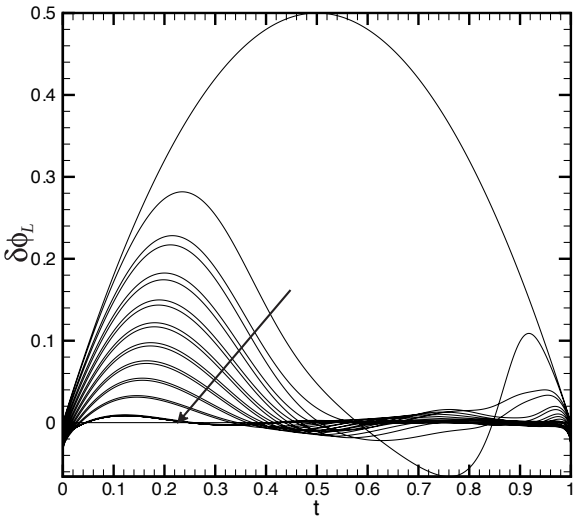

Figure C.7: Iteration history for the error in the Dirichlet optimal control with $p = 4$. The arrow shows the direction of increasing optimization iterations.

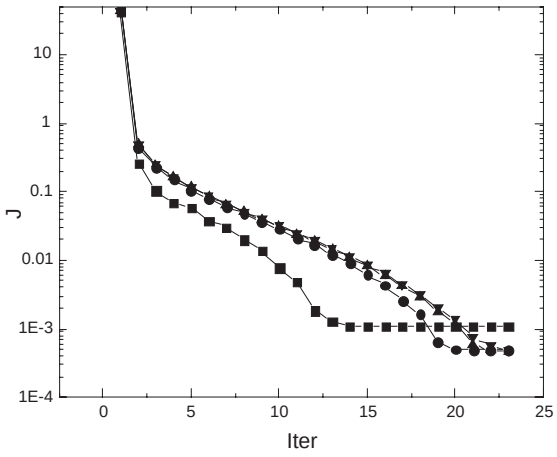

Figure C.8: Evolution of the objective functional, J, for Dirichlet control, ▪ $p = 2$; • $p = 4$; △ $p = 6$; ▽ $p = 7$.

this problem is defined as

$$\begin{aligned} \mathcal{J} &= \frac{\ell_2}{2}\int_0^1 \phi_R^2 dt \\ &+ \frac{\omega_1}{2}\int_0^1\int_0^1 (u-\tilde{u})^2 dxdt \\ &+ \frac{1}{2}\omega_2\int_0^1 \left[u(x,t_f)-\tilde{u}(x,t_f)\right]^2 dx \end{aligned} \tag{C.18}$$

where $\omega_1 = 100,000$, $\omega_2 = 1$, and $\ell_2 = 1 \times 10^{-7}$. The initial control is the linear distribution $\phi_R = -31.52(1 - 2\sqrt{t_f})t/t_f$.

After several iterations, the optimal solution becomes almost identical to the target solution as seen by comparing the target solution (Fig. C.9) with the final optimal state solution after 24 optimization iterations (Fig. C.10).

Good convergence is also obtained in the control profiles (Fig. C.11), however, by plotting the difference between the optimal control and the target control (Fig. C.12) we see that even after 24 iterations there are noticeable differences between the two, especially for early times. These differences are larger than those encountered for

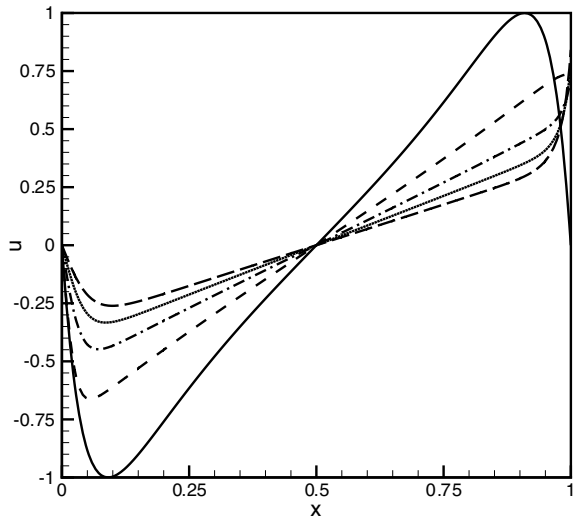

Figure C.9: State solution with prescribed Neumann boundary condition $\phi_R^* = -31.52(1 - 2\sqrt{t})$ using $p = 4$: —— initial profile; - - - - the profile at $t = 0.25$; —·— profile at $t = 0.5$; ····· profile at $t = 0.75$; – – – profile at $t = 1$.

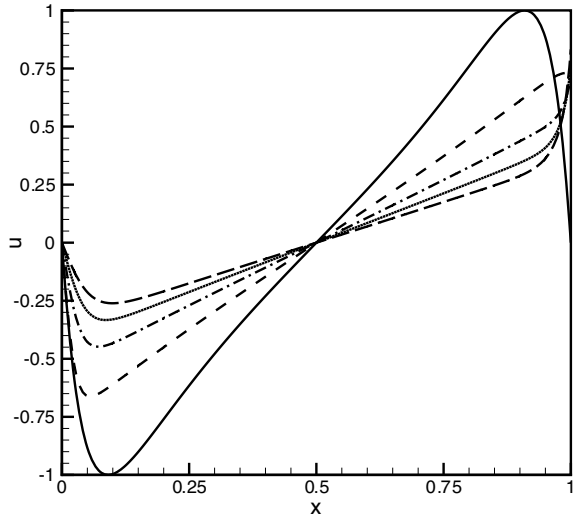

Figure C.10: Final optimal state solution for Neumann boundary control using $p = 4$: —— initial profile; - - - - the profile at $t = 0.25$; —·— profile at $t = 0.5$; ····· profile at $t = 0.75$; – – – profile at $t = 1$.

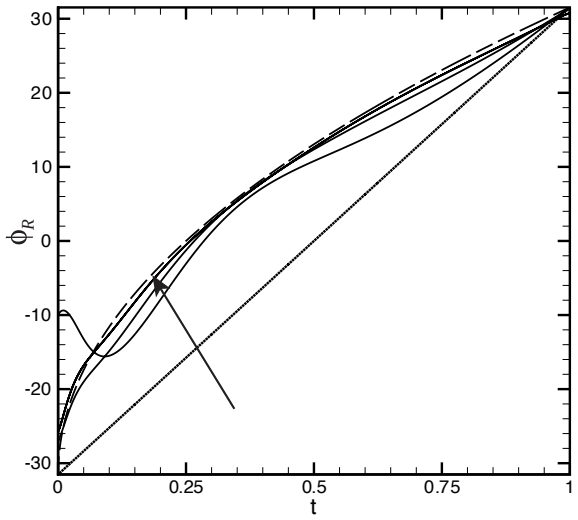

Figure C.11: Iteration history for Neumann optimal control using $p = 4$. The arrow shows the direction of increasing optimization iterations.

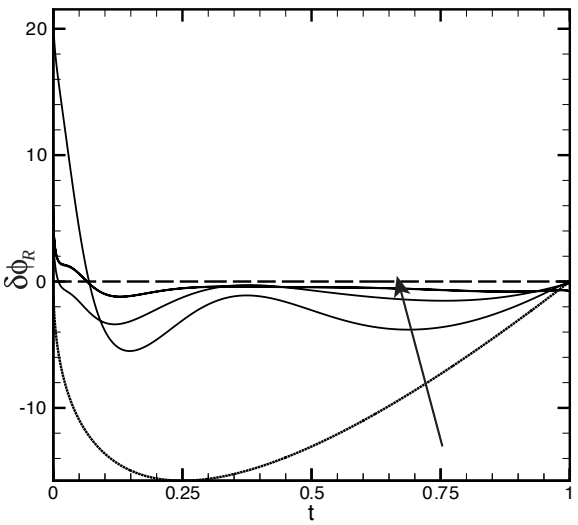

Figure C.12: Iteration history for the error in the Neumann optimal control for $p = 4$. The arrow shows the direction of increasing optimization iterations.

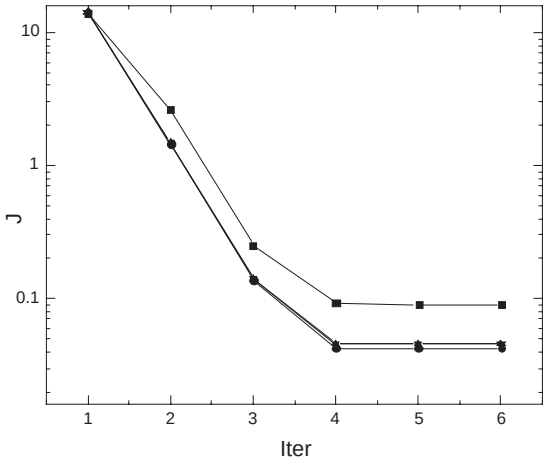

Figure C.13: Evolution of the objective functional, J, for optimal Neumann boundary control: ▪ $p = 2$; • $p = 4$; △ $p = 6$; ▽ $p = 7$.

Dirichlet control. Figure C.13 shows the convergence history for the objective function, J, for both $p = 4$ as well as other values of p. Increases in p beyond a value of 4 do not lead to a significant change in the optimal solution. It is important to remember that a gradient-based optimization algorithm only finds local minima — there is no guarantee that the global minima will be found. Thus it is possible that the current results are at a local optimum which would explain why we are not able to exactly recover the prescribed control profile for this inverse problem.

To determine whether an improved optimal solution can be obtained for this problem, we considered two additional initial guesses for the control profile. First, we added very small perturbations to the target control profile so that the initial control profile took the form $\phi_R = -31.52(1 - 2\sqrt{t}) + \varepsilon$. In this case the optimal control quickly converged to the target control. Next, we tried an initial control that contained a finite-amplitude oscillation about the target control, i.e. $\phi_R = -31.52(1 - 2\sqrt{t}) + 30t(1 - t)$. With this starting profile, Figs. C.14 and C.15 show that after several iterations, the optimal control almost recovers the target control profile. This is also seen in Fig. C.16 which compares the evolution of J given two

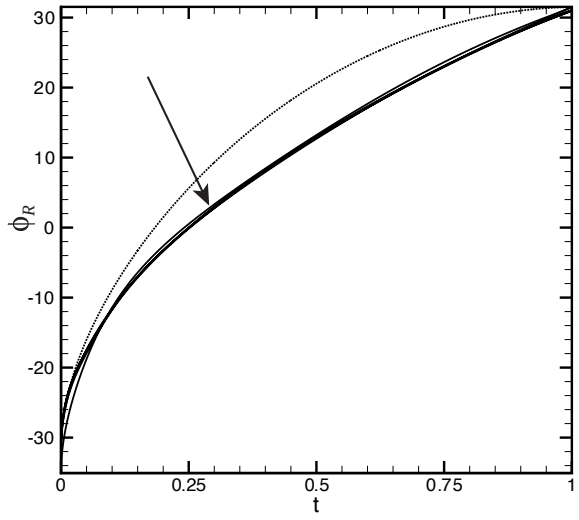

Figure C.14: Iteration history for Neumann boundary control starting from initial control $\phi_R = -31.52(1 - 2\sqrt{t}) + 30t(1 - t)$ and using $p = 6$. The arrow shows the direction of increasing optimization iterations.

different initial control distributions. Clearly, these two cases lead to a more optimal solution confirming the fact that the first case was a local minimum.

C.3.3 Summary of Burgers Control

In the prior sections we have described our continuous adjoint formulation and implementation for optimal control of problems governed by the unsteady Burgers equation where both the state and adjoint equations are discretized using discontinuous Galerkin in space. Results were presented for distributed control as well as both Dirichlet and Neumann boundary control and, in all cases, reductions in the objective function of at least one order of magnitude (or more) were obtained with a modest number (less than 6) of optimization iterations. Similar reductions in the gradient of the objective function (not shown here, but see Fig. 6.13 for similar results for Navier–Stokes flows) are also obtained indicating that our solutions are indeed approaching optimality. These results for Burgers control give us confidence in both our formulation and implementation of the continuous adjoint equation, boundary

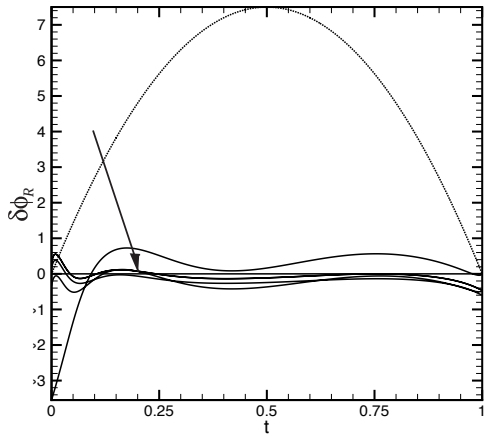

Figure C.15: Iteration history for the error in the Neumann boundary control starting from initial control $\phi_R = -31.52(1 - 2\sqrt{t}) + 30t(t_f - t)$ and using $p = 6$. The arrow shows the direction of increasing optimization iterations.

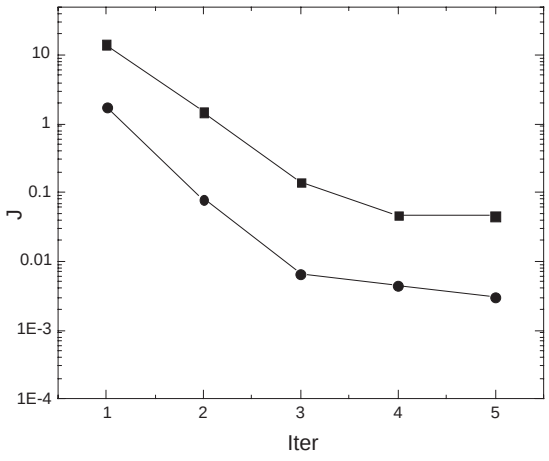

Figure C.16: Comparison of objective functionals J for Neumann control with different initial control profiles using $p = 6$: ▲ initial control profile $\phi_R = -31.52(1 - 2\sqrt{t_f t/t_f})$; ● initial control profile $\phi_R = -31.52(1 - 2\sqrt{t}) + 30t(t_f - t)$.

conditions, and gradient evaluation.

Bibliography

[1] F. Abergel and R. Temam. On some control problems in fluid mechanics. *Ther. Comp. Fluid Dyn.*, 1:303–325, 1990.

[2] R. Arieli and M. E. Tauber. Computation of subsonic and transonic flow over helicopter rotor blades. *AIAA Paper 79-1667*, 1979.

[3] D. N. Arnold, F. Brezzi, B. Cockburn, and L. D. Marin. Unified analysis of discontinuous Galerkin methods for elliptic problems. *SIAM J. Numer. Anal.*, 2001. submitted.

[4] D. N. Arnold, F. Brezzi, B. Cockburn, and L. D. Marin. Unified analysis of discontinuous Galerkin methods for elliptic problems. *SIAM J. Numer. Anal.*, 39(5):1749–1779, 2002.

[5] H. L. Atkins. Continued development of the discontinuous Galerkin method for compuational aeroacoustic applications. *AIAA Paper 97-1581*, 1997.

[6] H. L. Atkins and D. P. Lockard. A high-order method using unstructured grids for the aeroacoustic analysis of realistic aircraft configurations. *AIAA Paper 99-1945*, 1999.

[7] J. D. Baeder. Passive design for isolated blade-vortex interaction noise reduction. In *Proceedings of the 53rd Annual Forum of the American Helicopter Society*, volume Part 1, 1997.

[8] F. Bassi and S. Rebay. A high-order accurate discontinuous finite element method for the numerical solution of the compressible Navier–Stokes equations. *J. Comp. Phys.*, 131:267–279, 1997.

[9] F. Bassi and S. Rebay. A high order discontinuous Galerkin method for compressible turbulent flows. In B. Cockburn, G. E. Karniadakis, and C.-W. Shu, editors, *Discontinuous Galerkin Methods: Theory, Computation, and Applications*, number 11 in Lecture Notes in Computational Science and Engineering, pages 77–88. Springer, 2000.

[10] C. R. Berezin and L. N. Sankar. An improved navier-stokes/full potential coupled analysis for rotors. *Mathematical Computational Modeling*, 19(3/4):125–133, 1994.

[11] M. Berggren, R. Glowinski, and J. L. Lions. A computational approach to controllability issues for flow-related models. (I): Pointwise control of the viscous Burgers equation. *International Journal for Numerical Methods in Fluids*, 7:237–252, 1996.

[12] T. R. Bewley, P. Moin, and R. Teman. DNS-based predictive control of turbulence: an optimal target for feedback algorithms. *J. Fluid Mech.*, 447:179–225, 2001.

[13] P. J. Bismuti and D. A. Kopriva. Solution of acoustic scattering problems by a staggered-grid spectral domain decomposition method. In *Second Computational Aeroacoustics(CAA) Workshop on Benchmark Problems*, pages 69–78, 1997.

[14] D. A. Boxwell and F. H. Schmitz. Full-scale measurements of blade-vortex interaction noise. *Journal of American Helicopter Society*, 27(4), 1982.

[15] K. Brentner. Numerical algorithms for acoustic integrals- the devil is in the details. *AIAA Paper 96-1706*, 1996.

[16] K. Brentner. Modeling aerodynamically generated sound: Recent advances in rotor noise prediction. *AIAA Paper 2000-0345*, 2000.

[17] K. S. Brentner and F. Farassat. An analytical comparison of the acoustic analogy and kirchhoff formulation for moving surfaces. In *the American Helicopter Society 53rd Annual Forum*, 1997. Electronically available from http://techreports.larc.nasa.gov/ltrs/ PDF/1998/jp/NASA-98-aj-ksb.pdf .

[18] F. X. Caradonna and M. P. Isom. Subsonic and transonic potential flow over helicopter rotor blades. *AIAA J.*, 10(12):1606–1612, 1972.

[19] D. H. Chambers, R. J. Adrian, P. Moin, and D. S. Stewart. Karhunen–Lo'eve expansions of Burgers' model of turbulence. *Phys. Fluids*, 10:2573–2582, 1988.

[20] Y. Chang. *Reduced Order Methods for Optimal Control of Turbulence*. PhD thesis, Rice University, Mechanical Engineering and Materials Science, 2000.

[21] G. Chen and S. S. Collis. Optimal control of viscous flow using the discontinuous galerkin method. draft, 2003.

[22] G. Chen and S. S. Collis. Toward optimal control of aeroacoustic flows using discontinuous Galerkin discretizations. *AIAA paper 2004-0364*, January 2004.

[23] H. Choi, T. Temam, P. Moin, and J. Kim. Feedback control for unsteady flow and its application to the stochastic Burgers equation. *J. Fluid Mech.*, 253:509–543, 1993.

[24] B. Cockburn, editor. *High-order methods for computational applications, Lecture Notes in Computational Science and Engineering*, chapter Discontinuous Galerkin methods for convection-dominated problems, pages 69–224. Springer, Berlin, 1999.

[25] B. Cockburn, G. Karniadakis, and C.-W. Shu, editors. *Discontinuous Galerkin Methods: Theory, Computation, and Applications*. Springer, 2000.

[26] C. Coclici, W. Wendland, and J. Heiermann. A heterogeneous domain decomposition for initial-boundary value problems with conservation laws and electromagnetic fields.

[27] C. A. Coclici. *Domain Decomposition Methods and Far–Field Boundary Conditions for Compressible Flows Around Airfoils*. PhD thesis, Mathematical Institute A, University of Stuttgart, Pfaffenwaldring 57, D-70569 Stuttgart, Germany, 1998.

[28] C. A. Coclici, G. Morosanu, and W. L. Wendland. Asymptotic correction of the numerical solution to a heterogeneous domain decomposition for compressible plasma flows. In preparation, 2000.

[29] S. S. Collis. *A Computational Investigation of Receptivity in High-Speed Flow Near a Swept Leading-Edge*. PhD thesis, Stanford University, March 1997.

[30] S. S. Collis. The DG/VMS method for unified turbulence simulation. *AIAA Paper 2002-3124*, 2002.

[31] S. S. Collis. Discontinuous Galerkin methods for turbulence simulation. In *Proceedings of the 2002 Center for Turbulence Research Summer Program*, pages 155–167, 2002.

[32] S. S. Collis and K. Ghayour. Discontinuous Galerkin for compressible DNS. *ASME paper number FEDSM2003-45632*, 2003.

[33] S. S. Collis, K. Ghayour, and M. Heinkenschloss. Optimal control of aeroacoustic noise generated by cylinder vortex interaction. *Int. J. Aero*, 1(2):97–114, 2002.

[34] S. S. Collis, K. Ghayour, and M. Heinkenschloss. Optimal control of aeroacoustics: Transpiration boundary control. *AIAA Paper 2002-2757*, 2002.

[35] S. S. Collis, K. Ghayour, and M. Heinkenschloss. Optimal control of aeroacoustics: Transpiration boundary control. *AIAA J.*, 41(7), July 2003.

[36] S. S. Collis, K. Ghayour, M. Heinkenschloss, M. Ulbrich, and S. Ulbrich. Numerical solution of optimal control problems governed by the compressible Navier–Stokes equations. In *International Series of Numerical Mathematics*, volume 139, pages 43–55. Birkhäuser Verlag, 2001.

[37] S. S. Collis, K. Ghayour, M. Heinkenschloss, M. Ulbrich, and S. Ulbrich. Towards adjoint-based methods for aeroacoustic control. *AIAA Paper 2001-0821*, 2001.

[38] S. S. Collis, K. Ghayour, M. Heinkenschloss, M. Ulbrich, and S. Ulbrich. Optimal control of unsteady compressible viscous flows. *Inter. J. Num. Meth. Fluids*, 40:1401–1429, 2002.

[39] S. S. Collis and S. K. Lele. A computational approach to swept leading-edge receptivity. *AIAA Paper 96-0180*, 1996.

[40] S. S. Collis and S. K. Lele. A computational investigation of receptivity in high-speed flow near a swept leading-edge. Technical Report TF-71, Flow Physics and Computation Division, Department of Mechanical Engineering, Stanford University, April 1997.

[41] T. Colonius, P. Moin, and S. K. Lele. Direct computation of aerodynamic sound. Technical Report TF-65, Thermoscience Division, Department of Mechanical Engineering, Stanford University, Stanford, CA 94305, June 1995.

[42] D. G. Crighton, A. P. Dowling, J. E. F. Williams, M. Heckl, and F. G. Leppington. *Mordern Methods in Analytical Acoustics: Lecture Notes*. Springer-Verlag, 1992.

[43] G. Djambazov, C. Lai, and K. Pericleous. Development of a domain decomposition method for computational aeroacoustics. In *DD9 Proceedings*. John Wiley & Sons, 1997. Electronically available from http://www.gre.ac.uk/ dg06/papers/norpap.ps.

[44] G. Djambazov, C. Lai, and K. Pericleous. Efficient computation of aerodynamic noise. *Comptemporary Mathematics*, 218:506–512, 1998. Electronically available from http://www.gre.ac.uk/ dg06/papers/colpap.ps.

[45] D.Stanescu, M.Y.Hussaini, and F. Farassat. Aircraft engine noise scattering -a discontinuous spectral element approach, 2002.

[46] F. Farassat. Introduction to generalized functions with applications in aerodynamics and aeroacoustics, corrected copy. Technical paper 3428, NASA, 1994. Electronically available from ftp://techreports.larc.nasa.gov/pub/techreports/larc/94/tp3428.ps.Z.

[47] F. Farassat and M. K. Myers. Extension of kirchhoff's formula to radiation from moving surfaces. *Journal of Sound and Vibration*, 123(3):451–460, 1988.

[48] P. Francescantonio. A new boundary integral formulation for the prediction of sound radiation. *Journal of Sound and Vibration*, 202:491–509, 1997.

[49] F. B. Freund. Noise sources in a low reynolds number turbulent jet at mach 0.9. *J. Fluid Mech.*, (438):277–305, 2001.

[50] F. B. Freund, S. K. Lele, and P. Moin. Numerical simulation of a Mach 1.92 turbulent jet and its sound field. *AIAA J.*, 38(11):2023–31, 2000.

[51] J. B. Freund. A simple method for computing far-field sound in aeroacoustic computations. *J. Comp. Phys.*, 157:796–800, 1997.

[52] J. B. Freund, S. K. Lele, and P. Moin. Matching of near/far-field equation sets for direct computations of aerodynamic sound. *AIAA Paper 93-4326*, 1993.

[53] A. R. George and A. S. Lyrintzis. Acoustics of transonic blade-vortex interactions. *AIAA Journal*, 26:769–776, 1988.

[54] W. W. Hager. Runge–Kutta methods in optimal control and transformed adjoint system. *Numerische Mathmatik*, 87(2):247–282, 2000.

[55] J. C. Hardin and M. Y. Hussaini, editors. *Computational Aeroacoustics*. Springer-Verlag, 1993.

[56] A. A. Hassan, F. K. Straub, and B. D. Charles. Effects of surface blowing/suction on the aerodynamics of helicopter rotor blade-vortex interactions (bvi) – a numerical simulation. *The Journal of the American Helicopter Society*, 1997.

[57] C. Hirsch. *Numerical Computation of Internal and External Flows, Vol. II: Computational Methods for Inviscid and Viscous Flows*. Wiley, New York, 1990.

[58] C. Homescu, I. M. Navon, and Z. Li. Suppresion of vortex shedding for flow around a circular cylinder using optimal control. *International Journal for Numerical Methods in Fluids*, Volume 38, Issue 1:43–69, 2002.

[59] F. Q. Hu, M. Y. Hussaini, and P. Rasetarinera. An analysis of the discontinuous Galerkin method for wave propagation problems. *J. Comp. Phys.*, 151:921–046, 1999.

[60] C. A. Hunter and R. H. Thomas. Development of a jet noise prediction method for installed jet configuration. *AIAA Paper 2003-3196*, 2003.

[61] A. Jameson, L. Martinelli, and N. A. Pierce. Optimum aerodynamic design using the Navier–Stokes equations. *Ther. Comp. Fluid Dyn.*, 10(1–4):213–237, 1998.

[62] A. Jameson, S. Shankaran, L. Martinelli, and B. Haimes. Aerodynamic shape optimization of complete aircraft configuration. *AIAA Paper 2004-0533*, 2004.

[63] H. E. Jones. Full-potential modeling of blade-vortex interactions. *NASA Technical Paper 3651*, 1997.

[64] R. D. Joslin, M. D. Gunzburger, R. A. Nicolaides, G. Erlebacher, and M. Y. Hussaini. A self-contained automated methodology for optimal flow control validated for transition delay. *NASA Contractor Report 198215*, ICASE 95-64, 1995.

[65] E. J. Kerschen. Active aerodynamic control of wake-airfoil interaction noise theory. *DGLR/AIAA Paper 92-02-039*, 1992.

[66] G. Kirchhoff. Zur theorie der lichtstrahlen. *Annalen der Physik und Chemie*, 18:663–695, 1883.

[67] D. A. Kopriva and J. H. Kolias. Solution of acoustic workshop problems by a spectral multi-domain method. In *ICASE/LARC Workshop on Benchmark Problems in Computational Aeroacoustics*, pages 117–124, 1995.

[68] S. Krishnamoorthy and J. S. Marshall. Three-dimensional blade-vortex interaction in the strong vortex regime. *Phys. Fluids*, 10(11):2828–2845, 1998.

[69] K. Kunisch and S. Volkwein. Control of Burger's equation by a reduced order approach using proper orthogonal decomposition. *J Opt Theor App*, 102(2):345–371, 1999.

[70] E. Lee and S. S. Collis. Complex flow modelling with the discontinuous galerkin method, 2002.

[71] S. Lee. Reduction of blade-vortex interaction noise through porous leading edge. *AIAA Journal*, 32(3):480–488, 1994.

[72] S. K. Lele. Compact finite difference schemes with spectral-like resolution. *J. Comp. Phys.*, 103(1):16–42, 1992.

[73] J. W. Leverton and F. W. Taylor. Helicopter blade slap. *Journal of Sound and Vibration*, 4, 1966.

[74] Z. Li, I. M. Navon, M. Hussaini, and F. L. Dimet. Optimal control of cylinder wakes via suction and blowing. *Computers & Fluids*, Volume 32, Issue 2:149–171, 2003.

[75] L. M. Lighthill. On sound generated aerodynamically, i. general theory,. In *Proceedings of The Royal Society*, volume 221A, pages 564–587, London, 1952.

[76] G. M. Lilley. On the noise from jets: Noise mechanisms. *AGARD-CP-131*, pages 13.1–13.12, 1974.

[77] T. B. Lim, L. N. Sankarand, N. Hariharan, and N. N. Reddy. A technique for the prediction of propeller induced acoustic loads on aircraft structures. *AIAA Paper 93-4340*, 1993.

[78] A. Lyrintzis, R. R. Mankbadi, O. Baysal, and M. Ikegawa, editors. *Computational Aeroacoustics-1995*. ASME, 1995.

[79] A. S. Lyrintzis. Review: The use of kirchhoff's method in computational aeroacoustics. *Transactions of the ASME, Journal of Fluids Engineering*, 116:665–676, 1994.

[80] A. S. Lyrintzis. Surface integral methods in computational aeroacoustics – from the (cfd) near-field to the (acoustic) far-field. *International Journal of Aeroacoustics*, 2(2):95–128, 2003.

[81] A. S. Lyrintzis and A. Uzun. Integral techniques for jet aeroacoustics calculations. *AIAA Paper 2001-2253*, 2001.

[82] A. S. Lyrintzis and Y. Xue. Study of the noise mechanisms of transonic blade-vortex interactions. *AIAA Journal*, 29:1562–1572, 1991.

[83] R. M. Martin and W. R. Splettstoesser. Blade-vortex interaction acoustic results from a 40% model rotor in the dnw. *Journal of American Helicopter Society*, 33(1), 1988.

[84] M. S. McCluer. Helicopter blade-vortex interaction noise with comparisons to CFD calculations. Technical Report NASA TM-110423, NASA Ames Research Center, 1996.

[85] C. Min and H. Choi. Suboptimal feedback control of vortex shedding at low reynolds numbers. *J. Fluid Mech.*, 401(1):123–156, 1999.

[86] R. P. Morgans. The kirchhoff formula extened to a moving surface. *Philosophical Magazine*, 9:141–161, 1930.

[87] P. M. Morse and K. U. Ingard. *Theoretical Acoustics*, pages 400–405. Princeton University Press, 1968.

[88] R. Morvant. *The Investigation of Blade-Vortex Interaction Noise Using Computational Fluid Dynamics*. PhD thesis, University of Glasgow, 2004.

[89] Y. Nakamura. Prediction of blade vortex interaction from measured blade pressure. *AHS Seventh European Rotorcraft Powered Lift*, 1981.

[90] V. Parameswaran and J. Baeder. Reduction of blade vortex intera ction noise using prescribed pitching. *AIAA Paper 96*, 1995.

[91] M. Paraschivoiu, X. Cai, D. Y. M. Sarkis, and D. Keyes. Multi-domain multi-model formulation for compressible flows: Conservative interface coupling and parallel implicit solvers for 3d unstructured meshes, 1999.

[92] M. Paraschivoiu and X.-C. Cai. A unigrid multi-model full potential and euler formulation for transonic flows.

[93] D. Park, D. Ladd, and E. Hendricks. Feedback control of karman vortex shedding, 1992.

[94] N. Peake and D. G. Crighton. Active control of sound. *Annual Review of Fluid Mechanics*, 32:137–164, 2000.

[95] O. M. Phillips. On the generation of sound by supersonic turbulent shear layers. *JFM*, 9:1–28, 1960.

[96] T. J. Poinsot and S. K. Lele. Boundary conditions for direct simulations of compressible viscous flows. *J. Comp. Phys.*, 101(1):104–129, 1992.

[97] W. H. Press, S. A. Teukolsky, W. T. Vetterling, and B. P. Flannery. *Numerical Recipes*. Cambridge University Press, 1996.

[98] A. Quarteroni and A. Valli. *Domain Decomposition Methods for Partial Differential Equations*. Cambridge University Press, 1999.

[99] P. Rasetarinera, M. Y. Hussaini, and F. Q. Hu. Some remarks on the accuracy of the discontinuous galerkin method. In B. Cockburn, G. E. Karniadakis, and C.-W. Shu, editors, *Discontinuous Galerkin Methods: Theory, Computation, and Applications*, number 11 in Lecture Notes in Computational Science and Engineering, pages 407–412. Springer, 2000.

[100] P. Rasetarinera, D. A. Kopriva, and M. Y. Hussaini. Discontinuous spectral element solution of aeroacoustic problems. In *Third Computational Aeroacoustics(CAA) Workshop on Benchmark Problems*, pages 103–115, 2000.

[101] P. Rasetarinera, D. A. Kopriva, and M. Y. Hussaini. Discontinuous spectral element solution of acoustic radiation from thin airfoils. *AIAA Journal*, 39(11):2070–2075, 2001.

[102] L. N. Sankar, B. K. Bharadvaj, and F. L. Tsung. Three-dimensional navier-stokes/full potential coupled analysis for transonic viscous flow. *AIAA J.*, 31(10), 1993.

[103] F. H. Schmitz. Reduction of blade-vortex interaction (BVI) noise through X-force control. *Journal of the American Helicopter Society*, 43(1):14–24, 1998.

[104] F. H. Schmitz and D. A. Boxwell. In flight far-field measurement of helicopter impulsive noise. *Journal of American Helicopter Society*, 21(4), 1976.

[105] T. Schwartzkopff, M. Dumbser, and C.-D. Munz. Caa using domain decomposition and high order methods on structured and unstructured meshes. In *Proceedings of the AIAA/CEAS Aeroacoustics Conference 2004*, 2004.

[106] J. Sesterhenn. A characteristic–type formulation of the navier–stokes equations for high order upwind schemes. *Computers & Fluids*, 30:37–67, 2001.

[107] J. C. Simonich, P. Lavrich, T. G. Sofrin, and D. A. Topol. Active aerodynamic control of wake-airfoil interaction noise-experiment. *DGLR/AIAA Paper 92-02-038*, 1992.

[108] B. Soemarwoto. The variational method for aerodynamic optimization using navier-stokes equation. NASA Contract Report ICASE Report No. 97-71, NASA Langley Research Center, December 1997.

[109] S. Sritharan, Y. Ou, D. Park, and D. Ladd. Optimal control of viscous flow past a cylinder: mathematical theory, computation and experiment-part i. actual problems of aviation and aerospace systems. *Russ-Am Sci J*, 1:5–15, 1996.

[110] S. Sritharan, Y. Ou, D. Park, and D. Ladd. Optimal control of viscous flow past a cylinder: mathematical theory, computation and experiment-part ii. actual problems of aviation and aerospace systems. *Russ-Am Sci J*, 2:7–18, 1996.

[111] D. Stanescu, D. Ait-Ali-Yahia, W. G. Habashi, and M. P. Robichaud. Multidomain spetral computations of sound radiation from ducted fans. *AIAA Journal*, 37(3):296–302, 1999.

[112] J. M. Summa. Potential flow about 3-dimensional lifting configurations with applications to wings and rotors. *AIAA Paper 75-126*, 1975.

[113] C. K. W. Tam and Z. Dong. Radiation and outflow boundary conditions for direct computation of acoustic and flow disturbances in a nonuniform mean flow. In *First Joint CEAS/AIAA Aeroacoustics Conference*, number CEAS/AIAA Paper 95-007, pages 45–54, 1995.

[114] C. K. W. Tam and J. C. Webb. Dispersion-relation-preserving finite difference schemes for computational acoustics. *J. Comp. Phys.*, 107:262–281, 1993.

[115] T. E. Tezduyar. Stabilized finite element formulations for incompressible flow computations. *Adv. Appl. Mech.*, 28:1–44, 1991.

[116] K. W. Thompson. Time-dependent boundary conditions for hyperbolic systems. *J. Comp. Phys.*, 68:1–24, 1987.

[117] K. W. Thompson. Time-dependent boundary conditions for hyperbolic systems, II. *J. Comp. Phys.*, 89:439–461, 1990.

[118] A. Uzun, G. A. Blaisdell, and A. S. Lyrintzis. 3-d large eddy simulation for jet aeroacoustics. *AIAA Paper 2003-3322*, 2003.

[119] K. Viswanathan and L. N. Sankar. Toward the direct calculation of noise: Fluid/acoustic coupled simulation. *AIAA Journal*, 33(12):2271–2279, 1995.

[120] K. Viswanathan, L. N. Sankarand, and N. N. Reddy. A fluid/acoustic coupled simulation of supersonic jet noise. *AIAA Paper 94-0137*, 1994.

[121] S. E. Widnall. Helicopter noise due to blade-vortex interactions. *Journal of the Acoustical Society of America*, 50(1), 1971.

[122] J. F. Williams and D. Hawkings. Sound generation by turbulence and surfaces in arbi-trary motion. *Phil. Trans. Roy. Soc.*, pages 321–342, 1969.

[123] Y. Xue and A. S. Lyrintzis. Rotating Kirchhoff method for three-dimensional transonic blade-vortex interaction hover noise. *AIAA J.*, 32(7):1350–1359, 1994.

[124] W. S. Yu and B. Lakshminarayana. Numerical simulation of the effects of rotor-stator spacing and wake/blade count ratio on turbomachinery unsteady flows. *J. Fluid Eng.*, 117(4):639–646, 1995.

[125] Y. H. Yu. Rotor blade-votex interaction noise. *Prog. Aero. Sci.*, 36(2):97–115, February 2000.

[126] Y. H. Yu, B. Gmelin, W. Splettstoesser, J. J. Philippe, J. Prieur, and T. F. Brooks. Reduction of helicopter blade-vortex interaction noise by active rotor control technology. *Prog. Aero. Sci.*, 33(9–10):647–687, 1997.